Search for Lepton Flavour violating decayB0 → K⋆0τ ±e with the LHCb experiment,contribution in Rare Decay trigger configuration andimplementation of isolation tools for the Upgrade of the detector

Tommaso Fulghesu





Sorbonne Université (SU)
Sciences de la Terre et de l'Environnement et Physique de l'Univers de Paris (STEP'UP 560)

Search for Lepton Flavour violating decay $B^0 \to K^{*0}\tau^{\pm}e^{\mp}$ with the LHCb experiment, contribution in Rare Decay trigger configuration and implementation of isolation tools for the Upgrade of the detector

par **Tommaso FULGHESU**
Thèse de doctorat en physique des particules
Dirigée par **Pascal VINCENT** et **Francesco POLCI**

Thèse présentée et soutenue publiquement le 19/09/2024

Membres du jury:

Examinatrice: Mme. Sacha DAVIDSON
Rapporteur: M. Frédéric MACHEFERT
Examinateur: M. Marco PAPPAGALLO
Directeur de thèse: M. Francesco POLCI
Rapporteuse: Mme. Justine SERRANO
Présidente du jury: Mme. Sophie TRINCAZ-DUVOID
Directeur de thèse: M. Pascal VINCENT

Abstract

University name: Sorbonne Université (SU)
Ecole doctorale: Ecole doctorale des Sciences de la Terre et de l'environnement et Physique de l'Univers, Paris (STEP'UP 560)
Laboratory: Laboratoire de physique nucléaire et des hautes énergies (LPNHE)
Thesis title: Search for Lepton Flavour violating decay $B^0 \to K^{*0}\tau^{\pm}e^{\mp}$ with the LHCb experiment, trigger selections and isolation implementation for the Upgrade of the detector

In this thesis, I present my two main contributions to the LHCb experiment. The first one concerns the development and configuration of the LHCb software trigger for the LHCb Upgrade. Multiple accomplishments were achieved. First, I developed several software algorithms and tools, named ThOr functors, oriented to fast and parallel programming logic. Part of this work is functional in implementing within the software framework a powerful tool called "isolation", which is used for background suppression in many physics analyses. Additionally, I performed rate and bandwidth studies needed to define the trigger selections for the physics analysis of the LHCb Rare Decays working group, in particular for Lepton Flavour Violation searches and Lepton Flavour Universality tests.
The second main contribution is the first-ever search for the Lepton Flavour Violating decay $B^0 \to K^{*0}\tau^{\pm}e^{\mp}$ using data collected at LHCb during Run 2 for a total integrated luminosity of 5.6 fb^{-1}. I performed all the steps of the analysis: the definition of the selection, the evaluation of its efficiency, the determination of the systematic uncertainties, the fit to the data, the evaluation of the expected upper limit on the branching fractions of these decays, which correspond to $\sim 3 \times 10^{-6}$.

Résumé

Dans ce mémoire de thèse, je présente deux de mes principales contributions à l'expérience LHCb. La première porte sur le développement et la configuration de logiciels de déclenchement de l'expérience LHCb. Dans ce cadre, de nombreuses études ont été réalisées. Tout d'abord, j'ai développé plusieurs algorithmes et outils logiciels, appelés "ThOr functors", orientés vers une logique de programmation rapide et parallélisé. Une autre partie du travail a consisté à mettre en œuvre, dans l'environnement logiciel de l'expérience, un outil performant nommé "isolation". Cet outil est utilisé pour optimiser la suppression de bruits de fond dans de nombreuses analyses de physique au sein de la collaboration. En outre, j'ai réalisé des études sur les limites que les taux de déclenchement des données peuvent atteindre compte tenue de la bande passantes disponible pour leur transfert et leur stockage. Cela m'a amené à définir les critères de sélection des événements pour les analyses de physique du groupe de travail sur les désintégrations rares de la collaboration LHCb; en particulier pour les recherches de violation de la saveur des leptons et les tests d'universalité de la saveur leptonique. La deuxième contribution principale est la toute première recherche de la désintégration $B^0 \to K^{*0}\tau^{\pm}e^{\mp}$ violant la saveur leptonique à l'aide des données collectées au LHC pendant la seconde compagne de prise de données (nommée "Run 2") qui a permis d'accumuler une luminosité intégrée totale de 5,6 fb$^-$1. J'ai réalisé toutes les étapes de l'analyse : la définition de la sélection des données, l'évaluation de son efficacité, la réduction des différents bruits de fond, la détermination des incertitudes systématiques jusqu'à l'ajustement de mon analyse aux données de l'expérience. J'ai pour en extraire une évaluation de la limite supérieure attendue des fractions d'embranchement de ces désintégrations, que j'ai estimé à 3×10^{-6}.

Acknowledgments

The incredible journey of my PhD within the LHCb collaboration and at LPNHE has been largely thanks to the exceptional guidance of my advisors. Francesco and Pascal are remarkable physicists who have supported me throughout this journey, helping me grow scientifically to become independent. They also taught me how to embrace French culture, from the language and traditions to the food.

I am deeply grateful to the many people I've met along the way who have helped me through both the carefree and challenging moments. In Paris and at CERN, I received support and formed friendships that were essential during these years. Thanks to the A-team, to my colleagues and to all the other people I met along this way - too many to name everyone, sorry. I will always carry these connections with me. I especially want to thank Gio, who has always been there to support (and endure) me throughout the last couple of years, particularly in the process of writing and finalizing this thesis. She believes in me more than I believe in myself.

Un ringraziamento speciale va ai ragazzi della Coop, una compagnia indissolubile che esiste da sempre. I miei amici più cari, coloro che ci sono sempre stati e sempre ci saranno. Gran parte dei miei traguardi è merito loro. Grazie alla mia famiglia: papà, mamma e nonni. Senza di loro non sarei arrivato fin qua. Grazie di aver creduto nelle mie capacità, spero di avervi reso orgogliosi.

Finally, I would like to thank Dorothea and the group in Marseille. They have placed their trust in me and given me a great opportunity. A new adventure is about to begin, one that will require starting from scratch. It will be challenging and stressful, with more responsibilities and fewer hours of sleep. Yet, I can't wait to dive in headfirst and embrace this challenge.

Contents

Acronyms

ACBDT anti-combinatorial BDT. 96

ACMVA anti-combinatorial multivariate analysis. 96

ALICE A Large Ion Collider Experiment. 34

ATLAS A Toroidal LHC ApparatuS. 34

AUC area under the curve. 100, 101, 108, 226, 291

BR branching ratio. 26, 173, 175, 176, 279, 288

BSM Beyond the SM. 20, 21, 23, 24, 37, 89

CKM Cabibbo–Kobayashi–Maskawa. 14, 19–21, 75, 200, 279

CL confidence level. 90, 188, 302

cLFV Charged Lepton Flavour Violation. 14, 20, 21, 24

CMS Compact Muon Solenoid. 34

DAQ data acquisition system. 54

DPA Data Processing & Analysis. 67

DSCB Double-Sided Crystal Ball. 154, 157, 161, 171–173, 175, 176, 180, 271–276, 288, 297, 304

DTF DecayTreeFitter. 93–95, 97, 154, 159, 160, 282, 283, 287, 288, 300

ECAL Electromagnetic CALorimiter. 41, 50, 51, 60, 281

EFT Effective Field Theory. 14, 23, 24

EW electroweak. 13, 16–18, 20, 21, 23–27, 56

FCNC flavour-changing neutral current. 20, 21, 279

FD flight distance. 120

FunTuple Functional Tuple. 70, 71

GEC Global Event Cut. 139

HCAL Hadronic CALorimeter. 41, 50, 51, 60, 265, 281, 296

HL-LHC High-Luminosity LHC. 36

HLT High-Level Trigger. 52

HLT1 High Level Trigger 1. 41, 52–54, 62, 66, 98, 100, 168

HLT2 High Level Trigger 2. 41, 52, 54, 62, 63, 66–68, 75, 84, 98, 100

IP impact parameter. 44

IsoFisher Fisher isolation. 96

IsoMVA isolation multivariate analysis. 96

IT Inner Turicensis. 43, 46–48, 280, 281

L0 Level 0. 41, 52, 53, 61, 65, 98–100, 300

LFU Lepton Flavour Universality. 20, 21

LFUV Lepton Flavour Universality Violation. 66

LFV Lepton Flavour Violation. 13, 14, 21, 28, 66

LHC Large Hadron Collider. 33–37, 52, 65, 67, 280, 299

LHCb Large Hadron Collider beauty. 34

LHCf Large Hadron Collider forward. 35

LINAC 2 LINear ACcelerator 2. 34

LQ *leptoquark*. 27, 28, 280

LS1 Long Shutdown 1. 36

LS2 Long Shutdown 2. 36, 41

LS4 Long Shutdown 4. 42

MaPMT multi-anode photo-multipliers. 60

MC Monte Carlo. 87, 88, 90–92, 99, 101, 104, 108, 109, 111, 114, 115, 117, 119, 121, 126, 127, 132–135, 139, 144–149, 155, 156, 161, 162, 164, 165, 167–169, 180, 182, 183, 212, 221, 223–225, 228–230, 251, 253, 283–288, 290–292, 300, 301, 303, 304

MCM minimally corrected mass. 92, 95, 282

MoEDAL Monopole and Exotics Detector At the LHC. 35

NP New Physics. 13, 14, 18, 23, 24, 26–28, 34, 87, 279

OC opposite-charge. 88–90, 120, 121, 123–131, 154, 157–159, 165, 172, 173, 175, 176, 178, 180, 182, 233–235, 237, 240–244, 273–278, 285–289, 292–294, 297, 300

OS opposite-sign. 89, 100, 101, 104, 106, 108–117, 119–123, 126–128, 131, 220, 222, 224–232, 234, 237, 238, 271, 277, 278, 283–286, 290–293, 297

OT Outer Turicensis. 43, 46, 47, 280

PDG Particle Data Group. 93, 97, 124, 168, 169

PID particle identification. 60, 77, 117, 118, 148, 284

PM partial mass. 93, 95, 282

PMNS Pontecorvo-Maki–Nakagawa–Sakata. 20, 21, 23, 279

PS PreShower. 41, 50, 60

PS Proton Synchrotron. 34, 50, 51, 281

PV primary vertex. 40, 43, 44, 54

QCD quantum chromodynamics. 27

QFT Quantum Field Theory. 191

RD Rare Decay. 66, 75, 84

RF radio-frequency. 37, 280

RICH Ring Imaging CHerenkov detector. 40, 48, 54, 60, 98

ROC receiving operating characteristic. 100, 107, 108, 111, 220, 221, 226, 284, 290, 291

RTA Real-Time Analysis. 66

SC same-charge. 89, 90, 120, 121, 123–131, 154, 157, 160, 165, 172, 173, 175, 176, 178, 180, 182, 233–235, 238, 245–250, 273–278, 285, 286, 288, 289, 292–295, 297, 300

SciFi Scintillating Fibers. 54, 59, 60, 281

SIMD Single Instruction, Multiple Data. 71

SiPM silicon photomultiplier. 59

SM Standard Model. 5, 13–21, 23–25, 27, 28, 37, 87, 195, 279, 299

SMEFT Effective Field Theory of the SM. 21

SOA structure-of-arrays. 69, 71

SPD Silicon Pad Detector. 41, 50, 51, 53, 60, 281

SPS Super Proton Synchrotron. 34

SS same-sign. 89, 101, 104–111, 113–115, 117, 121, 123, 126, 129, 220, 222, 224–232, 235, 266, 267, 283–285, 290–292, 296

SSB Spontaneous Symmetry Breaking. 16, 21, 23, 195–197

SV secondary vertex. 40, 54

TauBDT τ identification BDT. 96

TauMVA τ identification multivariate analysis. 96

TCK Trigger Configuration Key. 99, 212, 303

ThOr Throughput Oriented. 65, 68–71, 82

TIS Triggered Independent on Signal. 98, 165

TMVA Toolkit for Multivariate Analysis. 100, 107

TOS Triggered On Signal. 98, 165

TOTEM TOTal Elastic and diffractive cross-section Measurement. 35

TT Tracker Turicensis. 43, 46, 47, 49, 58, 280

UT Upstream Turicensis. 54, 58, 63, 281

VELO VErtex LOcator. 40, 43–45, 49, 52–54, 57, 58, 63, 280, 281

Glossary

CP-violation Violation of both charge conjugation symmetry and parity symmetry. As a consequence, the laws of physics are not the same if particle and antiparticle are interchanged and spatial coordinates are inverted

bandwidth Maximum rate per unit time at which data could be processed

chirality Fundamental propriety (Lorentz invariant) of the particle related to how its quantum mechanical wave function behaves when the particle is rotated. For massless particles, it corresponds to helicity. For massive particles, it is possible to find a reference frame where the two differ

flight distance Distance travelled by a particle from its origin point to the point where it decays into other particles.

helicity Projection of the spin vector onto the momentum vector, distinguishing between "left" and "right" handed. It is not a Lorentz invariant property

impact parameter Perpendicular distance between the particle's trajectory and the primary interaction point. Fundamental for the identification of particles originating from secondary vertex

luminosity Property of an experiment to produce collision events, measured as number of particle collisions per unit area and unit time

primary vertex Reconstructed point in the detector data that represents the origin of the particles produced in the proton-proton collision

pull Discrepancy between the measured value and the expected value, normalized by the uncertainty of the measurement

secondary vertex Reconstructed point in the detector data that represents the origin of the particles produced by the decay of another particle. It is located at some distance from the primary vertex

throughput Data processed per unit time

vacuum expectation value Value of the Higgs field in its lowest energy state, or vacuum state

Introduction

This thesis summarizes the work I did at the LPNHE in Paris during my three-year PhD in the context of the LHCb experiment and under the supervision of Dr. Francesco Polci and Prof. Pascal Vincent.
The first part of my work involved implementing and developing software tools and trigger selections used in the LHCb Upgrade software framework. The contributions at this juncture are motivated by the need to process data online at an input rate of 30 MHz, corresponding to $\sim$ 5 Tb/s. These studies contribute to reducing the data volume to $\sim$ 3.5 Gb/s of offline processing. Moreover, I provided software functionalities to analyse the data that are being collected with the LHCb Upgrade.
The second part of my work was focused on searching for the first time the lepton flavor violating $B^0 \to K^{*0}\tau^{\pm}e^{\mp}$ decays using data collected by LHCb in 2016, 2017 and 2018. After having shown good performances in the reconstruction of these channels with preliminary studies, I performed all the steps of this challenging search at LHCb. The thesis describes the entire data analysis and the expected limits on the branching fractions of these decays.

The thesis is organized as follows.

- The first chapter (1) gives an overview of the theory behind the $B^0 \to K^{*0}\tau^{\pm}e^{\mp}$ decays. The Standard Model's electroweak theory, one of the most valuable theories explaining two fundamental forces together, the electromagnetic and the weak one, is described. A direct consequence of the theory is the mixing of the quark sector and conservation principles from global symmetries. In particular, Lepton Flavour and Lepton Universality are conserved by the theory. Despite the numerous stringent tests that the theory passed, the observation of neutrino oscillations showed the incompleteness of the Standard Model. Although the mixing in the lepton sector theoretically makes lepton flavor-violating processes possible, their expected branching ratios remain much below any experimental sensitivities. However, numerous theorists have formulated effective field theories and New Physics models that could enhance the branching ratios of these processes and make them eventually observable.

- The second chapter (2) describes the Large Hadron Collider at CERN and the LHCb detector. An overview of the various subdetectors of the LHCb is presented. The end of the chapter is focused on the LHCb Upgrade, describing the major changes for each component of the detector.

- The third chapter (3) collects the work done for the preparation of the LHCb Upgrade data taking. In particular, the LHCb Upgrade software framework is briefly described. My contributions are mostly focused on the development and documentation of algorithms and tools for the selection of signal candidates and particles accompanying them, but they belong to the rest of the event. This is achieved using functional objects, namely functors, which guarantee a flexible structure thanks to their property of separating configuration and execution. Besides their capability of working in an online environment, these functors are also employed in the offline processing of the LHCb Upgrade software framework. I implemented and used these functors to elaborate on a pipeline to derive "isolation" information, which is widely used in physics analyses at LHCb for discriminating signals against partially reconstructed and combinatorial backgrounds. Finally, I designed selections for the LHCb Rare Decays physics working group, concentrating my studies on lepton flavor violating $Y_b \to X\tau l$ channels. Much work is dedicated to evaluating rate and bandwidth studies to validate the selections.

- The last chapter (4) describes the search for the lepton flavor violating $B^0 \to K^{*0}\tau^{\pm}e^{\mp}$ decays. It defines the reconstruction and selection strategies employed to look for this decay in the LHCb dataset corresponding to the 2016, 2017, and 2018 years of data taking. Efficiencies and systematic uncertainties studies are fundamental ingredients for evaluating the expected limit on these decays' branching fractions, which are set at 90% and 95% of confidence levels.

Chapter 1

Theoretical overview

The Standard Model (SM) of particle physics is a quantum field theory that describes elementary particles and their electromagnetic, weak, and strong interactions. It is one of the most recognized theories in particle physics, passing many stringent tests for more than 30 years since its initial formulation elaborated between the 1960s and 1970s. Many scientists believe that, even if the SM is not a complete description of the particle physics world, it constitutes at least a valid subset of the true theory of particle physics [1].

Despite the remarkable success of the SM and many stringent tests confirming the validity of its predictions, there are still many unresolved problems and indications to believe that it is incomplete, even if valid. One of these arouses the curiosity and interest of scientists working on flavour physics experiments. The CP-violation is a necessary condition for *baryogenesis*[1]. However, the measured CP-violation is not large enough to explain this phenomenon and other sources are needed to explain the cosmological matter-antimatter asymmetry observed in the Universe.

One of the main and most clear evidence of New Physics (NP) could come from the Lepton Flavour Violation (LFV). LFV processes do not conserve the lepton family number associated with their mass eigenstates. Including the neutrino oscillation in the formulation of the SM makes these processes possible. The branching ratios estimated for these phenomena are way below any experimental sensitivity [2]; therefore, any observation will constitute a clear probe of NP.

An overview of the electroweak (EW) theory, which unifies electromagnetic and weak interaction of the SM for energies above 100 GeV, is given in Section 1.1. After briefly introducing the theory's main ingredients, the EW theory's mathematical

[1]The process of creating an excess of baryons over anti-baryons in the early Universe, starting from a Universe with equal numbers of both.

formulation is presented in Section 1.1.1. The flavour mixing of the quark sector and the Cabibbo–Kobayashi–Maskawa (CKM) matrix are discussed in Section 1.1.2. Conclusions of the first part of the chapter are dedicated to symmetries of the model (Section 1.1.3), in particular, the accidental global symmetries of baryon and lepton numbers.

The second part of the chapter is dedicated to reviewing the main theoretical concepts behind LFV. The argument is introduced by extending the SM by adding the neutrino masses to the theory (Section 1.2.1). Section 1.2.2 presents the Effective Field Theory (EFT) elaborated to include LFV in a mass-invariant formulation. Different NP scenarios, including LFV, are shown in Section 1.2.3. Finally, a general overview of the main searches for lepton flavour violation in the charged sector (cLFV) in LHCb and other experiments is given in Section 1.2.4.

1.1 The electroweak theory

Depending on their spin [3], particles can be distinguished into fermions, with half-integer spin, and bosons, with integer spin. Figure 1.1.1 shows a schematic representation of this distinction [4].

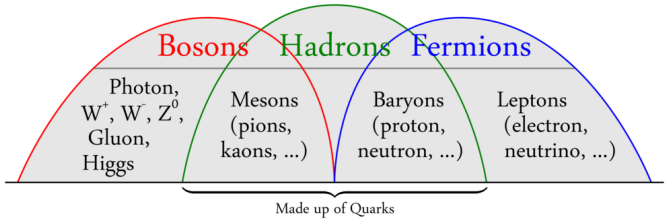

Figure 1.1.1: Classification of particles on the base of their spin [5]. Building blocks of the matter (quarks and leptons) are all fermions, while the mediators of interactions are bosons.

Among fermions, fundamental building blocks of matter are quarks (q) and leptons (l) [6]. The former have fractional electric charges, while the latter have integer ones. Another major difference between the two is that there is no observation yet of any quark individually. Quarks interact strongly and are bound to each other through gluons to form hadrons. Hadrons are named mesons if they are composed of an even number of quarks and baryons if they are composed of an odd number of quarks. Both quarks and leptons are split into three families or flavour generations based on their weak interaction structure [7]. They are the constituents of matter and interact through the exchange of a force-mediating boson [8]. These mediators are the photons (γ), as force carriers of the electromagnetic field [9]; W^+, W^-, and Z bosons, for the weak field [10–13]; gluons (g), for the strong interaction [14]. A schematic representation of the SM can be found in Figure 1.1.2.

Another main distinction between particles, relevant in charged weak interaction, depends on their spin and momentum, separating the so-called left-handed particle and right-handed particles on the base of the helicity and chirality.

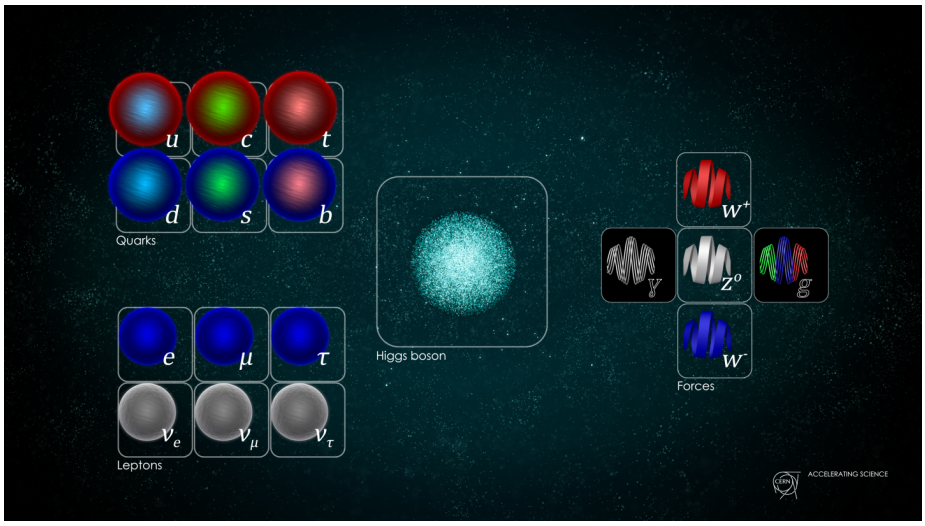

Figure 1.1.2: Matter content in the SM [15]. Quarks and leptons are fundamental constituents of matter, while gluons, photons, $W^{\pm}$ and Z^0 are bosons mediating the strong, the electromagnetic and the weak interactions, respectively. The Higgs boson is responsible for giving mass to the particles through a process named spontaneous symmetry breaking, discussed in Appendix C

The SM respects the principle of local gauge invariance for the symmetry group $SU(3)_C \times SU(2)_L \times U(1)_Y$[2], where:

- $SU(3)_C$ is the group responsible for the strong interaction. It has eight gauge boson generators of the algebra of the group. These eight one-spin particles are called gluons. The subscript C refers to colour. Any particle that couples with the gluon is said to be strongly interacting. The description of the strong interaction physics provided by quantum chromodynamics is beyond the purpose of this thesis, so it will not be discussed.

- $SU(2)_L$ has three associated spin-one particles as generators of the group. The subscript L indicates that only left-handed fermions carry this quantum number.

- $U(1)_Y$ is generated by one boson, and Y indicates the weak hypercharge, defined by the Gell-Mann–Nishijima formula as:

$$Y = 2(Q - I_z) \tag{1.1.1}$$

  where I_z is the third component of the isospin, and Q is the electric charge.

[2]The Lagrangian of the SM do not change under the local transformation of this group. The Lagrangian is therefore defined invariant.

$SU(2)_L \times U(1)_Y$ describes the EW interaction. Strong interaction can be studied independently from the EW interactions since the symmetry under $SU(3)_C$ is unbroken and does not mix with the $SU(2)_L \times U(1)_Y$ sector. In the EW theory, left-handed chiral components of the quarks and leptons are grouped into weak isospin doublets, while those of right-handed chirality are singlets. Table 1.1.1 summarizes quantum numbers involved in EW interactions for leptons and quarks [8]. To have local gauge invariance, the two $SU(2)$ massless vector gauge bosons and the $U(1)$ massless vector gauge boson acquire mass through the Spontaneous Symmetry Breaking (SSB) process. This process is caused by a scalar Higgs field, which acquires a non-zero vacuum expectation value and induces:

$$SU(2)_L \times U(1)_Y \rightarrow U(1)_{Q=I3+Y} \tag{1.1.2}$$

After the spontaneous symmetry breaking, the EW theory remains invariant under the group $U(1)_Q$ transformation. This invariance explains the presence of the massless photons associated with electromagnetic interactions.

Leptons				
Particle	**I**	$\mathbf{I_z}$	**Q**	**Y**
l_L^-	$\frac{1}{2}$	$-\frac{1}{2}$	-1	-1
l_R^-	0	0	-1	-2
ν_{lL}	$\frac{1}{2}$	$+\frac{1}{2}$	0	-1
l_L^+	$\frac{1}{2}$	$+\frac{1}{2}$	+1	+1
l_R^+	0	0	+1	+2
$\bar{\nu}_{lL}$	$\frac{1}{2}$	$-\frac{1}{2}$	0	+1

Quarks				
Particle	**I**	$\mathbf{I_z}$	**Q**	**Y**
u_L	$\frac{1}{2}$	$+\frac{1}{2}$	$+\frac{2}{3}$	$+\frac{1}{3}$
u_R	0	0	$+\frac{2}{3}$	$+\frac{4}{3}$
d_L	$\frac{1}{2}$	$-\frac{1}{2}$	$-\frac{1}{3}$	$+\frac{1}{3}$
d_R	0	0	$-\frac{1}{3}$	$-\frac{2}{3}$
$\bar{u}_R^+$	$\frac{1}{2}$	$-\frac{1}{2}$	$-\frac{2}{3}$	$-\frac{1}{3}$
$\bar{u}_L$	0	0	$-\frac{2}{3}$	$-\frac{4}{3}$
$\bar{d}_R^+$	$\frac{1}{2}$	$+\frac{1}{2}$	$+\frac{1}{3}$	$-\frac{1}{2}$
$\bar{d}_L$	0	0	$+\frac{1}{3}$	$+\frac{2}{3}$

Table 1.1.1: Properties for left and right-handed leptons (and anti-leptons) on the left table and quarks (and antiquarks) on the right table: isospin, its third component, electric charge, and hypercharge. Charged right-lepton (left anti-lepton) are isospin singlets, and right neutrinos (left antineutrinos) do not exist in the SM.

1.1.1 Formulation for the electroweak interaction

The complete SM formalism is described in Appendix A. This section provides the minimal notions of the mathematical formulation of the EW theory.
The invariance under local gauge transformation of the EW Lagrangian is maintained if the derivative ∂_μ is replaced by the *covariant derivative* ∇_μ, as presented in Appendix B:

$$\nabla_\mu = \partial_\mu + i\frac{g'}{2}B_\mu \mathbb{1} + i\frac{g}{2}A_\mu^a \sigma_a \tag{1.1.3}$$

where B_μ is the massless mediator of the field of the $U(1)$ group with coupling constant g' and A_μ^a $(a = 1, 2, 3)$ are the three massless mediators of the field of the $SU(2)$ group

with coupling constant g.
The Lagrangian $\mathcal{L}_f$, which describes the fermion behaviour, is:

$$\mathcal{L}_f = i\bar{\psi}\gamma^\mu \nabla_\mu \psi - m\bar{\psi}\psi \tag{1.1.4}$$

Another term should be added to $\mathcal{L}_f$, namely a term $\mathcal{L}_b$ describing the kinematics of the gauge bosons and the self-interaction:

$$\mathcal{L}_b = -\frac{1}{4}(F^a)_{\mu\nu}(F^a)^{\mu\nu} - \frac{1}{4}G_{\mu\nu}G^{\mu\nu} \tag{1.1.5}$$

with $(F^a)_{\mu\nu} = \partial_\mu A^a_\mu - g\epsilon_{abc}A^b_\mu A^c_\nu$ and $G_{\mu\nu} = \partial_\mu B_\nu - \partial_\nu B_\mu$. Since no quadratic terms are present for the boson gauge field, the bosons associated with those fields are massless.

The physical bosons that come out from the theory as natural fields are the results of the spontaneous symmetry-breaking process, described in the Appendix C, which gives mass to $\mathcal{W}^\pm_\mu$ and $\mathcal{Z}^0_\mu$ and leaves $\mathcal{A}_\mu$ (photon) massless. The physical fields of the weak and electromagnetic interaction are related to the non-physical ones by a rotation θ_W of the fields in the $SU(2) \times U(1)$ space:

$$\begin{aligned} \mathcal{W}^\pm_\mu &= \sqrt{\frac{1}{2}}(A^1_\mu \mp iA^2_\mu) \\ \mathcal{Z}^0_\mu &= -B_\mu \sin\theta_W + A^3_\mu \cos\theta_W \\ \mathcal{A}_\mu &= B_\mu \cos\theta_W + A^3_\mu \sin\theta_W \end{aligned} \tag{1.1.6}$$

The angle θ_W is called the Weinberg or weak mixing angle. The EW theory is strongly constrained by two relations that derive from neutral and charge couplings. The first is the key feature of the unification between electromagnetic and weak forces and helps to recover the electromagnetic coupling e from the coupling g and g':

$$e = g\sin\theta_W = g'\cos\theta_W \tag{1.1.7}$$

The second one relates the Weinberg angle to the masses of the bosons mediator of the weak interaction:

$$\frac{M_W^2}{M_Z^2\cos^2\theta_W} = 1 \tag{1.1.8}$$

These predictions are valid at tree-level in the SM, and loop deviations have been observed.

1.1.2 The flavour structure of the SM and the CKM matrix

The clearest confirmation of the SM theory is the observation of the conjectured gauge bosons mediator of the weak interaction and the Higgs scalar boson, discovered at CERN in 1983 [16] and in 2012 [17] [18], respectively. Measurements of the masses and the decay features of these bosons are nowadays compatible with the theoretical predictions, giving robustness to the SM. As discussed in Chapter 2, improving the measurements' precision in the upcoming years will allow physicists to search for possible deviations from the theory that could be hints of NP.

Another success of the EW theory in the SM is given by the compatibility of this extended theory to the low-energy limit of the Fermi theory of the weak interaction [19]. Fermi's studies on the β-decay led to the formulation of the theory with vector-axial and point-like interaction. In the limit of $q^2 \lll M_W^2$, the energy scale of the processes is too small to observe the effect of virtual particles mediator of weak interaction, which can be considered point-like. The Fermi constant G_F[3], introduced by the theory as coupling strength of the point-like interaction, is related to the mass of the $W^{\pm}$ as:

$$G_F = \frac{\sqrt{2}g^2}{8M_W^2} = \frac{1}{\sqrt{2}v^2} \tag{1.1.9}$$

where g is the weak coupling constant, M_W is the mass of the W boson and v is the *vacuum expectation value*. An illustrative schema of the Fermi's interaction is presented in Figure 1.1.3.

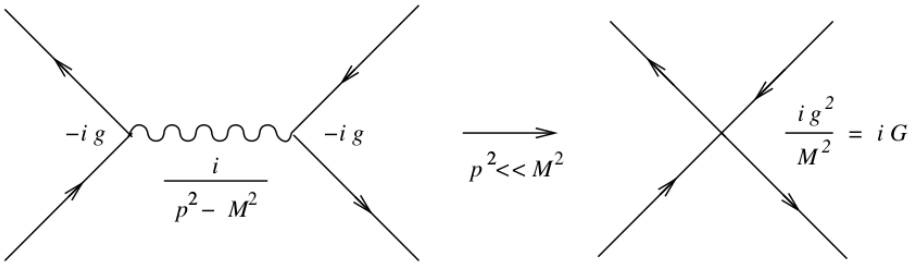

Figure 1.1.3: Schematic representation of Fermi's interaction. At low energy regime ($q^2 \lll M_W^2$), the interaction behaves point-like, and the coupling is proportional to G_F.

When the Higgs boson is coupled to the three lepton generations, it gives mass to the quarks and the charged leptons (electron, muon, and tau). The absence of a right-handed neutrino as the counterpart of the left-handed ν_L ensures that only charged lepton acquires mass with the Higgs mechanism, and no flavour mixing is present in the lepton sector. Extensions of the SM to include right-handed neutrinos

[3]According to Fermi's theory of β-decay, G_F describes the probability per unit time of a neutron to transform into a proton, an electron and an antineutrino

are introduced in Section 1.2.1.

In the quark sector, the structure description is much more complicated by the flavour mixing. The complete description of the weak interaction is encoded in the CKM matrix [20] [21], which describes weak decay processes and oscillation of neutral mesons. The diagonalization process of the mass matrix leads to a rotation of the original flavour eigenstates into new mass eigenstates. If V_d is the matrix that changes the flavour eigenstate d (down type quark) into the correspondent mass eigenstate and V_u the matrix that transforms the flavour eigenstate u (up type quark) into the correspondent mass eigenstate, the 3×3 complex matrix $V_{CKM} = V_u V_d^\dagger$ contain elements that define the strength of mixing of the flavours. The complex nature of the CKM matrix is the origin of CP-violation in the SM (see Appendix D). This matrix, by unitarity, can be parameterized by four parameters (three mixing angles and the CP-violating mixing phase). Using the Wolfenstein parameterization [22], it is possible to express the CKM matrix in terms of A, ρ, and η:

$$V_{CKM} = \begin{pmatrix} 1 - \frac{1}{2}\lambda^2 & \lambda & A\lambda^3(\rho - i\eta) \\ -\lambda & 1 - \frac{1}{2}\lambda^2 & A\lambda^2 \\ A\lambda^3(1 - \rho - i\eta) & -A\lambda^2 & 1 \end{pmatrix} + \mathcal{O}(\lambda^4) \tag{1.1.10}$$

where:

$$\begin{aligned} A = \frac{\sin\theta_{23}}{\sin^2\theta_{12}}, \quad \lambda = \sin\theta_{12}, \\ \rho = \frac{\sin\theta_{13}\cos\delta}{\sin\theta_{12}\sin\theta_{23}}, \quad \eta = \frac{\sin\theta_{13}\sin\delta}{\sin\theta_{12}\sin\theta_{23}}. \end{aligned} \tag{1.1.11}$$

The θ_{ij} $(i, j = 1, 2, 3,\ i \neq j)$ are the mixing angles between the three quark generations, and δ is the irreducible complex phase which allows CP-violation in the weak interaction. The off-diagonal terms are relatively small, implying that weak interaction between quarks of different generations is suppressed, particularly between the first and the third family. It is important to perform precise measurements of the CKM matrix parameters to constrain the theory and test its validity. Measurements of the unitary triangle parameters derived from the CKM matrix, explained in Appendix E, have been conducted in the past and still nowadays, in particular by the B-factories [23], like BaBar [24], Belle [25], Belle-II [26], and LHCb [27], confirming up to now the existence of a unique CP-violating phase in the quark sector and the validity of the CKM description.

1.1.3 Symmetries and quantum number conservation

In physics, the symmetries of a theoretical model allow us to identify the conservation laws that regulate nature [28, 29]. However, it is crucial to understand which

predictions of the model are of general validity and which depend, instead, on the approximation scheme used to formulate the theory.

The Weinberg-Salam model of EW interaction predicts, as a direct symmetry of the theory, the Lepton Number Conservation. The EW Lagrangian is invariant under gauge transformation of global $U(1)$ symmetry for the three lepton generations. Linked to this symmetry, there is the impossibility of having a flavour-changing neutral current (FCNC) process in the lepton sector. The flavour and the lepton quantum number are conserved since no flavour mixing matrix is predicted for the lepton sector. The Lagrangian in the lepton sector exhibit also CP-symmetry[4] (an explanation of this symmetry is provided in Appendix D). Instead, these symmetries and conservation laws are invalid for the quark sector due to the flavour mixing encrypted in the CKM matrix. As an accidental symmetry of the theory, the weak interaction of the charged leptons with the boson mediators is independent of the lepton flavour. This prediction is called Lepton Flavour Universality (LFU) and will be further discussed in the next Section 1.2.

1.2 Charged Lepton Flavour Violation

The observation of the neutrino oscillations [30–34] proved that mixing phenomena between mass and weak eigenstates also happen in the lepton sector, even though the origin of the neutrino masses is still one of the biggest mysteries of particle physics nowadays. After giving a theoretical interpretation of neutrino masses, Section 1.2.1 treats the mixing for neutrinos, explaining why the neutrino flavour oscillates through the Pontecorvo-Maki–Nakagawa–Sakata (PMNS) matrix. The neutrino oscillation makes FCNC processes possible in weak interactions, as presented in Figure 1.2.1. However, their rates are proportional to $(\Delta m^2_{ij}/M^2_W)^2$, where Δm^2_{ij} is the mass-squared difference between the i-th and the j-th neutrino mass eigenstates and M^2_W is the W boson mass-squared. The Δm^2_{ij} difference is very small, leading to predicted branching ratios below any current experimental sensitivity. In particular, for the $B \to K^* \tau e$ decay treated in this thesis, the Δm_{13} is not directly measured. From global fits [35] an upper limit for normal mass ordering ($m_1 < m_2 < m_3$) is set to $\sim 2.6 \times 10^{-3}$ eV^2 ($\sim 2.5 \times 10^{-3}$ eV^2 considering inverted mass hierarchy $m_3 < m_1 < m_2$[5]). The expected branching ratio for cLFV decays involving the first and the third lepton generation is $\mathcal{O}(10^{-50})$, way below any experimental sensitivity. Therefore, observation of cLFV processes would represent a clear sign of physics Beyond the SM (SM).

[4]The physics of particles described in a right-handed coordinate system is the same as the physics of antiparticles described in a left-handed coordinate system.

[5]No experimental measurements established yet the neutrino mass ordering, although from solar (and reactor) neutrino experiments Δm_{12} is positive, leading to $m_2 > m_1$

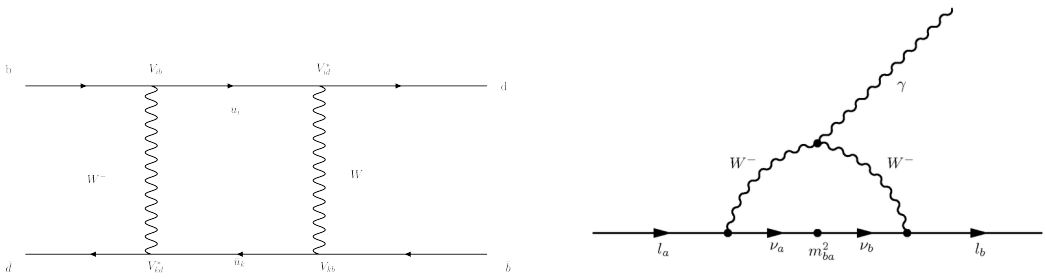

Figure 1.2.1: Examples of diagrams of FCNC processes in the quark (left) and lepton (right) sectors. On the left, these processes are suppressed by the Standard Model at the tree level but can occur through higher-order loop diagrams. The CKM matrix elements suppress its branching ratio. The FCNC process on the right can occur in the lepton sectors only via neutrino oscillation. In this case, the flavour mixing parameters, encoded in the PMNS matrix, are suppressing the process.

Some tensions with the SM predictions in the LFU ratios have been observed in the semileptonic $b \to c$ decays [36]:

$$R_{D^{(*)}} = \frac{BR(B \to D^{(*)}\tau\nu)}{BR(B \to D^{(*)}l\nu)} \tag{1.2.1}$$

Data shows a deviation of about 2σ from the SM expectations in the two-dimensional plot of $R(D)$ and $R(D^*)$, as shown in Figure 1.2.2. Results from LHCb [37–39], Belle-II [40], Belle [41–43], and BaBar [44, 45] are included in the calculation of the deviation. If LFU does not hold in B hadrons decays, it might be a hint that the lepton flavour could not be conserved [46].
In previous analyses, also, $b \to sl^+l^-$ measurements of lepton universality from LHCb showed some tensions with the predictions [48]. However, the most recent measurements [49] of the ratio:

$$R_{(K^+,K^*)} = \frac{BR(B^{(+,0)} \to K^{(+,*0)}\mu^+\mu^-)}{BR(B \to K^{(+,*0)}e^+e^-)} \tag{1.2.2}$$

show good agreement with the SM expected unitarity (see Figure 1.2.3).
A first approximation of the BSM theory that could explain LFV processes is described in Section 1.2.2, based on the elaboration of an Effective Field Theory of the SM (SMEFT). In addition, some examples of NP models are presented in Section 1.2.3. Finally, an overview of cLFV searches in hadron decays through different experiments is provided in Section 1.2.4.

1.2.1 Lepton sector mixing

Extending the SM to the case of right-handed neutrinos introduces an extra mass component for neutrinos into the Lagrangian Yukawa term. After the EW SSB, the

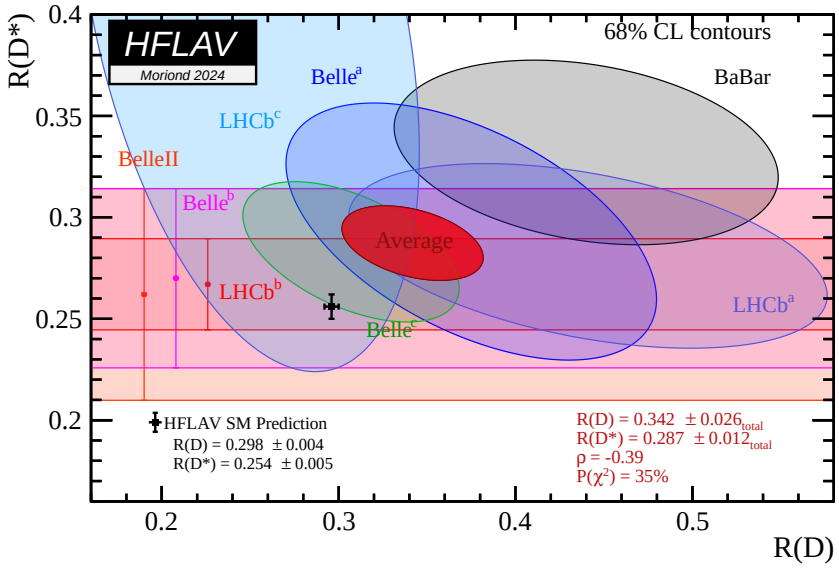

Figure 1.2.2: Latest experimental constraint on $R(D)$ and $R(D^*)$. Results show a tension of $\sim 3\sigma$ with the SM. The plot is taken from the HFLAV website [47] and refers to the status at the Moriond conference in 2024.

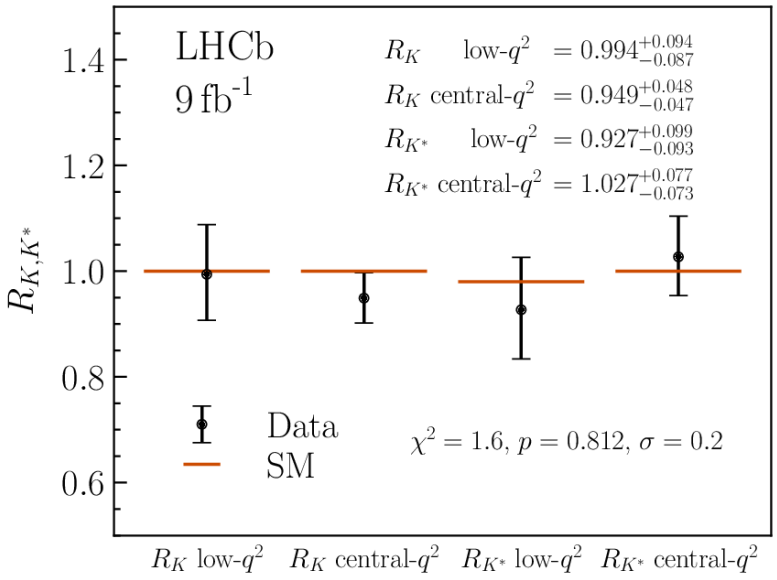

Figure 1.2.3: Measured values of lepton universality observables for $B^+ \to K^+ l^+ l^-$ and $B^0 \to K^{*0} l^+ l^-$. Results are compatible with the SM [50].

Dirac neutrino obtains mass m_D proportional to the Yukawa neutrino coupling y_ν. Unlike charged leptons, neutrinos are experimentally constrained to have a mass below the eV. Although no precise measurement can determine the neutrino masses, several bounds have been set by satellites detecting cosmic microwave background [51], direct neutrino experiment [52, 53] and neutrinoless double beta decay experiments

$(0\nu\beta\beta)$ [54, 55]. Yukawa couplings should be of $O(10^{-13})$ to get appropriate values for the masses. Another possibility is considering neutrinos as Majorana fermions, a particle corresponding to its antiparticle ($\nu_L^C = \nu_R$). The Majorana mass term would break any global $U(1)$ symmetry, violating the lepton numbers by two units. The term is not gauge invariant and cannot be introduced directly in the SM. An EFT that generates an invariant mass term is needed in this case. Introducing a non-renormalizable 5-dimensional operator that generates the Majorana mass term [56] is possible. After SSB, the term becomes:

$$\mathcal{L}_5 = \frac{1}{2} C^{(5)} \frac{v^2}{\Lambda} \bar{\nu}_L^c \nu_L + h.c. \tag{1.2.3}$$

where $C^{(5)}$ is a coupling constant, and Λ is the NP energy scale with the dimensions of mass. At an energy scale of 10^{14} GeV, close to the unification scale of EW and strong theory, it is possible to accommodate the requirement on the neutrino masses if $C^{(5)} \sim 1$. Although the Majorana mass term conserves electric charges, it breaks the lepton conservation number [57, 58].

Treating the neutrinos as Dirac or Majorana fermions leads to different phenomenological consequences. Most BSM theories have considered neutrinos as Majorana particles, but no experimental proof supports this assumption. Transitions violating the lepton number are the most sensitive processes, particularly the neutrinoless double β decay. Experiments in this sector [54, 55] set stringent bounds to the half-lives of the decay and, consequently, to the neutrino masses. Unfortunately, it is not yet possible to exclude or confirm a hypothesis on their nature.

Neutrino flavour oscillations result from the presence of neutrino masses and mixing in the neutrino sector. These oscillations, whose detailed explanation is given in Appendix F, were first observed in the 1960s from a deficit in the number of solar electron neutrinos compared to the ones predicted [59]. Several other observations confirmed the neutrino oscillations [60–64]. The oscillation parameters depend on how the flavour structure mixes. The weak eigenstates result in a superimposition of mass eigenstates:

$$\begin{pmatrix} \nu_e \\ \nu_\mu \\ \nu_\tau \end{pmatrix} = U \begin{pmatrix} \nu_1 \\ \nu_2 \\ \nu_3 \end{pmatrix} \tag{1.2.4}$$

The PMNS matrix U [65, 66] is a 3×3 matrix which parameterizes the unitary transformation between mass eigenstates and flavour eigenstates. It depends on the mixing angles θ_{ij} between neutrinos and the complex Dirac phase δ. This phase contributes to the CP-violating difference in the oscillation probability of $P_{\nu_\alpha \to \nu_\beta}$

and $P_{\bar{\nu}_\alpha \to \bar{\nu}_\beta}$ [67–69]. Denoting c_{ij} as $\cos(\theta_{ij})$ and s_{ij} as $\sin(\theta_{ij})$, for $i, j = 1, 2, 3$, the matrix can be written as:

$$U = \begin{pmatrix} c_{12}c_{13} & s_{12}c_{13} & s_{13}e^{-i\delta} \\ -s_{12}c_{23} - c_{12}s_{23}s_{13}e^{i\delta} & c_{12}c_{23} - s_{12}s_{23}s_{13}e^{i\delta} & s_{23}c_{13} \\ s_{12}s_{23} - c_{12}c_{23}s_{13}e^{i\delta} & -c_{12}s_{23} - s_{12}c_{23}s_{13}e^{i\delta} & c_{23}c_{13} \end{pmatrix} \times P \tag{1.2.5}$$

where the matrix P corresponds to the identity if neutrinos have Dirac masses, while it contains two extra phases α_1 and α_2 for Majorana neutrinos:

$$P = \begin{pmatrix} 1 & 0 & 0 \\ 0 & \exp^{i\alpha_1} & 0 \\ 0 & 0 & \exp^{i\alpha_2} \end{pmatrix} \tag{1.2.6}$$

The measured observables in neutrino experiments are the mixing parameters and the mass differences.

1.2.2 Effective Lagrangian for cLFV

Much inspiration to write this Section comes from [70]. An EFT framework adequately describes physical observables at a certain energy scale without knowing the dynamic at higher energy scales. An example of a successful EFT is the Fermi theory for the EW interaction, as discussed in Section 1.1.2. The Lagrangian of an EFT explaining BSM phenomena, such as cLFV, would assume the general form:

$$\mathcal{L}_{EFT} = \mathcal{L}_{\text{SM}} + \frac{1}{\Lambda} C^{(5)} O^{(5)} + \frac{1}{\Lambda^2} \sum_n C_n^{(6)} O_n^{(6)} + \mathcal{O}\left(\frac{1}{\Lambda^3}\right) \tag{1.2.7}$$

where the renormalizable SM Lagrangian $\mathcal{L}_{\text{SM}}$ contains up to dimension-four operators. The other terms include higher-dimensional operators, presented here up to dimension-six. There is only one dimension-five operator $O^{(5)}$, also known as the Weinberg operator, and it is responsible for the generation of Majorana neutrino masses, as shown in Equation 1.2.3. The Wilson coefficients $C^{(5)}$ and $C^{(6)}$ represent the strength of the couplings at the energy scales of Λ and Λ^2, respectively. Several dimension-six operators $O_n^{(6)}$ arise at the leading order in the EFT expansion presented in Equation 1.2.7 when integrating out the heavy degrees of freedom (top quark, W and Z bosons, Higgs and potential heavy new particles). Terms at higher dimensions, such as dimension-seven operators of the order of $(1/\Lambda^3)$, contribute very little compared to dimension-six operators and are not considered. It is possible to parameterize the NP effects at the EW scale in terms of the various operators and the associated Wilson coefficients. When choosing a specific model, the Wilson coefficients can be calculated as a function of model parameters by matching the NP

model under consideration to the effective SM [71–74].

Among the dimension-six operators, we can identify dipole operators and four-fermions operators, which can potentially contribute to B-decays. The notation with superscripts $'$ is used to label operators obtained by flipping the chirality, and they're usually suppressed compared to the un-primed counterparts. The subscripts L and R represent the left and right chirality, respectively [75]. The operators can be evaluated taking as reference the $B \to K^* \tau e$ decay:

- the electromagnetic dipole operator O_7 contributes through the electromagnetic penguin diagrams
$$O_7^{(\prime)} \propto (\bar{s}_{L(R)} \sigma_{\mu\nu} b_{R(L)}) F^{\mu\nu} \tag{1.2.8}$$
where $\sigma_{\mu\nu}$ are the Pauli matrices and $F^{\mu\nu}$ is the electromagnetic field tensor;

- the chromomagnetic dipole operator O_8 contributes through the gluonic penguin diagrams
$$O_8^{(\prime)} \propto (\bar{s}_{L(R)} \sigma_{\mu\nu} T_a b_{R(L)}) G^{a\mu\nu} \tag{1.2.9}$$
where $\sigma_{\mu\nu}$ are the Pauli matrices, T_a are the $SU(3)$ generators and $G^{a\mu\nu}$ is the gluon field tensor;

- semileptonic $O_9^{\tau e}$ and $O_{10}^{\tau e}$ operators, involved into vector lepton current
$$\begin{aligned} O_9^{(\prime)\tau e} &\propto (\bar{s}_{L(R)} \gamma_\mu b_{L(R)})(\bar{\tau} \gamma^\mu e) \\ O_{10}^{(\prime)\tau e} &\propto (\bar{s}_{L(R)} \gamma_\mu b_{L(R)})(\bar{\tau} \gamma^\mu \gamma^5 e) \end{aligned} \tag{1.2.10}$$
where γ^μ are the Dirac matrices;

- $O_S^{\tau e}$, $O_P^{\tau e}$ and $O_T^{\tau e}$ operators, involved respectively into scalar, pseudoscalar and tensor interactions between quarks and leptons
$$\begin{aligned} O_S^{(\prime)\tau e} &\propto (\bar{s}_{L(R)} b_{R(L)})(\bar{\tau} e) \\ O_P^{(\prime)\tau e} &\propto (\bar{s}_{L(R)} b_{R(L)})(\bar{\tau} \gamma_5 e) \\ O_{T(5)}^{\tau e} &\propto (\bar{s} \sigma_{\mu\nu} b)(\bar{\tau} \sigma^{\mu\nu} (\gamma_5) e) \end{aligned} \tag{1.2.11}$$

Only some of these operators are relevant for $b \to s l l'$ decays, described in the SM by the one-loop diagrams shown in Figure 1.2.4. They are obtained by evaluating the Lagrangian in Equation 1.2.7 at the EW scale of b-quark mass. From calculations [76], it is possible to derive that:

1. Some operators, like tensor operators, do not appear from the integration of W and Z bosons at leading order ($C_T = C_{T5} = 0$);

2. At b-quark mass scale, where we're searching for $b \to sll'$ processes, the most relevant [75] Wilson coefficients are C_9, C_{10}, C_S, C_P and their primed counterparts. Some of them are correlated: $C_S = -C_P$ and $C'_S = C'_P$.

3. Other contributions may be subject to constraints arising purely at higher energy scales, for example, Z and Higgs decays.

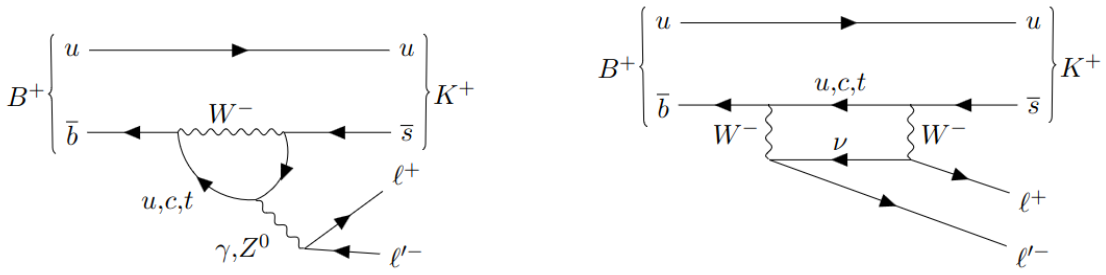

Figure 1.2.4: Feynman diagrams for $B^+ \to K^+ll'$ [75]. Replacing u-quarks by d-quarks leads to a similar diagram for $B^0 \to K^{*0}ll'$.

Predictions on observables in the EW effective theory at the b-quark mass scale can be done using the `flavio` package [77] under the assumption of certain NP models by fixing the values of the Wilson coefficients. In particular, for the $B \to K^*\tau e$ decay, the predicted branching ratio (BR) is:

- $(BR = 8.0 \pm 0.6) \times 10^{-8}$ for a scalar model with $C_S^{e\tau} \neq 0$ if $\Delta C_S^{e\tau} = 1$
- $BR = (4.0 \pm 0.4) \times 10^{-8}$ for a left-handed model with $C_9 = -C_{10} \neq 0$ if $\Delta C_9^{e\tau} = 1$

where $\Delta C^{e\tau} = x$ means $C_{SM}^{e\tau} + x$ and refers to the NP contributions only. Figure 1.2.5 shows the predicted BR as a function of the Wilson coefficients values fixed.

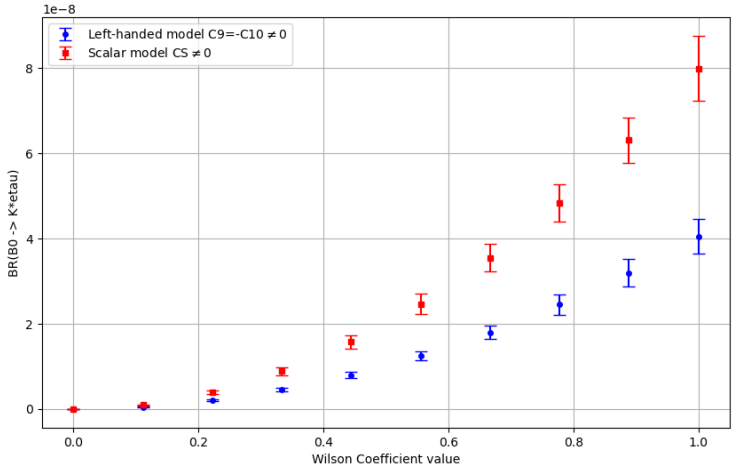

Figure 1.2.5: BR of $B \to K^*\tau e$ decay predicted by different NP model as a function of the Wilson coefficient fixed.

1.2.3 Different New Physics scenarios

Several NP models have been developed in order to account for the observed anomalies in the flavour sector, as discussed at the beginning of Section 1.2. Among the most cited ones are the *leptoquark* (LQ) and *heavy vector boson* (Z') models, as shown in Figure 1.2.6.

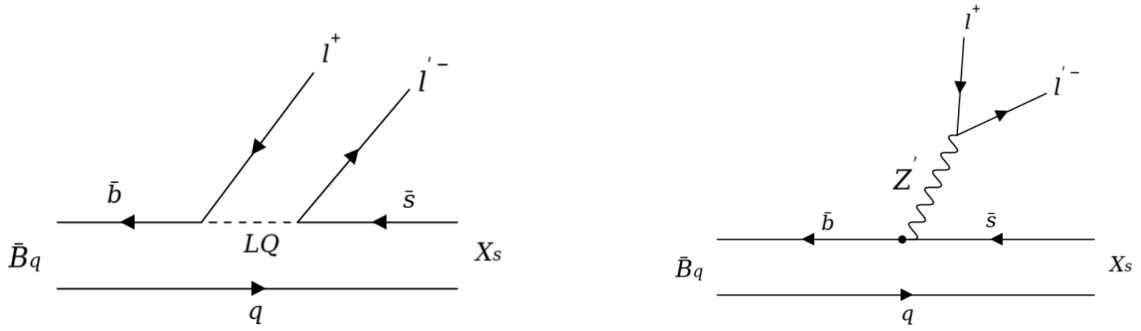

Figure 1.2.6: Example of diagrams of $b \to sll'$ transitions in LQ (left) and Z' (right) models.

A LQ is a particle that carries both baryonic and leptonic numbers at the same time, coupling to both leptons and quarks. They can be (spin-0) scalar [35, 78] or (spin-1) vector [79, 80] states. They can have different quantum numbers related to the QCD and EW symmetries, as listed in Figure 1.2.7, depending on their interaction with SM fermions.

Spin	$3B+L$	$SU(3)_c$	$SU(2)_W$	$U(1)_Y$	Allowed coupling
0	-2	$\bar{3}$	1	1/3	$\bar{q}_L^c \ell_L$ or $\bar{u}_R^c e_R$
0	-2	$\bar{3}$	1	4/3	$\bar{d}_R^c e_R$
0	-2	$\bar{3}$	3	1/3	$\bar{q}_L^c \ell_L$
1	-2	$\bar{3}$	2	5/6	$\bar{q}_L^c \gamma^\mu e_R$ or $\bar{d}_R^c \gamma^\mu \ell_L$
1	-2	$\bar{3}$	2	$-1/6$	$\bar{u}_R^c \gamma^\mu \ell_L$
0	0	3	2	7/6	$\bar{q}_L e_R$ or $\bar{u}_R \ell_L$
0	0	3	2	1/6	$\bar{d}_R \ell_L$
1	0	3	1	2/3	$\bar{q}_L \gamma^\mu \ell_L$ or $\bar{d}_R \gamma^\mu e_R$
1	0	3	1	5/3	$\bar{u}_R \gamma^\mu e_R$
1	0	3	3	2/3	$\bar{q}_L \gamma^\mu \ell_L$

Figure 1.2.7: LQ and their quantum numbers [81].

On the contrary, the Z' is a massive vector boson electrically neutral heavier than the Z boson. The Z' couples with fermion as:

$$\mathcal{L}_{\text{int}} = g_{q_{ij}} \bar{q}_j \gamma^\mu q_i Z'_\mu + g_\ell \bar{\ell}_j \gamma^\mu \ell_i Z'_\mu \tag{1.2.12}$$

where g_q and g_ℓ are the coupling constants for quarks and leptons. The couplings are

written in a model-dependent way with indices $i, j = 1, 2, 3$ labeling quark and lepton fields.

Parameters describing LQ and Z' models are subject to theoretical constraints. In particular extensions of the SM, some models are favoured with respect to others. Furthermore, experimental searches are conducted exploring different lepton couplings in the final state. Some models, like scalar LQ [78, 82], are more sensitive to B-decays, since they involve both leptons and quarks.

1.2.4 Experimental setup overview

Experimental observables depend on the combination of the operators discussed in Section 1.2.2 and describing the process. For example, the different operators contribute differently to the branching ratios, and the Wilson coefficients express their weight. Therefore, the coefficients give information on the properties of the NP particle mediator. Since these properties can depend on the lepton couplings involved in the LFV processes, all modes covering all possible couplings must be explored. There is not a specific *golden channel* for the LFV searches [83]. The general experimental overview of the most stringent limits set for different LFV channels across experiments is provided in this section. Table 1.2.1 summarizes the LFV searches in B decays with $e\mu$, $\tau\mu$ and τe lepton combinations in the final state. The current best experimental sensitivity for these decays is $O(10^{-9})$ for $e\mu$, $O(10^{-6})$ for $\tau\mu$ and $O(10^{-5})$ for τe. This thesis provides the first limits on the $B \to K^*\tau e$ decay, for which no previous limits exist. LFV decays are also searched for in other hadrons decays, as shown in Table 1.2.2. Results for decays of μ and τ leptons, where better experimental sensitivity can be achieved, are collected in Table 1.2.3.

Leptons	Decay	Limit (90% C.L.)	Integrated luminosity	Experiment
$e\mu$	$B^0 \to e^{\mp}\mu^{\pm}$	1.0×10^{-9} [84]	$3fb^{-1}$	LHCb
	$B_s^0 \to e^{\mp}\mu^{\pm}$	5.4×10^{-9} [84]	$3fb^{-1}$	LHCb
	$B^0 \to \pi^0 e^{\mp}\mu^{\pm}$	1.4×10^{-7} [85]	472M BB ($426fb^{-1}$)	BaBar
	$B^+ \to \pi^+ e^{\mp}\mu^{\pm}$	1.7×10^{-7} [85]	472M BB ($426fb^{-1}$)	BaBar
	$B^0 \to K^0 e^{\mp}\mu^{\pm}$	3.8×10^{-8} [86]	772M BB ($771fb^{-1}$)	Belle
	$B^0 \to K^{*0} e^{\mp}\mu^{\pm}$	10.1×10^{-9} [87]	$9fb^{-1}$	LHCb
	$B^0 \to K^{*0} e^{-}\mu^{+}$	5.7×10^{-9} [87]	$9fb^{-1}$	LHCb
	$B^0 \to K^{*0} e^{+}\mu^{-}$	6.8×10^{-9} [87]	$9fb^{-1}$	LHCb
	$B^+ \to K^{+} e^{+}\mu^{-}$	7.0×10^{-9} [88]	$3fb^{-1}$	LHCb
	$B^+ \to K^{+} e^{-}\mu^{+}$	6.4×10^{-9} [88]	$3fb^{-1}$	LHCb
	$B^+ \to K^{*+} e^{-}\mu^{+}$	9.9×10^{-7} [89]	472M BB ($426fb^{-1}$)	BaBar
	$B^+ \to K^{*+} e^{+}\mu^{-}$	1.3×10^{-6} [89]	472M BB ($426fb^{-1}$)	BaBar
	$B^+ \to D^{-} e^{+}\mu^{+}$	1.8×10^{-6} [90]	772M BB ($771fb^{-1}$)	Belle
	$B_s^0 \to \phi e^{\pm}\mu^{\mp}$	1.6×10^{-8} [87]	$9fb^{-1}$	LHCb
$\tau\mu$	$B^0 \to \tau^{\mp}\mu^{\pm}$	1.4×10^{-5} [91]	$3fb^{-1}$	LHCb
	$B_s^0 \to \tau^{\mp}\mu^{\pm}$	4.2×10^{-5} [91]	$3fb^{-1}$	LHCb
	$B^+ \to \pi^+ \tau^{+}\mu^{-}$	4.5×10^{-5} [85]	472M BB ($426fb^{-1}$)	BaBar
	$B^+ \to \pi^+ \tau^{-}\mu^{+}$	2.45×10^{-5} [85]	472M BB ($426fb^{-1}$)	BaBar
	$B^0 \to K^{*0} \tau^{+}\mu^{-}$	1.0×10^{-5} [92]	$9fb^{-1}$	LHCb
	$B^0 \to K^{*0} \tau^{-}\mu^{+}$	9.8×10^{-6} [92]	$9fb^{-1}$	LHCb
	$B^+ \to K^{+} \tau^{+}\mu^{-}$	5.9×10^{-6} [93]	772M BB ($771fb^{-1}$)	Belle
	$B^+ \to K^{+} \tau^{-}\mu^{+}$	2.45×10^{-5} [93]	772M BB ($771fb^{-1}$)	Belle
	$B_s^0 \to \phi \tau^{\pm}\mu^{\mp}$	1.0×10^{-5} [94]	$9fb^{-1}$	LHCb
τe	$B^0 \to e^{\mp}\tau^{\pm}$	1.6×10^{-5} [95]	772M BB ($771fb^{-1}$)	Belle
	$B_s^0 \to e^{\mp}\tau^{\pm}$	1.4×10^{-3} [96]	772M BB ($771fb^{-1}$)	Belle
	$B^+ \to K^{+} e^{+}\tau^{-}$	1.53×10^{-5} [97]	772M BB ($771fb^{-1}$)	Belle
	$B^+ \to K^{+} e^{-}\tau^{+}$	1.51×10^{-5} [97]	772M BB ($771fb^{-1}$)	Belle
	$B^+ \to \pi^{+} e^{+}\tau^{-}$	7.4×10^{-5} [98]	472M BB ($426fb^{-1}$)	BaBar
	$B^+ \to \pi^{+} e^{-}\tau^{+}$	2.0×10^{-5} [98]	472M BB ($426fb^{-1}$)	BaBar

Table 1.2.1: Searches for LFV B decays, classified by the presence of $e\mu$, $\tau\mu$ or τe in the final state.

Leptons	Decay	Limit	Experiment
$e\mu$	$\pi^0 \to e\mu$	3.6×10^{-10} [99] (90% C.L.)	KTeV
	$K^+ \to \pi^+\mu^+e^-$	1.3×10^{-11} [100] (90% C.L.)	BNL-E-0865
	$K^+ \to \pi^+\mu^-e^+$	6.6×10^{-11} [101] (90% C.L.)	NA62
	$K_L^0 \to e\mu$	4.7×10^{-12} [102] (90% C.L.)	BNL-E-0871
	$K_L^0 \to \pi^0 e\mu$	7.6×10^{-11} [99] (90% C.L.)	KTeV
	$K_L^0 \to \pi^0\pi^0 e\mu$	1.7×10^{-10} [99] (90% C.L.)	KTeV
	$J/\psi \to e\mu$	1.6×10^{-7} [103] (90% C.L.)	BES-III
	$D^+ \to \pi^+ e^+\mu^-$	2.1×10^{-7} [104] (90% C.L.)	LHCb
	$D^+ \to \pi^+ e^-\mu^+$	2.2×10^{-7} [104] (90% C.L.)	LHCb
	$D_s^+ \to \pi^+ e^+\mu^-$	1.1×10^{-6} [104] (90% C.L.)	LHCb
	$D_s^+ \to \pi^+ e^-\mu^+$	9.4×10^{-7} [104] (90% C.L.)	LHCb
	$D_s^+ \to K^+ e^-\mu^+$	5.6×10^{-7} [104] (90% C.L.)	LHCb
	$D^0 \to e^\pm\mu^\mp$	1.3×10^{-8} [105] (90% C.L.)	LHCb
	$D^0 \to \pi^0 e^\pm\mu^\mp$	8.0×10^{-7} [106] (90% C.L.)	BaBar
	$D^0 \to \eta e^\pm\mu^\mp$	2.25×10^{-6} [106] (90% C.L.)	BaBar
	$D^0 \to \omega e^\pm\mu^\mp$	1.71×10^{-6} [106] (90% C.L.)	BaBar
	$D^0 \to \rho e^\pm\mu^\mp$	5.0×10^{-7} [106] (90% C.L.)	BaBar
	$D^0 \to \phi e^\pm\mu^\mp$	5.1×10^{-7} [106] (90% C.L.)	BaBar
	$D^0 \to \bar{K}^0 e^\pm\mu^\mp$	1.74×10^{-6} [106] (90% C.L.)	BaBar
	$D^0 \to K^{*0} e^\pm\mu^\mp$	1.25×10^{-6} [106] (90% C.L.)	BaBar
	$D^0 \to \pi^+\pi^- e^\pm\mu^\mp$	1.71×10^{-6} [106] (90% C.L.)	BaBar
	$D^0 \to K^+K^- e^\pm\mu^\mp$	1.00×10^{-6} [106] (90% C.L.)	BaBar
	$D^0 \to \pi^+K^- e^\pm\mu^\mp$	1.90×10^{-6} [106] (90% C.L.)	BaBar
	$\Upsilon(1S) \to e^\pm\mu^\mp$	3.9×10^{-7} [107] (90% C.L.)	Belle
	$\Upsilon(1S) \to \gamma e^\pm\mu^\mp$	4.2×10^{-7} [107] (90% C.L.)	Belle
	$\Upsilon(3S) \to e^\pm\mu^\mp$	3.6×10^{-7} [108] (90% C.L.)	BaBar
	$Z \to e\mu$	2.62×10^{-7} [109] (95% C.L.)	ATLAS
	$H \to e\mu$	4.4×10^{-5} [110] (95% C.L.)	CMS
	$t \to e^\pm\mu^\mp u$	7×10^{-8} [111] (95% C.L.)	CMS
	$t \to e^\pm\mu^\mp c$	8.9×10^{-7} [111] (95% C.L.)	CMS
$\tau\mu$	$J/\psi \to \tau\mu$	2.0×10^{-6} [103] (90% C.L.)	BES
	$\Upsilon(1S) \to \tau^\pm\mu^\mp$	2.7×10^{-6} [107] (90% C.L.)	Belle
	$\Upsilon(1S) \to \gamma\tau^\pm\mu^\mp$	6.1×10^{-6} [107] (90% C.L.)	Belle
	$\Upsilon(2S) \to \tau^\pm\mu^\mp$	2.3×10^{-7} [112] (90% C.L.)	Belle
	$\Upsilon(3S) \to \tau^\pm\mu^\mp$	3.1×10^{-6} [113] (90% C.L.)	BaBar
	$Z \to \tau\mu$	6.5×10^{-6} [114] (95% C.L.)	ATLAS
	$H \to \tau\mu$	1.5×10^{-3} [115] (95% C.L.)	CMS
	$t \to \tau^\pm\mu^\mp q$	8.7×10^{-7} [116] (95% C.L.)	ATLAS
τe	$J/\psi \to e\tau$	7.5×10^{-8} [103] (90% C.L.)	BES-III
	$\Upsilon(1S) \to e^\pm\tau^\mp$	2.7×10^{-6} [107] (90% C.L.)	Belle
	$\Upsilon(1S) \to \gamma e^\pm\tau^\mp$	6.5×10^{-6} [107] (90% C.L.)	Belle
	$\Upsilon(2S) \to e^\pm\tau^\mp$	1.12×10^{-6} [112] (90% C.L.)	Belle
	$\Upsilon(3S) \to e^\pm\tau^\mp$	4.2×10^{-6} [113] (90% C.L.)	BaBar
	$Z \to e\tau$	5.0×10^{-6} [114] (95% C.L.)	ATLAS
	$H \to e\tau$	0.20% [117] (95% C.L.)	ATLAS
	$t \to \tau^\pm e^\mp q$	1.9×10^{-5} [118] (95% C.L.)	ATLAS

Table 1.2.2: Searches for LFV hadron decays other than B decays, classified by the presence of $e\mu$, $\tau\mu$ or τe in the final state.

Leptons	Decay	Limit (90% C.L.)	Experiment
μ decays	$\mu^+ \to e^+\gamma$	4.2×10^{-13} [119]	MEG
	$\mu^+ \to e^+e^-e^+$	1.0×10^{-12} [120]	SINDRUM
	$\mu^-N \to e^-N$	$6.1(7.1) \times 10^{-13}$ Ti(Au) [121]([122])	SINDRUM-II
	$\mu^-N \to e^-N'$	5.7×10^{-13} [123]	SINDRUM-II
τ decays	$\tau^\pm \to e^\pm\gamma$	3.3×10^{-8} [124]	BaBar
	$\tau^\pm \to \mu^\pm\gamma$	4.4×10^{-8} [124]	BaBar
	$\tau \to eee$	2.7×10^{-8} [125]	Belle
	$\tau \to \mu\mu\mu$	2.1×10^{-8} [125]	Belle
	$\tau \to \mu ee$	1.8×10^{-8} [125]	Belle
	$\tau \to e\mu\mu$	2.7×10^{-8} [125]	Belle
	$\tau \to e\pi\pi$	2.3×10^{-8} [126]	Belle
	$\tau \to \mu\pi\pi$	3.9×10^{-8} [126]	Belle
	$\tau \to e\pi K$	3.7×10^{-8} [126]	Belle
	$\tau \to \mu\pi K$	4.8×10^{-8} [126]	Belle
	$\tau \to eKK$	3.4×10^{-8} [126]	Belle
	$\tau \to \mu KK$	4.7×10^{-8} [126]	Belle
	$\tau \to eK^0_sK^0_s$	7.1×10^{-8} [127]	Belle
	$\tau^- \to e^-\pi^0$	8.0×10^{-8} [128]	Belle
	$\tau^- \to \mu^-\pi^0$	1.1×10^{-7} [129]	BaBar
	$\tau^- \to e^-K^0_s$	2.6×10^{-8} [127]	Belle
	$\tau^- \to \mu^-K^0_s$	2.3×10^{-8} [127]	Belle
	$\tau^- \to e^-\eta$	9.2×10^{-8} [128]	Belle
	$\tau^- \to \mu^-\eta$	6.5×10^{-8} [128]	Belle
	$\tau^- \to e^-\rho^0$	2.2×10^{-8} [130]	Belle
	$\tau^- \to \mu^-\rho^0$	1.7×10^{-8} [130]	Belle
	$\tau^- \to e^-\omega$	2.4×10^{-8} [130]	Belle
	$\tau^- \to \mu^-\omega$	3.9×10^{-8} [130]	Belle
	$\tau^- \to e^-K^{*0}$	1.9×10^{-8} [130]	Belle
	$\tau^- \to \mu^-K^{*0}$	2.9×10^{-8} [130]	Belle
	$\tau^- \to e^-\bar{K}^{*0}$	1.7×10^{-8} [130]	Belle
	$\tau^- \to \mu^-\bar{K}^{*0}$	4.3×10^{-8} [130]	Belle
	$\tau^- \to e^-\phi$	2.0×10^{-8} [130]	Belle
	$\tau^- \to \mu^-\phi$	2.3×10^{-8} [130]	Belle

Table 1.2.3: Searches for LFV decays of μ and τ leptons.

Chapter 2

The LHCb experiment at the LHC

CERN's Large Hadron Collider (LHC) [131], briefly introduced in Section 2.1, represents the world's most powerful collider for Particle Physics research ever built. Its primary mission consists of exploring the universe's fundamental building blocks and unravelling the mysteries of the cosmos. The LHC is at the forefront of scientific discovery thanks to its outstanding energy and instantaneous luminosity, a record for a hadronic collider that will be further increased in the upcoming years (Section 2.1.1). The purpose of the collider is to accelerate protons to high energy and induce collisions at various points, where specialized detectors are constructed to detect the particles produced. Among the main detectors, the LHCb experiment [27], described in Section 2.2, is specialized in studying the differences between matter and anti-matter. Detectors of such large dimensions have a highly complex structure that allows them to achieve the goal of reconstructing the particles produced from the proton-proton interaction. A detailed description of the different LHCb components is presented in this chapter, making a classification based on the primary purposes of the sub-detectors: the tracking (Section 2.3), the particle identification (Section 2.4) and the trigger system (in Section 2.5). LHCb underwent a major Upgrade of the detector in 2018 to profit from higher instantaneous luminosity while conserving or improving its performance despite the busier environment. The restart of the LHC operation, initially planned for 2020, was postponed due to the slowdowns caused by the COVID-19 pandemic. In July 2022, the LHCb Upgrade detector recorded the first collision at the increased LHC centre-of-energy of 13.6 TeV. Since then, the detector has regularly collected data, as discussed in Section 2.2.1. Section 2.6 gives an overview of the sub-detectors, the read-out system and the trigger strategy of the LHCb Upgrade.

2.1 The LHC at CERN

The LHC is located 100 m underground in the Swiss-France area close to Geneva. The accelerator has a circumference of 27 km. It is designed to accelerate two proton beams up to an energy of 7 TeV in opposite directions and to make them collide at the centre-of-mass energy[1] of 14 TeV. The beams are made of 2808 bunches containing $\sim 1.15 \times 10^{11}$ protons each, separated by 25ns, leading to a nominal expected collision rate of 40 MHz. The designed instantaneous luminosity[2] corresponds to $10^{34}\text{cm}^{-2}\text{s}^{-1}$. Before the injection into the LHC ring, the beams are pre-accelerated by several steps as shown in Figure 2.1.1 and listed below:

1. Protons are obtained by removing electrons from hydrogen atoms;
2. These protons are accelerated by LINear ACcelerator 2 (LINAC 2) up to 50 MeV;
3. They are then injected into the BOOSTER, which increases their energy up to 1.4 GeV;
4. The Proton Synchrotron (PS) accelerates the protons up to 26 GeV;
5. The beam is injected in the Super Proton Synchrotron (SPS), reaching 450 GeV before being circulated clockwise and counter-clockwise in the LHC ring.

More than 12 thousand superconducting Niobium-Titanium dipole magnets bend protons in the accelerator's orbit, delivering a magnetic field of 8.3 T. Proton beams are kept stable and focused while propagating, thanks to 392 quadrupole magnets. Collisions happen in four distinct interaction points around the LHC, and seven different experiments have the purpose of covering a wide and diverse physics program.

- **ATLAS** [132] (A Toroidal LHC ApparatuS) and **CMS** [133] (Compact Muon Solenoid) detectors are designed to study collisions producing particles with high transverse momentum p_t. The main focus of their program consists of studying the Higgs boson properties and searching for direct evidence of NP.
- **LHCb** [27] (Large Hadron Collider beauty) is an experiment dedicated to heavy flavour physics, designed and optimized for the study of decays of hadrons with a charm and/or a bottom quark (see Section 2.2 for the detailed description).
- **ALICE** [134] (A Large Ion Collider Experiment) is dedicated to the study of quark-gluon plasma in heavy ion collisions, taking advantage of the LHC runs using lead ion beams.

[1] The energy measured in the centre-of-mass reference frame, so the reference frame centred in the weighted average position of all the masses

[2] A measurement of the number of collisions that could be produced in the detector per cm^2 and second

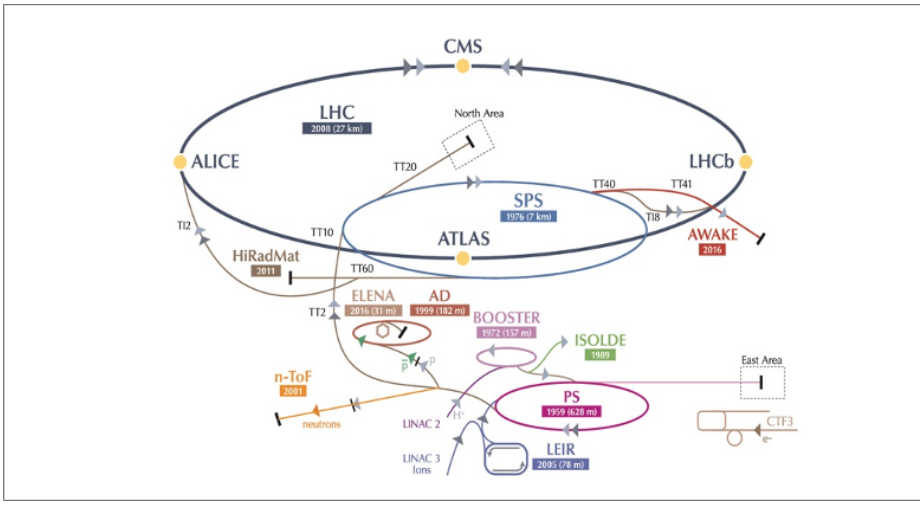

Figure 2.1.1: CERN's acceleration complex, composed of different machines that progressively accelerate the protons extracted from a hydrogen source, up to the nominal collision energy in the LHC.

- **LHCf** [135] (Large Hadron Collider forward) studies particles produced in the forward region by the collisions and performs laboratory measurements supporting cosmic rays studies.
- **TOTEM** [27] (TOTal Elastic and diffractive cross-section Measurement) studies proton-proton cross-section, elastic scattering, and diffractive dissociation. It is also used to measure the LHC luminosity.
- **MoEDAL** [136] (Monopole and Exotics Detector At the LHC) searches for the magnetic monopole.

Furthermore, the LHC has the capability of colliding lead ions, and some data-taking periods have been dedicated to this operational mode. A sizeable part of the LHC physics program is dedicated to lead-lead and proton-lead collisions. One main objective for the lead-ion running is to produce tiny quantities of matter known as quark-gluon plasma and study its evolution. Heavy-ion collisions provide a unique environment for studying very hot and dense matter, recreating similar conditions to the ones present a few milliseconds after the Big Bang.

The nominal instantaneous luminosity at the LHCb experiment during Run 1 was $\mathcal{L} = 1.5 \times 10^{32}\text{cm}^{-2}\text{s}^{-1}$, while for Run 2 it reached $\mathcal{L} = 4 \times 10^{32}\text{cm}^{-2}\text{s}^{-1}$. This is about two orders lower than at ATLAS and CMS experiments. Given the configuration of the LHCb detector, the reduced luminosity helps achieve excellent performance and data quality in the high-multiplicity hadronic environment. In fact, identification and reconstruction of the production vertex of the b quarks and the whole decay chain

is fundamental to the LHCb physics goals. LHC also applies luminosity levelling to regulate the distance between the beams, i.e., keeping the instantaneous luminosity almost constant during operations.

2.1.1 LHC operations and prospects

The first proton beam was injected into the LHC ring in September 2008. Nevertheless, the operation was blocked due to an accident a few weeks later [137]. The LHC was successfully commissioned in 2010, and protons collided at the centre-of-mass energy of 7 TeV until April 2012 and 8 TeV from April 2012 until the end of the first data-taking period (Run 1), with 50 ns of separation bunches. After a period of shutdown (LS1), data taking for Run 2 restarted in 2015 and continued until 2018, with the machine operating at center-of-mass energy of 13 TeV and proton bunches separated at 25 ns. The instantaneous luminosity reached a value doubled ($2 \times 10^{34}\text{cm}^{-2}\text{s}^{-1}$) compared to Run 1. In October 2018, the last proton beams filled concluded Run 2 of the LHC. During the second shutdown period (LS2), which lasted until July 2022, detectors started renovating components of the systems. In particular, LHCb and ALICE experiments underwent significant upgrades of the detector to face the new conditions foreseen for the upcoming data-taking periods.

Run 3, started on the 5^{th} of July 2022, at a record of centre-of-mass collision energy of 13.6 TeV. However, in July 2023, the beam was dumped due to an electrical perturbation [138] that caused the quenching of several superconducting magnets[3]. On this occasion, quenches led to the degradation of the insulation vacuum, needing important interventions, causing the stop of the *pp* collisions for 2023. Operations have successfully restarted in April 2024.

The LHC will need a major upgrade to increase the total number of collisions by a factor of 10 and extend its discovery potential further. The High-Luminosity LHC (HL-LHC) is scheduled to be operational in 2029. Table 2.1.1 summarizes the LHC operating conditions for each Run, including the planned ones for the High-Luminosity phase.
One of the main ingredients for this new project is the use of crab cavities at the interaction region. The crab cavities can "tilt" the proton bunches in each beam, maximizing their overlap at the collision point [139]. In this way, every single proton in the bunch is forced to pass through the whole length of the opposite bunch, which increases the probability that it will collide with another particle, as represented in Figure 2.1.2. After being tilted, the proton bunches' motion appears sideways – just like a crab [140]. During the High Luminosity phase, a peak luminosity between 5

[3]When the magnets lose their superconductive states

Runs	s (TeV)	$\mathcal{L}$ ($\mathrm{cm^{-2}s^{-1}}$)	L ($\mathrm{fb^{-1}}$)
Run 1	7 (2011), 8 (2012)	1×10^{34}	30
Run 2	13	2×10^{34}	190
Run 3	13.6	2×10^{34}	450(?)
Run 4	13.6/14(?)	$5/7.5(?) \times 10^{34}$	1000(?)
Run 5	13.6/14(?)	$5/7.5(?) \times 10^{34}$	3000(?)
Run 6	13.6/14(?)	$5/7.5(?) \times 10^{34}$	5000(?)

Table 2.1.1: LHC condition for Runs 1, 2 and 3 and HL-LHC runs, as of February 2022. The table contains the centre-of-mass energy of the collisions, the instantaneous luminosity and the integrated luminosity in ATLAS/CMS. Question marks flank numbers when they are just an estimation.

and $7.5 \times 10^{34}\mathrm{cm^{-2}s^{-1}}$ is expected [141].

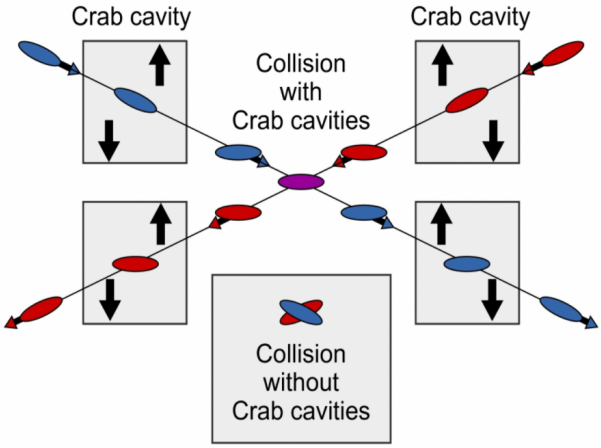

Figure 2.1.2: At the moment, the counter-propagating (red and blue) proton bunches meet with a crossing angle (see bottom central square). Crab cavities will administer a transverse RF kick that tilts the bunches so they appear to move sideways, causing them to collide head-on (purple) at the collision point.

2.2 The LHCb experiment at the LHC

The main physics program of the LHCb experiment consists of studying the properties of particles containing b and c quarks to explore the differences between matter and antimatter. Some critical studies performed at LHCb investigate the CP-violation by measuring precisely the difference in decay rates and the properties of B and D mesons and their antimatter counterpart. The amount of CP asymmetry measured in SM processes does not explain why our universe is essentially made of matter. BSM contributions could appear in new CP-violating processes, indirectly accessed via heavy flavour meson and baryon decays. These effects could be measured as a discrepancy from the SM predictions or a direct search of SM forbidden processes.

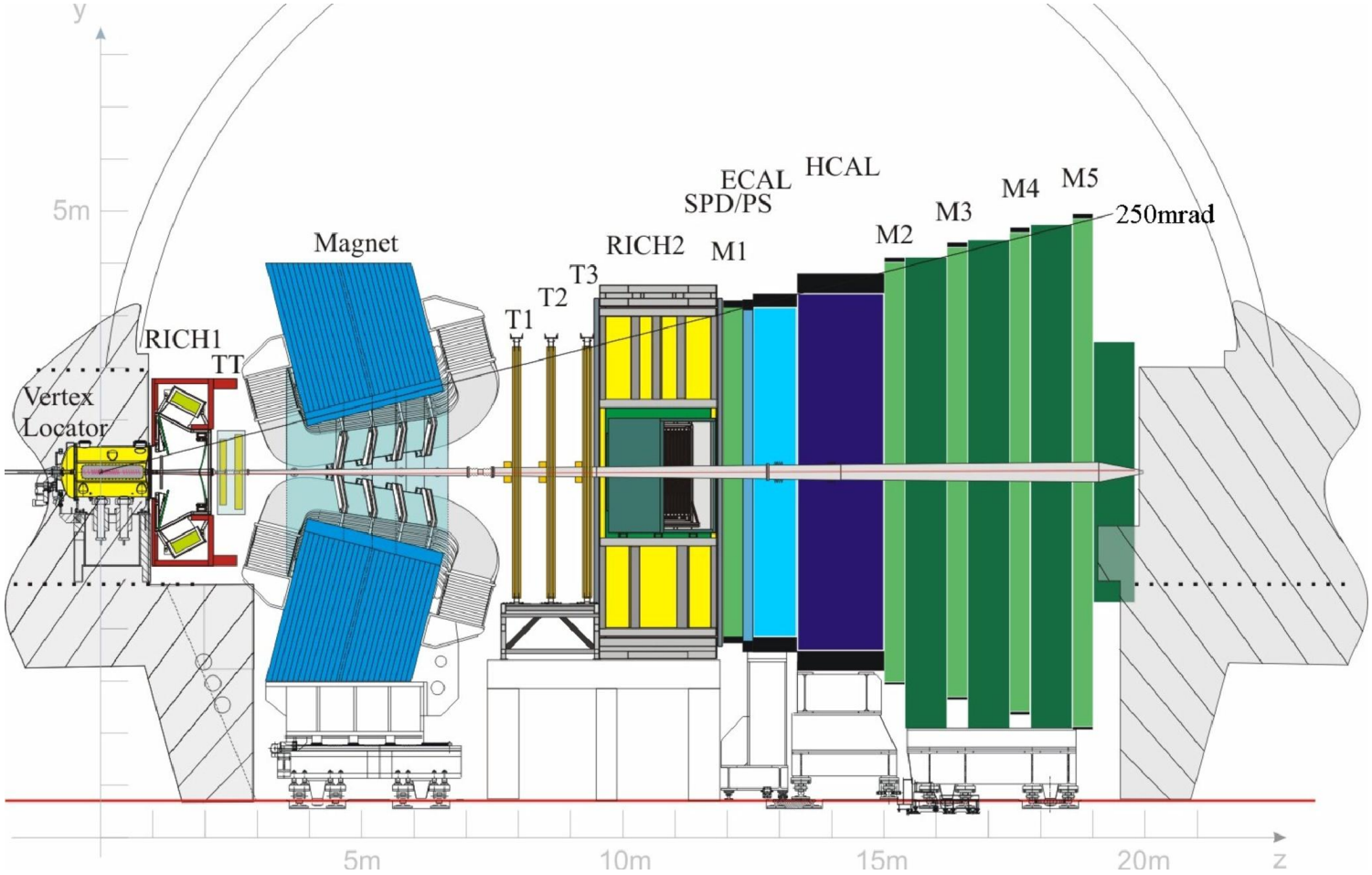

Figure 2.2.1: LHCb detector from the side view.

The LHCb detector [27], shown in Figure 2.2.1, is a 4500 tons forward single-arm spectrometer that stretches for 20 meters along the beam pipe. Given that, throughout Run 2, LHCb operated at a levelled instantaneous luminosity of $4 \cdot 10^{32}\text{cm}^{-2}\text{s}^{-1}$ and the inelastic cross section σ_{inel} in the nominal pseudorapidity[4] range of $2 < \eta < 5$ at centre-of-mass energy of 13 TeV is about 75mb [142], the expected rate of pp collision in the detector is 10 MHz. From the knowledge that $b\bar{b}$ production cross-section integrated over the full η range is $\sim 560\mu$b at $\sqrt{s} = 13$ TeV [143], an event containing a b hadron is expected to be produced once every 134 pp collision in LHCb, on average. Because of the $b\bar{b}$ production mechanism characteristics in proton collisions, the angular distribution of $b\bar{b}$ pairs is maximal in the forward and backward directions with respect to the proton beams direction, as shown in Figure 2.2.2 [144]. The LHCb detector has been designed to cover regions between 2 and 5 in pseudorapidity η, where b hadrons are relatively abundant. A comparison with the CMS coverage, whose acceptance range is $-2.4 < \eta < 2.4$, is presented in Figure 2.2.3.

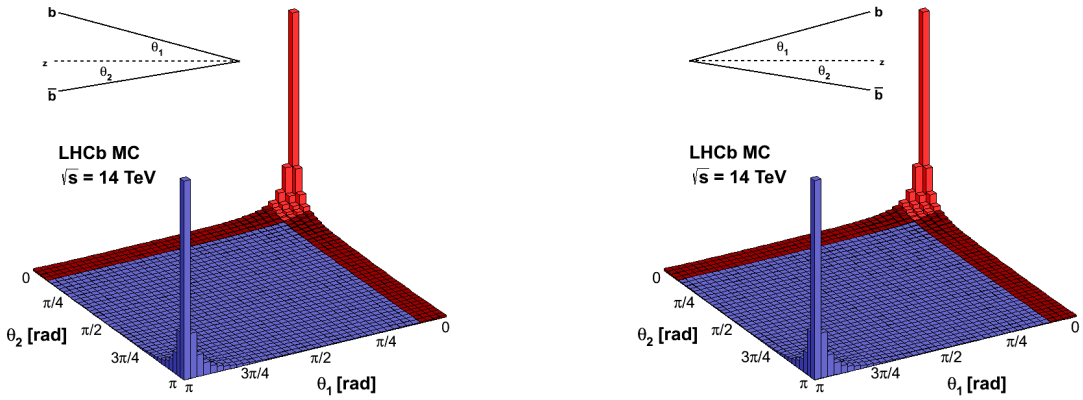

Figure 2.2.2: Production angles for $b\bar{b}$ pairs for left (left) and right (right) production at a centre-of-mass energy of 14 TeV. The distributions are peaking in the forward and backward region with respect to the proton beam direction

A right-handed coordinate system is defined for LHCb as follows:

- the origin of the coordinate system is the interaction point;
- z-axis is aligned with the beam axis in the detector and points from the interaction point towards the LHCb detector;
- x-axis is horizontal and points towards the outside of the LHC ring;
- y-axis is vertical, perpendicular to the x-axis and the beamline.

[4]The pseudorapidity is defined as $\eta = -\log\left[\tan\left(\frac{1}{2}\theta\right)\right]$, with θ denoting the angle from the beam axis.

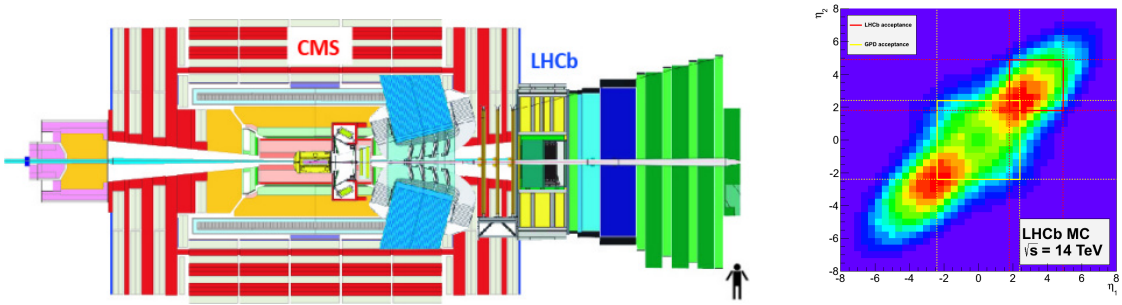

Figure 2.2.3: Comparison of LHCb and CMS detectors acceptance. On the left, a superimposition of the two detector designs highlights the difference in terms of coverage between the two. On the right, $b\bar{b}$ production is represented as function of pseudorapidities of the produced b (η_1) and $\bar{b}$ (η_2) for a centre-of-mass energy of 14 TeV. Yellow (red) lines mark the CMS (LHCb) acceptance.

The transverse $x - y$ plane defines transverse components of a particle's kinematic quantities, such as the transverse momentum p_T and the transverse energy E_T.

The following descriptions of the various subsystem components refer to the detector version before the Upgrade. All the major changes to the detector for the Upgrade are collected in Section 2.6.

An excellent tracking system, particle identification, and trigger strategy are the key ingredients for the LHCb collaboration to achieve the physics goals successfully. The tracking system, discussed in Section 2.3 is composed of a VErtex LOcator (VELO), a dipole magnet and a series of tracking stations placed upstream and downstream with respect to the magnet. The tracks are bent by the dipole magnet with a bending power of 4 Tm and a magnetic field along the y direction. Hits collected by the tracking detectors before and after the magnet allow us to reconstruct charged particle trajectories and measure their momenta. The LHCb has an angular acceptance of [10, 300] mrad in the non-bending plane $y - z$ and [10, 250] mrad in the bending plane $x - y$. This allows the capture of around 27% of the b or $\bar{b}$ quarks produced in the pp collisions at LHC. Furthermore, one of the main ingredients for achieving the physics goal of the collaboration is the excellent resolution of the vertices reconstruction, as ensured by the VELO. The average momentum p of the b or c hadrons produced in the collisions is 80 GeV/c, leading on average to approximately a 1 cm travelling distance before they decay. The reconstruction of the primary vertex (PV), correspondent to the production point of a b or c hadrons, and the secondary vertex (SV), correspondent to its decay position, plays a crucial role in the event selection.

Particle species are instead distinguished thanks to the sub-detectors described in Section 2.4. Different types of hadrons are identified through the two Ring Imaging

CHerenkov detectors (RICHs) placed upstream and downstream of the dipole magnet. Photon and electron signatures are distinguishable thanks to a Silicon Pad Detector (SPD), a PreShower (PS) and an Electromagnetic CALorimiter (ECAL), while the Hadronic CALorimeter (HCAL) ensure the identification of charged and neutral hadrons. Muon stations, placed downstream of the calorimeter system, identify the muons.

Finally, an environment with a very high collision rate, such as the LHCb one, requires an efficient and fast trigger system. Section 2.5 provides a detailed description of this system. This is based on a hardware trigger called L0, collecting information from the electronics of the calorimeters and muon stations to identify the interesting events and to reduce the input rate from 40 MHz to 1 MHz. This rate is further reduced by a software trigger executed by an online CPU farm and organized in two steps: HLT1, performing a first simple event reconstruction, and HLT2, performing a full event reconstruction. The trigger ensures that a maximum number of events interesting to the physics program are collected, which is compatible with the available computing storage resources.

2.2.1 LHCb operations and prospects

The LHCb detector collected a total integrated luminosity of ~ 3 fb^{-1} during Run 1 and ~ 6 fb^{-1} during Run 2. Figure 2.2.4 shows the recorder integrated luminosity by the LHCb detector during the various data-taking periods as a function of the month of the year at the end of Run 2 [145].

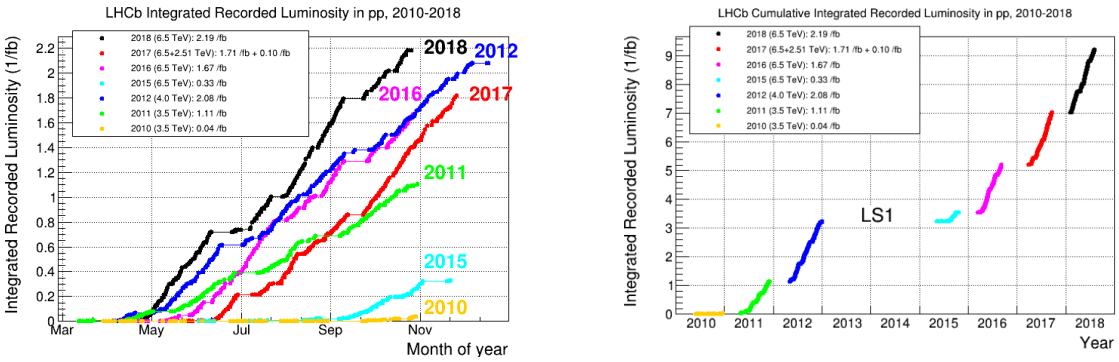

Figure 2.2.4: Integrated luminosity at LHCb: on the left, the evolution of the integrated luminosity is shown for the various years; on the right, the cumulative distribution is shown.

During the LS2, following the end of the Run 2 data-taking period, the LHCb underwent major changes to various detector components, some of which were completely changed. The new detector configuration is identified as LHCb Upgrade. These changes will allow for a profit of a higher instantaneous luminosity, about a factor of

five larger than in Run 2. Indeed, for Run 3, the LHCb deals with an instantaneous luminosity of $\mathcal{L}$=$2 \times 10^{33}\text{cm}^{-2}\text{s}^{-1}$. Figure 2.2.5 shows the increased luminosity collected at LHCb so far during the period of data-taking for year 2024 compared to the other years.

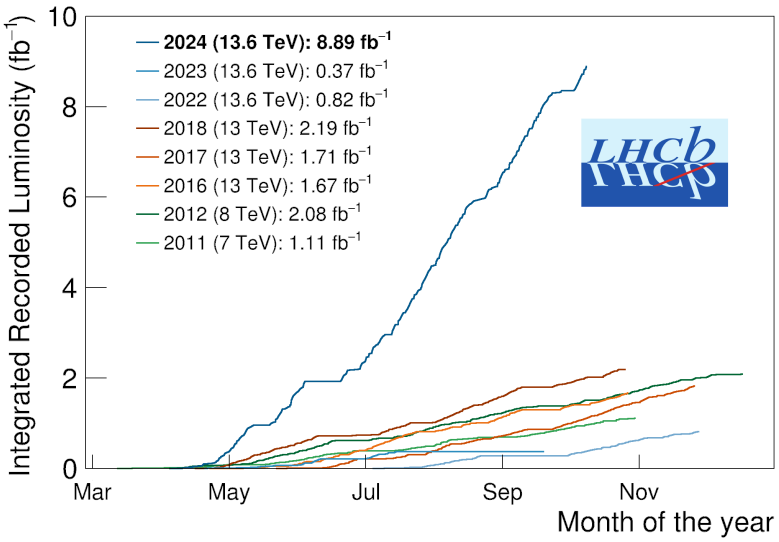

Figure 2.2.5: Updated plot of integrated luminosity at LHCb as a function of the month of the year. The blue line corresponds to the luminosity recorded from 2024 data-taking.

A second major modification of the detector, named Upgrade II, is foreseen for the Long Shutdown 4 (LS4), following Run 4, to cope with the High-Luminosity LHC scenario. This foresees that the LHCb detector will operate at an instantaneous luminosity between $1 \times 10^{34}\text{cm}^{-2}\text{s}^{-1}$ and $2 \times 10^{34}\text{cm}^{-2}\text{s}^{-1}$ [146]. Table 2.2.1 collects for different Runs information about instantaneous and integrated luminosity and the average number of visible pp interactions per bunch crossing μ, both measured and expected.

Runs	s **(TeV)**	$\mathcal{L}$ **(cm^{-2}s^{-1})**	**L (fb^{-1})**	**Average μ**
Run 1	7 (2011), 8 (2012)	$2(2011)/4(2012) \times 10^{32}$	3	~ 1.6
Run 2	13	4×10^{32}	6	~ 1.2
Run 3	13.6	2×10^{33}	14(?)	$\sim 5/6(?)$
Run 4	13.6/14(?)	$2(?) \times 10^{33}$	50(?)	$\sim 5/6(?)$
Run 5	13.6/14(?)	$1/2(?) \times 10^{34}$	150(?)	28/55(?)
Run 6	13.6/14(?)	$1/2(?) \times 10^{34}$	300(?)	28/55(?)

Table 2.2.1: LHCb operating conditions for different Runs, including the luminosity scenario for the Upgrade II. The table contains the centre-of-mass energy, the instantaneous luminosity, the integrated luminosity and the average number of visible pp interactions per bunch crossing. Question marks flank numbers when they are just an estimation. Data taken from [147] and [146]

.

2.3 LHCb tracking system

Charged particles produced in pp collisions are seen as tracks in the LHCb tracking system and are composed of different elements. The VELO, described in Section 2.3.1, allows the identification of the collision point, the decay vertices of b and c hadrons and reconstructs the first segment of the particles' tracks. The momentum of charged particles is evaluated by measuring the bending downstream of the VELO caused by the dipole magnet, briefly discussed in Section 2.3.2. The rest of the tracking system (see Section 2.3.3) is composed by the Tracker Turicensis (TT), placed upstream of the magnet, and by the Inner Turicensis (IT) and Outer Turicensis (OT), positioned downstream of the magnet. The momentum resolution is $\Delta p/p = 0.4\%$ at $p = 5$ GeV/c and $\Delta p/p = 0.6\%$ at $p = 100$ GeV/c and the reconstruction efficiency above 96%. According to the way tracks are reconstructed inside the LHCb detector, we have different categories, schematically represented in Figure 2.3.1 and listed below:

- **VELO tracks** have hits only in the VELO. They are used to determine primary vertexs (PVs) and the first segments (called "seeds") of tracks, later matched with hits in the tracker downstream the magnet;

- **Upstream tracks** are characterised by hits in the VELO and the Upstream Tracker. They help identify the particles decaying very close to the interaction point, which is often the case for short-lived particles. They help suppress background originated by secondary interaction, improving the signal purity, and they furnish additional information that complements RICH1 detector information;

- **T tracks** have hit only in the tracker system downstream of the magnet. They're essential to improve RICH2 performances since information about secondary interaction can be deduced from them;

- **Downstream tracks** are reconstructed using hits from the other tracking detectors upstream and downstream the magnet; they are significant to enhance detection efficiency of relatively long-lived composite particles, such as K_S and Λ^0, decaying outside the VELO;

- **Long tracks** are reconstructed using hits in VELO and IT or OT and possibly in TT. They are associated with charged particles produced close to the interaction point and fly throughout the whole detector. They are generally the most relevant for physics analysis, given the precision on reconstructing the particle momenta and vertices.

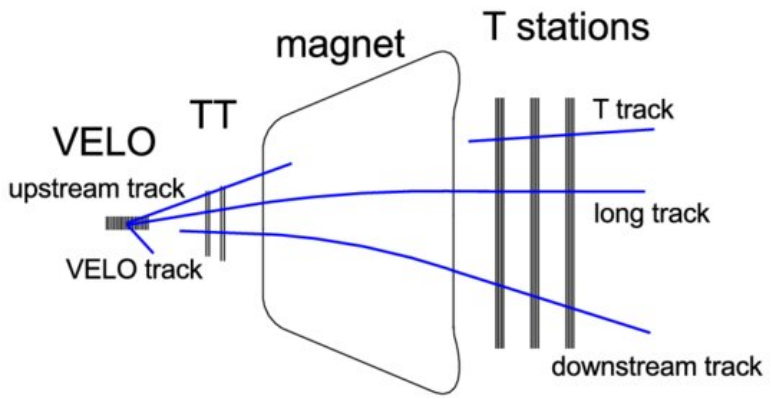

Figure 2.3.1: Graphical representation of different types of tracks reconstructed at LHCb.

2.3.1 The VErtex LOcator (VELO)

The VELO [148], shown in Figure 2.3.2, surrounds the interaction point. The detector aims to reconstruct and distinguish prompt tracks, i.e., tracks coming directly from the pp collisions and tracks coming from the decay of b and c hadrons. Prompt tracks will identify the PV of the pp collision, while the tracks from b and c hadrons identify the secondary vertices. For each track, the VELO allows the evaluation of the impact parameter (IP), defined as the distance of the track's closest approach to the given vertex. While PV resolution is fundamental for correctly measuring CP-violation parameters, lifetime of heavy hadrons, and oscillation frequencies of heavy mesons, IP resolution is crucial to suppress combinatorial background composed by candidates in which one track is associated with the wrong decay vertex.

VELO performances are achieved thanks to its very unique design. It comprises two retractable halves of 21 silicon modules placed perpendicularly to the beam line. Modules are made of semi-circular silicon strip sensors with an external radius of 42 mm and an internal radius of 8 mm. For each module, we can distinguish R and ϕ sensors, measuring the radial distance and the azimuthal coordinate of the traversing charged particles. Two additional pile-up sensors are installed upstream of the interaction region to guarantee a fast trigger at the hardware level using the measurement of the backwards-charged track multiplicity and the identification of multiple interaction events. During injection and unstable beam conditions, the two halves are separated from each other by a distance of 6 cm. In contrast, the two halves overlap in stable beam conditions, covering the full acceptance. A schematic representation of VELO sensors is given in Figure 2.3.3.

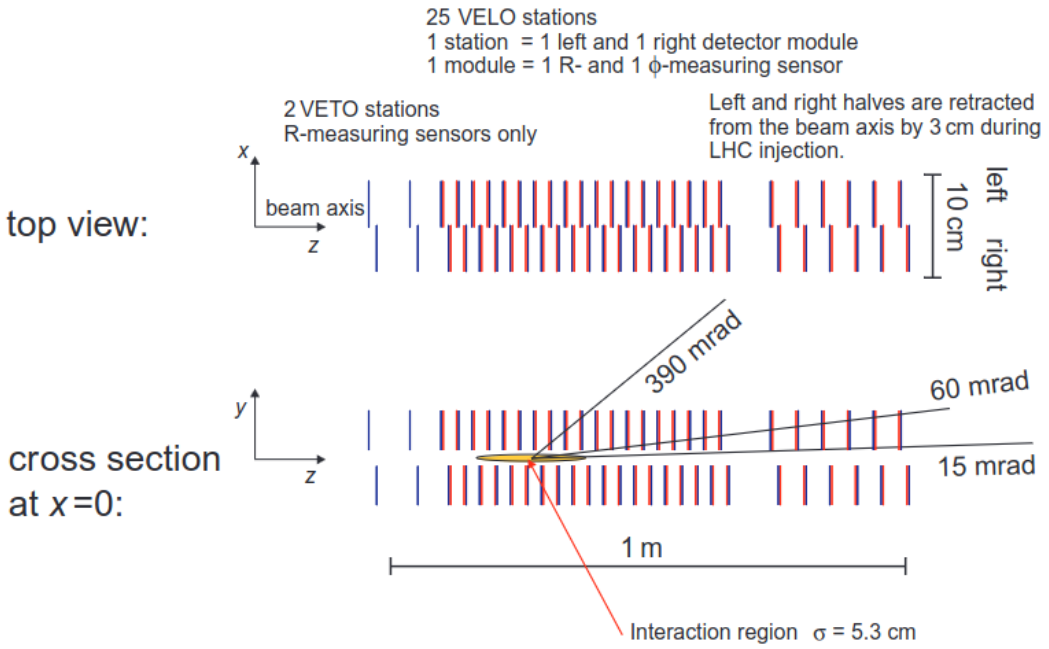

Figure 2.3.2: VELO detector layout.

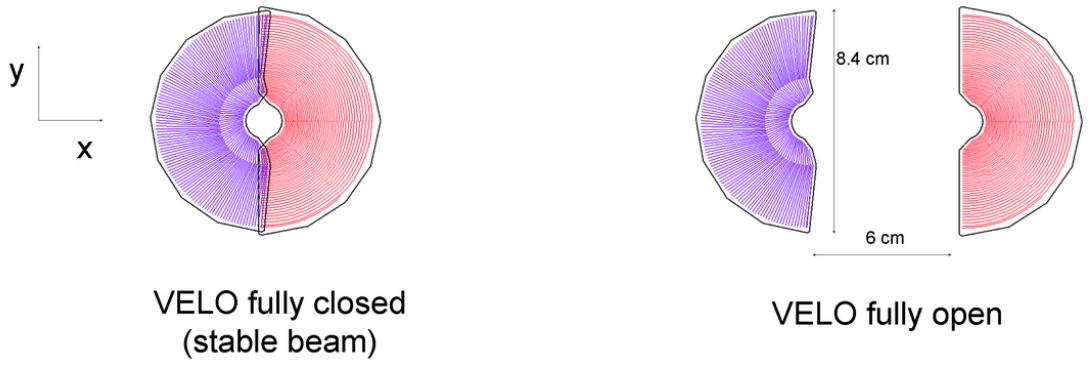

Figure 2.3.3: Front view of the VELO modules in both cases of fully closed (left) and open (right) positions. R (ϕ) sensors are illustrated in red (blue).

2.3.2 LHCb dipole magnet

LHCb adopts a non-superconductive dipole magnet composed of two mirror-symmetric coils with an overall bending power of 4 Tm [149]. A sketch of the LHCb dipole magnet is represented in Figure 2.3.4. The main $\vec{B}$ component is along the y-axis, allowing to bend particles in the vertical plane and measure their momentum.
The magnetic field polarity is regularly reversed during data-taking to keep under control systematics due to left-right asymmetric effects in the detector.
Low momentum particles are affected by a more significant deflection from the dipole and might be swept out of the LHCb acceptance by the dipole. Their reconstruction relies only on the VELO and upstream tracker.

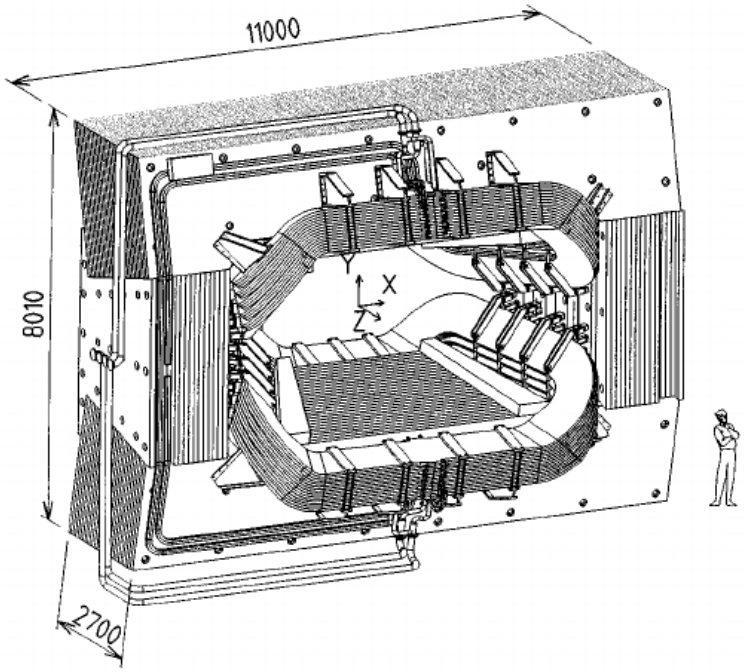

Figure 2.3.4: Sketch of the LHCb dipole magnet.

2.3.3 Tracker Turicensis (TT), Inner Tracker (IT), Outer Tracker (OT)

The other detector components responsible for the tracking are the TT, placed upstream of the magnet, the IT [150] and the OT [151], located downstream the magnet. The TT consists of four layers of silicon strip sensors, organized in two stations separated by ~ 30 cm in z direction, named TTa and TTb, as represented in Figure 2.3.5. The four layers are disposed of perpendicular to the beam axis in the $x-u-v-x$ stereo configuration: the first and last layers provide the x coordinate, while the middle layers are rotated in the opposite direction around the beam of $-5°$ and $+5°$, respectively, to provide the u and v coordinates. The combination of u and v measurements allows the extraction of the track's $y(z_{layer})$, i.e. its y coordinate at the z position of the layer.
Each module contains seven sensors in a row. Sensors comprise 512 read-out strips, leading to an excellent position resolution of $\sim 50\mu$m in the bending plane.

The IT and the OT cover the inner (higher occupancy) and outer region of the three tracking stations $T1$, $T2$, and $T3$ after the magnet. Both the IT and the OT use layers arranged in the $x-u-v-z$ stereo configuration.

The inner region of the T stations consists of a silicon strip sensor disposed in four boxes. The top and bottom boxes contain a single silicon sensor, while the left and right boxes contain two rows of silicon sensors. A scheme of the Layout of the IT is

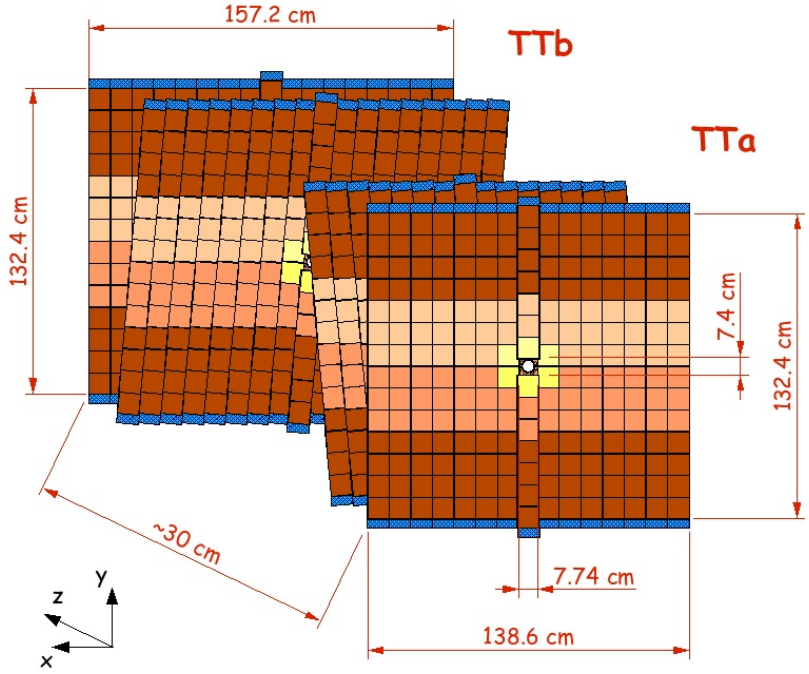

Figure 2.3.5: Layout of the TT subsystem. The four layers are collected in two stations (TTa and TTb), separated along the z-axis. Colour coding highlights the grouping of silicon sensors.

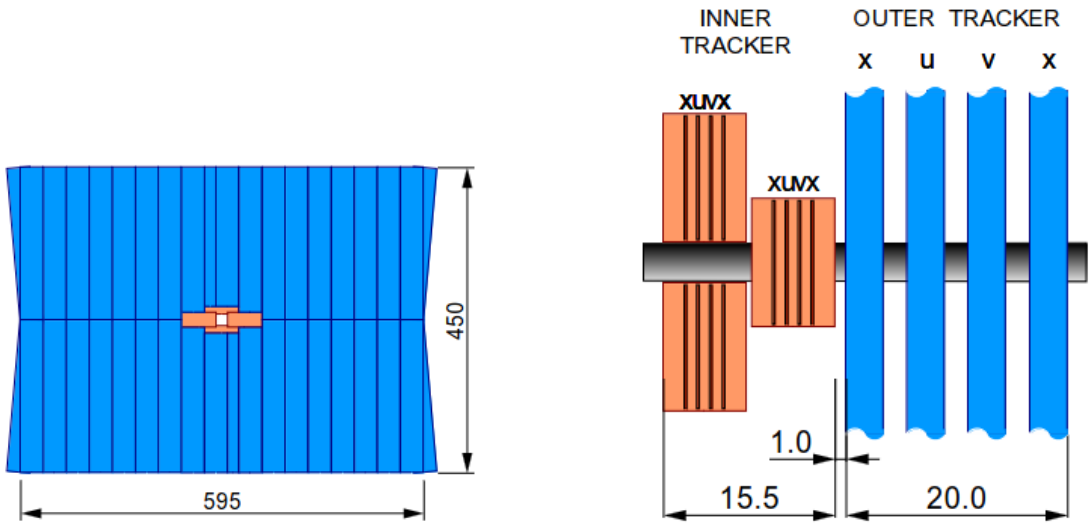

Figure 2.3.6: Layout of IT and OT subsystem. On the left (right), inner in orange and outer in blue tracking detectors from the front (lateral) view.

presented in Figure 2.3.7. Even if the IT covers only 2% of the LHCb acceptance, it contains 20% of tracks produced in pp collisions, given the high density of tracks expected close to the beam pipe.

The outer region of the T stations comprises 128 straw-gs drift tubes for each module.

Each straw is filled with a gas mixture of 70% of Ar and 30% of CO_2, which allows a drift time of less than 50 ns and a resolution of 200 μm. The tube walls are made of conductive material to collect the charge produced by the gas ionisation induced by the traversing charged particle.

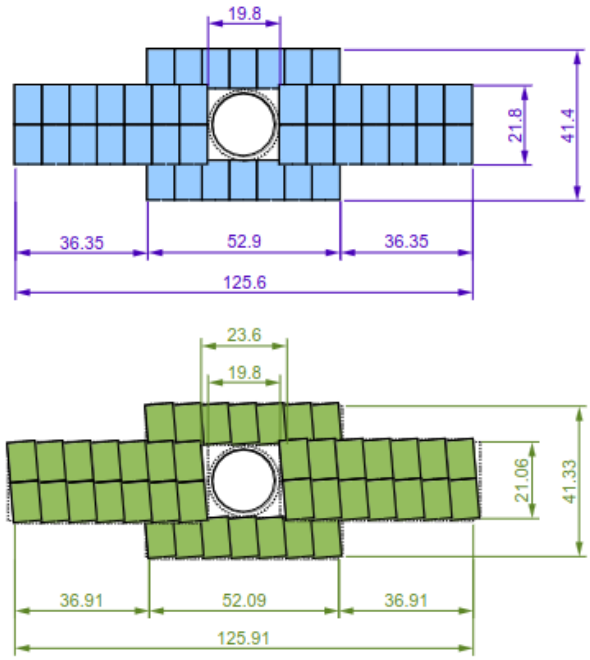

Figure 2.3.7: Layout of the x layer (top) and the stereo layer (bottom) of the IT.

2.4 LHCb particle identification system

In LHCb, the identification of particle species is guaranteed by three detectors: the RICH (see Section 2.4.1), composed by RICH1, upstream the magnet, and RICH2, downstream the magnet; the calorimeter system (see Section 2.4.2), and the muon system (see Section 2.4.3).

2.4.1 RICH detectors

The RICH detectors, shown in Figure 2.4.1, aim to identify final state particles in different momentum ranges, particularly π and K [152]. They exploit the property of Cherenkov photon emission by a charged particle traversing a dielectric medium with a velocity ($\beta = v/c$) higher than the medium's light speed. If n is the refractive index of the medium, the photon is emitted in a cone with a given angle θ_C:

$$\cos\theta_C = \frac{1}{n\beta} \tag{2.4.1}$$

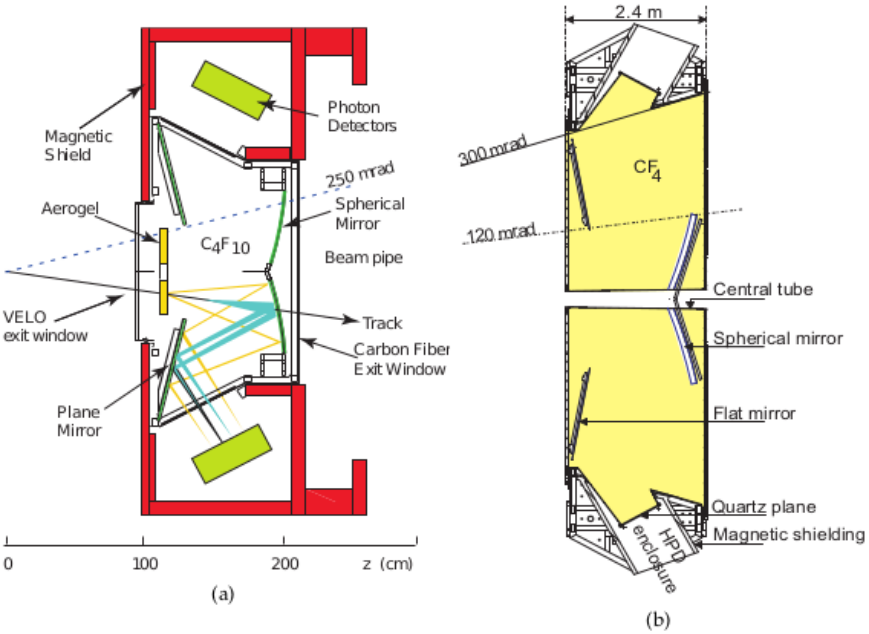

Figure 2.4.1: Schematic representation of the side view of the RICH1 (left) and the RICH2 (right) detectors.

RICH1 is located upstream of the magnet, between VELO and TT. It is designed to identify low-momentum particles with p in the range [1,60] GeV/c. It is filled by aerogel and fluorobutane C_4F_10, optimized for particle identification of particles with momentum in the nominal range. A spherical and flat mirror reflects photons emitted by particles traversing RICH1. They are collected by a matrix of hybrid photon detectors to detect reflected light cones. The radius of the ring appearing as an image is used to infer the value of θ_C, thus the value of β. The combination of the β measurement and the momentum measurement from the track reconstruction allows us to assign a mass to the particle, therefore identifying it.

RICH2 is located downstream of the magnet, after the last T station and works similarly to RICH1. However, it deals with higher momentum particles (p in the range [15,100] GeV/c) and covers a smaller acceptance region. The main difference is that the dielectric medium used for RICH2 is tetrafluoromethane CF_4, which has an optimal lower refractive index to distinguish higher momentum particles.

2.4.2 Calorimeters

The LHCb calorimeter system [153] aims to identify and measure the position and energy of electrons, photons, and hadrons. They are also used by the L0 trigger, discussed in Section 2.5, to reduce the rate at the hardware stage. The calorimeter

system is composed of SPD, PS, ECAL and HCAL. A graphical representation of the signatures of different particles in the LHCb calorimeter system is given in Figure 2.4.2.

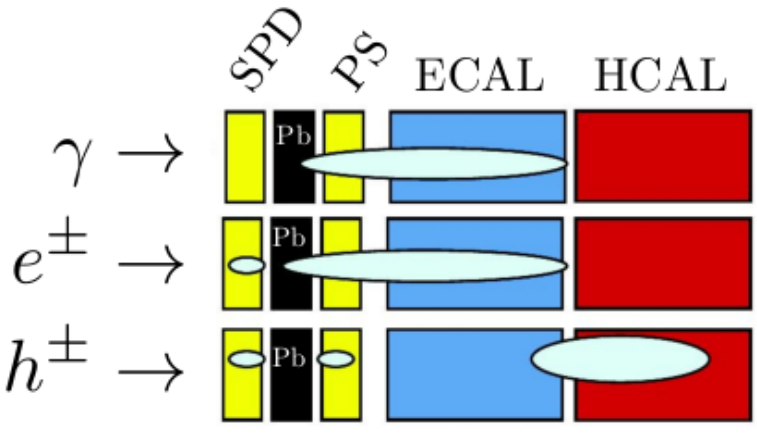

Figure 2.4.2: Signatures in the LHCb calorimeter system for photons, electrons, and hadrons

The PS and SPD are made of two planes of scintillator pads separated by a 15 mm thick lead plane between them. The lead corresponds to 2.5 electromagnetic interaction length X_0, but only ~ 0.06 hadronic interaction length λ_l. The scintillating material used for PS and SPD allows charged particles to initiate their shower, and it is particularly effective on electrons and photons. Hadronic showers are mostly initiated at a position downstream of the ECAL. Electrons start showering already in the SPD, contrary to the photons. This helps discriminate between electrons and photons within the calorimeter. PS separates photons and neutral hadrons: unlike neutral hadrons, photons are fully converted into electron-positron pairs and interact with the detector. The ECAL comprises 66 layers of 4mm thick scintillating material alternating 2mm thick lead layers to cover 25 electromagnetic radiation lengths X_0 and around one hadronic radiation length. Photons, electrons, and neutral pions are reconstructed using the information from ECAL. The HCAL, placed downstream of all the other calorimeter sub-systems, is made of 3mm thick scintillating material alternating 1mm thick iron layers, used as an absorber. It covers a total of 5.6 hadronic radiation length.

PS, SPD, and ECAL are designed to have three regions with different granularities (inner, middle, and outer) in the transverse plane to cope with detector occupancy. In comparison, HCAL comprises only two regions (inner and outer), as represented in Figure 2.4.3. Overall the ECAL and HCAL energy resolution corresponds to $\frac{\sigma_E}{E} = \frac{10\%}{\sqrt{E}} \oplus 1\%$ and $\frac{\sigma_E}{E} = \frac{65\%}{\sqrt{E}} \oplus 9\%$, with energy in GeV. The HCAL's worse resolution than ECAL is due to lower granularity and lower light yield (by a factor ~ 30 smaller in HCAL with respect to ECAL).

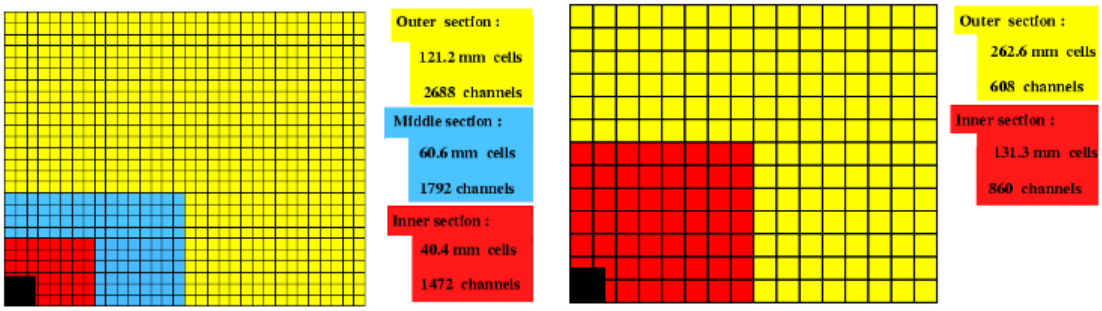

Figure 2.4.3: On the left, segmentation of the SPD, PS, and ECAL. On the right, segmentation of the HCAL

2.4.3 Muon stations

The LHCb muon system [154] plays a crucial role in performing a very efficient muon identification and characterization, measuring momentum and transverse momentum in both hardware and software triggers. The muon system comprises five muon stations (M1 to M5) at the end of the LHCb spectrometer. The first muon station, M1, placed downstream of the calorimeter preshower, is used by the Level 0 trigger to provide the transverse momentum estimation of muon tracks. The other stations are interleaved with the muon shield, comprising electromagnetic and hadronic calorimeter and three iron filters, for a total absorber thickness of $\sim 20\lambda_l$ (nuclear interaction length). Each station is divided into two sides (A and C). Each side has four different regions (R1 to R4) composed of multi-wire proportional chamber with different granularity, except for the inner region (R1) of the first station M1, where Gas Electron Multipliers (GEM) are used due to the higher particle flux. The detector gas is a mixture of Ar, CO_2, and CF_4, allowing to gather information with time-resolution smaller than 5 ns.

The system guarantees a high muon identification efficiency of 97%, with a probability of misidentification of pion to muon from 1% to 3%. A sketch of the system and the station layout is presented in Figure 2.4.4.

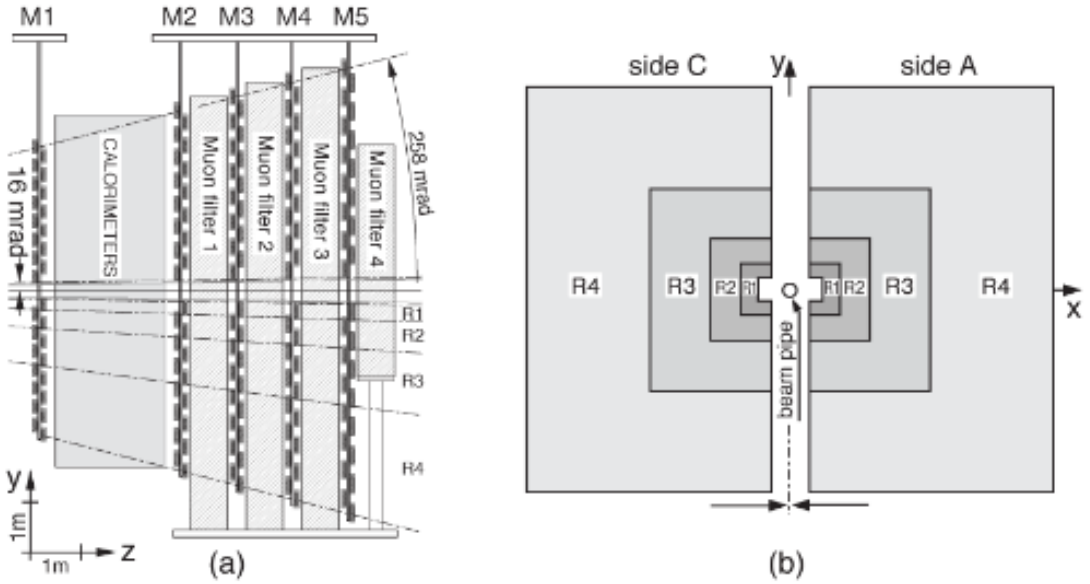

Figure 2.4.4: On the left: side view of the muon system. On the right: station layout, with the four regions R1-R4 indicated.

2.5 LHCb trigger system

The LHCb trigger system [155] aims at reducing the 40 MHz LHC collision rate, corresponding to 30 MHz of visible interaction for LHCb, to a manageable rate for which interesting data can be stored on disk. This rate corresponds to 5 kHz ($\sim$ 0.3 Gb/s) for Run 1 and 12.5 kHz ($\sim$ 0.6 Gb/s) for Run 2. LHCb trigger schemes are shown for Run 1 and Run 2 data-taking period in Figure 2.5.1.

The rate reduction is performed in three different steps. The first stage, called L0, is the hardware trigger. It exploits information from the calorimeter, muon, and VELO pile-up systems to reduce the bunch-crossing rate to 1.1 MHz. This is described in Section 2.5.1. The other stages comprise C++ software applications named High-Level Trigger (HLT). To optimise the computational power, the HLT is separated into two parts: HLT1, discussed in Section 2.5.2, runs online a fast reconstruction and reduces the rate to 80 kHz, while HLT2, treated in Section 2.5.3, executes inclusive and exclusive event selection to reduce rate and bandwidth further.

For the Run 2 data-taking period, LHCb has introduced a real-time detector alignment and calibration. Data collected at the start of the fill are processed in a few minutes and used to update the alignment, while calibration constants are re-evaluated for each LHC run[5]. Updated alignment and calibration constants are used at the HLT2

[5]A "fill" corresponds to the period from the beginning of the collision of the beams in the LHC to the dump of the beams, while a "run" is the time interval of an LHCb data taking, with a maximum length of

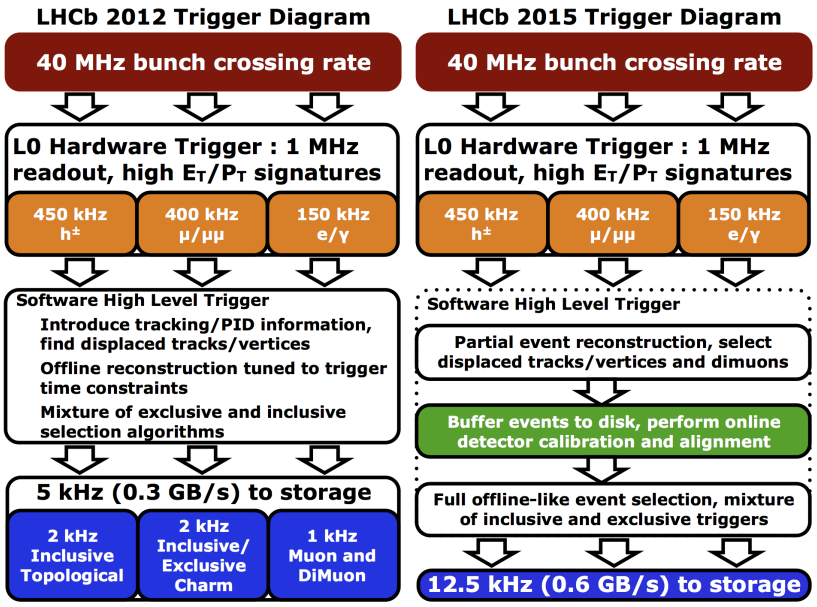

Figure 2.5.1: LHCb trigger schemes. The left (right) schema corresponds to the 2012 (2015) data-taking period.

step, providing online performances of similar quality to what was achieved by the end of the year offline processing in Run 1. The real-time alignment and calibration also introduced the possibility of performing direct physics analysis on the trigger output, thanks to the so-called "turbo" stream.

2.5.1 Level 0 (L0)

The trigger's hardware stage, called the Level 0 (L0) trigger, makes decisions based on electronic inputs from the calorimeter, the muon system and the VELO pile-up sensors. It brings the input rate down to ∼1 MHz. Since the B hadrons are massive ($m > 5\text{GeV/c}^2$), interesting final states are characterised by particles with large p_T or E_T. In particular, the calorimeter trigger system reconstructs and selects the highest E_T electron, photon and hadron in the event while the muon trigger system reconstructs the highest p_T muon or the highest muon pair $p_T^{12} = \sqrt{p_T^{high} \times p_T^{2^{nd}high}}$. Furthermore, events that are too busy are excluded thanks to VELO pile-up system information and SPD multiplicity measurements.

2.5.2 High Level Trigger I (HLT1)

The HLT1 uses partial event reconstruction to reduce the output rate from L0 by an additional factor of 30. The HLT1 algorithms select events with high-momentum tracks. For this reason, the impact parameter with respect to the primary vertex

one hour.

is evaluated and used as a discriminating variable. Secondary vertices are also reconstructed, and their properties are used to reject background events.

2.5.3 High Level Trigger II (HLT2)

Events surviving the HLT1-triggered decision are fully reconstructed and selected by the HLT2 trigger. At this stage, exclusive and inclusive decay modes are chosen by specific lines and stored. Most of the B decays with a displaced vertex and at least two charged particles in the final state are selected by three topological lines (`HLT2TopoTwoBodyMVA`, `HLT2TopoThreeBodyMVA` and `HLT2TopoFourBodyMVA`). Topological lines are highly efficient, providing a significant background rejection with good decision time performances [156]. The inclusiveness of the line is reached by excluding cuts on selection variables such as the mass of the B candidates and the agreement of their momentum direction with the direction from the PV to the SV. Furthermore, cuts based on vertices qualities are avoided to trigger efficiently on B decays with long-lived resonances, like D mesons. In addition to the lines mentioned above, HLT2 contains other inclusive lines dedicated to muon identification (using the muon system information) and electron identification (exploiting VELO clusters). Exclusive selection lines are also used in the HLT2, requiring that all the particles of the exclusive decay are reconstructed. In the majority of the cases, these lines are dedicated to exclusive channels containing muons in the final state or for prompt charm hadron production studies.

2.6 The LHCb Upgrade

The LHCb Upgrade I [157] represents a major change in the experiment's configuration to improve the measurements' precision and sensitivity [158]. The detector has been almost wholly renewed to cope with higher instantaneous luminosity, about five times larger than the nominal one in Run 2. Key features of the LHCb Upgrade include the removal of the hardware trigger in favour of a full-software trigger and an entirely new tracking system comprising a pixel vertex detector, a silicon tracker upstream (UT) of the dipole magnet, and three scintillating fibres tracking stations (SciFi) downstream of the magnet. The photon detection system of the RICH has been changed, as well as the mirror system of RICH1. The readout electronics of all the subsystems, including the RICH, the calorimeters and the muon systems, have been overhauled, and the data acquisition system (DAQ) has been modified to allow a readout at the beam crossing rate of 40 MHz. Finally, the computing model has been revised, and the software of the experiment rewritten [159], as partially discussed in Chapter 3 [160].

In this chapter, we will remind the physics motivations for the LHCb Upgrade in

Section 2.6.1 and provide a description of the main changes in the various systems. In particular, Section 2.6.2 describes the tracking system; Section 2.6.3 discusses the particle identification; Section 2.6.4 is dedicated to the trigger strategy.

2.6.1 Physics motivation

The LHCb experiment has a broad flavour physics program, which covers topics such as studies of CP-violation, measurement of weak phase in B_s^0 oscillations, search for physics beyond the standard model in rare decays of the type $B \to l^+l^-$ and $B \to Xl^+l^-$ (with l indicating a lepton). During Run 1 and Run 2, LHCb has produced several world-best measurements of these types. Some examples are the tests of lepton flavour universality via the ratio $R(K^{(*0)}) = \mathcal{B}(B^{+(/0)} \to K^{+(/*0)}\mu^+\mu^-)/\mathcal{B}(B^{+(/*0)} \to K^+e^+e^-)$ or in semileptonic $b \to cl\nu$, as well as the CP-violation in charm sector and tests on CKM observables like the angle γ. These crucial flavour physics measurements are statistically limited [161], with an experimental precision not comparable to the uncertainties of the theoretical predictions. The sensitivity of the measurements is expected to improve significantly with the upgraded detector. In fact, being able to collect data at a higher instantaneous luminosity, the experiment will considerably increase the sample of b- and c- hadrons. In addition, the full software trigger will remove the limitations of the hardware trigger for fully hadronic and electronic signatures that were discussed in Section 2.5.1. Examples of how some measurements could potentially improve are presented in Table 2.6.1, including in the High Luminosity scenario [162]. The LHCb physics scope, however, extends beyond the flavour sector, with possibilities of exciting discoveries in searches for Majorana neutrinos, exotic Higgs decays and precision electroweak measurements, often complementary to analogous measurements performed by other experiments. In any scenario, the LHCb upgrade will provide measurements essential to understanding the physics landscape this decade will unveil [163].

Observable	R_K(**EW penguin**) $1.1 \leq q^2 \leq 6$ GeV^2/c^4	R_{K^*} (**EW penguin**) $1.1 \leq q^2 \leq 6$ GeV^2/c^4	$R(D^*)$ (**LFU in** $b \to cl\nu$)
Current LHCb	0.042	0.072	0.024
LHCb 2025	0.025	0.028	0.007
Upgrade II	0.007	0.008	0.002
Observable	γ (**CKM test**)	$\sin 2\beta$ (**CKM test**), with $B^0 \to J/\psi K^0_s$	$\Delta A_{CP}(KK \to \pi\pi)$
Current LHCb	4° [164]	0.017 [165]	2.9×10^{-4} [166]
LHCb 2025	1.35°	0.005	1.3×10^{-4}
Upgrade II	0.35°	0.001	3.3×19^{-5}

Table 2.6.1: Summary of prospects at the end of the Upgrade 1 and 2 of some flavour observables at LHCb taken as an example [162]. The projected sensitivities do not consider detector improvement apart from the trigger ones.

2.6.2 Tracking system upgrade

The whole tracking system of the LHCb experiment has been changed for the LHCb Upgrade. Materials for this Section come from [167].

VELO Upgrade

Most of the VELO described in Section 2.3.1 has been replaced to cope with the expected higher signal rate. The Upgraded VELO reuses a large part of the mechanical infrastructure of the previous design, but the sensors and most of the internal components are changed [168].

The number of detection planes has increased to 26, and each one is composed of two retractable modules. In nominal running conditions, the modules will be placed 5.1 mm from the beam pipe. The modules are organized into two halves and enclosed in radio frequency (RF) boxes that separate the machine vacuum from the secondary vacuum in which they are located. The module has a L-shape, with two sensors containing three ASICs[6], called VeloPix [169]. The VeloPix is designed to provide the required readout performance at the high instantaneous luminosity conditions of the LHCb Upgrade. It comprises a matrix of 256×256 square pixels of $55 \times 55 \mu m^2$. A total of 41 million pixels enhances the track reconstruction speed and precision. A schematic layout of the Upgraded VELO in different configurations depending on the activity of LHCb and a representation of the module are given in Figure 2.6.1.

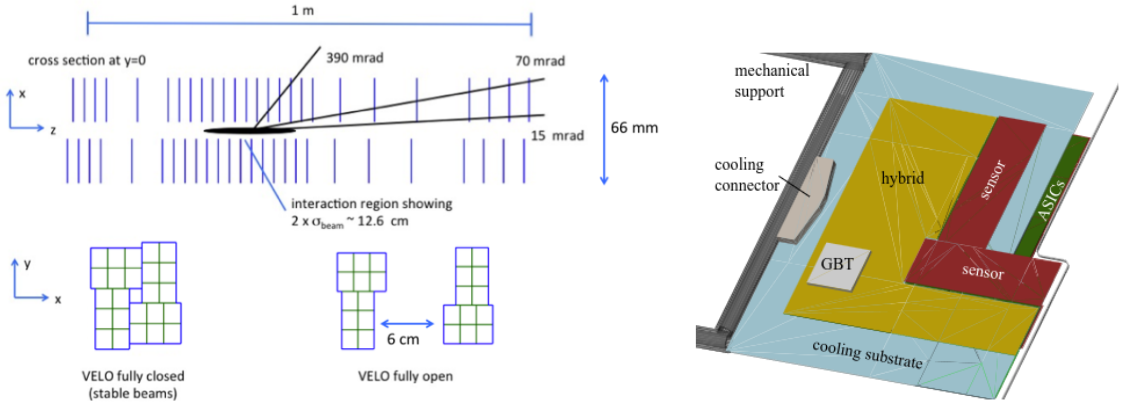

Figure 2.6.1: On the left, the Upgraded VELO layout shows the different configurations during and outside the stable beams period. On the right, the layout of the module shows the positions of the major components.

The module cooling design has been upgraded to protect the sensors from thermal

[6]The application-specific integrated circuit is an integrated electronic circuit chip customized for a particular use

runaway effects and to cope with the high-speed pixel ASIC power dissipation. Sensors are cooled at $-20°$C using evaporated CO_2 circulating in microchannel substrate.

Upstream Tracker (UT)

The TT, described in Section 2.3.3, has been replaced by the Upstream Turicensis (UT) [170]. This tracker comprises four planes of silicon strips with thinner sensors, finer segmentation, and more extensive coverage than the TT. This allows faster and more efficient track reconstruction and coping with the increased multiplicity of the event. The four layers are disposed in the $x - u - v - x$ configuration, i.e. with the first and last plane with vertical strips and the middle two with strips tilted by $\pm 5°$ with respect to the vertical axis. The two upstream planes comprise 16 staves representing a vertical column, while the downstream planes have 18 staves. Each stave consists of 14 sensors of 98.88×98.88 mm^2, except for the central region. To increase granularity in the high occupancy region around the beam, some sensors near the beam are half-pitch, and some are half-pitch and half-length. Each stave is designed to provide mechanical support and cooling for the front-end electronics. The UT layout and the stave structure are presented in Figure 2.6.2.

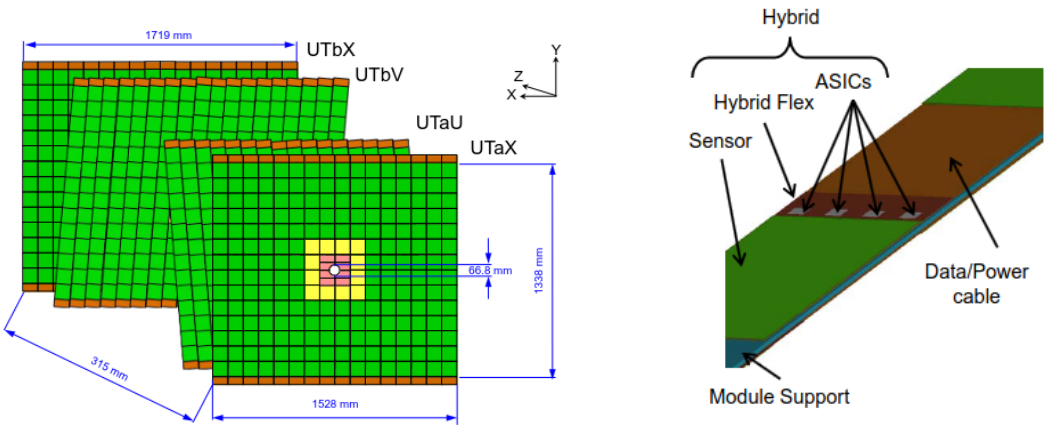

Figure 2.6.2: On the left, the layout of the UT tracker with modules differentiated by geometry and granularity represented with different colours. The UT stave structure is on the right, with a silicon strip sensor and readout ASICs attached to the hybrid flex.

As already discussed for the TT, the UT is fundamental to reconstructing long-lived particles, such as K_s^0 and Λ^0, when they decay outside the VELO. In addition, it is possible to estimate tracks' and transverse momentum using hits from VELO and UT. This estimation can be used in the software trigger to tighten the search windows for hits in the tracker downstream of the magnet, thus speeding up the reconstruction algorithms. Finally, the additional hits in the UT allow us to reduce the number of fake tracks.

Downstream tracker (SciFi)

The three-track stations placed downstream of the tracker have been entirely replaced by a homogeneous tracker using scintillating fibres as active material, which gave the name SciFi to the project [170]. The SciFi consists of three stations with four detection planes following the $x - u - v - x$ configuration, separated by an air-filled gap of 50 mm. The station closest to the magnet (T1) comprises ten modules, while the other two stations (T2 and T3) are larger and comprise twelve modules each. The modules are composed of four fibre mats, each separated in the middle by a mirror surface used to increase the light yield of the scintillating fibres. Fibres in the mat are disposed of along six glued layers. The polymer is excited by the ionization energy deposited (few eV) [171]. An organic fluorescent dye with matched excitation energy level structures is added to the polystyrene base to improve the efficiency of the scintillation mechanism. The dye is chosen to have high quantum efficiency, fast decay time, and a particular emission wavelength. The scintillation light is guided by the fibres to the two extremities of each mat, where it is collected by multi-channel silicon photomultipliers (SiPMs), cooled down to -40°C. The signal is then digitized using a custom ASIC. In the Front-End electronics, dedicated FPGAs process the SiPM output and evaluate the information relative to the clusters. The layout of one of the layers of the SciFi is presented in Figure 2.6.3.

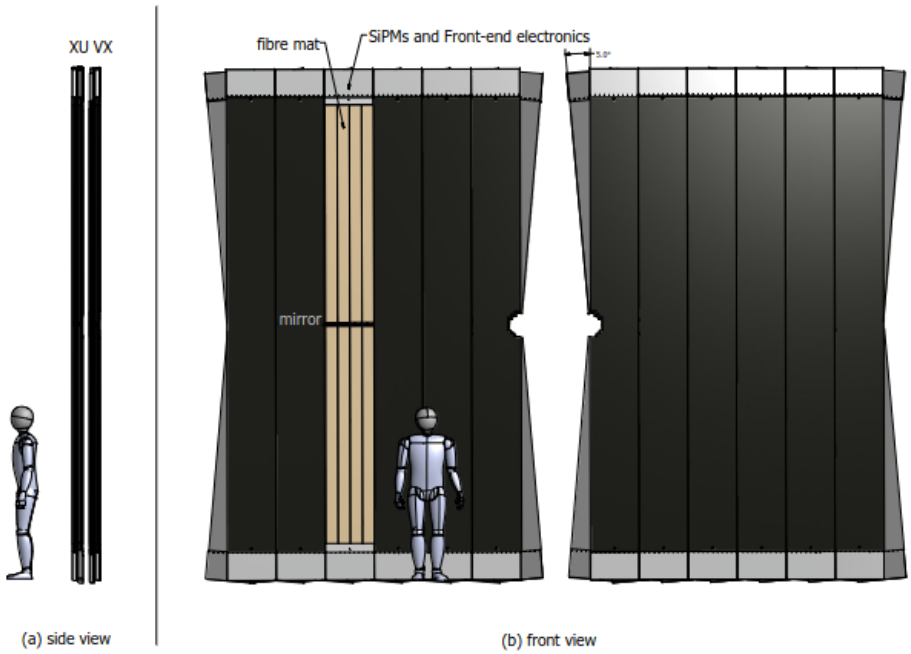

Figure 2.6.3: Layout of one of the SciFi stations for the LHCb Upgrade [172]. Each station comprises four layers, each composed of 10 or twelve modules. Each module is composed of four fibre mats, made up of six layers of scintillating fibres with a diameter of 250 μm.

The SciFi key features are the high detection efficiency, better than 99%, the limited material budget (less than 1% X_0 per detection layer) and a position resolution better than 100 μm [173].

2.6.3 Particle identification system upgrade

The upgrade of the LHCb detector includes partial modifications of the particle identification subsystems, formed by RICH, calorimeters and muon system, to maintain good PID performances when operating at the increased instantaneous luminosity [174].

RICH Upgrade

Both RICHes kept the layout adopted for Run 1 and Run 2. However, two significant changes are applied to the detectors. The Hybrid Photon Detectors (HPD) have been replaced by multi-anode photo-multipliers (MaPMT) with external readout at 40 MHz. The design is similar for RICH1 and RICH2: 8×8 pixels MaPMTs are distributed over the active area of the sub-detectors. To fight the higher occupancy, the RICH1 spherical mirrors adopted during the previous Runs have been replaced by new ones with larger curvature radius, leading to an increased focal length. Flat mirrors have also been replaced with higher reflectivity ones.

Calorimeter system

ECAL and HCAL is not changed with respect to Run 1 and Run 2 (Section 2.4.2), except for the readout electronics, which have been substituted to provide a 40 MHz readout. The PS and SPD, which were used mainly for particle identification in L0 trigger decisions, have been removed. A critical aspect of the calorimeter system is the ageing of the photomultipliers. To face this problem, the front-end boards have been implemented with an amplifier system with higher gain.

Muon system

The muon system didn't require particular changes to meet the LHCb Upgrade specification and maintain satisfactory muon identification in the new environment. Only a few changes were applied to the system described in Section 2.4.3. The first station (M1), used by the L0 trigger, was removed. Moreover, a tungsten shield around the beam pipe has been added in front of the M2 station to reduce the particle flux in the innermost region, which is expected to increase significantly with the higher instantaneous luminosity. The readout electronics have been substituted for a 40 MHz readout [175].

2.6.4 The new trigger

The L0 hardware trigger adopted in Run 1 and Run 2 would have been a limiting factor for collecting a large amount of data with the LHCb Upgrade. Some channels, such as $B_s^0 \to J/\psi(\to \mu^+\mu^-)\phi(\to K^+K^-)$ and $B^+ \to J/\psi(\to \mu^+\mu^-)K^+$, selected by a trigger on muons, have performances that do not degrade dramatically increasing the pile-up, as shown in [163]: the fraction of triggered signal over the background is independent of the number of primary vertices. On the contrary, other channels relying on the calorimeter trigger (i.e. selecting photons, electrons or hadrons with transverse energy higher than a specific threshold) are strongly impacted by the higher pileup. This is because the thresholds should be increased to compensate for the higher calorimeter occupancy. For example, this happens to fully hadronic final states, as $B_s^0 \to \phi(\to K^+K^-)\phi(\to K^+K^-)$.
This effect is reported in [176] and shown in Figure 2.6.4.

The entire software trigger results are essential for discriminating the signal channel based on full event reconstruction and selection. The new trigger strategy, the higher luminosity, and correspondingly higher pile-up required a renewal of LHCb detectors and readout electronics to read events at 40 MHz LHC bunch crossing rate and to cope with the bigger event multiplicity.

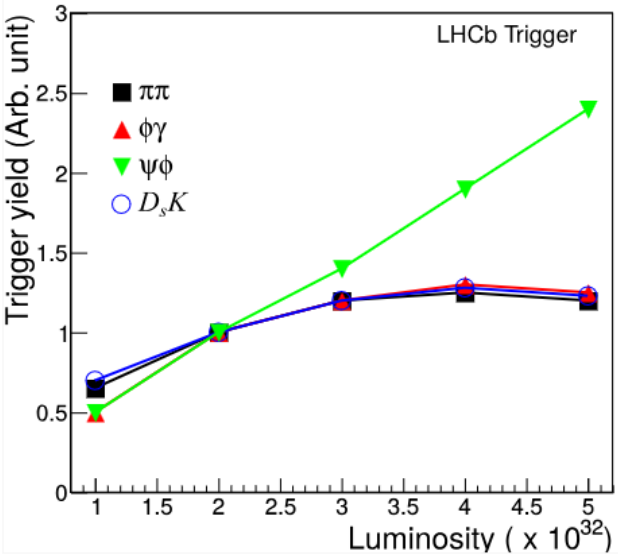

Figure 2.6.4: Trigger yields as a function of the instantaneous luminosity for different decays, normalized to $\mathcal{L} = 2 \times 10^{32}\text{cm}^{-2}\text{s}^{-1}$.

The new full-software trigger strategy allows real-time reconstruction of events at the visible interaction rate of $\sim$ 30 MHz. The real-time analysis approach already

experimented in Run 2 and discussed in Section 2.5 requires a full online reconstruction, enabled by alignment and calibration of the detector. The rate reduction is achieved with the following steps:

- A partial reconstruction performed in the HLT1, primarily based on charged particle reconstruction, is responsible for reducing the event rate to a level (~ 1 MHz) at which the data can be buffered to a disk. The throughput[7] corresponds to around 90 hours of HLT1 accepted events.
- Alignment and calibration constants are evaluated in real-time using dedicated samples and are updated in the database if needed.
- The HLT2 performs a full reconstruction of the event and applies selections to identify physics signatures.

HLT1 selections should be able to reconstruct tracks and vertices displaced from the primary vertices to select any event containing long-lived hadrons or τ leptons. Furthermore, leptons reconstruction, particularly muons, regardless of their displacement from primary vertices, is necessary to select events for spectroscopy studies, exotic searches, and electroweak physics. The main objective of HLT1 is to discard candidates formed by random combinations of tracks or including fake tracks.

While HLT1 needs only a limited number of inclusive selections to select interesting events, HLT2 performs the full reconstruction and applies thousands of selection algorithms, each tuned for a particular signal topology. Because more accurate selection can be applied at an early stage, the real-time analysis paradigm increases the rate of recorded signal events. In addition, the volume of stored data could be reduced, limiting the amount of information persisted from online to offline. This mechanism allows total flexibility on the amount of stored event information. HLT2 selections are grouped into different *streams*, with all selections belonging to a stream sharing common physics goals and recording similar sets of event information. Further details about division into the stream and bandwidth[8] considerations will be given in Chapter 3.

The real-time detector alignment and calibration allow the achievement of earlier reconstruction and particle identification of the same quality as what would have been obtained by offline processing. This provides more uniform selections throughout the analysis chain, reducing systematic uncertainties. The selections are also more efficient. In addition, because offline data calibration is no longer needed, physics analysis can be performed directly using data from the trigger output. The online

[7]The number of events processed per unit time, expressed in Hz.
[8]Amount of data per unit of time that could be processed

HLT2 reconstruction is divided into four components: charged particle recognition, calorimeter reconstruction, particle identification and Kalman fit of the reconstructed tracks, which improves the tracks' parameters accuracy. The main track reconstruction steps of the online and offline strategies are:

1. Segment of the VELO are searched, and each segment is matched with a list of hits in the Upstream tracker;

2. The produced tracks, called VELO-UT, with their estimated momentum and charge, are used to look for matching segments in the SciFi in the search window reduced just to the interest one;

3. Using the reconstructed tracks, the primary vertices are reconstructed

Schemes of the trigger configuration and the main track reconstruction sequence for the LHCb upgrade are given in Figure 2.6.5.

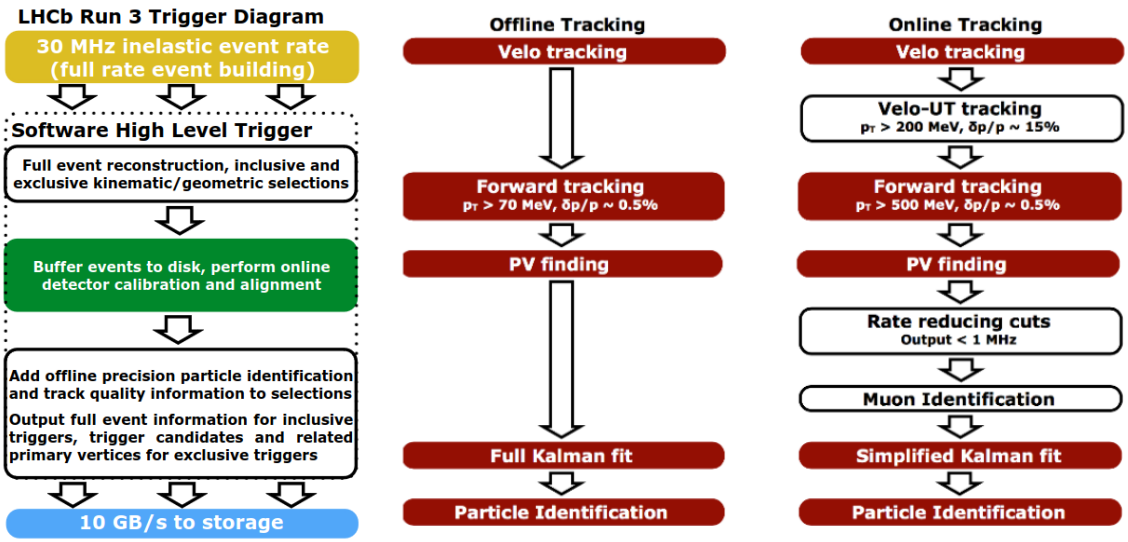

Figure 2.6.5: Trigger scheme (left) and offline (centre) and online (right) tracking sequence comparison for the LHCb Upgrade.

Chapter 3

Trigger selection and isolation for Run 3

The entire LHCb trigger system has been fully redesigned to remove the L0 hardware trigger and move to a fully-software trigger. The L0 would not allow to fully profit from the increased instantaneous luminosity of the LHCb Upgrade. In particular, it would have saturated for hadronic channels. For this reason, a more flexible, complete software trigger has been conceived for the LHCb Upgrade. At the instantaneous luminosity of the LHCb Upgrade, the LHC produces around 6 pp collisions per bunch crossing. The total throughput that can be recorded to permanent storage is around 3.5 Gb/s; hence, the trigger can save around 100 kHz of full raw data events. This is below the rate of interesting signal that can be partially reconstructed in the LHCb, as shown in plot 2.6.4. However, the majority of the analysis of LHCb does not require the full detector information. Moreover, the reconstruction can be run in real-time, using full offline-quality detector calibration and alignment. To achieve the desired baseline throughput, a big effort has been made to limit the data saved offline and improve the online selection.

This chapter explains the work done during the thesis period to help achieve the challenging goal previously discussed. My activities could be classified into three main domains:

- Contributions in developing and documenting Throughput Oriented (ThOr) functors, efficient tools for online selection and offline data processing, described in Section 3.1. After a brief introduction to the online and offline software framework, the operation of filtering and combinations are explained in Section 3.1.1 and used to anticipate the ThOr functors in Section 3.1.2. These objects are largely used for online selection and offline processing. I have contributed in three fields: deriving properties related to the decay structure (Section 3.1.4); getting properties of particles and simulation (Section 3.1.5); deriving conditions

from the online database (Section 3.1.6).

- Improvement of trigger configuration for Rare Decays working group, including bandwidth studies and reduction (see Section 3.2). After furnishing information about the expected bandwidth and rates in the Upgrade, the specific case of Rare Decay (RD) working group will be discussed in Section 3.2.1. I actively worked in the review process of the trigger lines and the bandwidth reduction studies, covering the role of Deputy Migration coordinator for the working group. In addition, I implemented a module of about sixty trigger lines, including some LFUV and LFV channels, discussed in Section 3.2.2.

- Implementation of isolation algorithms, tools and variables for the Upgrade software selection framework, treated in Section 3.3. The main algorithm to evaluate the isolation of the signal candidates, adopted in the Upgrade software framework, is presented in Section 3.3.1. Section 3.3.2 and Section 3.3.3 are dedicated to optimising bandwidth to save isolation as extra information using selective persistency. Section 3.3.4 shows the method implemented to retrieve isolation variables offline. Finally, the isolation framework, as painted in the previous Sections, is reproduced for the trigger configuration of the Rare Decay working group in Section 3.3.5.

Some final considerations about the work ongoing and the upcoming projects are discussed in Section 3.4.

3.1 The Upgrade software selection framework

The Real-Time Analysis (RTA) project aims to limit the event size and reduce the general bandwidth to fit within the limited resources by performing an online reconstruction and selection with very high performances [177]. This can be achieved by processing the data according to the following workflow [178, 179].

1. The data-acquisition system, made of 163 servers, retrieves information from almost 1 million electronic channels from the detector for a total data rate of 5 Tb/s;

2. Data are sent to GPUs located in the same servers of the DAQ to minimize the network connections. In the first trigger stage, HLT1, the GPUs process 150 thousand events per second, reducing the rate by a factor of 15-30. This is done by performing fast-track reconstruction and selecting pp collision events based on one- and two-track objects.

3. The events selected by HLT1 are then passed to the second trigger stage, HLT2, which is implemented on a farm of 3700 CPU servers. Data output of the HLT1

process are buffered to disk for alignment, calibration and other processes. The disk buffer allows HLT2 to be executed even when the LHC is not colliding with protons, maximizing the utility of LHCb's computing resources. These machines perform the ultimate-quality reconstruction of the full detector and apply around 1500 different selections to reduce the data volume by a factor of 10 and send 10 Gigabytes of data per second to offline processing.

Once the data are stored, the Data Processing & Analysis (DPA) project is mostly responsible for three aspects of the data workflow [180].

1. The so-called "Sprucing", i.e. the data skimming and trimming of data before they are saved on disk;

2. Tupling the information with centralized analysis productions for different physics working groups and users to perform offline analysis;

3. Data preservation and open data.

The entire data workflow from proton-proton collision to the data storage and usage for the LHCb analysis is presented in Figure 3.1.1.

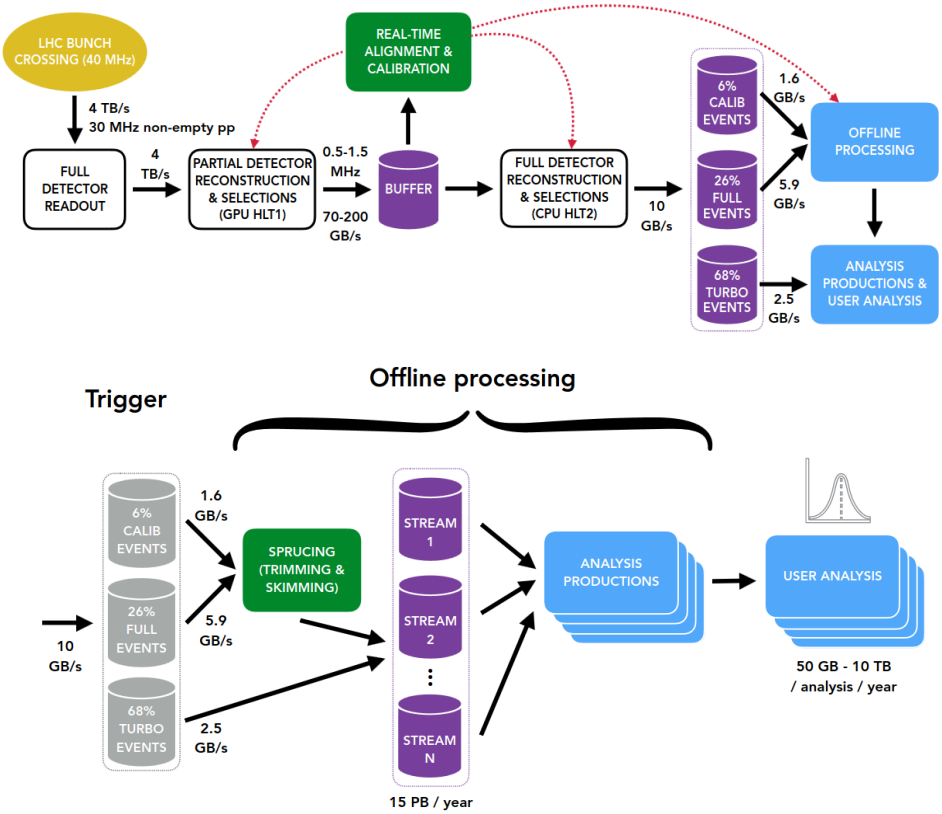

Figure 3.1.1: The online (top) and offline (bottom) data processing diagram, as reported in [181].

3.1.1 Filtering and combinations

Physics analysis is conducted via the measurement of properties of objects produced through some processes. The fraction of particles produced in the decay and that will be considered stables are pions, protons, kaons, electrons, muons, photons, and deuterons. From now on, we will refer to these particles as *basics*. Unstable objects, which have a much shorter lifetime, are formed as combinations of these. They are generally called composites. During the reconstruction, properties are derived from tracks and other information in the detector, such as energy clusters. Trajectory, momentum and charge are assigned to the basics and their production in space represents a vertex. All this information is computed when building a candidate that matches the required decay process. A vertex fit with an established selection is performed with the decay products to build the candidates.

The selection algorithms used by the trigger lines are mainly the `HLT2Conf.algorithms_thor.ParticleF` and the
`HLT2Conf.algorithms_thor.ParticleCombiner`. The `ParticleFilter` is applied on a container of particles that could be basic or composites, and returns a container with candidates passing a specific requirement, expressed in the `Cut` argument. Instead, the `ParticleCombiner` is used with a list of N input particle containers to make N-body combinations and return a composite. The `DecayDescriptor` argument specifies the decay process that is reconstructed in the builder. Before undergoing a vertex fit, the number of combinations of products is filtered by applying a `CombinationCut`. Candidates built are then filtered after the vertex fit by applying the requirements specified in the `CompositeCut`.

The filter and combiner algorithm selections are guaranteed by *functor expression*. Specifically, ThOr functors, discussed in the following Section 3.1.2, use modern and parallel CPU architecture to increase throughput. In addition, they have a more handle and user-friendly implementation compared to the LoKi functors, previously used in the selection framework for Run 1 and Run 2.

3.1.2 Throughput Oriented (`ThOr`) functors

The ThOr functors [182] are used mainly in the trigger selection and for storing offline variables in the Run 3 software framework. A functor is generically a *function object* in C++, hence a class or struct that works like a function. To create a functor, the operator `()` is overloaded [183]. ThOr functors are used in the selection framework of the trigger Upgrade due to their property of separating configuration and execution. As in many other LHCb applications, in the Python configuration, the

objects define data[1] and control[2] flow of the application. The Python configuration informs which algorithm and selection should be executed and when. During the execution, the Python objects are interpreted as C++ objects and then executed according to the order established by the data and control flow. While decoding the configuration, a C++ component of the Gaudi [185] application figures out what other C++ components should be instantiated and what values their various properties should have. Hence, ThOr functors defined in the configuration work in this way:

1. They encode a string representing the full C++ functor expression to be evaluated.

2. The string is decoded and converted into a C++ object by the `FunctorFactory` service. This takes the various components embedded in the string representation and returns a C++ functor object, which can then be called. While doing this, it decides whether to JIT[3] compile the C++ functor or retrieve it from a functor cache to create the final C++ object.

The functor cache is a shared object library that contains a hash associated with each C++ string corresponding to the functor expression. During initialisation, the functor helpers use the functor string hash to load the corresponding C++ functor object from the functor cache, which the algorithm can then execute.
Moreover, ThOr functors are designed to accommodate the structure-of-arrays (SOA)[4] data model, initially foreseen to be adopted for Run 3 and now in preparation for Run 4. The SOA model layout is optimised for fast data access and improving CPU cache[5] efficiency, but results in some considerable API differences compared to the array-of-structures (AOS)[6] model, used in Runs 1 and 2. Examples of the layout and memory management with SOA and AOS structures are shown in Figure 3.1.2.

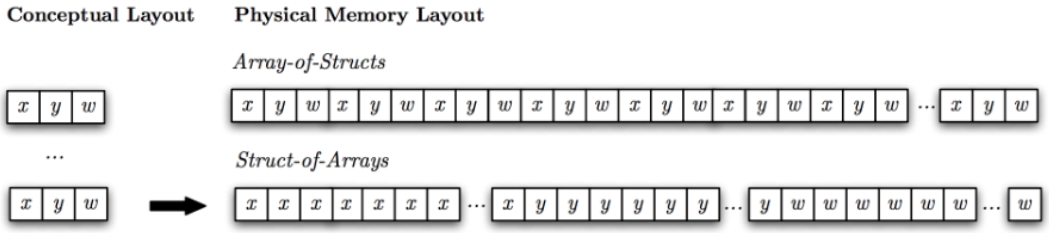

Figure 3.1.2: Comparison of SOA and AOS layouts [186].

[1]The inputs necessary to create a given output
[2]The order in which algorithm should run, see [184]
[3]Just-In-Time compilation to compile during the execution of a program rather than before.
[4]Structure of arrays separates elements of a record (or struct) into one parallel array per field (or property). In this way, data and operation manipulation can be handled more easily using SIMD (single input, multiple data) instructions
[5]Small high-speed memory of the CPU designed to store data and instructions frequently accessed.
[6]Array of structures present more intuitively data for different fields is interleaved.

Functor composition

An additional ThOr functor property in the Python configuration is the possibility of composing them through operations. The composition of functors creates new functors. Therefore, it is possible to develop new ThOr functors by applying algebraic operations between them and transforming them into predicates using comparison operations.

Furthermore, other operators could help users handle more complex compositions: chaining and binding. The chaining operator `@` is a binary operator between functors that applies the output of the functor on the right as the input of the functor on the left. Mathematically, if we have two functors `B` and `C`, we can define a new functor `A = B @ C` which acts as `A(input) = B(C(input))` when executed. The binding operator `bind` is a function that is applied to a given functor and expects a list of functors to bind. The net effect when the composed functor is called is that the functor before the bind will have as an input argument the outputs of the functors bound. More explicitly, if we have a functor `A = B.bind(C, D)`, with `B`, `C` and `D` functors themselves. When executed, the expression will translate as `A(input) = B(C(input), D(input))`.

The ThOr functor's chaining and binding operations provide powerful features for composing functions, enabling users to create concise code that efficiently enfolds several functionalities. During my doctoral studies, I contributed to sharing and documenting these components to help analysts define new functions.

Documentation

ThOr functor's documentation is automatically generated from the `Functor` python package, and the docstrings are rendered in [187]. More in detail, we have two different kinds of functors: basic and composed ones. Basic functors are documented via their docstring adequately attributed and the C++ string encoded in the object. Composed functors, instead, have the Python form of the composition presented. Loki functors with similar or equivalent functionalities are also reported in the documentation of a functor. Figure 3.1.3 and Figure 3.1.4 show an example of basic and composed functors, respectively, with their implementation and their reference page in the dedicated documentation.

3.1.3 NTupling with FunTuple

The Functional Tuple (FunTuple) structure, is an innovative component of the offline analysis introduced with the LHCb Upgrade software [188]. It enables the computa-

```cpp
/** @brief Charge, as defined by the charge() accessor.
 */
struct Charge : public Function {
  template <typename Data>
  auto operator()( Data const& d ) const {
    return Sel::Utils::deref_if_ptr( d ).charge();
  }
};
```

CHARGE()

Compute the charge

C++ Representation

`::Functors::Combination::Charge{}`

LoKi Equivalent

- `Q`

Figure 3.1.3: Example of basic functor definition as a C++ struct (left) and its referenced documentation (right).

```python
# Track momentum at "ClosestToBeam" state if available
# otherwise returns momentum at the "FirstMeasurement" state
TRACK_PT = setComposedFunctor(
    PT @ TRACK, "TRACK_PT",
    """Get the transverse momentum of a track (see :py:func:`~TRACK` for definition)

                            Functor's call operator expects a ChargedBasic"""
)
```

TRACK_PT()

Get the transverse momentum of a track (see `TRACK()` for definition)

Functor's call operator expects a ChargedBasic

Python Representation

RHO_COORDINATE @ THREEMOMENTUM @ TRACK

Figure 3.1.4: Example of composed functor definition in the Python implementation (left), with the referenced documentation (right).

tion and storage of a diverse range of observables for both real and simulated events. FunTuple's design and interface are entirely templated in C++ to enable the leverage of Single Instruction, Multiple Data (SIMD) vectorisation along with the SOA event model.

Furthermore, the FunTuple is configured with ThOr functors, used to retrieve and store information about `LHCb::Event`, `LHCb::Particle` and `LHCb::MCParticle`. The `LHCb::Event` component comprises reconstructed or simulated events, where each event represents a single bunch crossing. It contains event-based information that could be extended with conditions derived from the online database, as discussed in Section 3.1.6. `LHCb::Particle` and `LHCb::MCParticle` identify reconstructed and simulated objects that could be accessed directly from the decay structure. Some examples in the DaVinci project of option files using FunTuple component will be presented in further discussions as a test of the validity of the functors implemented.

3.1.4 Exploring *DecayTree* structure

One of the primary focuses of my work on functor development revolves around extracting information from the decay products of a composite. If we take a process like $B^0 \to K^{*0}(\to K^+\pi^-)\tau^\pm(\to \pi^\pm\pi^\pm\pi^\mp)e^\mp$ we may need to access to properties of the products of the τ decay or we may need to select only those π that compose the τ lepton. For this purpose, the following functors have been developed:

- `GET_ALL_BASICS` to get the list of all the final products of the decay;
- `GET_ALL_DESCENDANTS` to get the list of all the products of the decay, including the intermediate states;

- `GET_GENERATION` to get the list of all the particles belonging to a given generation, specified by an integer parameter.

A schematic representation of the decay-level information that can be accessed with the previously described functors is shown in Figure 3.1.5.

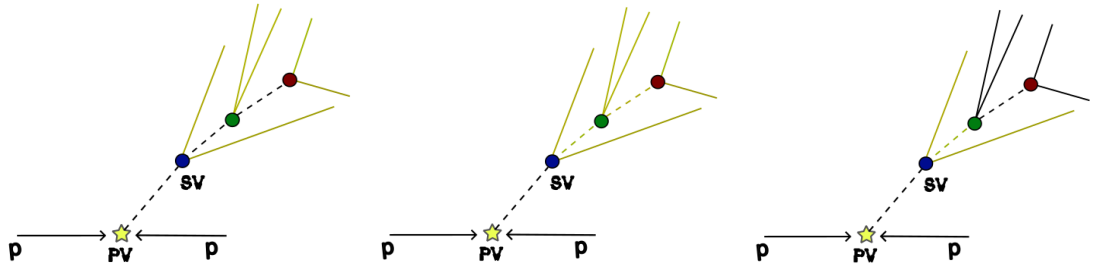

Figure 3.1.5: Diagrams showing the decay tree information that could be accessed using the functors `GET_ALL_BASICS` (left), `GET_ALL_DESCENDANTS` (center) and `GET_GENERATION(1)` (right). Particles saved are highlighted in yellow in the schemes.

It is now possible to make different variants of compositions to get several observables. `MINTREE` functor, which evaluates the minimal value of the application of a given `Functor` through the `DecayTree` filtered by a `Predicate`, is composed as:

```
def MINTREE(Predicate, Functor):
    return MIN_ELEMENT @ MAP(Functor) @ FILTER(Predicate) @
    GET_ALL_DESCENDANTS
```

Listing 3.1: Python composition of `MINTREE` functor composed from `GET_ALL_DESCENDANTS`

In a similar way, also `MAXTREE`, `INTREE`, `NINGENERATION`, and `NINGENERATION` have been defined.
Furthermore, an algorithm named `ThOrParticleSelection` has been developed exploiting functors that allow us to navigate through the decay tree structure. A more detailed discussion about the algorithm's functionality is reserved in Section 3.3.2.

3.1.5 `LHCb::Particle` and `LHCb::MCParticle` properties

`Particles` and `MCParticles` are characterized by properties derived from the event reconstruction, such as the mass and the particle ID, unique to each type of particle. For this reason, `PARTICLE_PROPERTY` functor is introduced to retrieve the particle property matching a string representation of the particle ID. Hence, `PARTICLE_PROPERTY("pi+")` returns the property of the positively charged pions, and similarly `PARTICLE_PROPERTY("K-")` returns the particle property of the negatively charged kaon.

Using the functor composition, it was possible to define the following functors:

```
def IS_ID(particle_name:str):
    return (PARTICLE_ID @ PARTICLE_PROPERTY(particle_name) == PARTICLE_ID)
```

Listing 3.2: `IS_ID` functor check if particle id marches the specific id represented by the string argument

```
def IS_ABS_ID(particle_name:str):
    return (ABS @ PARTICLE_ID @ PARTICLE_PROPERTY(particle_name) == ABS @
    PARTICLE_ID)
```

Listing 3.3: `IS_ABS_ID` functor check if absolute value of particle id marches the specific abs(id) represented by the string argument (IS_ABS_ID("pi+") is equivalent to IS_ABS_ID("pi-"))

```
def PDG_MASS(particle_name:str):
    return (MASS @ PARTICLE_PROPERTY(particle_name))
```

Listing 3.4: `PDG_MASS` functor gives the PDG mass for the specific id represented by the string argument

```
def SIGNED_DELTA_MASS(particle_name:str):
    return MASS - PDG_MASS(particle_name)
```

Listing 3.5: `SIGNED_DELTA_MASS` functor gives the signed difference between the reconstructed and the PDG mass

```
def ABS_DELTA_MASS(particle_name:str):
    return ABS @ SIGNED_DELTA_MASS(particle_name)
```

Listing 3.6: `ABS_DELTA_MASS` functor gives the signed difference between the reconstructed and the PDG mass

3.1.6 Derivation of LHC condition from online database

The last topic related to functor developments concerns deriving information from the online condition database. More precisely, the condition database of the LHCb detector provides versioned, time-dependent geometry and conditions data for all LHCb data processing applications [189] [190]. The conditions are classified using three variables:

- The condition id, which is usually a path to XML or YAML file);
- The version (a tag, like a commit or a branch);
- The Interval Of Validity, proportional to the range of events.

Among these conditions, the ones related to the LHC state, such as the fill ID, the collision energy and the LHCb clock phase, belong to the `Online` partition. Thanks to a newly implemented functor named `DELHCB`, it is possible to access the conditions in this partition directly. Exploiting functors' composition, we can define the functors

FILL_NUMBER, LHC_ENERGY and LHCB_CLOCKPHASE to derive the condition directly. The three have been added to a so-called FunctorCollection named LHCInfo. These collections are used to append a set of branches to the nTuples within FunTuple framework. An example of an application of LHCInfo functor collection can be found in [191]

3.2 HLT2 bandwidth division and sprucing

The trigger bandwidth is optimized based on physics and operations needs. The optimization is made by separating the events into streams. The main streams are Turbo, FULL and Turcal. For the Turbo streams, the signal candidates and the reconstructed particles associated with its *pp* collision vertex are saved. On top of this information, the possibility of persisting just a few extra particles or vertices, wisely chosen according to specific criteria, is added. The so-called *selective persistency* has been implemented in several trigger lines from different working groups to save information such as flavour tagging and isolation. This latter case is discussed more in detail in section 3.3.2. Instead, the Full stream collects data related to events fully reconstructed, while raw data, encoding information from each sub-detector and more resources-consuming, are by default discarded. An example of different models that are applied to the trigger to reconstruct and select the $D^0 \to K^-\pi^+$ charm decay is shown in Figure 3.2.1.
The Turbo stream is dedicated to data passing exclusive[7] trigger lines, while Full stream includes mainly inclusive[8] trigger selections and some semi-leptonic channels. The Turcal stream is reserved to the calibration samples. The complete raw event data must be saved for these events to allow an accurate understanding of the detector reconstruction and performance and the development of new reconstruction and calibration techniques.

The throughput baseline, presented in Figure 3.2.2, assumes that 10.0 Gb/s of data can be saved on tape split differently for the three main streams, whereas only 3.5 Gb/s can be saved on disk. Just a fraction of 25% of the event rate, but up to 60% of the bandwidth of the tape will be devoted to the Full stream. Before being moved to disk storage, events stored on the disk buffer undergo the *Sprucing* stage, a set of offline selections to reduce the event size further and bring the throughput to the disk of the Full stream to 0.8 Gb/s. Also, in the case of Turcal stream, data are slimmed and raw event information is discarded at the Sprucing stage. Turbo events undergo a pass-through sprucing, saving everything on the disk.

[7] Dedicated to one specific decay channel
[8] Covering multiple processes

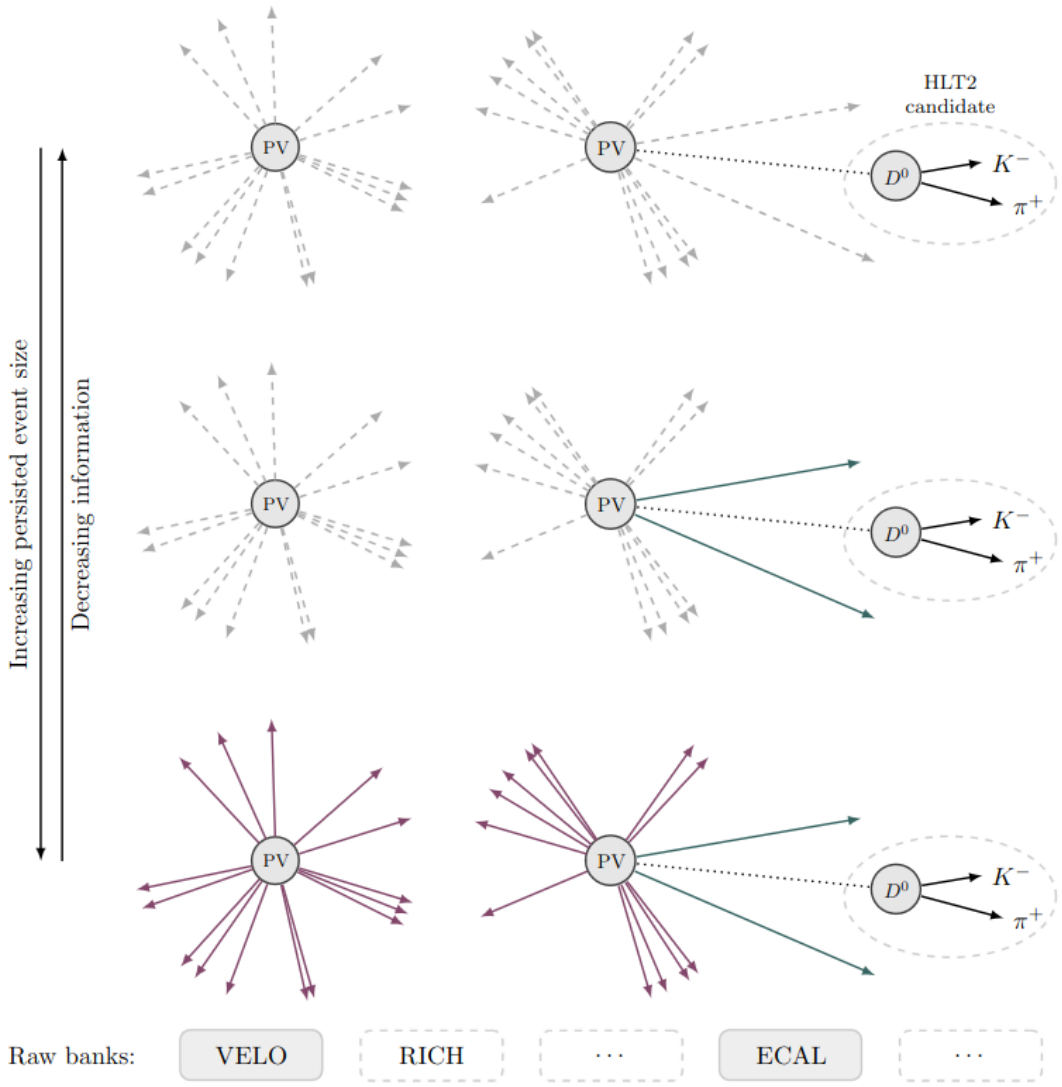

Figure 3.2.1: Sketch of reconstructed events according to different trigger models: `Turbo` (top), `Turbo` with selective persistency (middle) and `Full` (bottom) [192].

3.2.1 Rare Decays working group

The RD group is a physics working group focused on studying loop and CKM-suppressed processes and performs searches of forbidden searches, including lepton flavour-violating ones. Decays studied by RD are characterized by very low branching fractions and have excellent sensitivity to new physics phenomena.

3.2.2 $Y_b \to X\tau l$ $(l = e, \mu, \tau)$ trigger lines

Part of my contributions to the preparation of Rare Decays trigger configuration for the Run 3 data taking involves the development and maintenance of the HLT2 selections contained in `Hlt2lines.lines.rd.b_to_xtaul_hlt2` and

stream	rate fraction	throughput (GB/s)	bandwidth fraction
FULL	26%	5.9	59%
Turbo	68%	2.5	25%
TurCal	6%	1.6	16%
total	100%	10.0	100%

stream	throughput (GB/s)	bandwidth fraction
FULL	0.8	22%
Turbo	2.5	72%
TurCal	0.2	6%
total	3.5	100%

Figure 3.2.2: Throughput to tape (first table) and to disk (second table) for the three streams, according to the Computing Model of the Upgrade LHCb experiment TDR [159]

`Hlt2lines.lines.rd.builders.b_to_xtaul_builder` modules. These modules define the set of exclusive trigger lines and builders adopted selecting processes belonging to $Y_b \to X\tau^{\pm}l^{\mp}$ category, with $l^{\mp} = e^{\mp}, \mu^{\mp}, \tau^{\mp}$ lepton and τ hadronically decaying into three pions. The selections aim at triggering signal candidates of the following list of processing

- B^0 or B_s candidates decaying into intermediate meson, τ and the other lepton. The mesons included are $K^{*0}(\to K\pi)$, $\phi(\to KK)$, $\rho(\to \pi\pi)$, $\eta^{'}(\to \pi\pi\gamma)$ and $K_s(\to \pi\pi)$;
- $B^{\pm}$ candidates decaying into K^+ or $K1(1270)(\to K\pi\pi)$, τ and the other lepton;
- Λ_b^0 candidates decaying into $K^{\pm}$, $p^{\mp}$, τ and the other lepton.

The entire module comprises $\sim$ 60 exclusive trigger lines. The selection has been optimized to keep the rate of each line below 50 Hz.

Multiplicity issue

One of the main issues for bandwidth reduction with the hadronic τ lepton decays trigger lines involves storing extra information based on candidates, such as isolation, given the high multiplicity that characterizes the processes. The effect of candidate multiplicity is even more accentuated in the case of $\tau\tau$ topology, where the swapped pions effects increase the number of multiple candidates than $\tau\mu$ and τe cases. A few precautions are considered in the selections to suppress the combinatorial and physics backgrounds brought by the high multiplicity:

- Tight electron and muon PID requirements are applied to try to reduce lepton mis-ID background;
- More strict cuts are used on neutral combinations of pions from τ leptons compared to Run 2 one. At the price of a small percentage of efficiency loss, it is possible to suppress a good fraction of charmed meson decays [193];
- For the same reason as the previous point, tighter requirements are applied to τ candidate mass.
- A selection based on the pseudo vertex τ^+-τ^- separation $\sim \chi^2$ is applied. The variable is defined as: [194]

$$\sim \chi^2 = \frac{\tau^+\tau^-\text{dist}}{\sum_{i=X,Y,Z} |\tau_i^+ - \tau_i^-| \sqrt{\tau_{\Delta i}^{+2} + \tau_{\Delta i}^{-2}}} \tag{3.2.1}$$

  where $\tau_i^{\pm}$ $(i = X, Y, Z)$ represents the i-th coordinate of the decay vertex of the $\tau^{\pm}$ and $\tau_{\Delta i}^{\pm}$ $(i = X, Y, Z)$ represents the error on this coordinate. The variable, which does not correspond to a real χ^2 because it ignores the correlation between X, Y and Z, was revealed to be very helpful in fighting the pions swapping effect and reducing bandwidth for $X\tau\tau$ lines. Figure 3.2.3 shows an illustrative representation of the swapping pions issue that increases the candidate multiplicity and the $\sim \chi^2$ introduced to fight this combinatorial background.

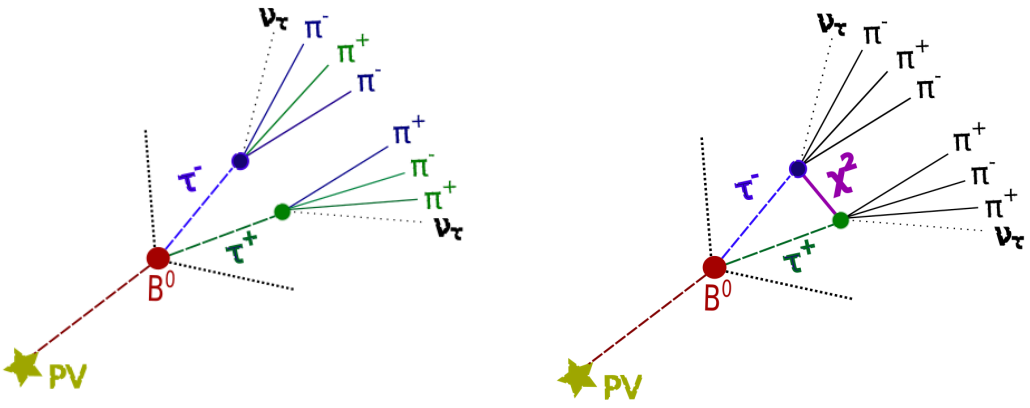

Figure 3.2.3: When combining particles to create signal candidates, the π could be interchanged if the two vertices of the τ leptons are relatively close, increasing the multiplicity of the candidates, as shown in the left diagram. A cut on the pseudo vertex τ^+-τ^- separation is applied to avoid this effect.

The entire selection applied to the `b_to_xtaul` HLT2 lines module is reported in Appendix G.

3.3 Isolation in the LHCb Upgrade software framework

Isolation is a tool that allows to discriminate signal decay from other tracks and neutral objects during reconstruction and offline studies. It helps to reject the mostly partially reconstructed background by checking the properties of underlying particles. Isolation algorithms require information about other tracks or neutrals outside the signal in the events. We derive charged and neutral isolation information from these particles, evaluating variables related to the so-called cone and vertex isolation. The first collects track and neutral properties associated with particles within a cone open around the signal candidates. Similarly, vertex isolation provides information about how much a signal is isolated, deriving variables that encode knowledge of the vertex of the decay. An illustrative scheme about how cone and vertex isolation works with a given signal candidate is shown in Figure 3.3.1.

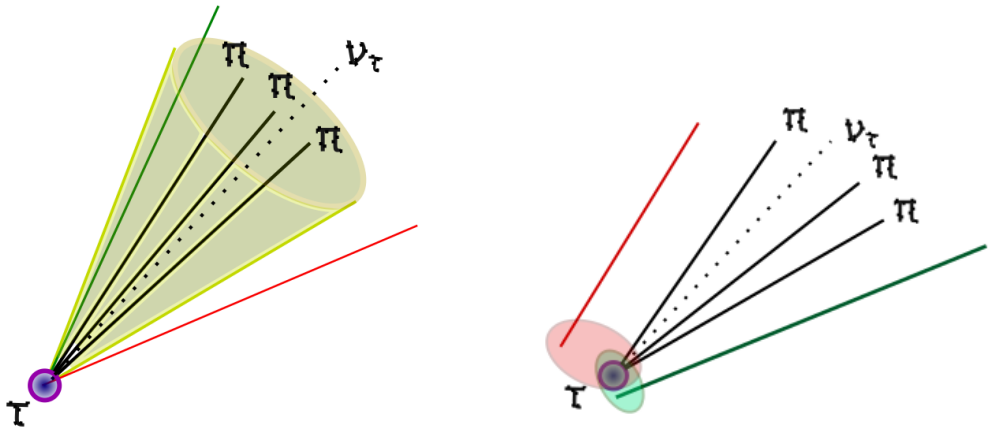

Figure 3.3.1: Cone (left) and vertex (right) isolation of τ signal candidates decaying into three pions and a neutrino. Requirements are set to select particles that are not decay products belonging to the rest of the event. Variables related to the candidate isolation are derived offline as explained in Section 3.3.4.

Most of the time, multi-variate approaches exploiting isolation variables as input are trained using part of the data as a proxy for the background. Given the large variety of physics backgrounds suppressed using isolation, a single decay or a cocktail of multiple decay simulations could possibly lead to limitations in applying the classifier trained. For this reason, an approach consists on saving information related the rest of the event on disk using the selective persistency, and evaluate isolation variables offline. Separating the processing of computation of isolation quantities in two steps allows us to validate the variables and use them as input for classifier training. The described pipeline has been embraced by various working groups at the beginning

of the Run 3 data-taking period to process isolation observables. One of the main ingredient consists on the usage of structures, named `RelationTables`, that ensure the addition of information to already existing objects.

3.3.1 `RelationTable` format and *binary* functors

The `RelationTable` is a C++ object defined within the LHCb software framework. It has a convenient format to store information that could be related to existing objects. The isolation represents a typical example of when a relation table could be convenient. However, it is broadly used in other contexts, such as primary vertex association and neutral object properties. Generally, the `RelationTable` format encloses the relation of templated types of objects. The relation table comprises a `FROM` side of the relation and a `TO` side of the relation. A description of the algorithm implemented (`WeightedRelTableAlg`) exploiting the format of `RelationTable` will be furnished in the following. Their utility is extended to cases above the isolation one, as shown in Figure 3.3.2.

`WeightedRelTableAlg` is a C++ algorithm that I have implemented, and it is suited to evaluate relations between two containers of particles, for example, the signal and extra particles in the events. The algorithm is instantiated with `ReferenceParticles` and `InputCandidates` parameters and a `Cut` predicate. The output of `WeightedRelTableAlg` algorithm is a table composed of a set of relations between `LHCb::Particle` and `LHCb::Particle` that are passing the predicate expressed in the `Cut` argument. This operates with *binary* ThOr functors, i.e., which receive two containers as input. However, users can access a single input using functor composition as follows.

- `Functor @ F.FORWARDARG0` applies `Functor` to `ReferenceParticles` container (`FROM` side of the relation table)
- `Functor @ F.FORWARDARG1` applies `Functor` to `InputCandidates` container (`TO` side of the relation table)

`SelectionFromWeightedRelTableAlg` is another algorithm defined to extract a `LHCb::Particle::Selection`, an LHCb container format for `LHCb::Particle`, from the output relation table of .`WeightedRelTableAlg`. The algorithm accepts a `InputRelation` parameter of type
`RelationTable<LHCb::Particle, LHCb::Particle>` and returns the selection of particles without duplicates in the `TO` side of the relation table, i.e. the extra particles saved in the relation table.

An application of the previously described algorithm is presented in the following example.

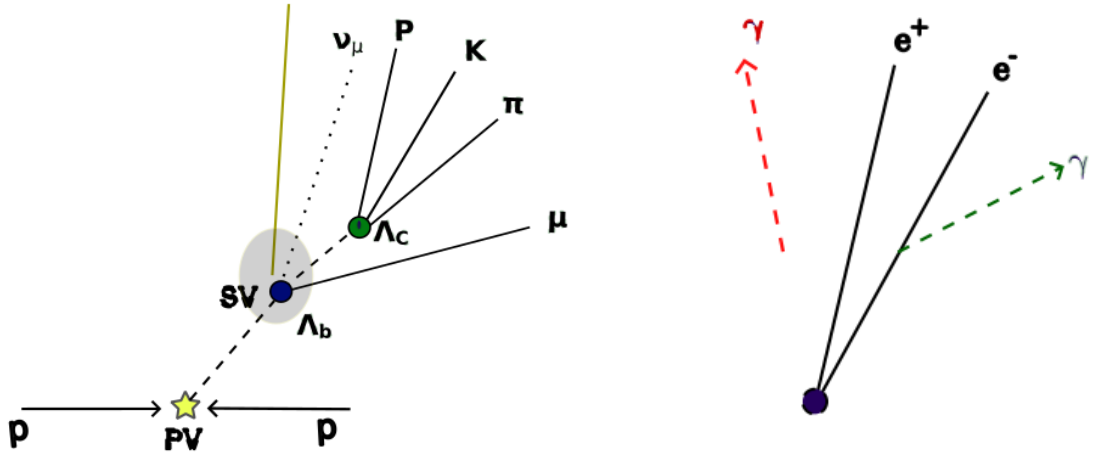

Figure 3.3.2: Representation of use cases of `WeightedRelTableAlg` algorithm aside the isolation. It could be used to perform hadron spectroscopy by reconstructing and associating to the signal decay (in blue the Λ_b vertex) another track (in yellow) belonging to the rest of the event, as shown in the left diagram. Similarly, the algorithm could be applied to the photon reconstruction for a dielectron signal, as shown on the right and presented in 3.7. In both cases, requirements on the invariant mass of the composite could be imposed for the selection of extra tracks or neutrals.

```
from PyConf.Algorithms import WeightedRelTableAlg,
    SelectionFromWeightedRelationTable

photons_table = WeightedRelTableAlg(
        InputCandidates=photons,
        ReferenceParticles=dielectrons,
        Cut=in_range(min_mass, F.COMB_MASS(), max_mass))
tes_pion_selection = SelectionFromWeightedRelationTable(
            InputRelations=photons_table.OutputRelations)).OutputSelection
```

Listing 3.7: `WeightedRelTableAlg` and `SelectionFromWeightedRelationTable` algorithms example to retrieve a selection of extra particles

In the previous example, we made a relation table between particles in the `dielectrons` container side and particles in the `photons` container. *Dielectron* and *photon* candidates will be saved as a relation only if their combined mass is within a range between `min_mass` and `max_mass` parameters.

Several *binary* functors have been implemented to be used when one needs to create a relation table with the previous algorithms. Among them, we have:

- geometry reconstruction deltas, such as `DETA`, `DPHI` and `DR2`;
- `COMB_MASS` to combine the mass of two particles;
- predicates to compare particle properties such as `SHARE_BPV` and `SHARE_TRACKS` to check if two particles share the same primary vertex or track, respectively;

- `FIND_IN_TREE` to check if the particle in the `TO` side is part of the decay of the particle in the `FROM` side.

Similarly, other functors have been developed with the purpose of "read-back" to retrieve variable values from information in the relation table. `RELATION` functor is implemented to get respectively the set of relations composing a relation table given the `FROM` side. Furthermore, using `TO` functor, it is possible to access the extra information saved in the relation table. Several other functors are defined using the functor combination to obtain the isolation variables discussed in Section 3.3.4.

3.3.2 Selective persistency for isolation

When defining a Turbo HLT2 or Spruce line that triggers the signal event and does not persist the reconstruction of the other particles, it is necessary to save extra information present in the event. To wisely choose just a fraction of the information to persist from the event data, we can exploit the so-called *selective persistency*. In this case, the full event information is not required, and objects can be persisted selectively by defining `extra_outputs` parameter of the `Moore.lines.Hlt2Line` object returned by the trigger line.

The primary method to get the list of particles of interest for isolation is defined in `Hlt2Conf.isolation`.

```
from PyConf.Algorithms import WeightedRelTableAlg,
  SelectionFromWeightedRelationTable

def extra_outputs_for_isolation(name, ref_particles, extra_particles,
  selection):

   RelTableAlg = WeightedRelTableAlg(
       InputCandidates=extra_particles,
       ReferenceParticles=ref_particles,
       Cut=selection)

   RelTable = RelTableAlg.OutputRelations

   selection_to_persist = SelectionFromWeightedRelationTable(
       InputRelations=RelTable)

   extra_outputs = [(name, selection_to_persist.OutputLocation)]

   return extra_outputs
```

Listing 3.8: `extra_outputs_for_isolation` function to save TES location in extra outputs based on selection of extra particles

The method builds a `RelationTable` between reference particles (`ref_particles` parameter) and extra particles (`extra_particles` parameter) handing the selection expressed through the `selection` parameter. From the output Relation Table, it gets the persistable object (selection of extra particles) stored in the TES[9] location explicitly identified by the `name` parameter. Hence, adding the output of `extra_outputs_for_isolation` method to the `extra_outputs` parameter of `Moore.lines` is sufficient to save the selection of particles in the given TES locations. In this way, the following TES locations are saved on the storage:

`/Event/HLT2/{line_name}/{tes_name}/Particle2VertexLocation`,
`/Event/HLT2/{line_name}/{tes_name}/Particles`,
`/Event/HLT2/{line_name}/{tes_name}/decayVertices`.

Thus, it is possible to inspect the content of the TES location offline.

3.3.3 `ThOrParticleSelection` algorithm

Persisting extra particles related to the signal could not be sufficient in most cases. We can store additional information related to extra particles offline if we want to compute isolation for the products of the signal decay. When writing a trigger line, as described in Section 3.1.1, one selects the signal combining different input particle containers. The number of input particles that enter inside a combination is larger than the number of output composite particles produced; therefore, saving extra information for each product will be highly inefficient in terms of bandwidth. `ThOrParticleSelection` is a C++ algorithm developed to limit this number and select just the decay products belonging to the signal. Two parameters define the algorithm. `InputParticles` corresponds to the particle container of the signal. `Functor` is configured by a ThOr functor that returns a vector of `LHCb::Particle`. We can exploit decay tree functors, introduced in Section 3.1.4, to get the selection of products belonging to the signal as in the following example.

```
1 from PyConf.Algorithms import ThOrParticleSelection
2
3
4   #Filter the descendants of input
5 code=(F.FILTER(F.IS_ABS_ID("pi+")) @ F.GET_ALL_DESCENDANTS())
6 pions_from_parent=ThOrParticleSelection(InputParticles=parent, Functor=
    code).OutputSelection
```

Listing 3.9: Selection of pions that descends from the signal using `ThOrParticleSelection` algorithm

[9]Transient Event Store, it corresponds to the data packing format for different streams

3.3.4 Cone and vertex isolation variables

Isolation variables are retrieved using `VertexAndConeIsolation` tool. This Python class gets configured by:

- `reference_particles` parameter containing the TES location of signal candidates
- `related_particles` parameter containing the TES location of the extra particles
- `cut`, which expresses further selection to apply when relating `reference_particles` with `related_particles`

The class creates an instance of `WeightedRelTableAlg` algorithm and uses the relation table to evaluate the attributes reported in Table 3.3.1. We can generally refer to these variables as cone and vertex isolation variables.

Variable	Description
MULT	Number of extra particles associated with a given signal candidate
CP CPX CPY CPZ CPT	Sum of the P, P_X, P_Y, P_Z, P_T of the particles associated to a given candidate
PASY PTASY PXASY PYASY PZASY	Asymmetry of P, P_X, P_Y, P_Z, P_T of the particle associated to a given candidate
DETA, DPHI	Delta η and ϕ coordinates between extra particle and signal candidate
MAXCP MAXCPX MAXCPY MAXCPZ MAXCPT	Maximum value of the P, P_X, P_Y, P_Z, P_T of the particles associated to a given candidate
Smallest_CHI2	Smallest χ^2 of the particle associated to a given candidate
Smallest_DELTACHI2	Smallest $\Delta\chi^2$ between extra particle and signal candidate
Smallest_Mass_DELTACHI2	Mass of the extra particle that has the smallest $\Delta\chi^2$ with the signal candidate

Table 3.3.1: Cone and vertex isolation variables. The cone isolation asymmetry is defined as $A = \frac{1-\sum_{\text{part}\in\text{cone}} var}{1+\sum_{\text{part}\in\text{cone}} var}$

An example of how cone and vertex isolation variables are retrieved offline can be found in [195]. Three collections of functors are defined and shown in the example to simplify the analyst's implementation of offline isolation variables. `ParticleIsolation`, `ConeIsolation` and `VertexIsolation` access to `VertexAndConeIsolation` class information and retrieve a defined set of isolation variables offline. The former adds to the NTuple information cone variables for neutral or charged particles, the second in both cases, and the latter includes vertex isolation variables.

3.3.5 Isolation for Rare Decays trigger

The isolation tools described have been applied to configure the Rare Decay trigger lines in preparation for the Run 3 data taking. The module `Hlt2line.lines.rd.builders.rd_isolation`

which contains several helper functions for the default implementation of isolation in the trigger lines, has been developed. Among the various methods, `parent_isolation_output` searches for extra candidates for a given signal within a cone with $\Delta R = 0.5$[10]. By default, both charged pions reconstructed from long tracks and photons matching the isolation criteria are stored in TES locations named {`name`}+"`_LongTrackIsolation`" and {`name`}+"`_NeutralIsolation`"
(with `name` parameter of `parent_isolation_output`). The methods are made configurable through boolean parameters to access and also save to other extra candidates, like charged pions reconstructed from other track types or neutral pions.

3.4 Summary and future prospects

Functors development has been significantly streamlined for analysts, enhancing both the implementation structure and the accompanying documentation. The simplification is achieved through a more flexible logic based on functor compositions, described in this chapter. The approach guarantees access to a wide range of information while reducing the need for C++ implementations, favouring a more intuitive Pythonic configuration instead. My contributions have been pivotal in this regard, providing functionalities that facilitate the preparation of HLT2 selections and analysis of data collected during the Run 3.
The other contributions emerged naturally as closely related to this enhancement. Through my efforts in preparing the trigger selections for RD working group, I gained a deeper understanding and improved sensitivity regarding signal selections and background reduction across multiple decay channels within the group. At the same time, this work provided a robust knowledge of the framework and the online trigger process. I aim to continue contributing to the validation of current online selections by studying data collected during Run 3 and utilizing offline studies to enhance these selections further.
As part of the RD trigger preparation, I implemented the pipeline for isolation studies, which has been extended to other working groups. Structuring this complex tool, which integrates both online and offline data processing, was a significant effort that required collaboration with many experts. By incorporating isolation variables, analysts can refine their selection criteria and improve the overall selections using multi-variate classifiers based on these inputs. A comprehensive understanding of many parts of the LHCb software framework was crucial in creating a pipeline that not only fits within the current event model but also operates in an orthogonal way with respect to the development of MVA simulation-based approaches. In this way, I ensured that the work complements other contributions rather than conflicts. The

[10] ΔR represent the cone opening, defined as $\Delta R = \sqrt{\Delta\phi^2 + \Delta\eta^2}$

isolation tools have the potential to refine the online selection criteria significantly, but further studies are needed to optimize their application. Moreover, the work done in the multi-variate approaches can be extended to the offline selection, improving its accuracy and efficiency. Another critical area for improvement is selective persistency: limiting the amount of saved information to only the variables of interest instead of the entire selection of particles, the data storage and processing can be made more efficient.

Chapter 4

Search for $B \to K^* \tau e$ decays

The search for the lepton flavour violating decay $B^0 \to K^{*0}\tau^{\pm}e^{\mp}$, based on 5.6 fb^{-1} of data collected by LHCb in 2016, 2017 and 2018, is presented in this chapter. As discussed in Chapter 1, according to the SM, this process is forbidden since it involves lepton flavour and lepton family number violation. Extending the SM with massive neutrinos and considering neutrino oscillations makes this process possible, even though it is extremely suppressed: calculations discussed in Section 1.2 estimate the process branching ratios $\mathcal{O}(10^{-50})$ in this scenario. This is below any experimental sensitivity. Therefore, an observation will constitute a clear evidence of NP. As presented in Section 1.2.4, the search presented in this thesis constitutes the first-ever search of this decay channel and the first search for first- and third-generation lepton coupling at LHCb.

In Section 4.1, an overview of the analysis strategy is provided. The tau lepton is reconstructed via its hadronic decay with three or four pions, i.e. as $\tau^{\pm} \to \pi^{\pm}\pi^{\mp}\pi^{\pm}\nu_{\tau}$ or $\tau^{\pm} \to \pi^{\pm}\pi^{\mp}\pi^{\pm}\pi^0\nu_{\tau}$. The first mode constitutes $\sim 9.3\%$ of the total τ decays, while the second $\sim 4.6\%$, as shown in Figure 4.0.1. The K^*, instead, decays via strong interaction into K^+ and π^-. The samples used in the analysis are described in Section 4.2. Section 4.3 describes the B mass reconstruction studies. Then, the entire selection chain employed to identify the decay of interest is described in Section 4.4. The branching ratio is determined by normalizing the signal yields to the yields of the $B \to D^- D_s^+$, with $D_s^+ \to K^+K^-\pi^+$ and $D^- \to K^+\pi^-\pi^-$ decay. We, therefore, refer to this sample as the normalization channel. This decay is chosen for its similarity with the signal topology, abundance in LHCb data, ease of selection, and well-known branching ratio. It is also used as a control channel to verify the Monte Carlo (MC) description of relevant variables. The selection of the normalization channel and the fit to the surviving events to extract the yields are explained in Section 4.5.
Section 4.6 reports the efficiencies of the selections for signal and normalization channels. They are mainly evaluated from the simulation, except for the tracking,

trigger, and particle identification efficiencies, which are estimated in a data-driven way.
Understanding the background is one of the key aspects of the analysis. Studies are performed to parameterize the background shape in data events at the end of the selection. The signal, instead, is modeled from MC events. Section 4.7 describes these results.
A description of the systematic uncertainties related to the analysis is provided in Section 4.8. Lastly, the expected upper limits on the branching ratios of $B^0 \to K^{*0}\tau^{\pm}e^{\mp}$ decays are given in Section 4.9.2.

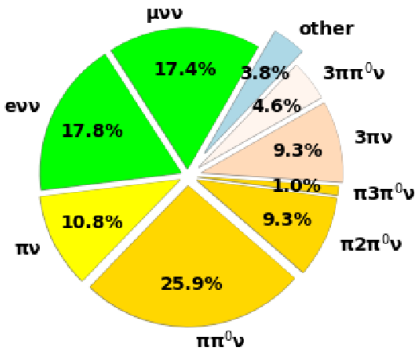

Figure 4.0.1: Chart representing τ lepton decays with relative fractions.

4.1 Analysis strategy

The analysis aims to set the first limit on the branching ratio for the decay channel $B \to K^*\tau e$. The MC simulation, used as a proxy for the signal in the analysis, is produced assuming a phase space uniform in the kinematics of the B decay. Efficiencies maps are provided as a function of the invariant masses squared of $K^*\tau$ and τe to eventually allow a re-casting of the result assuming different kinematics from different theoretical models. The τ lepton hadronic decays are implemented in the `TAUOLA` package [196] [197]. The full chain of the analysis selection, presented in Section 4.4, is optimized for $\tau \to \pi\pi\pi\nu_\tau$ decay, indicated as T5 by the name of the `TAUOLA` tuning. The selection efficiency is also estimated for $\tau \to \pi\pi\pi\pi^0\nu_\tau$ decay, named T8, for analogous reasons. This contributes to the signal because the neutral pion is not reconstructed. Therefore, from the reconstruction point of view, the two decays have the same final state.

Two main decay channels of the B meson should be distinguished, depending on the electric charge of the electron with respect to the kaon produced by the K^* meson decay. This leads to the definition of two categories: opposite-charge (OC)

$B^0 \to K^{*0}\tau^+e^-$ and same-charge (SC) $B^0 \to K^{*0}\tau^-e^+$ decays. OC and SC decays might behave differently in the context of a physics model BSM [198]. In addition, the composition of the physics background is different in the two cases. Therefore, physics background studies and limits on the branching fractions are done separately for $B^0 \to K^{*0}\tau^+e^-$ and $B^0 \to K^{*0}\tau^-e^+$ decays.

The data sample selected should contain candidates with a τ and an electron with opposite charges. This is indicated as opposite-sign (OS) sample. However, events with the two leptons having the same charge are also selected and used as a proxy for the background. They are labeled as same-sign (SS) samples.
The entire selection is made as much as possible independent of the phase-space assumption in the simulation. We can identify three main groups of requirements:

1. Preliminary selections. This step comprises the stripping selection (see Section 4.4.1), which indicates within the LHCb a collection of loose cuts used to preselect a class of similar decay and reconstruction requirements. In addition, fiducial cuts are applied to the final states, as shown in Section 4.4.2, and trigger requirements are specified in Section 4.4.3;

2. Multivariate methods. They are used to suppress a large part of the combinatorial and physics backgrounds, exploiting mostly the topology of the decay. Section 4.4.4 describes the classifier trained to suppress the combinatorial background, while in Section 4.4.5, isolation variables are used to build a method for partially reconstructed background suppression. Finally, Section 4.4.6 includes a multivariate classifier ad-hoc for τ-charm separation;

3. Additional selections. They are added on top of the previously described multivariate methods to reduce the remaining background further and identify the decay channel. In particular, particle identification cuts are described in Section 4.4.7. Moreover, a cut is applied to the invariant mass of K^{*0} (see Section 4.4.8). Finally, cuts on the τ flight distance and flight distance χ^2 are applied as described in Section 4.4.9) and final state combinations are vetoed to remove possible surviving physics background in Section 4.4.10.

Data in the B^0 refitted mass region of [4600, 6400] MeV, called signal region, are not looked at until the analysis procedure is finalized to avoid introducing biases in the selection. The mass variable adopted for the analysis is evaluated by refitting the whole decay chain, including the missing momentum carried by the unreconstructed neutrino from the τ lepton. A complete discussion about the refit method and a comparison with other methods is in Section 4.3. From the definition of the signal region, it is possible to automatically derive the definitions of upper (or right) and lower (or left) mass sidebands for the OS data (see Table 4.1.1).

Selection efficiencies are derived from MC. However, corrections are used to evaluate electron track reconstruction efficiencies and trigger efficiencies. The efficiency of the particle identification selection is evaluated, instead, using dedicated data control samples and the `PIDCalib2` software [199].
The normalization channel chosen for the analysis is $B \to D^- D_s^+$ and its charge conjugate, with $D^- \to K^+\pi^-\pi^-$ and $D_s^+ \to K^+K^-\pi^+$, because of the large branching fraction and the topology similar to the signal one. This sample is also used as a control channel to test the reliability of some variable distribution in MC and to access several systematic uncertainties on the signal efficiencies.
Data are fit separately for SC and OC decays. For each channel, the signal model has two components according to the recovery of bremsstrahlung photon: if one or more photons are associated with the reconstructed electron, the event is classified as *brem*, otherwise as *nobrem*. Upper limits are set using the confidence levels (CLs) method, described in Section 4.7.

Mass regions	**Mass window [MeV/c^2]**
Lower sideband	2000-4600
Signal region	4600-6400
Upper sideband	6400-12000

Table 4.1.1: Definitions of different mass regions: signal region, lower and upper sidebands

4.2 Dataset and simulated sample

4.2.1 Dataset description

Data used for the analysis have been collected by the LHCb detector (see Chapter 2) during part of the Run 2 operations, corresponding to 2016, 2017, and 2018 years of data taking, for a total collected luminosity of $\sim$5.6 fb^{-1} of $p-p$ collisions at center-of-mass energies of $\sqrt{s}$ = 13 TeV. Data have been preselected via the "Stripping" lines reported in Appendix H (Table H.0.1). The stripping lines contain sets of loose selections that are applied to all the data stored on the tape to identify a fraction of interesting events that can be stored on disk for easier access. Occasionally, depending on the availability of the resources and the interests of the various physics working groups within the collaboration, central productions, named "Stripping campaigns", are run. I implemented the stripping lines for selecting the channel $B \to K^*\tau e$, which did not exist before. They were run during a stripping campaign that ended in January 2024 and concerned the three years mentioned above.

The stripping selections are the same across the years for different stripping versions, and they are reported in Appendix I (Table I.0.3 for the signal channel and Table

I.0.4 for the normalization channel).

4.2.2 Monte Carlo simulation

MC simulated samples are used throughout the analysis to define the selection of the signal and normalization channel, estimate the efficiencies and analyze the background contributions. The proton-proton interaction is simulated in LHCb using Pythia8 [200], the complete decay chain using EvtGen [201] and the interaction of the particles with the different parts of the detector and its response is obtained using GEANT4 [202, 203]. No cut is imposed at the generation level to channel T5 of the τ decay ($\tau \to \pi\pi\pi\nu_\tau$). In contrast, requirements for the charged final particles to be inside the detector acceptance are demanded for channel T8 ($\tau \to \pi\pi\pi\pi^0\nu_\tau$). In addition, kaons and pions are required to have a transverse momentum respectively larger than 250 MeV and 220 MeV, and the momentum of the electrons has to be larger than 2 GeV. The efficiency of these requirements is listed in Section 4.6. This difference in the generation requirements is considered at the early stage of the offline selection. The fiducial cut, described in Section 4.4.2, aligns the fiducial requirements of T5 and T8 channels.
The key features of the simulated samples used along the analysis as signal, normalization, and background samples are listed in Appendix H (Table H.0.2).

In the simulated sample, several candidates are reconstructed for each event. The process to ensure that we can identify the signal among all the reconstructed decay in the simulation is named *truth matching*. This procedure is done in three steps:

1. For final state particles (pions, kaon, and electron) and composite states (K^*, τ, B) in the decay, we require that the particle IDs, described in Section 3.1.5, is the same for reconstructed and generated particles.

2. For each reconstructed composite object, we check the association of the decay products with the related composite MC parents. As an example, we require that the electron's parent matches with the reconstructed B candidate, that the parent of the K is the one of the K^*, and so on for all the particles in the decay.

3. We verify the correctness of the sign for τ and electron, and of the decay products for the $K^*(892)^0$.

A procedure similar to the previous one has been applied to the control sample, where the composite states are D and D_s mesons.

4.3 B mass reconstruction

The LHCb standard reconstruction provides the invariant mass of the final state particles, i.e. the four pions, the kaon and the electron. The neutrino coming from the tau lepton decay is not reconstructed. Hence, the invariant mass (M) of the reconstructed final state particles differs from the actual B mass. However, it is possible to reconstruct the missing momentum carried by the undetected neutrino using the principle of conservation of momenta. We can, in principle, reconstruct properly the B mass through different techniques exploiting the knowledge of the kinematic and topology of the decay, in particular, the position of the B vertex and the τ momentum, determined by the three pions in the final state, or otherwise using the τ vertex.

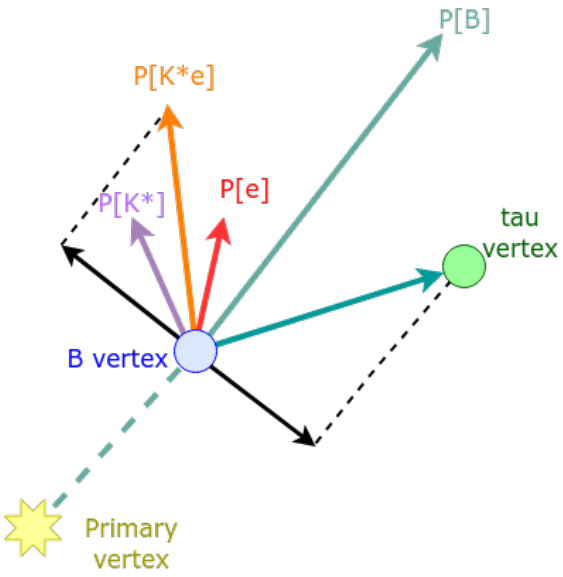

Figure 4.3.1: Schematic representation of $B \to K^*\tau e$ kinematics. Different techniques could be considered for the B^0 mass reconstruction. For the determination of the component of the τ momentum orthogonal to the B^0 direction of flight, several elements come into play, such as the vertexing of the B and the determination of the momentum for the system K^*e.

In the following, three different methods for reconstructing the mass of the B are compared. One approach is based on adopting the *minimally corrected mass* (MCM). The MC considers the correction of the component $P_\perp$ of the missing momentum perpendicular to the B^0 direction of flight:

$$\text{MCM} = \sqrt{P_\perp^2 + M^2} + P_\perp. \tag{4.3.1}$$

This technique is primarily used in other analyses. It is made possible thanks to the precision of the vertex measurement in the VELO [204].

Another technique, described in detail in [205], provides the *partial mass* (PM). This technique can be exploited when there are sufficient constraints to solve the kinematic problem of missing particles in partially reconstructed decay. Since the energy-momentum relation is a quadratic equation, the momentum of the missing neutrino, hence the mass of the B, has a two-fold ambiguity. Only one possible solution is chosen.

The third method simultaneously constrains the τ particle's mass to the PDG value [206] and the neutrino's mass to zero. This method takes the name of *DecayTreeFitter* (DTF) because it fits the kinematics, taking into account the vertices' and masses' constraints. An example of how the least square fit is implemented during the upstream reconstruction of the intermediate composite states starting from the reconstructed final state particles and how all the parameters are extrapolated is provided in [207]. The main algorithm has been modified to take in consideration the missing momentum carried by the neutrino. The fit requires a 2-body decay system to constrain the particles' masses. For this reason, the decay reconstructed differs from the original one by introducing a non-flying intermediate state, namely Y.

The mass reconstructed with the three different methods are compared in Figure 4.3.2. The histograms' peak positions and the StdDev90[1] are provided in Table 4.3.1. Errors on peak position and StdDev90 are estimated using the bootstrapping method. A thousand simulated samples are used to resample the dataset, and peak position and StdDev90 are evaluated for each of them. The standard deviation among the samples gives the uncertainties.

Peak position	2016	2017	2018
MCM	5239.0 ± 24.4	5275.0 ± 13.5	5257.0 ± 17.6
PM	5275.0 ± 22.7	5293.0 ± 19.8	5311.0 ± 19.3
DTF	$\mathbf{5257.0 \pm 10.2}$	$\mathbf{5275.0 \pm 18.7}$	$\mathbf{5257.0 \pm 0.8}$
StdDev90	2016	2017	2018
MCM	209.3 ± 2.4	210.2 ± 2.1	208.4 ± 2.6
PM	212.8 ± 2.7	215.5 ± 2.6	214.7 ± 2.8
DTF	$\mathbf{180.1 \pm 2.4}$	$\mathbf{175.8 \pm 2.1}$	$\mathbf{174.1 \pm 2.4}$

Table 4.3.1: Comparison between peak position and StdDev90 for the different reconstruction methods explored in the analysis. All measurements are expressed in MeV/c^2. The values for the baseline, correspondent to DTF, are in bold.

Given its better performances, the mass reconstructed through the DTF has been chosen for this analysis. From now on, we will refer to it as the *refitted mass* or simply *mass*, if not explicitly indicated otherwise.

[1] Standard deviation containing 90% of the distribution

The DTF reconstruction method is validated using $B \to D^- D_s^+$ decays as the control sample. For this specific channel, only five out of six final states are reconstructed, emulating the behaviour of the neutrino missing energy in this way. A systematic uncertainty is accessed by evaluating the data-MC discrepancies on the control sample for the mean value and resolution of the refitted mass, as discussed in Section 4.8.1.

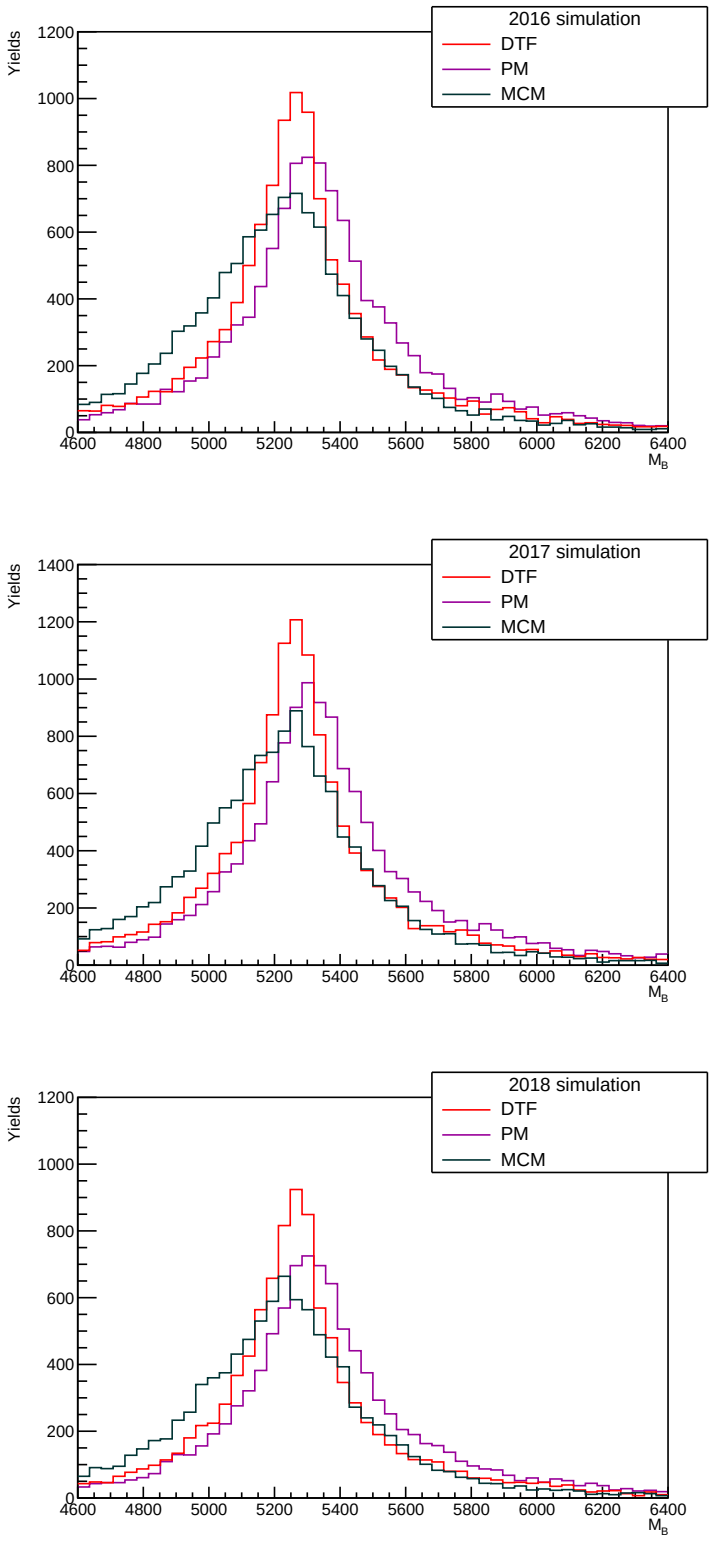

Figure 4.3.2: Comparison between different reconstruction methods to recover the missing energy of the neutrinos in the signal region ($[4600, 6400]$ MeV). The red solid line is obtained by refitting the decay using DTF, the cyan solid line is the MCM, and the magenta solid line represents the PM. Plots are divided per year of MC simulation: 2016 (left), 2017 (centre) and 2018 (right).

4.4 Event selection

The selection procedure consists of the following steps:

- *Reconstruction and Stripping*, used for the reconstruction of the decay chain and for imposing loose cuts to reduce the size of the datasets to a manageable size (4.4.1);
- *Fiducial cuts*, a preselection based on geometry constraints to consider only events in the detector acceptance (4.4.2);
- *Trigger selection*, including three different L0 trigger decisions (4.4.3) and software trigger requirements;
- *Anti-combinatorial BDT*, named `ACBDT` or `ACMVA`. It is a multivariate method trained on kinematic and topological variables, particularly efficient in suppressing the background from random combinations of tracks that arise during the reconstruction of the event (4.4.4);
- *Isolation Fisher*, named `IsoFisher` or `IsoMVA`. It is a multivariate classifier on isolation variables to suppress the partially reconstructed background (4.4.5);
- *Tau classifier*, named `TauBDT` or `TauMVA`. Another multi-variate classifier is used to select τ candidates and reject background containing D^0, D^+, and D_s^+ mesons, using kinematic properties of the decay products of the tau lepton in its reference frame (4.4.6);
- *Particle identification requirements*, applied to remove background with misidentified particles (4.4.7);
- K^{*0} *mass cut*, tightening the loose requirements present at the Stripping level(4.4.8);
- *Fiducial cuts on flight distance and its significance*, to reduce physics background for control samples selected for the background parameterization (4.4.9).
- *Mass vetoes*, specific cuts on the invariant mass combination of the particles in the final state rejecting specific physics background (4.4.10)

Some checks are performed at the end of the selection, and they're summarized in Section 4.4.12.

4.4.1 Reconstruction and Stripping Selection

The first step of the analysis consists of reconstructing the full decay chain and applying a loose selection to save the data to the disk through the "Stripping" process. The

Stripping versions and Stripping lines used are reported in Appendix H (Table H.0.1). The selection criteria for both signal and normalization channels are summarised in Appendix I (Table I.0.3 and I.0.4, respectively). Even though most of the requirements are related to the kinematics of the decay, loose high-level trigger (see Table I.0.2 in Appendix I) and particle identification selections are applied at the stripping stage to keep low the rates of the stripping lines.
Besides the requirements of the stripping for $B \to K^{*}\tau e$, additional cuts (reported in Appendix I) are applied during the reconstruction while creating the fake intermediate system $Y^{\pm}(K^{*0}(892)e^{\pm})$, which is needed by the DTF algorithm, as discussed in Section 4.3.
The efficiency of the stripping selection is reported for each simulation year in Section 4.6.

Refitting requirements

While refitting the decay, the mass of τ and ν are constrained to the PDG values and the direct B decay products are constrained to the origin vertex. In addition, requirements are applied to guarantee the goodness of the fit:

- the fit should converge successfully, i.e. its status should be 0;
- the value of the χ^2 per degree of freedom should be smaller than 12.

Distributions of these variables are shown for signal compared to opposite-sign data sidebands in Figure 4.4.1.

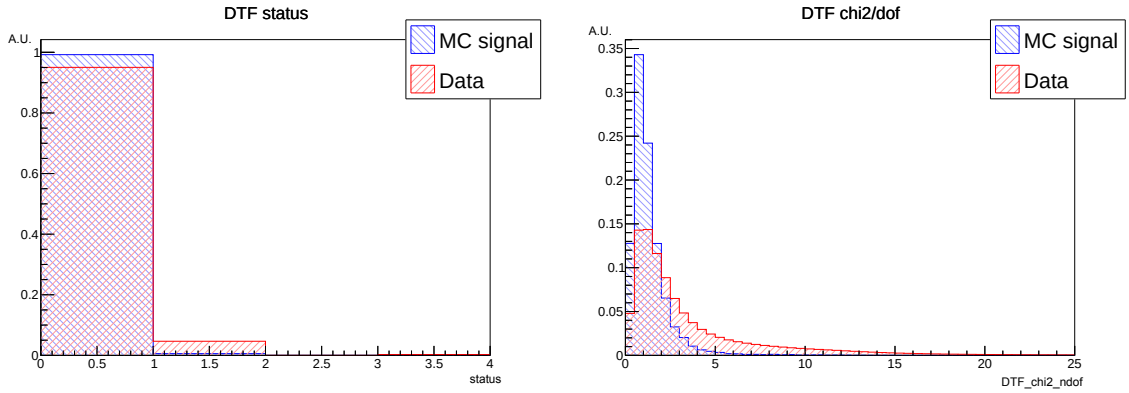

Figure 4.4.1: Distribution of the status (left) and the χ^2 per degrees of freedom (right) variables of the DTF for both data (red) and simulated events truth matched (blue). Distributions are cumulative for all the years. The requirement of convergence and good fit quality is represented by the status variable equal to zero and a small value of χ^2 per degree of freedom.

4.4.2 Fiducial region

Once the decay is reconstructed and the Stripping selection is applied, additional requirements are necessary to ensure that all the final state particles are inside the

detector acceptance. In addition, since the particle identification efficiency will be computed using a calibration sample, this step is also constructed to select only events with the same kinematics as the calibration sample. Each particle in the final state is required to have momentum smaller than 110 GeV, pseudorapidity between 2 and 4.9, and to be in the acceptance of the RICH detectors [152] ($hasRich$). Additionally, electron candidates need to have associated hits in the electromagnetic calorimeter ($hasCalo$) and be inside the electromagnetic calorimeter acceptance ($|x_{ECAL}| >$ 363.6mm and $|y_{ECAL}| >$ 282.6mm, $\text{Region}_{ECAL} \geq 0$, $InAccEcal$) [153]. Pions and kaons in the final state must be inside the hadronic calorimeter ($\text{Region}_{HCAL} \geq 0$). All the fiducial cuts are summarized in Table 4.4.1. The efficiency evaluated for each year on the simulated samples is reported in Section 4.6.

Particle	**Fiducial cut**
All final states	$2 < \eta < 4.9$ $p < 110$ GeV $hasRich$
π and K	$\text{Region}_{HCAL} \geq 0$
e	$hasCalo$ $InAccEcal$ $\|x_{ECAL}\| > 363.6$ || $\|y_{ECAL}\| > 282.6$ $\text{Region}_{ECAL} \geq 0$

Table 4.4.1: Fiducial cuts applied to the final state particles

4.4.3 Trigger Selection

The LHCb trigger in Run 2 [155] reduced the rate from approximately 30 MHz to 12.5 kHz of events written to the offline storage. To achieve this goal, three different trigger levels have been used: a hardware stage (L0) and two software applications (HLT1 and HLT2), as described in Section 2.5.

An essential piece of information is knowing whether the signal candidate was part of the signal decision [208]. Events are identified as TOS (Triggered On Signal) if the signal generates a positive trigger decision and as TIS (Triggered Independent on Signal) if any other particle produced a positive decision. The trigger efficiency can be evaluated in a data-driven way using the so-called TISTOS method [209].

The list of all the trigger lines' decisions for the analysis is reported in Table 4.4.3. The triggered events are classified into three separated exclusive categories, named according to the main L0 trigger line that selected the events:

- **eTOS**: events that are triggered by a reconstructed electron that came from a signal event (`L0ElectronDecision_TOS`);

- **TIS**: events that are triggered by a reconstructed particle that doesn't come from a signal event (`L0Global_TIS`) and not by `L0ElectronDecision_TOS` .
- **hTOS**: events that are triggered by a reconstructed hadron that came from a signal event (`L0HadronDecision_TOS`) and not by `L0ElectronDecision_TOS` nor `L0Global_TIS`;

The trigger configuration is encoded in the Trigger Configuration Key (TCK). Data are collected with different TCK values during the year. Instead, a single value for the trigger decisions is used in simulated events.
For *eTOS* and *hTOS* categories, the hardware trigger lines' behavior in signal simulation should be aligned with its real behavior during data-taking. To guarantee this, an additional fiducial selection on the electromagnetic (`L0ElectronAlignment`) and hadronic (`L0HadronAlignment`) calorimeters is imposed. In fact, the calorimeter detectors select data with a given transverse energy E_T cut varying with time, which is not the case in simulation. When computing the efficiencies, this must be considered with appropriate trigger corrections. Thresholds on the L0 electron trigger and L0 hadron trigger categories are usually expressed in ADC counts in the trigger. Still, they can be easily converted in MeV using the 24 MeV/ADC factor, valid for Run 2. The complete alignment selections for eTOS and hTOS categories are reported in Table 4.4.2. In contrast, no alignment is needed for TIS candidates.

TCK	Yr.	**ECAL** E_T^{L0}		**HCAL** E_T^{L0}	
0x6139160F	2016	100 ADC	2400 MeV	156 ADC	3744 MeV
0x62661709	2017	88 ADC	2112 MeV	144 ADC	3456 MeV
0x617d18a4	2018	99 ADC	2376 MeV	158 ADC	3792 MeV

Table 4.4.2: Threshold cuts for different transverse energy E_T measured in electromagnetic and hadronic calorimeters corresponding to different TCKs of the simulation samples. These requirements are necessary to align simulation with data.

The chosen combination of trigger decisions for HLT1 and HLT2 has been determined considering many lines and establishing a hierarchy using a figure of merit proportional to the significance, defined as:

$$f.o.m. = \frac{\epsilon_S}{\sqrt{B}}, \tag{4.4.1}$$

where ϵ_S is the efficiency of applying a given trigger line and B is the background yield. The figure of merit is evaluated using the signal truth-matched MC events. The background yield is estimated in the signal region from an extended maximum likelihood fit to the opposite-sign data sidebands, using a Gamma law model for the parameterization. Lines with a larger value for the figure of merit are selected first. Whenever the figure of merit values are comparable within error intervals, we rely on the maximal efficiency to establish the priority among the lines. Studies for

optimizing the figure of merit are reported in Appendix J. This optimization has been performed using 2016 and 2017 truth-matched simulated events and a subset of the 2016 data. Table 4.4.3 shows the list of trigger lines adopted in this analysis. The HLT1 line applied in the analysis exploits the kinematic properties of two tracks in the decay, requiring a combination between the two. The HLT2 selections are instead based on topological properties of two, three, and four body decays in the channel. `TopoE` lines differ from `Topo` because of requirements on election identification within the decay tree.

Category	L0 Trigger	HLT1	HLT2
eTOS	`L0ElectronDecision_TOS` & `L0ElectronAlignment`	`HLT1TwoTrackMVADecision_TOS`	`HLT2Topo(2|4)BodyDecision_TOS` || `HLT2TopoE(2|3|4)BodyDecision_TOS` ||
hTOS	`L0HadronDecision_TOS` & `L0HadronAlignment` & `!L0ElectronDecision_TOS` & `!L0GlobalDecision_TIS`	`HLT1TwoTrackMVADecision_TOS`	`HLT2Topo(2|3)BodyDecision_TOS` || `HLT2TopoE(2|3|4)BodyDecision_TOS` ||
TIS	`L0Global_TIS` & `!L0ElectronDecision_TOS`	`HLT1TwoTrackMVADecision_TOS`	`HLT2Topo(2|4)BodyDecision_TOS` || `HLT2TopoE(2|3|4)BodyDecision_TOS` ||

Table 4.4.3: List of all the combinations of trigger lines separated into three categories (*eTOS*, *hTOS* and *TIS*). The nomenclature of the categories follows the main exclusive L0 trigger decision.

4.4.4 Combinatorial background suppression

A multivariate approach has been developed to suppress the combinatorial background surviving the first stages of the selection. This kind of background arises from random combinations of tracks during the reconstruction. The *Toolkit for Multivariate Analysis* (TMVA) software package [210] is used for training and testing several classifiers combining a list of variables able to discriminate signal from combinatorial background. Different methods are compared through the ROC curves performances, and the best one is chosen. The MVA method providing the best performances in terms of AUC is a gradient-boosted decision tree with a low learning rate (`BDTG_LLR`). The signal proxy consists of truth-matched simulated events which survive the previously described preselections. The upper sideband ($M > 6400$ MeV/c^2) of OS data is used as a background proxy because it is dominated by a combinatorial background. The discriminating variables used as input to the classifier are chosen among those related to the topology of the decay chain, with good separation power and low correlations among them. These input variables include the quality of the vertex reconstruction, the flight distances, and the impact parameters of B candidates and decay products. The list is shown in Table 4.4.4. Their distributions, superimposing simulation, and data samples are presented in Figure 4.4.2 and the correlation between them in Figure 4.4.3. Table K.1.1 shows the set of hyper-parameters used to train the classifier. A kFolding procedure [211], using $k = 4$ folds, has been applied to avoid potential biases in training and evaluating the method. It divides the datasets for signal and background into k sub-samples of approximately the same size on the base of the

event number. $k-1$ sub-samples are used for the training phase and the remaining one for the testing phase. The procedure is repeated for every possible k^{th} sub-sample. Distributions of the output of the trained method giving the best performance and ROC (receiver operating characteristic) curves are superimposed for each kFolding sub-sample in Figures 4.4.4 and 4.4.5, respectively. For each kFold, the value of the AUC for `BDTG_LLR` method is 0.981. An example of ROC curves for different methods and the output distribution superimposed for training and testing sample for a kFold is shown in Figure K.1.1.
Once the classifier is trained, it is applied to the MC simulation, OS and SS data. A zoom of the output in the region $[0.8, 1]$ is shown in Figure 4.4.6. Furthermore, the classifier output dependency with the mass is checked, as shown in Figure K.1.2. No strong correlation is found.

Name	Input variables	Separation power
`LogBEVCHI2`	$\log(\chi^2)$ for B^0 end vertex	4.519e-01
`LogBFDCHI2`	log(flight distance χ^2) for B^0	3.142e-01
`LogKstFDCHI2`	log(flight distance χ^2) for K^*	2.311e-01
`BIP`	B^0 impact parameter	2.292e-01
`KstFD`	K^* flight distance	1.776e-01
`BFD`	B^0 flight distance	1.506e-01
`LogTauFDCHI2`	log(flight distance χ^2) for τ	2.570e-02
`LogTauEVCHI2`	$\log(\chi^2)$ for τ end vertex	2.436e-02

Table 4.4.4: List of the variables related to the kinematics of the decay adopted as input for training the MVA method to suppress combinatorial background. Each variable's separation power is reported in the right column prior to the MVA approach.

Validation of the anti-combinatorial BDT

The multivariate classifier should discriminate events based on genuine differences between signal and background and not on differences between simulation and real data. Therefore, a process of variable validation is put in place. It checks that the MC simulation correctly reproduces the input variables' behavior. This is assessed by checking that the control channel behaves similarly for MC and data. The decay $B \to D^- D_s^+$ (with $D^- \to K^+\pi^-\pi^-$and $D_s^+ \to K^+K^-\pi^+$) has been used as validation samples: the B^0, D^-, and D_s^+ mesons are used as proxies for the simulation quality of the input variables listed in Table 4.4.4. The simulated candidates are truth-matched. Additional requirements are applied to both data and MC to ensure that the distributions from data have negligible contamination from backgrounds. In particular, the PID requirements correspond to the ones used for pions and kaon in the signal final state, described in Section 4.4.7. Moreover, events for which the measured mass of either one of the charmed mesons lies outside a mass window of ± 20 MeV/c^2 around the PDG value are rejected, as well as those whose measured mass for the B^0 candidate differs more than 50 MeV/c^2 from the PDG value. The

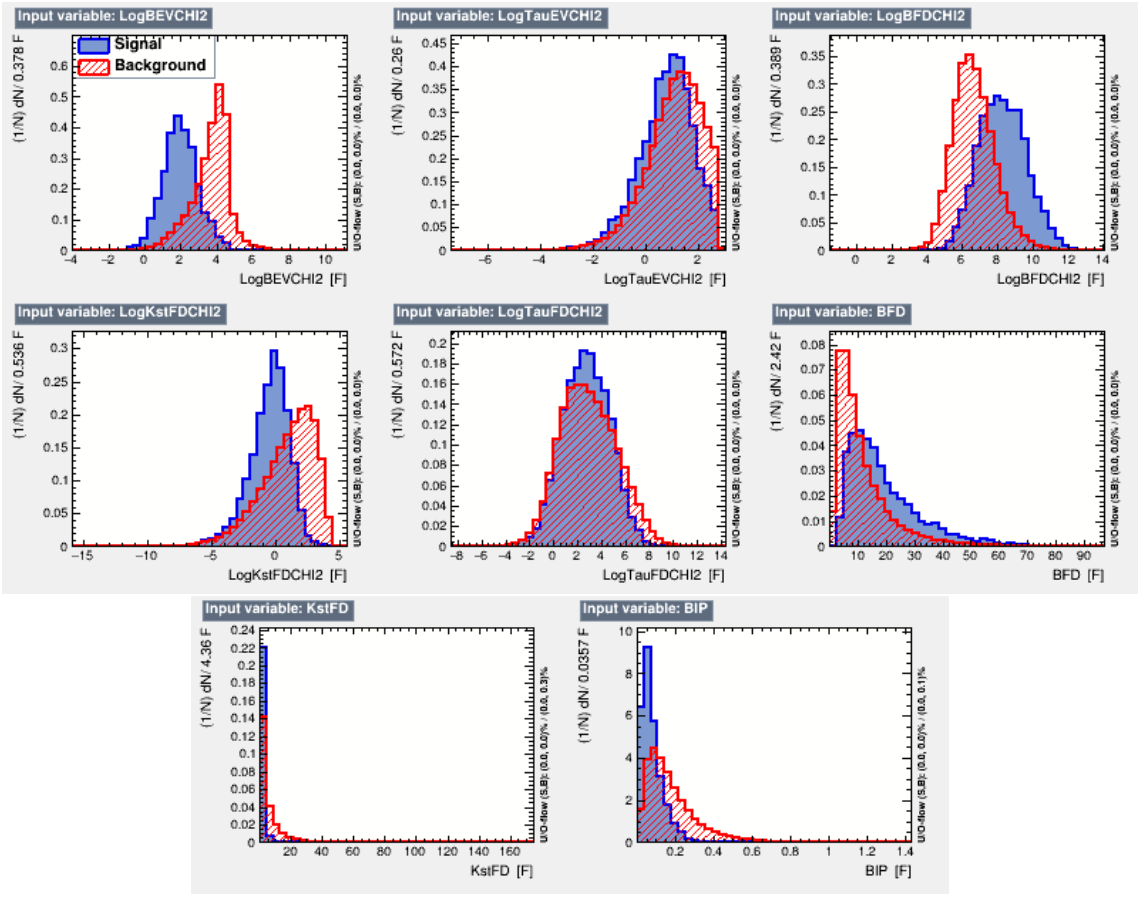

Figure 4.4.2: Signal (blue) and background (red) distributions of anti-combinatorial classifier input variables.

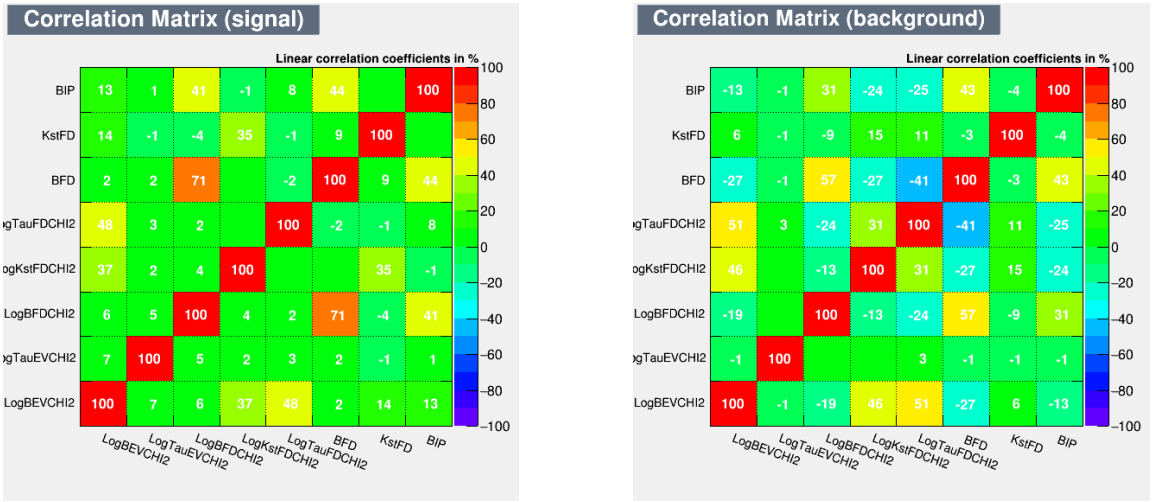

Figure 4.4.3: Correlation between anti-combinatorial classifier input variables for signal (left) and background (right).

subset extracted after the application of these cuts has purity $\frac{S}{S+B}$ 97%. The same requirements are also applied to simulated events to align data and MC samples.

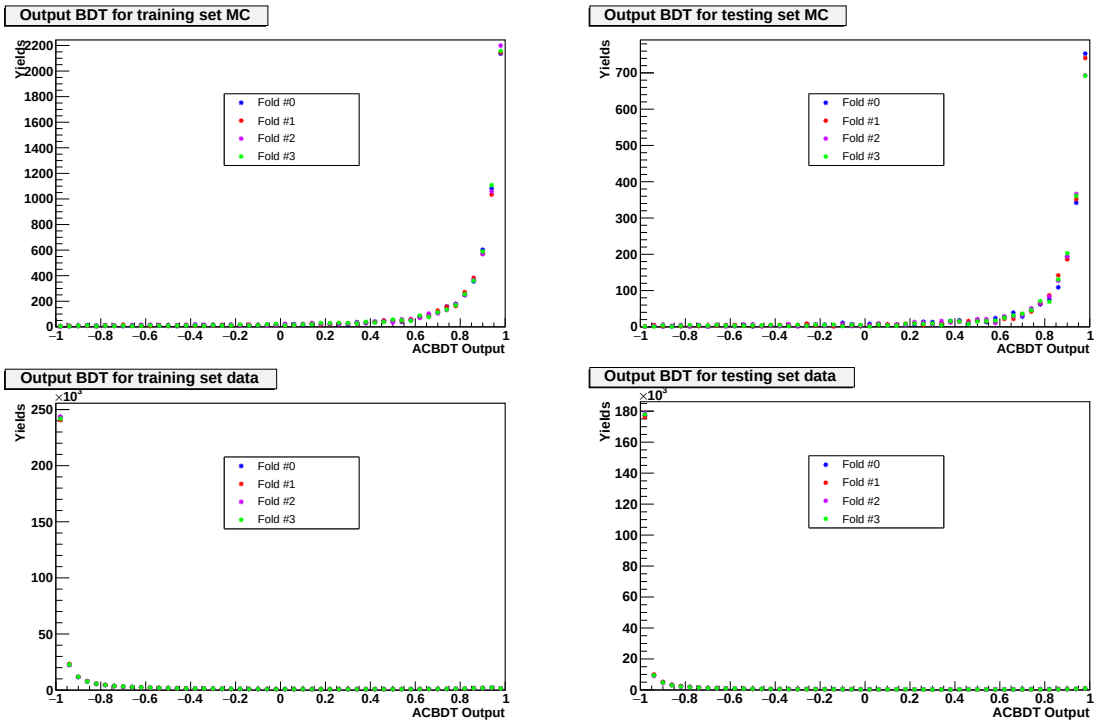

Figure 4.4.4: Classifier output for each *kFold* for training (left) and testing (right) samples of signal (upper part) and background (lower part).

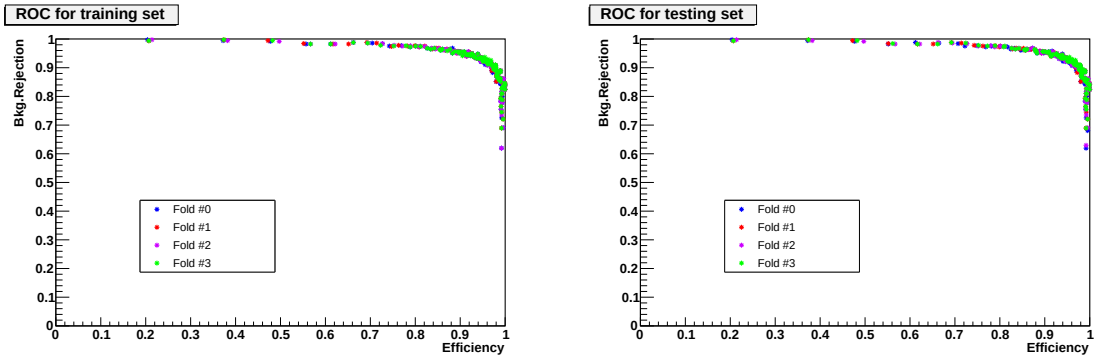

Figure 4.4.5: ROC curves for each *kFold* of the anti-combinatorial classifier for training (left) and testing (right) samples.

The comparison is shown in Figure K.1.3 and Figure K.1.4. The agreement between data and simulation is reasonable. Any residual discrepancy will be assessed as a systematic uncertainty, as discussed in Section 4.8.5.

Optimization of anti-combinatorial cut

A scan on several possible values has been performed to find the optimal value of the cut on the output of the anti-combinatorial classifier. The optimal cut is chosen as

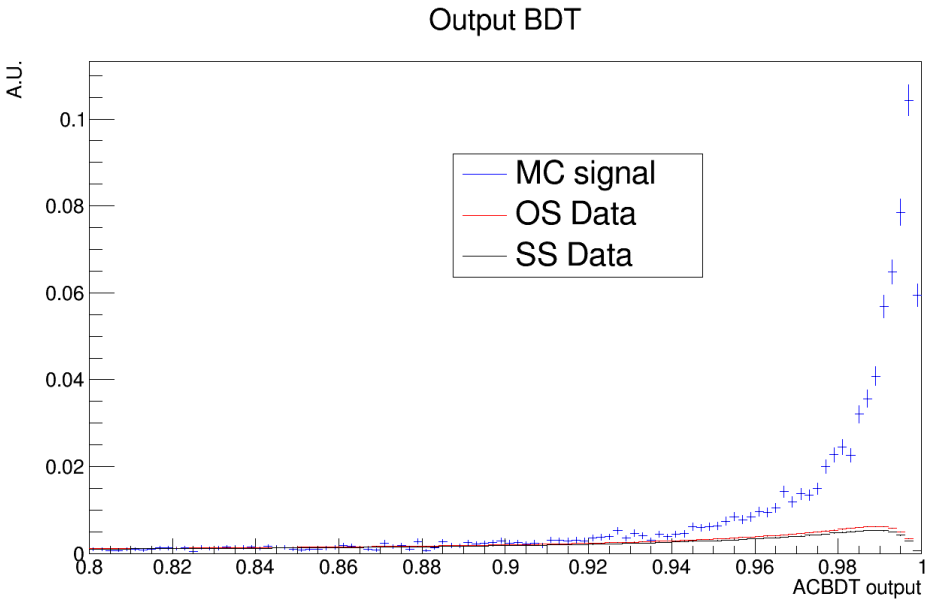

Figure 4.4.6: Anti-combinatorial classifier output for MC simulation (blue), OS data sidebands (red), and SS data (black) in the region [0.8, 1.].

the one that maximizes the Punzi figure of merit [212], defined as:

$$f.o.m = \frac{\epsilon}{\frac{\sigma}{2} + \sqrt{B}} \tag{4.4.2}$$

where ϵ is the efficiency of the selection, B is the background yield, and σ represents the number of standard deviations corresponding to one-sided Gaussian tests at the desired significance. Signal and background yields are evaluated on top of the previous cuts described in Sections 4.4.1, 4.4.2 and 4.4.3. In particular, the signal yield is extracted from the truth-matched simulated candidates in the signal region ($4600 < M < 6400$ MeV/c^2) surviving the selection up to this point, and it is used to calculate the signal efficiency. The background yield is obtained by fitting the B^0 refitted mass for the OS data sidebands events surviving up to this selection stage in the [3100,9000] MeV/c^2 range, excluding the signal region, using as model a Gamma law, and integrating the curve in the signal region. To account for possible bias in the extrapolation to the signal region, the background yield obtained is corrected using a factor evaluated on SS data, for which the fit can also be performed in the signal region. Figure 4.4.7 shows an example of the mass fit for SS and OS data. The correction to the background yield has been calculated from SS data as:

$$\frac{\Delta N}{N} = \frac{Y_{estimated} - Y_{counted}}{Y_{estimated}} \ [\%] \tag{4.4.3}$$

where:

- $Y_{estimated}$ is the background yield extracted from the extended maximum likeli-

hood fit on the SS data events surviving up to this selection stage in the signal region;

- $Y_{counted}$ is the background yield counted in the same region.

Figure 4.4.8 shows a small correlation between the correction and the classifier output cut. Therefore, the correction is evaluated and applied independently for each cut. The figure of merit is also evaluated without corrections, leading to the same result. The figure of merit is optimized for $\sigma = 3$, however also values of $\sigma = 0$ and $\sigma = 5$ and the purity S/B are tested and reported in Figure 4.4.9 for the same cut. The purity does not represent the best figure of merit for a search. The other figures of merit lead consistently to the choice of the cut $\texttt{ACBDT} > 0.9775$.

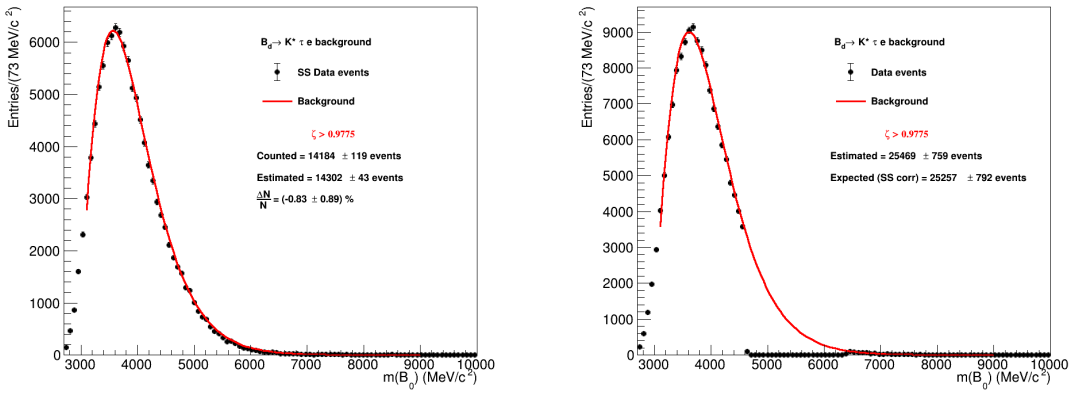

Figure 4.4.7: On the left: SS data fit for the optimal classifier output cut. On the right: OS data sidebands fit for the optimal classifier output cut. The background yields in the signal region are extracted from the extended likelihood fit on the OS data.

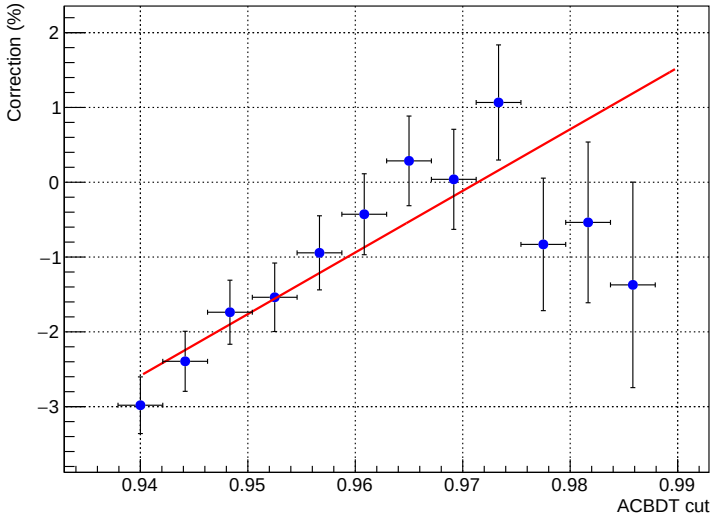

Figure 4.4.8: Correction factor $\frac{\Delta N}{N}$, evaluated as reported in Eq. 4.4.3, as function of the anti-combinatorial classifier output. Small dependence on the output is observed; however, corrections are really small, and they are evaluated and applied independently. As a cross-check, values of the correction extracted from the fit in the BDT output region [0.94, 0.99] are applied to estimate the background yield, leading to the same value of the optimized cut.

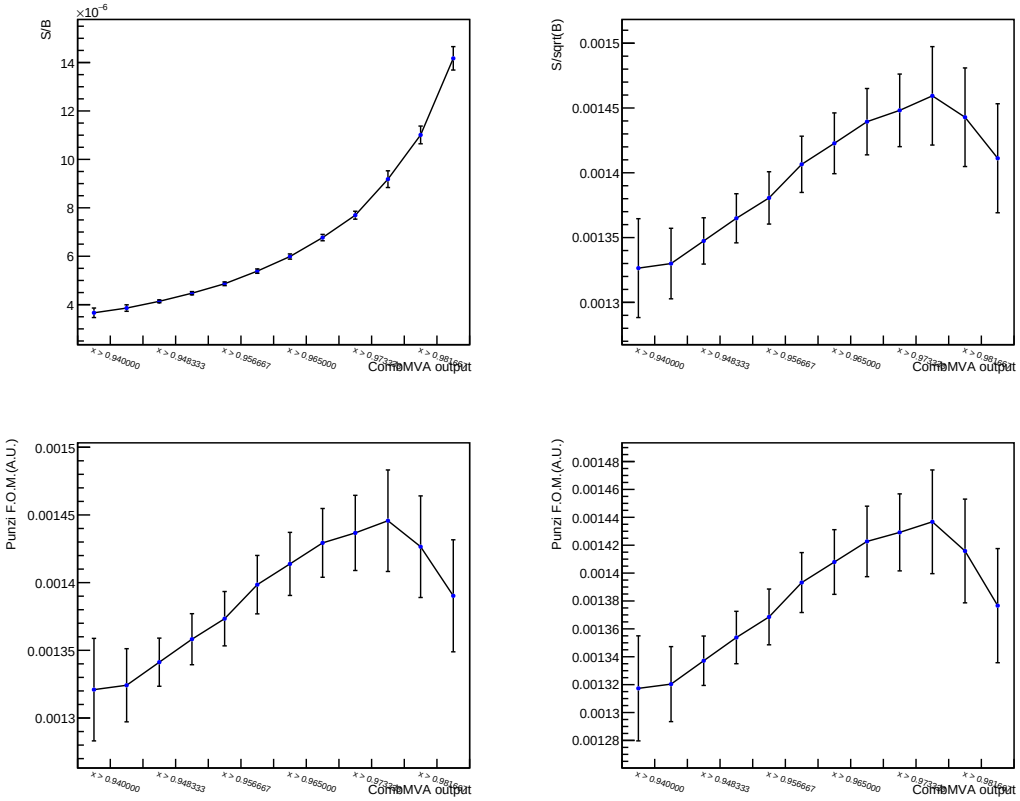

Figure 4.4.9: Figure of merit distributions for $\frac{S}{B}$ (up-left), $\frac{S}{\sqrt{B}}$ (up-right), $\frac{S}{\frac{3}{2}+\sqrt{B}}$ (down-left, adopted for the cut optimization) and $\frac{S}{\frac{5}{2}+\sqrt{B}}$ (down-right) scanning the output of the anti-combinatorial classifier in the region [0.94, 0.99].

4.4.5 Isolation

In order to further suppress the background, one can exploit the fact that the signal is expected to be more isolated from the rest of the event than partially reconstructed backgrounds. Another multivariate selection exploiting vertex and track isolation variables has been trained using TMVA. This information, as discussed in Section 3.3, is evaluated from the rest of the event.

Candidates in the SS sample within the signal region passing the upstream selection are used as background proxies. For signal, instead, simulated truth-matched candidates surviving to the selection up to this stage are used. Different methods are tested, providing similar performances. ROC curves comparison is on the left in Figure K.2.1 of Appendix K.2. The method chosen is `Fisher`, showing less possible over-training from the Kolmogorov–Smirnov test and less correlation with the mass. The list of track and vertex isolation variables used is reported in Table 4.4.5. Among them, the invariant mass of the candidate composed of the signal particle and one or two additional particles coming from the rest of the event and forming the vertex with the smallest $\Delta\chi^2$ results having good separation power. Similarly, other vertex

isolation variables are evaluated for B candidates and their decay products, and only the most discriminating ones are retained. In addition, the transverse momentum asymmetry property is exploited for track isolation. This quantity defined as $AsyPT = \frac{1-\sum_{\text{part}\in\text{cone}} PT}{1+\sum_{\text{part}\in\text{cone}} PT}$, where the sum is extended to all the particles within a cone with opening Δr. The chosen input variables are not presenting high correlations, as shown in Figures 4.4.10 and 4.4.11. Table K.2.1 shows the set of hyper-parameters used for the training of the classifier.
As already done for the anti-combinatorial classifier, the training adopts the kFolding procedure with $k = 4$. The output of the trained BDT and ROC curves are superimposed for each kFolding sample in Figures 4.4.12 and 4.4.13, respectively. The mean value of the AUC for the kFolds is 0.955. An example of ROC curves for different methods and the output distribution superimposed for training and testing samples for a kFold is shown in Figure K.2.1. Once the classifier is trained, it is applied to the MC simulation, OS, and SS data. The output is shown in Figure 4.4.14. Furthermore, the classifier output dependency with the mass is checked, as shown in Figure K.2.2. No strong correlation is found.

Name	Input variables	Separation power
B_VtxIsoDChi2MassOT	M of the candidate with smallest $\Delta\chi^2$ when adding one track to B^0 vertex	5.186e-01
tau_VtxIsoDChi2MassTT	M of the candidate with smallest $\Delta\chi^2$ when adding two tracks to τ vertex	4.199e-01
B_LogVtxIsoDChi2OT	$\log(\Delta\chi^2)$ when adding one track to B^0 vertex	3.733e-01
tau_LogVtxIsoDChi2TT	$\log(\Delta\chi^2)$ when adding two tracks to B^0 vertex	3.471e-01
Kst_VtxIsoDChi2MassTT	M of the candidate with smallest $\Delta\chi^2$ when adding two tracks to K^* vertex	3.347e-01
Kst_VtxIsoNum	Number of tracks within $\chi 2$ window when adding one track to K^* vertex	3.328e-01
tau_TrackIsoAsyPT_CC	P_T asymmetry for charged cone around τ with opening $\Delta r = 0.4$	3.123e-01
Kst_TrackIsoAsyPT_CC	P_T asymmetry for charged cone around τ with opening $\Delta r = 0.4$	2.530e-01
tau_TrackIsoAsyPT_NC	P_T asymmetry for neutral cone around τ with opening $\Delta r = 0.4$	1.488e-01
Kst_TrackIsoAsyPT_NC	P_T asymmetry for neutral cone around K^* with opening $\Delta r = 0.4$	1.235e-01

Table 4.4.5: List of the track and vertex isolation variables adopted as input for training the MVA method to suppress partially reconstructed background. Each variable's separation power is reported in the right column before any MVA approach.

Validation of the Fisher isolation

As explained in Section 4.4.4, the agreement between data and simulation should be checked to prove that the discriminating power of the input variables is genuine and not due to differences in simulation. Also in this case, the check has been performed using the $B \to D^- D_s^+$ sample. The same selection as described in 4.4.4 is applied to MC and data. The MC-data agreement is reported in Appendix K.2.1. It turns out that the variables are reasonably reproduced in simulation, so the MC does not need re-weighting. Possible residual discrepancies are accounted for as a systematic uncertainty.

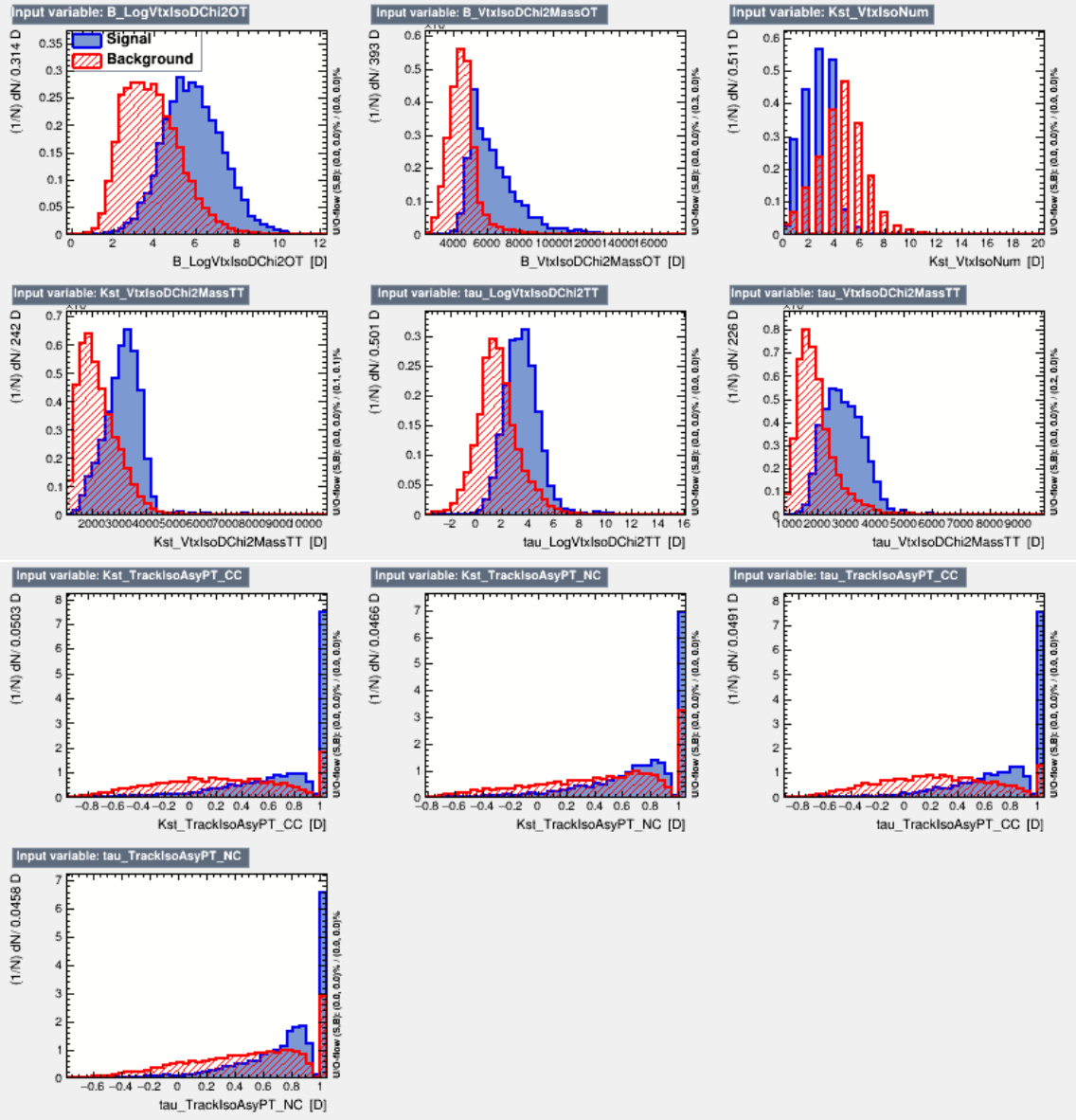

Figure 4.4.10: Signal and background distributions of isolation classifier input variables superimposed.

Optimization of isolation cut

The optimization of the cut on the isolation classifier follows a similar procedure as the one described in Section 4.4.4.
The signal yield is extracted by counting MC simulation truth-matched candidates in the signal region passing the previous selections, and the signal efficiency is derived from this number. Using a Gamma law model, the background yield is obtained from the fit on the B^0 refitted mass for the OS data sideband events surviving up to this selection stage in [3100, 9000] MeV/c^2 range.

SS corrections, evaluated as in Eq. 4.4.3, are extrapolated from the linear fit in the

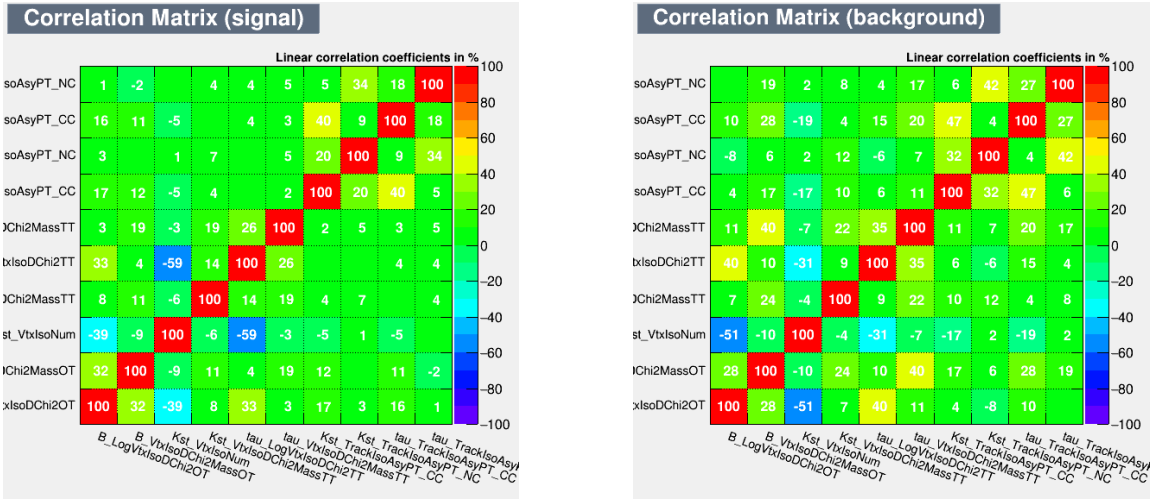

Figure 4.4.11: Correlation between isolation classifier input variables for signal (left) and background (right).

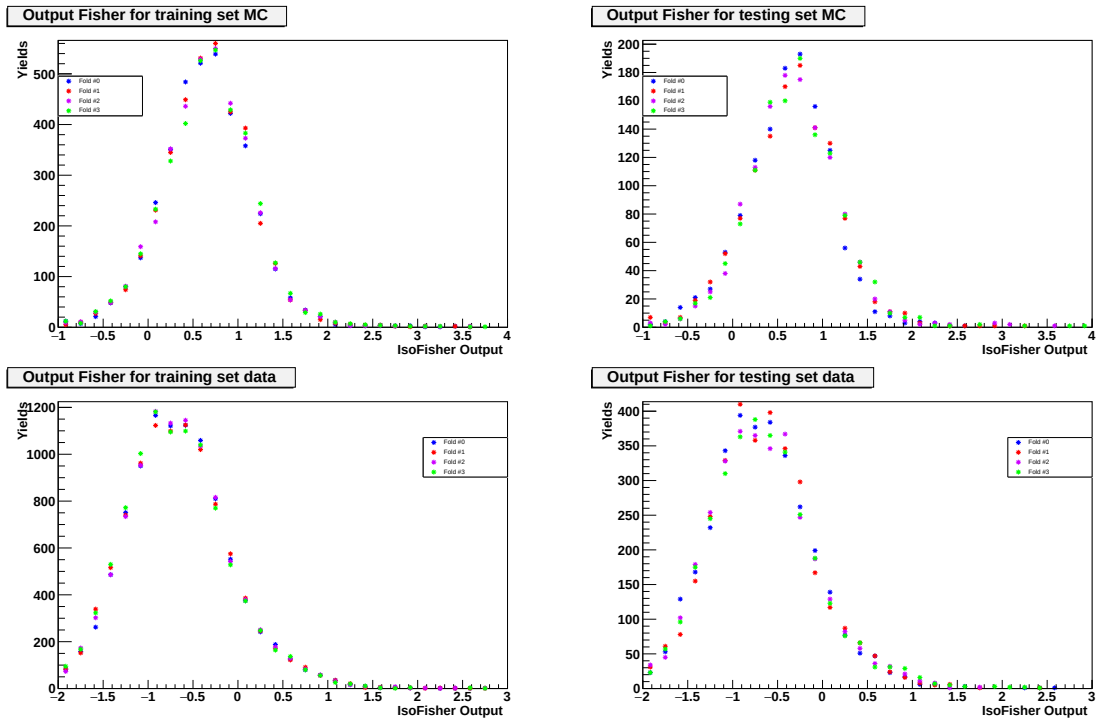

Figure 4.4.12: Classifier output for each *kFold* for training (left) and testing (right) samples of signal (upper part) in the output region [-1, 4] and background (lower part) in the output region [-2, 3].

region [0.2, 0.8] of the classifier output presented in Figure 4.4.16. The optimization procedure leads to choosing the cut `IsoFisher` > 0.48. Figure 4.4.17 shows the fit to SS data and OS data sidebands for the optimal cut.

The optimization of the figure of merit is both tested in case of no SS correction and applying SS corrections in the region [0.2, 0.8], leading to the same classifier output

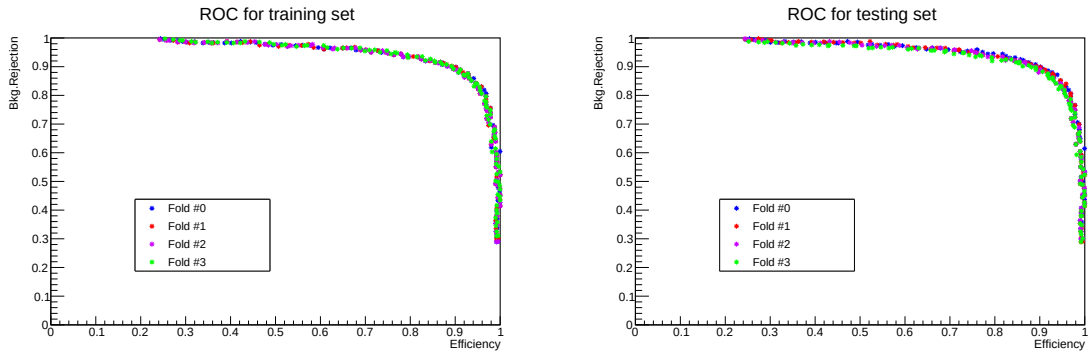

Figure 4.4.13: ROC curves for each *kFold* of the isolation classifier for training (left) and testing (right) samples.

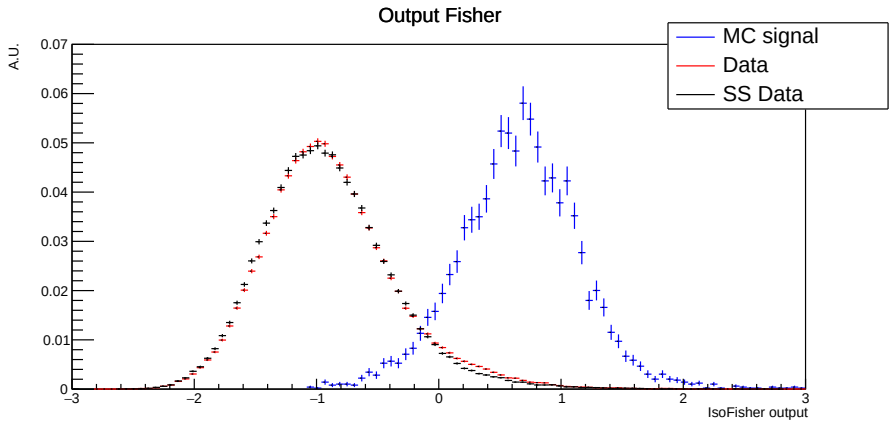

Figure 4.4.14: Isolation classifier output for MC simulation (blue), OS data sidebands (red), and SS data (black).

cut. Results of the figure of merit optimization are shown in Figure 4.4.15.

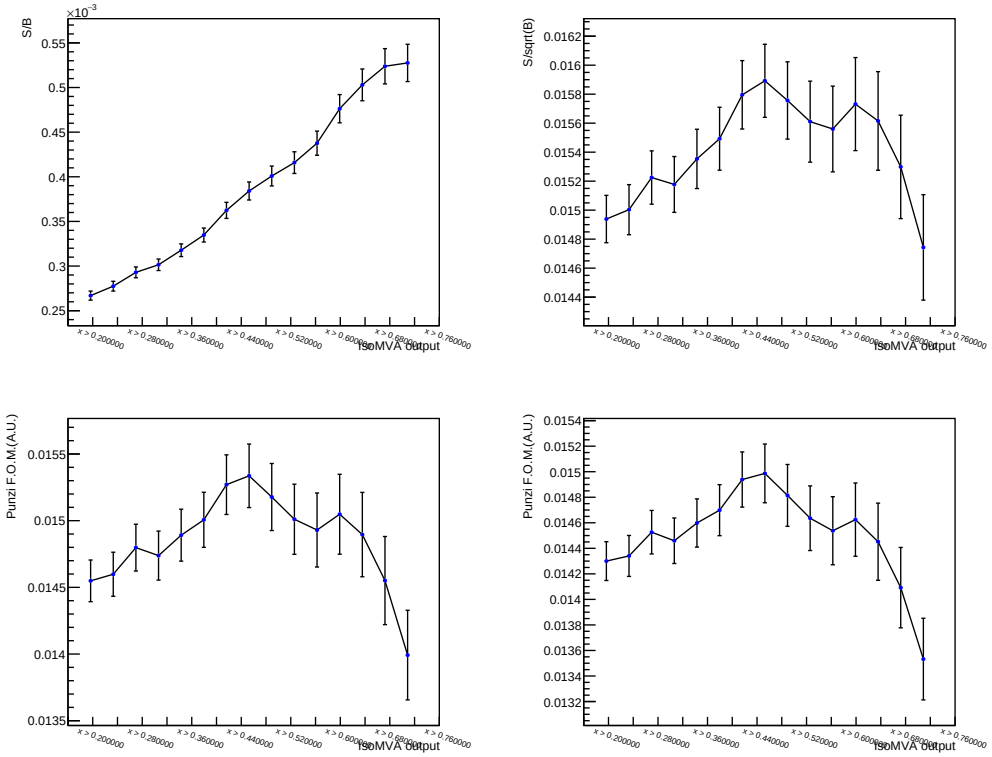

Figure 4.4.15: Figure of merit distributions for $\frac{S}{B}$ (up-left), $\frac{S}{\sqrt{B}}$ (up-right), $\frac{S}{\frac{3}{2}+\sqrt{B}}$ (down-left, adopted for the cut optimization) and $\frac{S}{\frac{5}{2}+\sqrt{B}}$ (down-right) scanning the output of the isolation classifier in the region [0.2, 0.8].

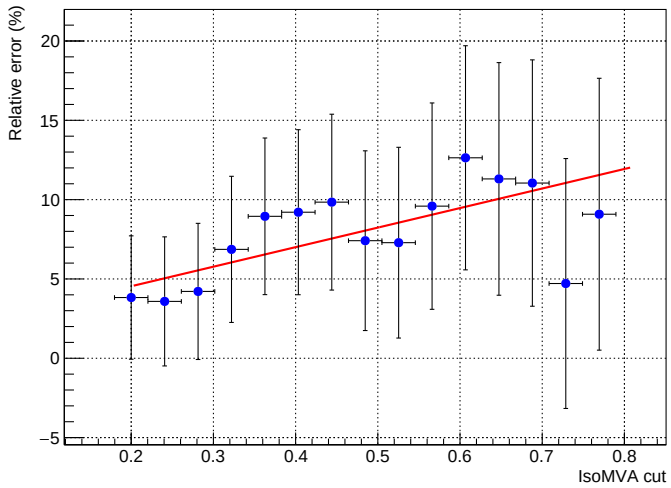

Figure 4.4.16: Correction factor $\frac{\Delta N}{N}$, evaluated as reported in Eq. 4.4.3, as function of the isolation classifier output. A linear fit on the correction factors has been performed in the region [0.2, 0.8] of the output classifier, and values are extrapolated and applied to OS data sidebands mass fit to estimate background yield.

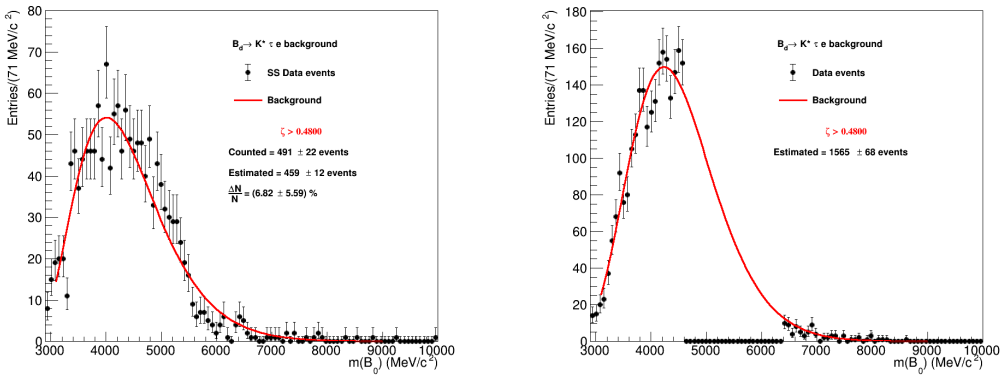

Figure 4.4.17: On the left: SS data fit for the optimal classifier output cut. On the right: OS data sidebands fit for the optimal classifier output cut. The background yields in the signal region are extracted from the extended likelihood fit on the OS data. The evaluation of the figure of merit optimization is also done by correcting the estimated number with the value of the SS correction extracted from the fit in the classifier output region [0.2, 0.8].

4.4.6 Tau multivariate selection

The multivariate selection used to distinguish τ leptons from charmed mesons is the same as the one adopted for the lepton flavour violation search $B^0 \to K^*\tau\mu$ [87]. This is possible because the classifier depends only on the kinematics and properties of the τ itself in the rest frame of the three-pions system. The main feature of the τ decay under study is that they first decay through an a_1 resonance, which decays into a ρ and a π. This shows up in the typical momenta distributions of the lepton children and the invariant mass of the neutral pion combination pairs, calculated in the τ reference frame. The classifier uses the minima and the maxima of momenta as input variables for the τ decay products and the minima and maxima of the masses of $\pi^+\pi^-$. The input variables used are listed in Table 4.4.6, and their distributions for $B^0 \to K^*\tau e$ MC simulation and OS sidebands events surviving up to this stage of the selection are represented in Figure 4.4.19. The classifier adopted was trained with the kFolding method in the $B^0 \to K^*\tau\mu$ analysis. Since it is applied to a dataset different from the one used during the training, it is possible to arbitrarily choose the set of weights to apply for the evaluation phase. Figure 4.4.18 shows the output distribution of the classifier once applied to OS data sidebands, SS data and truth-matched simulation surviving the selection up to this stage. The classifier output dependency with the mass is checked, as shown in Figure K.3.1. No strong correlation is found.

Name	Input variables
`minM`	Minimum invariant mass of the neutral pion combination pairs
`maxM`	Maximum invariant mass of the neutral pion combination pairs
`minP`	Minimum pion momentum
`maxP`	Maximum pion momentum

Table 4.4.6: List of kinematics variables related to the τ properties adopted as input for the MVA classifier trained in [87]. All the quantities are evaluated in the rest frame of the three pions system.

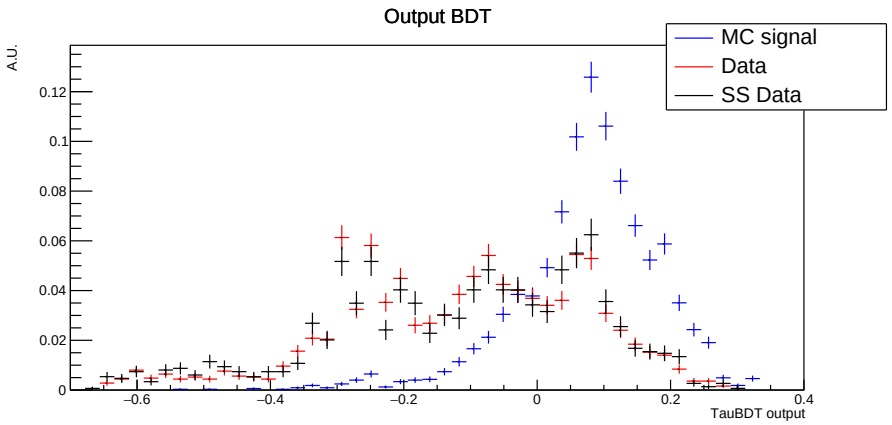

Figure 4.4.18: τ BDT output for MC simulation (blue), OS data sidebands (red) and SS data (black).

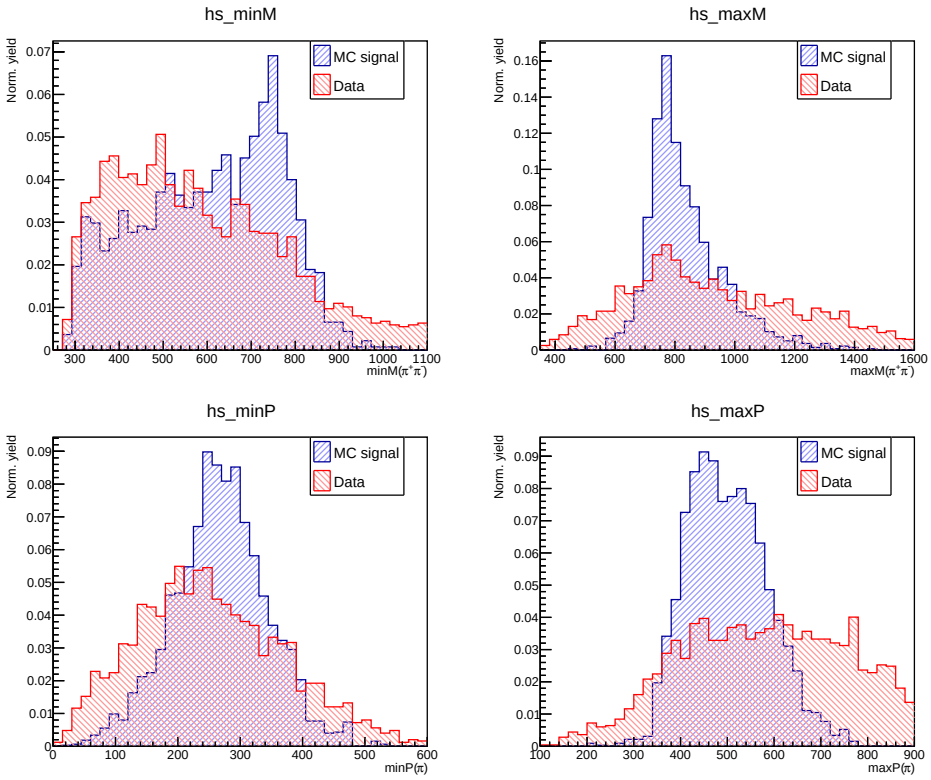

Figure 4.4.19: Signal (blue) and OS data sidebands (red) distributions of τ classifier input variables superimposed.

Optimization on tau BDT cut

The optimization of the cut on the classifier output follows a procedure similar to the previous ones. The signal yield is extracted by counting MC simulation truth-matched candidates in the signal region passing the previous selections, and the signal efficiency is derived from this number. The background yield is obtained by estimating the number of yields in the signal region by fitting OS data sidebands events surviving up to this selection stage in [3100, 9000] MeV/c^2 B^0 mass range (see Figure 4.4.20). The fit model adopted is the Gamma law. Figures of merits are evaluated according to Eq. 4.4.2 and reported in Figure 4.4.21. Fits on SS candidates for different output values are more unstable due to a lack of statistics at this selection stage. Therefore, figures of merits are evaluated without applying any correction to the yield estimated from the SS data fit. The optimization procedure leads to the cut `TauBDT` > -0.005.

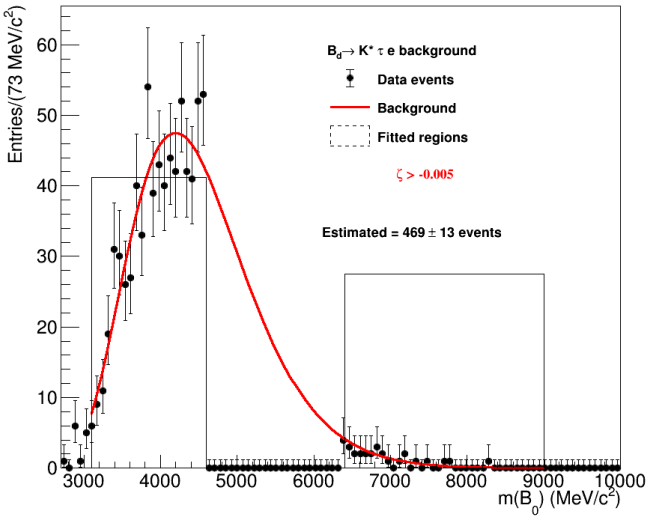

Figure 4.4.20: OS data sidebands fit for the optimal classifier output cut. The background yields in the signal region are extracted from the extended likelihood fit.

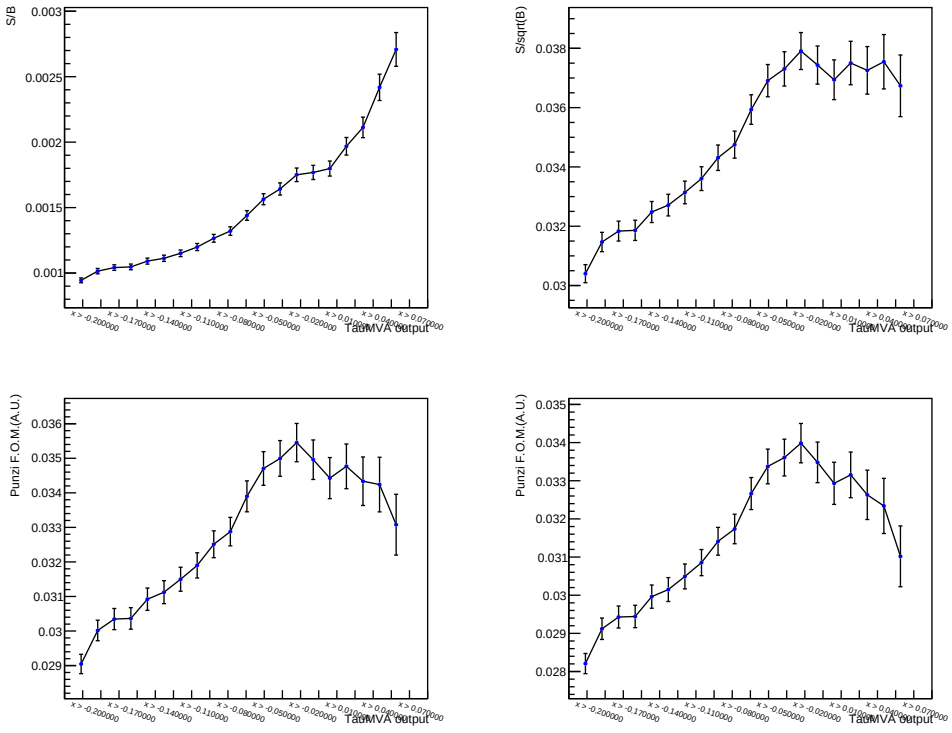

Figure 4.4.21: Figure of merit distributions for $\frac{S}{B}$ (up-left), $\frac{S}{\sqrt{B}}$ (up-right), $\frac{S}{\frac{3}{2}+\sqrt{B}}$ (down-left, adopted for the cut optimization) and $\frac{S}{\frac{5}{2}+\sqrt{B}}$ (down-right) scanning the output of the τ classifier in a region [-0.2, 0.1].

4.4.7 Particle identification requirements

On top of the selection performed by the multivariate classifiers described previously, requirements based on particle identification are applied. The selection is optimized via a simultaneous three-dimensional scan of cuts on the neural network variables `ProbNN`π, `ProbNNk` and `ProbNNe` related to the final state particles and evaluating the Punzi figure of merit in Eq. 4.4.2 with $\sigma = 3$ for each set of cuts. Distributions of the three variables are reported in Figure 4.4.22 for the electron and the kaon and the pion coming from the K^{*0} decay. The signal is extracted from the truth-matched MC candidates surviving the selection up to this point. The background yield is evaluated from the number of events in the blinded region extracted from the fit on OS data sidebands in the optimal point of `TauBDT`, as described in Section 4.4.6, scaled by the SS data event efficiency in the signal region. This procedure is adopted because the fit on the OS data sidebands shows instabilities due to a lack of statistics in the dataset when increasing the number of scanned values of cut combinations among the three variables. The two-dimensional distribution projections for sets of PID cuts with a figure of merit compatible at 1σ level with the optimal one are represented in Figure 4.4.24. Figure 4.4.23 shows the distributions of the values of the Punzi figure of merit within 1σ when projecting on each variable. The distributions are also given, fixing the other two variables' cuts to the optimal values. A wide range of possible sets of PID requirements gives analogous results, so there is some arbitrariness in the choice of the set of cuts, particularly for the `ProbNN`π variable. The working point chosen corresponds to the following cuts: `ProbNNe` > 0.125, `ProbNNk` > 0.82 and `ProbNN`$\pi >$ 0.725. The requirement on pion identification is applied to all the pions in the final state. The optimization procedure has been performed from the simulation without any corrections, reweightings, or resamplings to consider any data-MC difference. However, the efficiency will be evaluated data-driven, as discussed in Section 4.6.3.

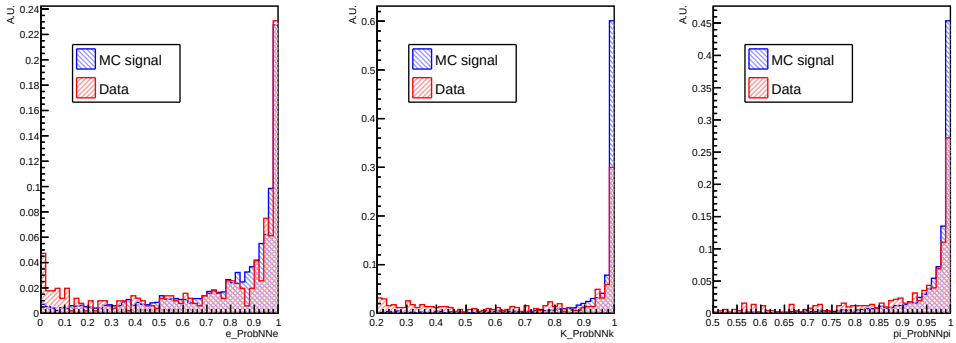

Figure 4.4.22: Distributions of NN-based particle identification variables for final states for MC simulation (blue) and OS data sidebands (red). Distributions refer to the electron (left), kaon (center), and pion (right) from the K^{*0} decay.

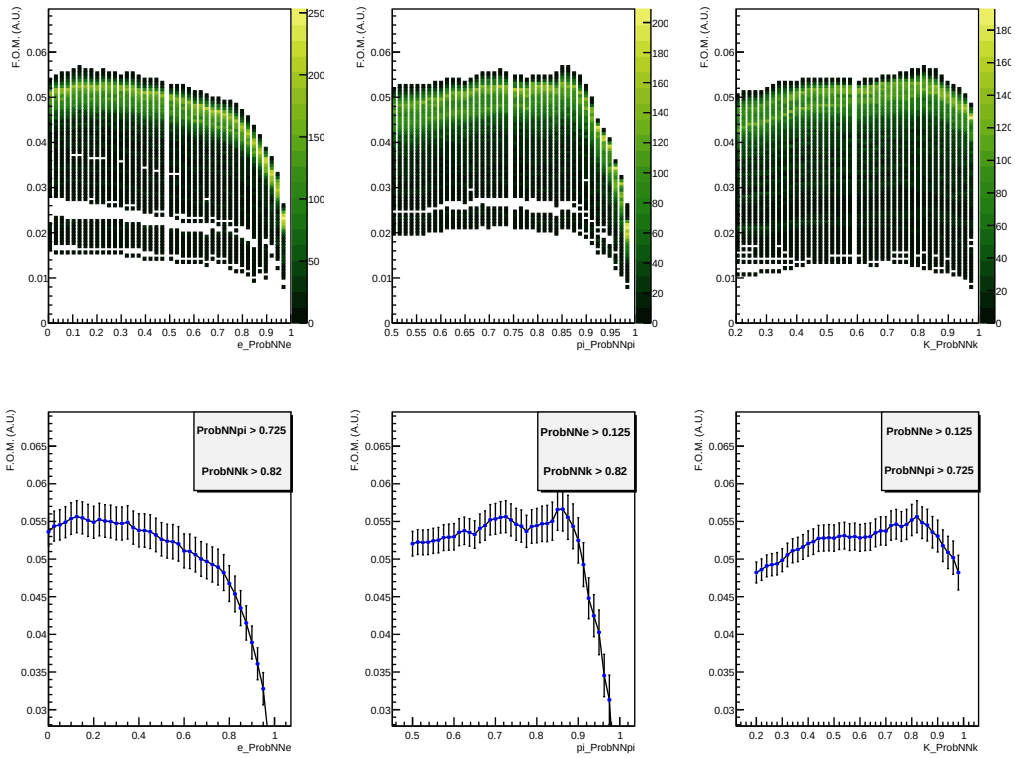

Figure 4.4.23: On the top: Projection of the Punzi figure of merit values ($\sigma = 3$), compatible with the best value within 1σ, on one PID variable's axis for electrons (left), pions (center), and kaons (right). On the bottom: Same distribution, fixing the other two cuts to the chosen optimal values.

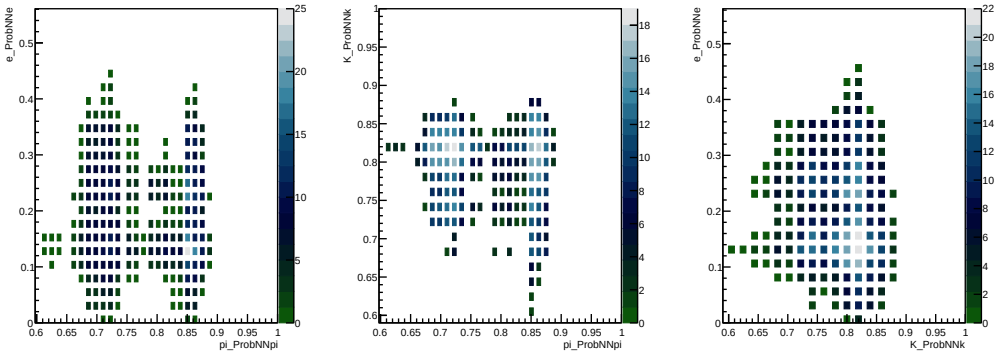

Figure 4.4.24: 2-dimensional projection on sets of two PID variables of the figure of merit values compatible with 1 σ with the optimal figure of merit value

4.4.8 Selection on the K^{*0} mass

Looking at the intermediate state mass distributions at this selection stage, it turns out that the K^{*0} meson mass still has a non-negligible background rejection power. A cut has been applied to remove events outside the range [842, 970] MeV/c^2. The mass window has been chosen to perform an optimization of the Punzi figure of merit

with $\sigma = 3$ ($\sigma = 0$ and $\sigma = 5$ are also tested and reported in Figure 4.4.26, leading to compatible results) by scanning over a set of one hundred possible simultaneous left and right side cuts. The final choice is quite arbitrary, particularly for the right cut, where several configurations give comparable values for the figures of merit. The signal yield is evaluated from MC truth-matched events for optimization. Instead, the background yield is extracted from the signal region, performing an extended maximum likelihood fit on the B^0 mass on OS data sidebands. In both cases, the optimization procedure is conducted using events surviving up to this selection stage. Distributions of the K^{*0} mass for OS data and MC truth-matched events are shown in Figure 4.4.25 before and after the selection.

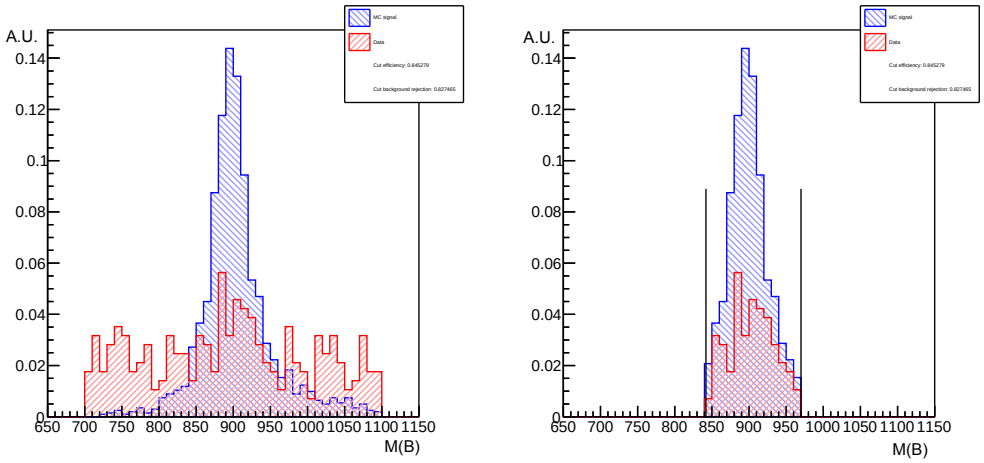

Figure 4.4.25: K^{*0} mass distributions for OS data (red) and MC simulation (blue) superimposed before (left) and after (right) the optimized cut.

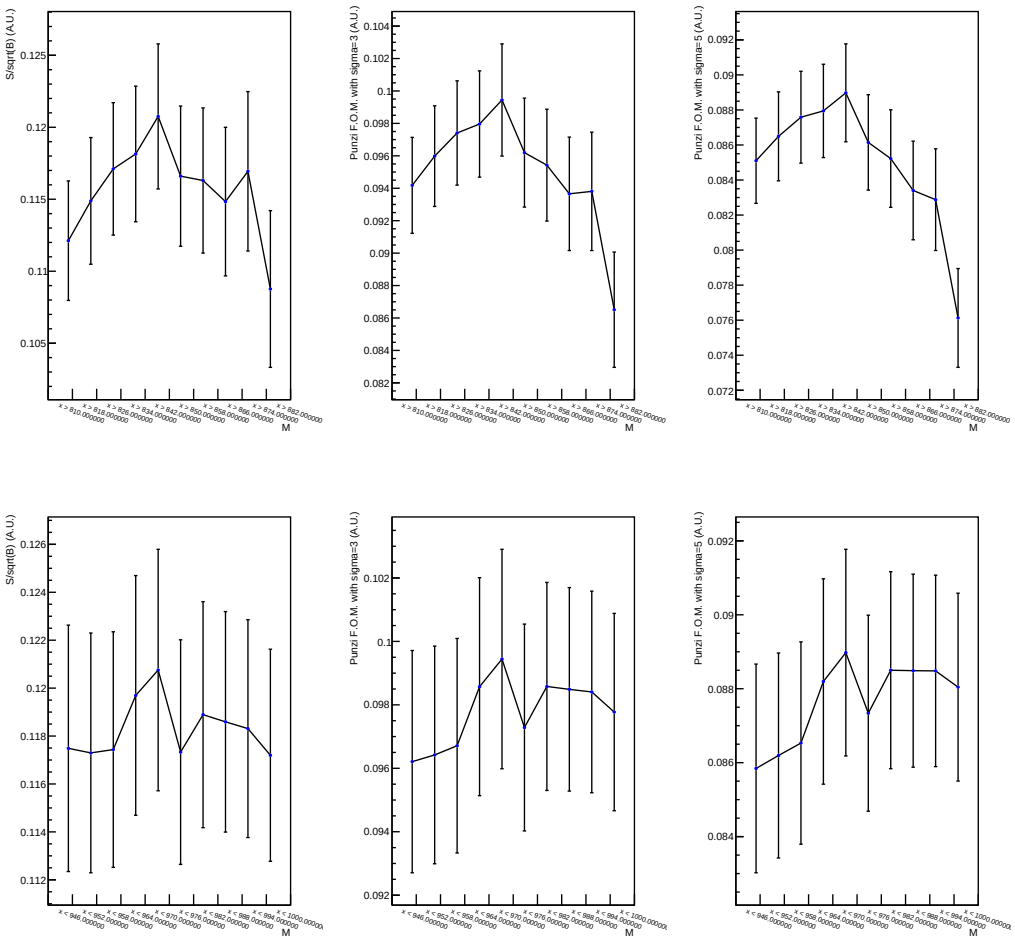

Figure 4.4.26: Distributions of Punzi figure of merit for $\sigma = 0$ (left), $\sigma = 3$ (centre) and $\sigma = 5$ (right), on the top/bottom fixing the upper/inferior cut to the optimal one.

4.4.9 Selection on flight distance

Intermediate charmed state mesons or other physics background sources could survive the selection chain up to this stage. Additional requirements are imposed in the next Section to cut off dangerous physics background that decays semileptonically. Before doing that, we can exploit the τ flight distance (FD) and its significance to understand and check whether it is possible to reduce these contributions.

Looking at the background from the OS data sample with all the selections applied, except for the anti-combinatorial classifier (see Section 4.4.4), which is instead reverted ($\texttt{ACBDT} < 0.9775$) in the signal region, one obtains the distributions of the logarithm of τ flight distance and its significance shown in red in Figure 4.4.27, compared to the signal distributions in blue. The events are separated between OC and SC final states. The distributions of the flight distance and its significance as a function of the output of the anti-combinatorial classifier and the mass of the B candidates are

shown in Appendix L. The distributions are also produced for SS data.

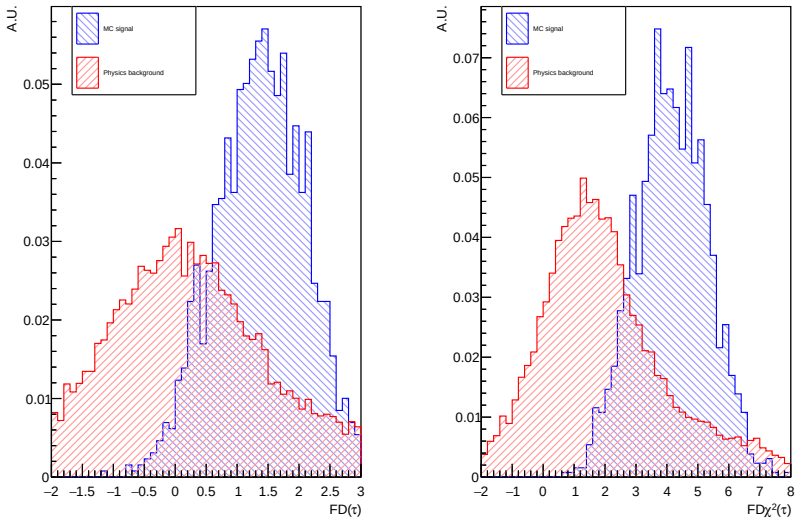

Figure 4.4.27: Distributions of the logarithm of the τ flight distance (left) and its significance (right) superimposed for signal (blue) and background (red). The proxy for the signal is truth-matched events surviving to the selection. The proxy adopted for the background is OS events selected by reverting the anti-combinatorial cut and applying the other selection steps.

In the selected background samples, these variables have discriminating power. However, when looking at data surviving the nominal selection chain, the flight distance and significance show no residual discrimination power (see Figure 4.4.28). Nevertheless, to be conservative, a very efficient cut is applied to exclude potential backgrounds in the signal-blinded region: $log(FD) > -0.5$ and $log(FD\chi^2) > 1.5$. The effect of the cut is represented in Figure 4.4.29 for signal MC simulation, OS data and background region in the OC and SC cases.
In addition, this cut reduces background components in the control regions that will be used for the background shape parameterization in the fit, as discussed in Section 4.7.2. In fact, these control samples are also extracted by reverting the `ACBDT` cut.

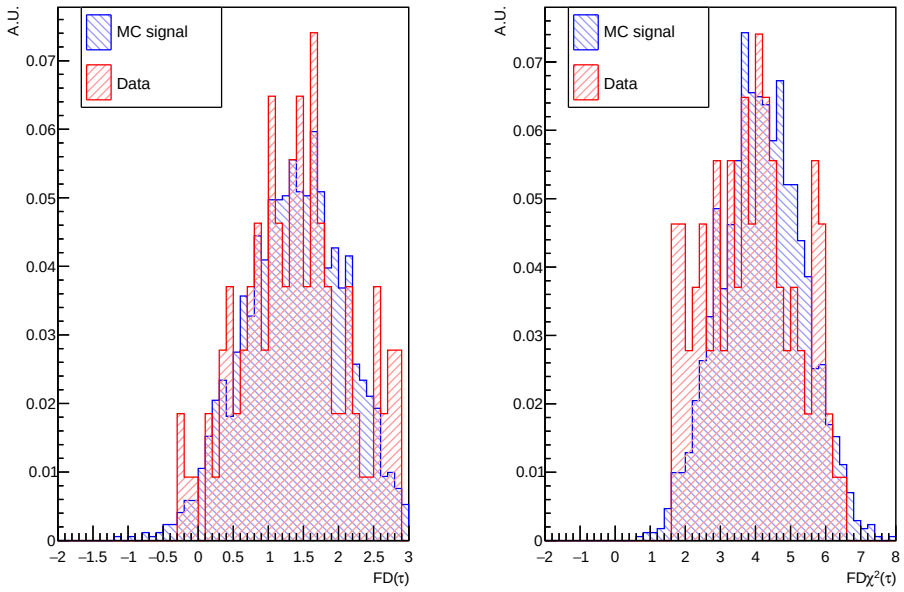

Figure 4.4.28: Distributions of the logarithm of the τ flight distance (left) and its significance (right) superimposed for signal (blue) and OS data sidebands surviving to the selection chain (red).

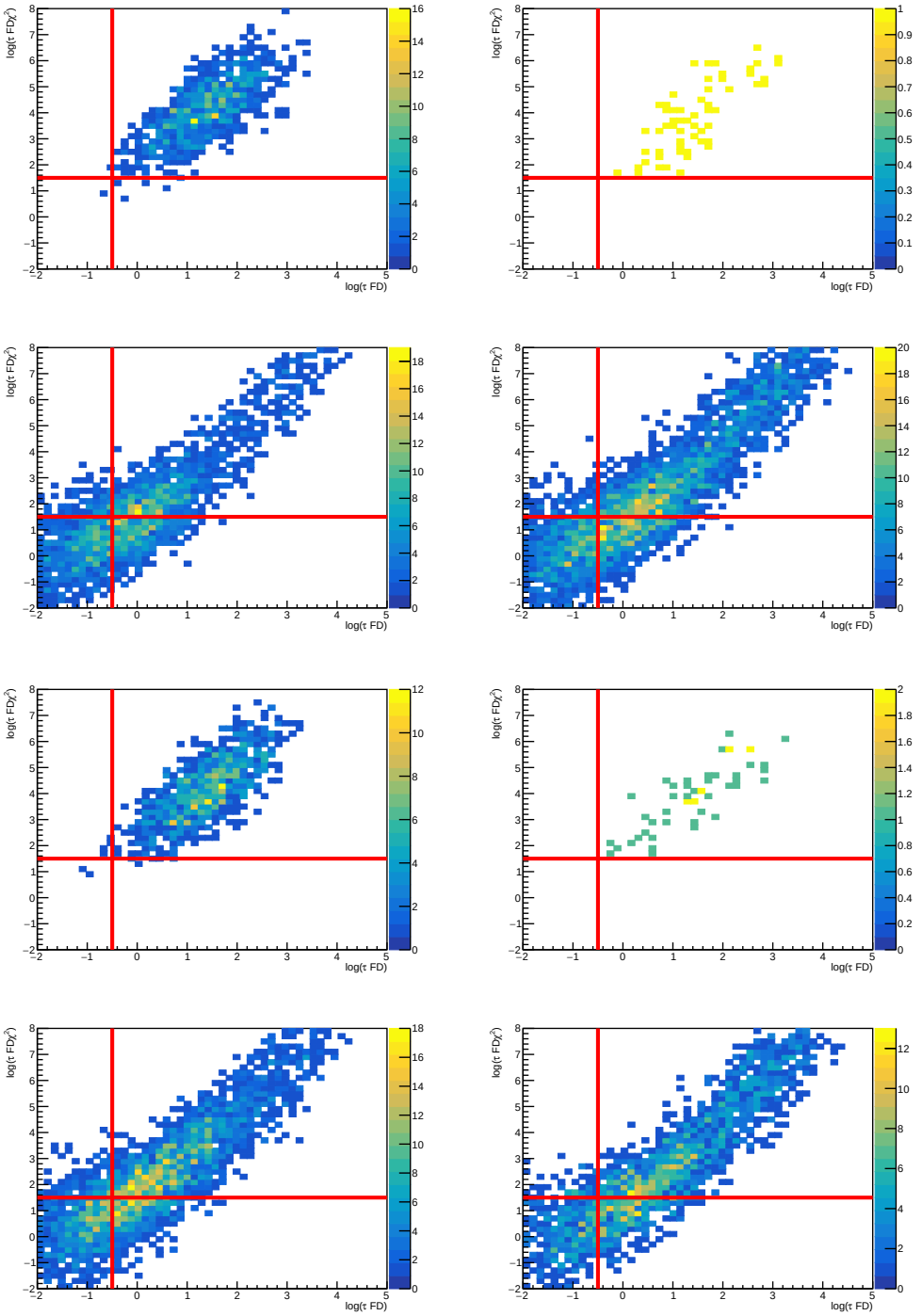

Figure 4.4.29: Cuts for flight distance and its significance applied to MC truth simulation (top-left frame), OS data sidebands (top-right), OS data in the signal region with reverted anti-combinatorial cut (bottom-left) and SS (bottom-right). The first four frames refer to the OC case ($B^0 \to K^{*0}\tau^+e^-$), while the last four to the SC case ($B^0 \to K^{*0}\tau^-e^+$)

4.4.10 Mass vetoes

Dangerous physics backgrounds are removed by applying vetoes to the invariant mass combinations of the particles in the final state. In particular, this allows the removal of contributions from charmed mesons that the previous selection steps have not yet suppressed. Because of different possible physics background contributions, separate vetoes are applied to SC and OC candidates, following the convention introduced in Section 4.1. Looking at the distribution of the invariant masses of combinations of two, three, four or five particles in the final state, also analyzed at different stages of the selection, it turns out that the three or four-body invariant mass distributions have some peaking contributions at values corresponding to the masses of some charmed mesons (shown in Appendix M). Possible D^0 and D^+ candidates are therefore excluded by applying a 60 MeV/c^2 cut around the PDG value of the corresponding charmed meson. As a consequence, the following decay channels are removed by these vetoes:

- semileptonic decays $B^0 \to DXe\nu_e$, including possible intermediate resonances such as $B \to D^*(\to D^0\pi)e\nu_e$, with $D^0 \to K\pi\pi\pi$ for both charge combinations.
- other decays involving $D^{\pm}(\to K^{\mp}\pi^{\pm}\pi^{\pm})$ intermediate meson, such as semileptonic $B^0 \to D^-\tau^+\nu_\tau$ or $B \to D^-\pi^+\pi^-e^+\nu_e$

Additional checks have been performed supposing single or double misidentification of particles in the final state, with proper mass hypothesis replacement. The following cases have been investigated:

- single misidentification of pion or kaon to electron, with $e \to \pi$ or $e \to K$ mass hypothesis replacement, assuming a full-hadronic final state combination;
- kaon to pion and electron to kaon or electron to pion double misidentification, with $K \to \pi$ and $e \to K$ or $e \to \pi$ mass hypothesis replacement, having full hadronic final states again;
- kaon and electron double misidentification, with $K \to e$ and $e \to K$ mass hypothesis replacement, reproducing the same final states as in the signal case.

Table 4.4.7 collects the list of vetoes applied. The following convention is adopted to distinguish the pions reconstructed in the final state: π stands for the pion from the K^{*0} decay; π_1, π_2 and π_3 are pions from the τ lepton decay such that π_1 and π_3 have the same charge and π_2 has the opposite charge.

Semileptonic $D \to Ke\nu_e$ decays

Particularly dangerous physics background are B decays with an intermediate D meson decaying into $Ke\nu_e$, such as $B^0 \to D^{*-}\tau^+\nu$, with $D^* \to \bar{D}^0\pi$, $\bar{D}^0 \to K^+e^-\nu_e$ and

Sample	Combination	Cut
SC	$K\tau$ Fig. M.2.6) $K^*\pi_2\pi_3$ (Fig. M.2.4) $K^*\pi_1\pi_2$ (Fig. M.2.5)	$\lvert M - M_{PDG}(D^0)\rvert \leq 60$ [MeV/c^2]
	$K^*\pi_1$ (Fig. M.2.1) $K^*\pi_3$ (Fig. M.2.2) $K\pi_1\pi_3$ (Fig. M.2.3)	$\lvert M - M_{PDG}(D^+)\rvert \leq 60$ [MeV/c^2]
OC	$K^*\pi_2\pi_3$ (Fig. M.1.4) $K^*\pi_1\pi_2$ (Fig. M.1.5)	$\lvert M - M_{PDG}(D^0)\rvert \leq 60$ [MeV]
	$K^*\pi_2$ (Fig. M.1.1) $K^*(\pi \to e)$ (Fig. M.1.2) $K\pi_2(\pi \to e)$ (Fig. M.1.3)	$\lvert M - M_{PDG}(D^+)\rvert \leq 60$ [MeV]

Table 4.4.7: Vetoes applied to SC and OC samples.

$\tau^+ \to \pi^+\pi^-\pi^+\nu$. These backgrounds do not peak in the invariant mass distribution of the kaon and electron due to the missing energy carried by the neutrino. Therefore, we cannot identify an efficient veto for these semileptonic decays. However, the behaviour of events with respect to the τ flight distance and its significance can provide insights. Distributions of the Ke invariant mass as a function of the flight distance and its significance are used to characterize these physics backgrounds (see Figure 4.4.30). Analogous distributions for the hadronic channels are reported in Appendix L.0.1. The cuts on $log(FD) > -0.5$ and $log(FD\chi^2) > 1.5$ help to reduce these backgrounds, even though they're not completely removed. The remaining component is assumed to be absorbed in the background shape parameterization, as discussed in Section 4.7.2.

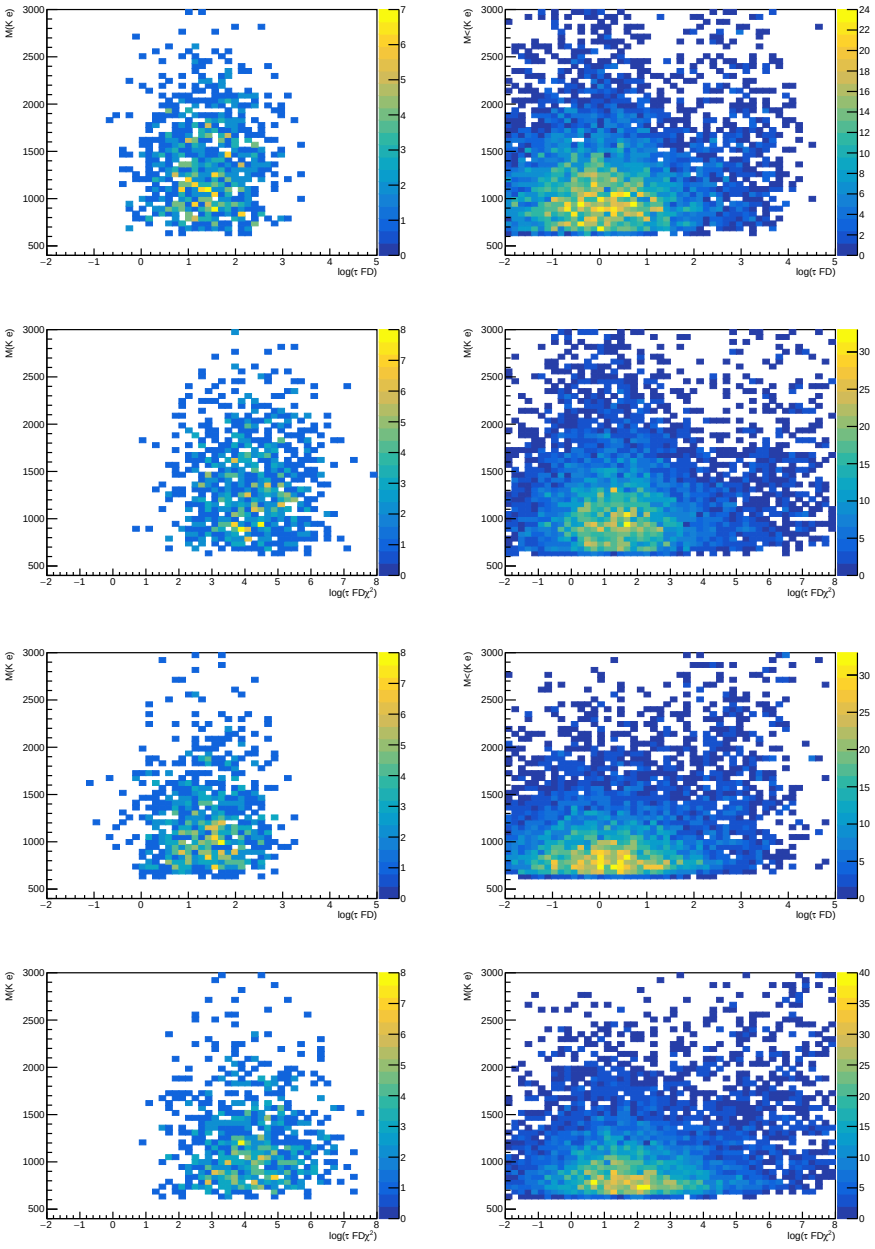

Figure 4.4.30: Invariant mass of Ke combination as a function of the logarithm of τ flight distance (top frames) and its significance (bottom frames) for signal MC (left) and background control region extracted from the OS data reverting the anti-combinatorial cut (right). The first four frames refer to the OC sample, while the last four refer to the SC sample.

4.4.11 Cut flow

The impact of the whole selection chain on the B^0 mass for MC signal truth matched events, OS data and SS data is shown in Figures 4.4.31, 4.4.32 and 4.4.33, respectively. Events are divided according to the charge combination of kaons and electrons in the final states. Figures 4.4.34 and 4.4.35 show the MC efficiency and background rejection divided per charge combinations. Both signal efficiency and background

acceptance for a given cut are defined as the ratio between the yield passing that selection and the yield surviving the previous one. Signal efficiency is evaluated on truth-matched simulation, while background acceptance is based on OS data. Apart from the mass vetoes, the entire selection chain is performed without distinguishing between the two charges subset. The similar performances obtained at different stages confirm the assumption that training and optimizations done cumulatively do not lead to a sub-optimal selection.

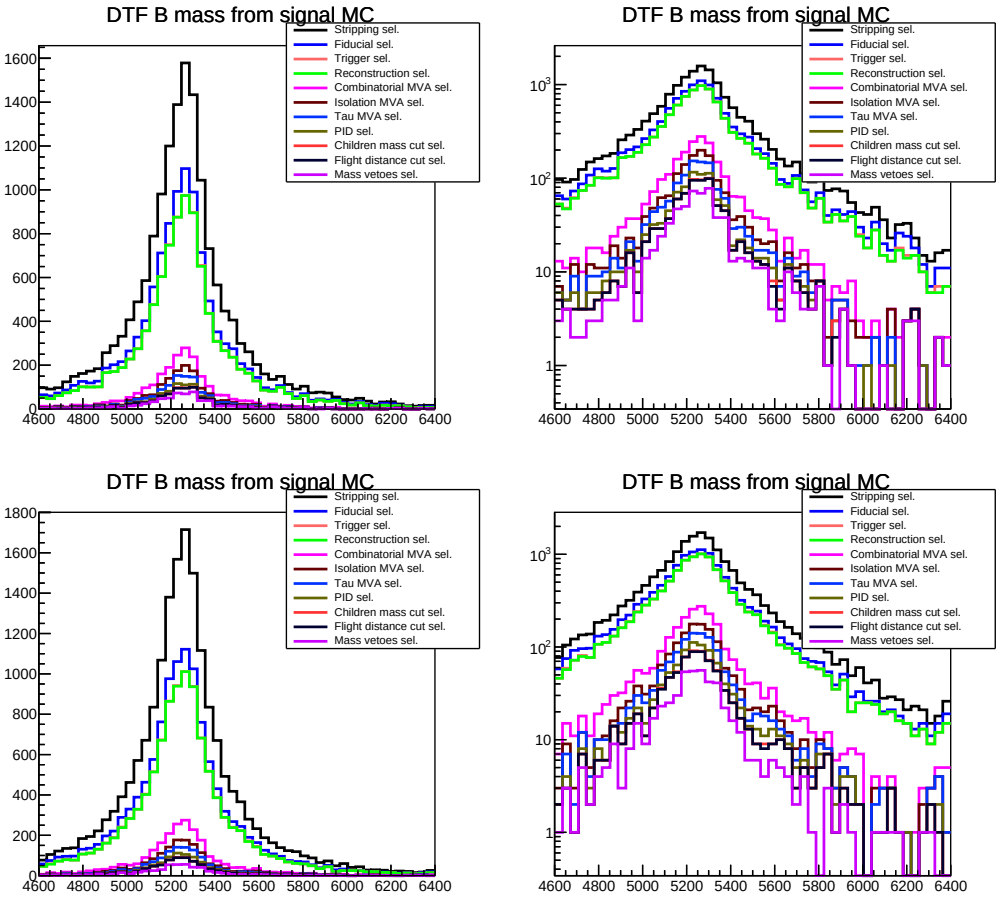

Figure 4.4.31: On the left: mass distribution evolution with the selection applied, starting from MC signal events after stripping until the last selection step as described in Section 4.4. On the right is a representation of the y-axis logarithmic scale. The first (second) row refers to the OC $B^0 \to K^{*0}\tau^+e^-$ (SC $B^0 \to K^{*0}\tau^-e^+$) case.

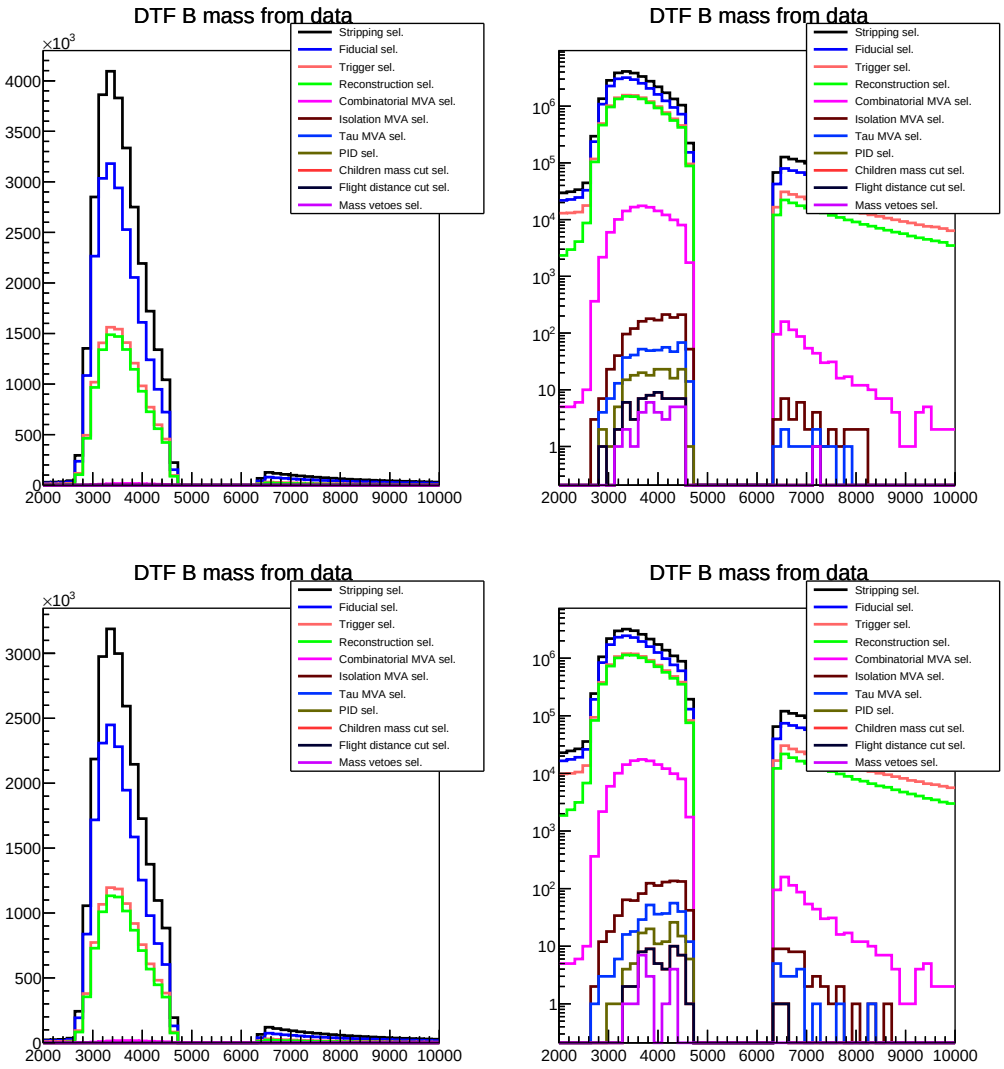

Figure 4.4.32: On the left: mass distribution evolution with the selection applied, starting from OS data events after stripping until the last selection step as described in Section 4.4. On the right is a representation of the y-axis logarithmic scale. The first (second) row refers to the OC $B^0 \to K^{*0}\tau^+e^-$ (SC $B^0 \to K^{*0}\tau^-e^+$) case.

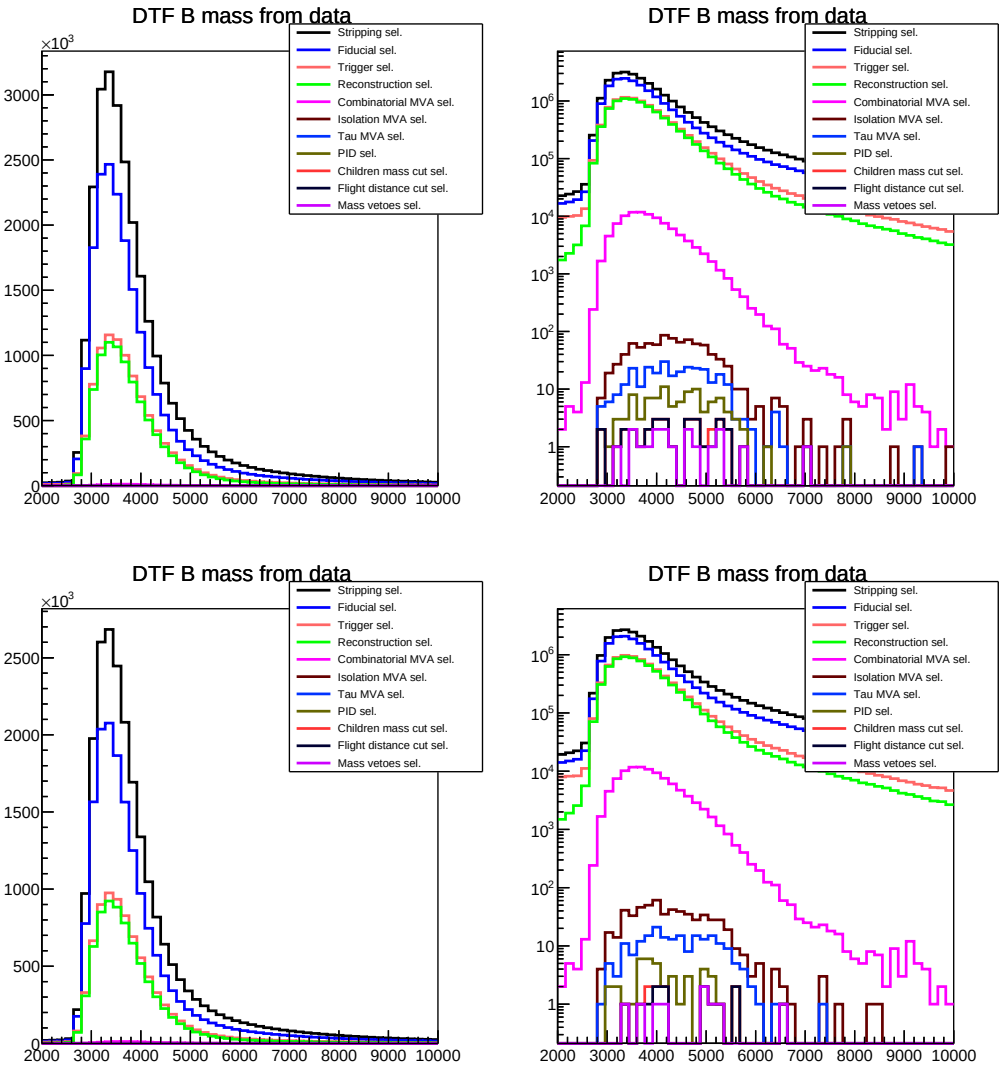

Figure 4.4.33: On the left: mass distribution evolution with the selection applied, starting from SS data events after stripping until the last selection step as described in Section 4.4. On the right is a representation of the y-axis logarithmic scale. The first (second) row refers to the OC $B^0 \to K^{*0}\tau^- e^-$ (SC $B^0 \to K^{*0}\tau^+ e^+$) case.

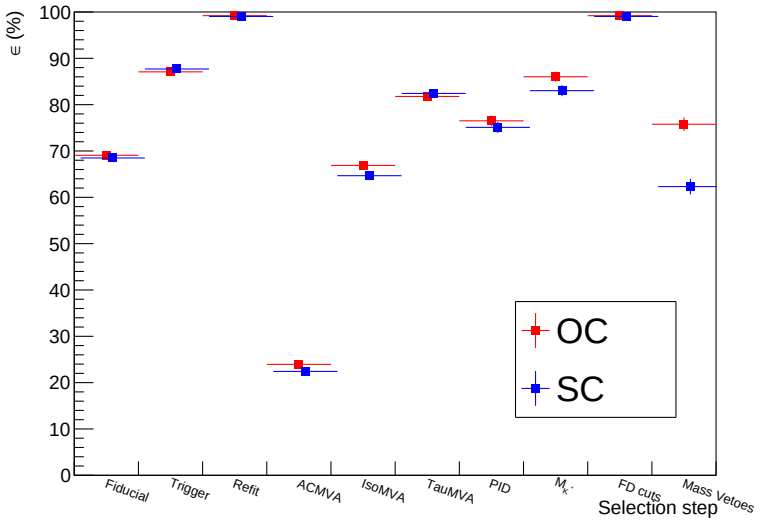

Figure 4.4.34: Efficiencies at various stages of the selection evaluated on truth-matched MC events for OC and SC combinations.

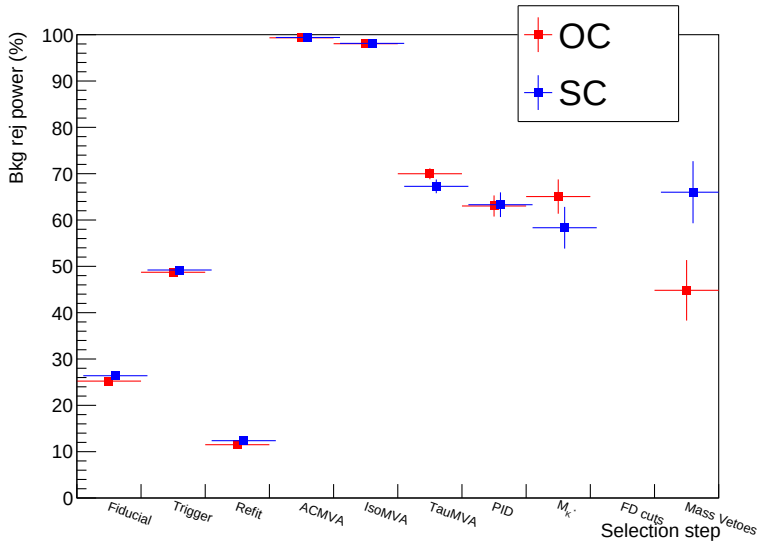

Figure 4.4.35: Background rejection at various stages of the selection evaluated on OS data events for OC and SC combinations.

4.4.12 Cross-checks at the end of the selection

At the end of the entire selection chain, we check the number of events for which more than one B^0 candidate survives. No events have multiple candidates. Another check involves looking for possible peaking background through SS events passing the entire selection chain. It results that no peaking background is present in the signal region, as shown by the distribution in Figure 4.4.36. Finally, the full selection chain is applied to some possible simulated exclusive background channels. Upper limits in the yield expected for those channels for 2016, 2017, and 2018 years of data taking are shown in Appendix N.

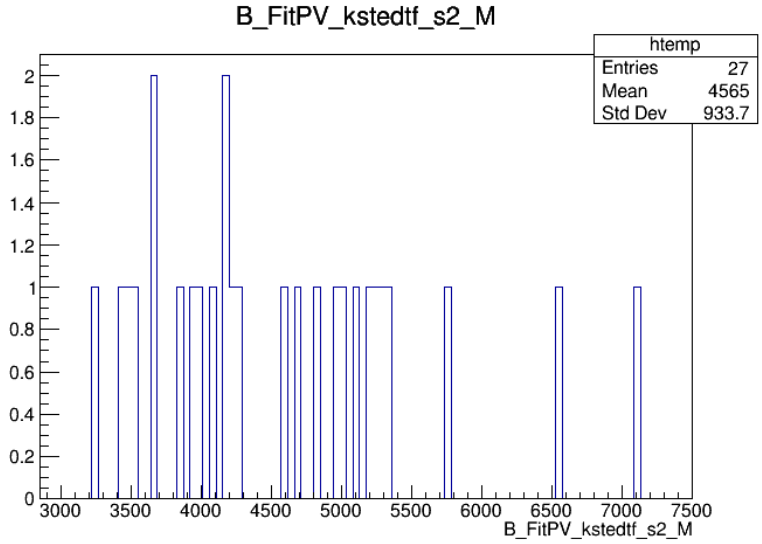

Figure 4.4.36: Distribution of same-sign events passing the signal region. No evident peaking background is present in the signal region.

4.5 Normalization channel

The decay $B \to D^- D_s^+$ with $D^- \to K^+\pi^-\pi^-$ and $D_s^+ \to K^+K^-\pi^+$ is chosen both as a normalization channel and control sample for the validation of the MC description of the variables used in the selection, having the same number of particles in the final state as the $B \to K^*\tau e$ decay and a similar topology. The selection applied to the normalization mode follows the following steps:

1. Preliminary cuts, including Stripping, fiducial, and trigger selection (Section 4.5.1);

2. Particle identification and intermediate states masses requirements (Section 4.5.2).

The yields are then extracted by a fit to the B^0 candidate invariant mass (Section 4.5.4).

4.5.1 Preliminary selection

The stripping line used to select $B \to D^- D_s^+$ candidates is described in Section 4.4.1, and the requirements applied are collected in Table I.0.4. The trigger lines differ from the signal one. Because of the absence of electrons in the final state, the electron trigger category is not used for the selection of the normalization channel. The L0 selection is based on `L0HadronTOS` or mutually exclusive `L0HadronTIS`, hence the totality of `L0Hadron` selected events. The software trigger lines selected are collected in Table 4.5.1. Finally, Table 4.5.2 shows the fiducial preselection cuts applied.

L0 Trigger	HLT1	HLT2
(L0HadronDecision_TOS & L0HadronCalibration) | (L0HadronDecision_TIS & !L0HadronDecision_TOS)	HLT1TrackMVADecision_TOS | HLT1TwoTrackMVADecision_TOS	HLT2Topo(2|3|4)BodyDecision_TOS

Table 4.5.1: Hardware and software trigger lines applied to the normalization sample. The MC has been calibrated with data using corrections to the calorimeter thresholds explained in Section 4.4.3.

Particle	**Fiducial cut**
All final states	$2 < \eta < 4.9$ $p < 110$ GeV $hasRich$ $\text{Region}_{HCAL} \geq 0$

Table 4.5.2: Fiducial cuts applied to the final state particles of normalization sample.

4.5.2 Particle identification and mass requirements

The same particle identification requirements discussed in Section 4.4.7 are applied to the MC simulation and data of the normalization channel. Since the final state particles are all hadrons, the PID cuts used are the following: `ProbNNk` > 0.82 and `ProbNN` $\pi > 0.725$. Given the precision for reconstructing intermediate states of the normalization channel, a mass requirement has been imposed on the D and D_s candidates: their mass should be within a 40 MeV window centred around the PDG mass values [206]. Distributions of the particle identification variables and of the D and D_s candidates' masses, both for truth-matched MC events and data, are represented in Figure 4.5.1 and Figure 4.5.2, respectively.

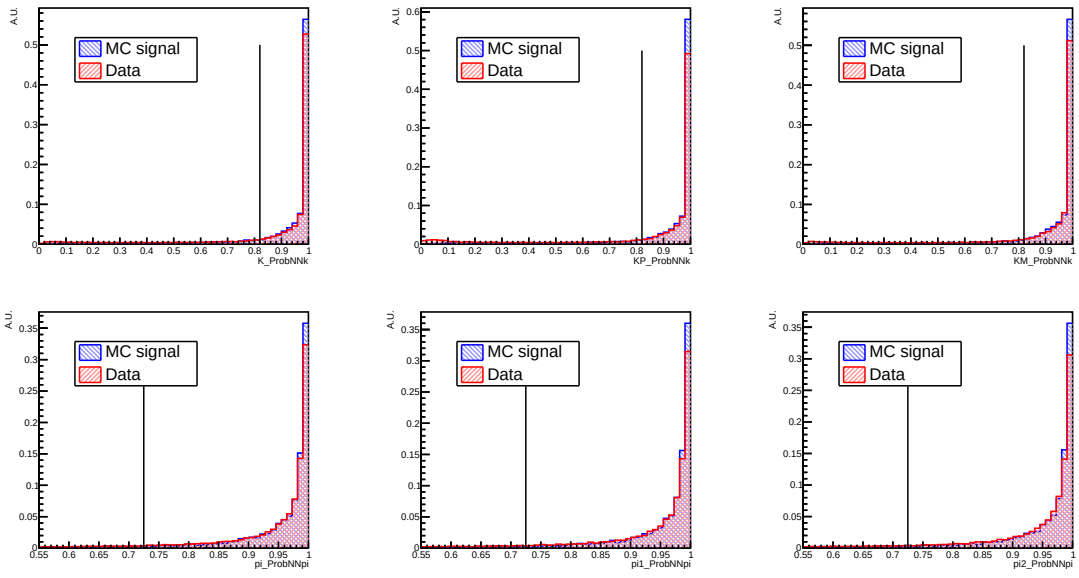

Figure 4.5.1: Distributions of particle identification variables for kaons (first row) and pions (second row) as final states of MC simulation ($B \to D^- D_s^+$) and data (red) for normalization channel. Solid lines represent the cut selected in Section 4.4.7. As convention K, $pi1$ and $pi2$ refer to the decay products of $D^- \to K^+\pi^-\pi^-$, while KP, KM and pi refer to the decay products of $D_s^+ \to K^+K^-\pi^+$.

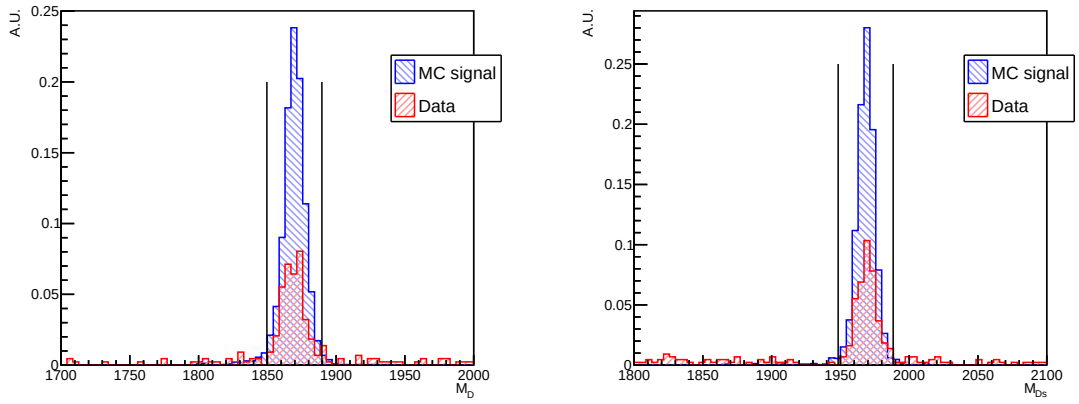

Figure 4.5.2: D (left) and D_s (right) mesons mass distributions for data (red) and MC simulation (blue) superimposed for normalization channel. Solid lines represent the window cut of 40 MeV centered around the PDG masses.

4.5.3 Cut flow for the normalization channel

The impact of the selection on truth-matched MC events and data is shown in Figure 4.5.3 and Figure 4.5.4.

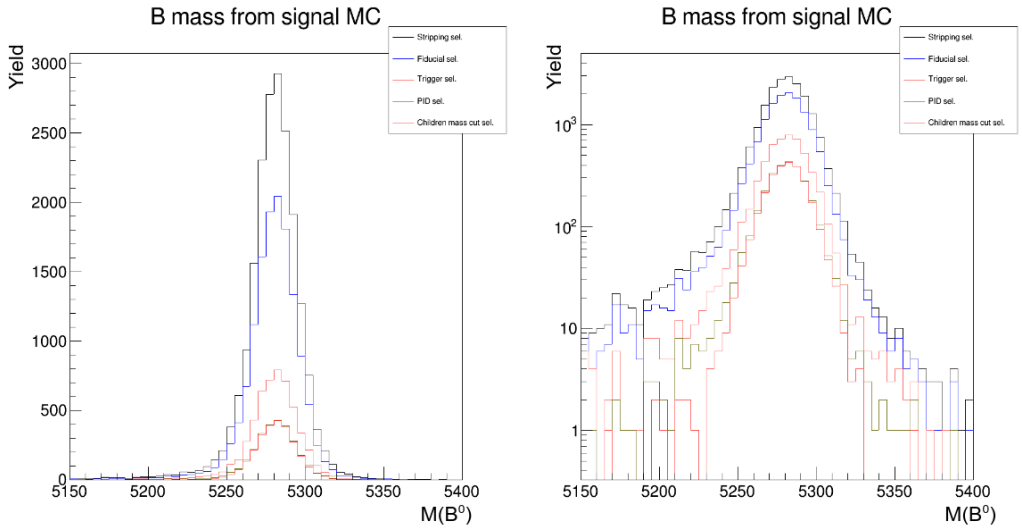

Figure 4.5.3: On the left: mass distribution evolution with the selection applied, starting from Monte-Carlo signal events of the normalization channel after stripping until the last step of the selection. On the right is a representation of the y-axis logarithmic scale.

4.5.4 Fit to the normalization channel

After the selection, a fit using a Gaussian model for the signal and an exponential function for the background is performed to the B^0 candidate mass in the range [5200,5400] MeV/c^2. The range is wide enough to include our B candidates and

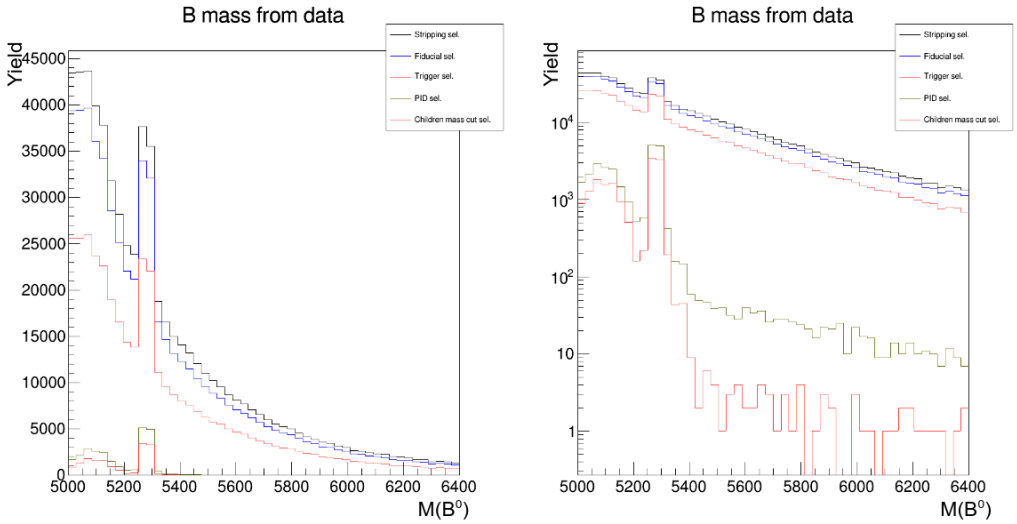

Figure 4.5.4: On the left: mass distribution evolution with the selection applied, starting from data events of the normalization channel after stripping until the last step of the selection. On the right is a representation of the y-axis logarithmic scale.

Year	Parameters	MC simulation	Data
2016	μ of Gaussian	5280.8 ± 0.4	5279.2 ± 0.3
	σ of Gaussian	12.7 ± 0.3	13.4 ± 0.3
	τ of exponential	-	-0.0080 ± 0.0016
2017	μ of Gaussian	5280.0 ± 0.4	5279.6 ± 0.3
	σ of Gaussian	12.8 ± 0.3	13.1 ± 0.2
	τ of exponential	-	-0.0106 ± 0.0017
2018	μ of Gaussian	5282.6 ± 0.5	5279.7 ± 0.3
	σ of Gaussian	12.4 ± 0.3	12.7 ± 0.2
	τ of exponential	-	-0.0046 ± 0.0012

Table 4.5.3: MC simulation and data model parameters comparison, divided per year.

excludes all the combinatorial and partially reconstructed background components in the lower region of mass. The fit is shown in Figure 4.5.5 for 2016, 2017 and 2018 years of data taking. The normalization yields are found to be 2054 ± 45 for 2016, 2086 ± 45 for 2017, and 2730 ± 52 for 2018. The results of the fit are compared with those obtained from a Gaussian fit of the simulated truth-matched events to validate the choice of the model. Results are collected in Table 4.5.3.

To check the absence of a bias in the fit procedure, a thousand toy MC samples are generated and fit using the same model, i.e., a Gaussian signal and an exponential background. Signal and background yields are generated according to a Poisson distribution. Figure 4.5.6 shows the distributions of the signal yield parameter for the toys and the corresponding pulls[2] for the different data-taking years. The pulls

[2]Discrepancy between the measured value and the expected value, normalized by the uncertainty of the measurement ($\frac{x-\hat{x}}{\sigma_x}$)

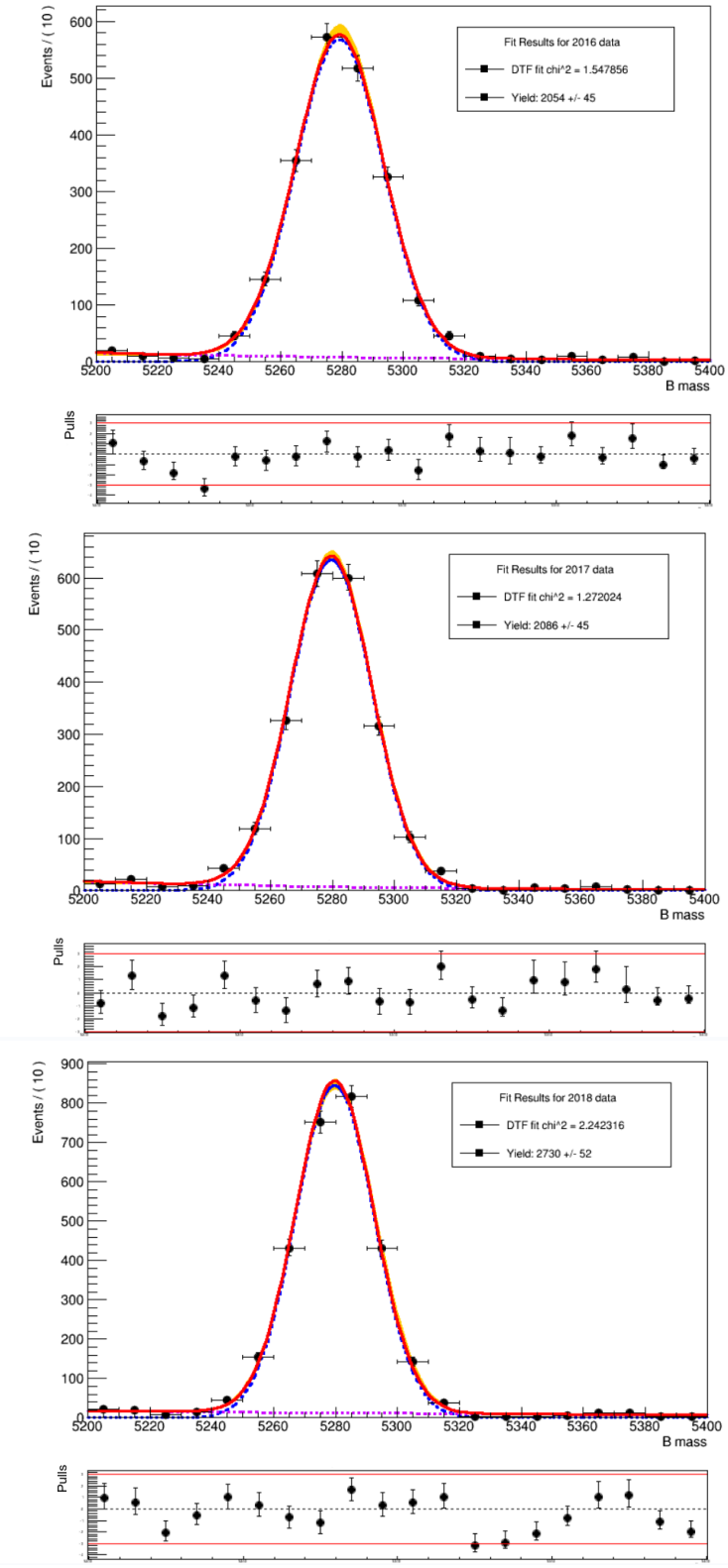

Figure 4.5.5: Mass fit on the normalization channel for 2016 (top-left), 2017 (top-right), and 2018 (bottom) year of data taking. The fit is performed using a Gaussian model for the signal (dashed blue line) and a decreasing exponential for the background (dashed violet line). The yellow bands represent the 1σ error of the fit. Below each plot, the distribution of pulls is shown.

are compatible within 3σ with a Gaussian with $\mu = 0$ and $\sigma = 1$, demonstrating the absence of a bias in the fit procedure.

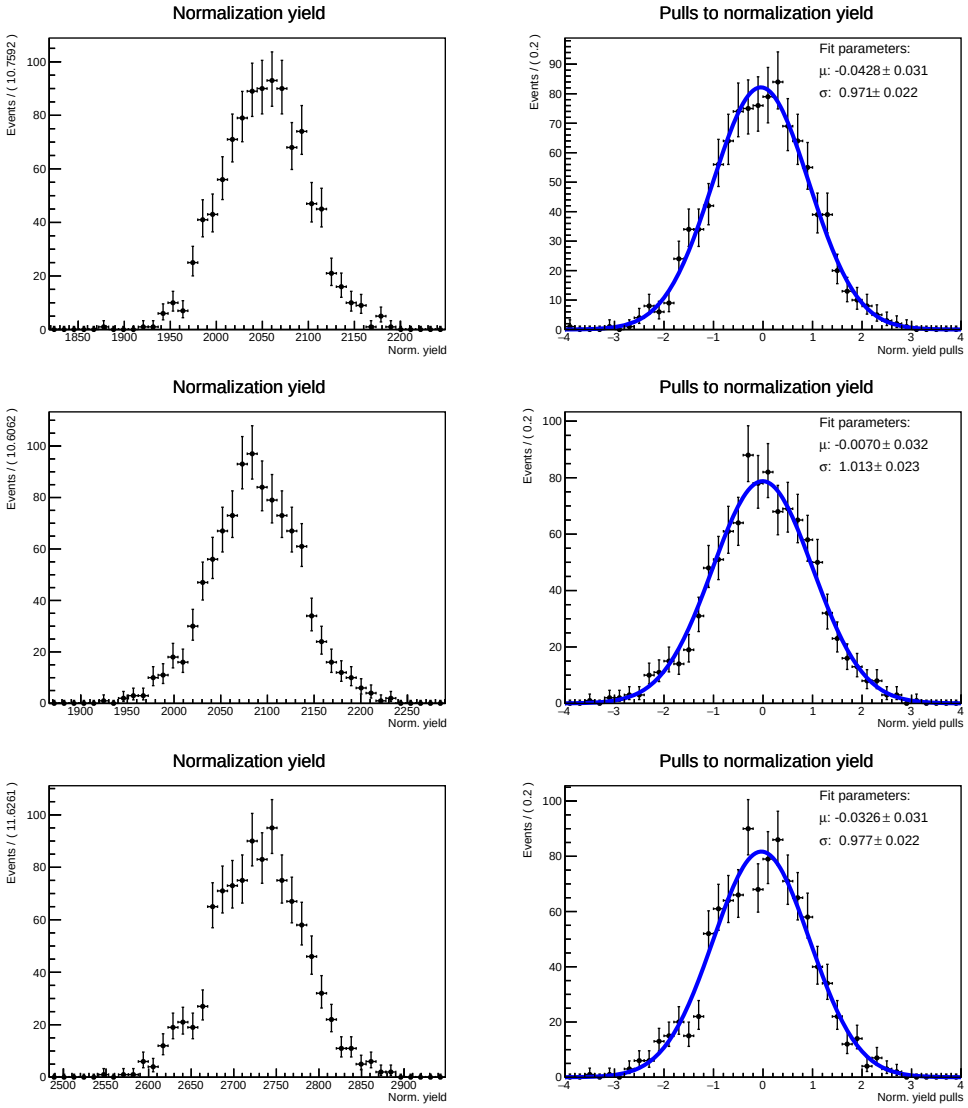

Figure 4.5.6: Distributions for the signal yield of the toys (left) and pulls (right) from the generated one for the normalization channel. Toys are obtained by simulating events for a thousand samples according to the data fit model and fluctuating signal and background yield according to a Poisson distribution. Distributions are referring to 2016 (left), 2017(center) and 2018 (right) years of data taking

4.6 Efficiencies

The selection efficiencies have been estimated separately for each year of data taking, using truth-matched reconstructed candidates from MC simulation samples, with the exception of the particle identification efficiencies determined on dedicated control samples. Trigger efficiencies, after being estimated on simulation, are corrected from control samples. Efficiencies are evaluated independently at different stages of the analysis to monitor step-by-step the effectiveness of the selection. The total efficiency is then the product of the individual selection steps efficiencies:

$$\epsilon_{tot} = \epsilon_{gen} \times \epsilon_{reco+str} \times \epsilon_{trg} \times \epsilon_{fid} \times \epsilon_{BDTs} \times \epsilon_{PID} \times \epsilon_{K^*mass} \times \epsilon_{FD} \times \epsilon_{vetoes} \quad (4.6.1)$$

where:

- ϵ_{tot} is the total efficiency of the analysis' selections;
- ϵ_{gen} is the efficiency at the generation level due to the Global Event Cut (GEC) that, as discussed in 4.2.2, requires the charged final state particles to be within the LHCb acceptance and cuts on their transverse momentum;
- $\epsilon_{reco+str}$ is the combined efficiency of reconstruction and Stripping. It considers the events that are reconstructed on top of those that are produced (after the application of the generator level cut) and the effects of the requirements listed in 4.4.1;
- ϵ_{fid} is the fiducial efficiency of the candidates passing the geometric constraints applied after the stripping selection (4.4.2);
- ϵ_{trg} is the trigger efficiency of the candidates passing the fiducial requirements. Different efficiencies are evaluated for each stage of the trigger (4.4.3);
- ϵ_{BDTs} is the efficiency for all the BDTs applied in the analysis on the top of the trigger selection; it includes the MVA classifier output cut efficiencies for the anti-combinatorial (Section 4.4.4), the isolation (Section 4.4.5) and the tau multivariate (Section 4.4.6) selections;
- ϵ_{PID} is the PID selection efficiency after the application of all the BDTs, discussed in 4.4.7;
- ϵ_{K^*mass} is the efficiency of the K^{*0} mass cuts (4.4.8) on top of the particle identification requirements;
- ϵ_{FD} is the efficiency on the flight distance and flight distance significance requirements (4.4.9).

- ϵ_{vetoes} is the efficiency of the final veto requirements to suppress physics backgrounds 4.4.10.

The efficiencies evaluated for each step of the analysis are summarized in Table 4.6.1, Table 4.6.2, and Table 4.6.3 for 2016, 2017, and 2018, respectively. Values shown consider tracking (see Section 4.6.1) and trigger (see Section 4.6.2) corrections for signal channels and data-driven particle identification efficiency (see Section 4.6.3) evaluation. For the normalization mode, the trigger efficiency is evaluated by performing background subtraction on data before and after the application of the cut.
Only statistical uncertainties are reported.

Decay channel	$B^0 \to K^{*0}\tau^+e^-$ (T5 oc)	$B^0 \to K^{*0}\tau^-e^+$ (T5 sc)	$B^0 \to K^{*0}\tau^+e^-$ (T8 oc)	$B^0 \to K^{*0}\tau^-e^+$ (T8 sc)	$B \to D^-D_s^+$
Generator level	15.72 ± 0.04	15.72 ± 0.04	3.946 ± 0.011	3.946 ± 0.011	12.54 ± 0.05
Reco & Strip	0.685 ± 0.012	0.729 ± 0.010	1.357 ± 0.016	1.348 ± 0.016	0.818 ± 0.009
Fiducial	68.8 ± 0.6	68.0 ± 0.6	68.9 ± 0.4	69.6 ± 0.4	70.0 ± 0.6
Trigger	70.0 ± 1.4	70.9 ± 1.3	70.0 ± 1.0	70.2 ± 1.0	57.1 ± 0.5
Refit	99.20 ± 0.15	99.20 ± 0.15	99.28 ± 0.10	99.22 ± 0.11	-
Anti-combinatorial BDT	23.6 ± 0.7	20.5 ± 0.5	22.1 ± 0.8	21.8 ± 0.5	-
Isolation Fisher	68.9 ± 1.6	63.3 ± 1.7	54.2 ± 1.4	57.6 ± 2.1	-
τ BDT	83.3 ± 1.6	82.6 ± 1.7	44.3 ± 1.8	41.8 ± 1.8	-
Particle identification	52.8 ± 1.8	54.9 ± 1.7	55.6 ± 2.5	57.8 ± 2.4	35.2 ± 1.4
Children mass cut	83.8 ± 2.0	87.4 ± 1.8	87.3 ± 2.2	80.0 ± 2.5	94.8 ± 0.7
Flight distance	100	98.9 ± 0.6	99.5 ± 0.5	99.0 ± 0.7	-
Vetoes	75.8 ± 2.5	61.2 ± 2.9	70.4 ± 3.5	59.8 ± 3.5	-
B mass window	-	-	-	-	99.5 ± 0.2
Total	0.00229 ± 0.00018	0.00168 ± 0.00015	0.00046 ± 0.00004	0.00036 ± 0.00004	0.0121 ± 0.0006

Table 4.6.1: Summary of efficiencies for the year 2016 for T5 ($\tau \to \pi\pi\pi\nu_\tau$) and T8 ($\tau \to \pi\pi\pi\pi^0\nu_\tau$) signal separated for charge categories and efficiencies of selection on normalization channel. All efficiencies are expressed as percentages (%). Only statistical uncertainties are provided. All efficiencies are corrected, as explained in the following Section.

Decay channel	$B^0 \to K^{*0}\tau^+e^-$ (T5 oc)	$B^0 \to K^{*0}\tau^-e^+$ (T5 sc)	$B^0 \to K^{*0}\tau^+e^-$ (T8 oc)	$B^0 \to K^{*0}\tau^-e^+$ (T8 sc)	$B \to D^-D_s^+$
Generator level	15.66 ± 0.04	15.66 ± 0.04	3.940 ± 0.009	3.940 ± 0.009	12.53 ± 0.05
Reco & Strip	0.679 ± 0.007	0.739 ± 0.007	1.369 ± 0.010	1.368 ± 0.010	0.819 ± 0.009
Fiducial	68.6 ± 0.6	69.6 ± 0.5	69.0 ± 0.5	69.8 ± 0.4	70.6 ± 0.4
Trigger	71.5 ± 1.3	74.5 ± 1.2	72.2 ± 1.0	73.4 ± 1.0	54.1 ± 0.4
Refit	99.01 ± 0.16	98.96 ± 0.15	99.38 ± 0.10	99.31 ± 0.10	-
Anti-combinatorial BDT	24.0 ± 0.7	22.2 ± 0.6	21.2 ± 0.5	20.5 ± 0.5	-
Isolation Fisher	65.2 ± 1.6	64.6 ± 1.5	53.7 ± 1.4	56.1 ± 1.3	-
τ BDT	81.0 ± 1.6	81.8 ± 1.5	46.9 ± 1.9	47.4 ± 1.8	-
Particle identification	61.7 ± 1.9	58.1 ± 1.9	57.3 ± 2.4	57.3 ± 2.3	40.8 ± 1.5
Children mass cut	87.1 ± 1.7	81.1 ± 2.0	85.4 ± 2.2	84.0 ± 2.3	93.3 ± 0.8
Flight distance	99.1 ± 0.5	99.1 ± 0.5	99.5 ± 0.5	99.1 ± 0.6	-
Vetoes	75.8 ± 2.8	62.1 ± 2.7	79.5 ± 2.8	66.2 ± 3.2	-
B mass window	-	-	-	-	99.8 ± 0.2
Total	0.00262 ± 0.00019	0.00200 ± 0.00017	0.00054 ± 0.00005	0.00047 ± 0.00004	0.0147 ± 0.0006

Table 4.6.2: Summary of efficiencies for the year 2017 for T5 ($\tau \to \pi\pi\pi\nu_\tau$) and T8 ($\tau \to \pi\pi\pi\pi^0\nu_\tau$) signal separated for charge categories and efficiencies of selection on normalization channel. All efficiencies are expressed as percentages (%). Only statistical uncertainties are provided. All efficiencies are corrected, as explained in the following Section.

Decay channel	$B^0 \to K^{*0}\tau^+e^-$ (T5 oc)	$B^0 \to K^{*0}\tau^-e^+$ (T5 sc)	$B^0 \to K^{*0}\tau^+e^-$ (T8 oc)	$B^0 \to K^{*0}\tau^-e^+$ (T8 sc)	$B \to D^-D_s^+$
Generator level	15.64 ± 0.03	15.64 ± 0.03	3.938 ± 0.009	3.938 ± 0.009	12.650 ± 0.009
Reco & Strip	0.687 ± 0.007	0.744 ± 0.007	1.373 ± 0.010	1.360 ± 0.010	0.817 ± 0.009
Fiducial	69.9 ± 0.7	67.6 ± 0.6	69.2 ± 0.5	68.6 ± 0.5	69.5 ± 0.6
Trigger	76.3 ± 1.5	79.0 ± 1.5	78.1 ± 1.1	77.5 ± 1.1	53.8 ± 0.4
Refit	99.49 ± 0.13	98.97 ± 0.18	99.04 ± 0.13	99.40 ± 0.10	-
Anti-combinatorial BDT	24.4 ± 0.8	22.3 ± 0.7	21.1 ± 0.5	20.5 ± 0.5	-
Isolation Fisher	66.9 ± 1.8	66.4 ± 1.8	54.4 ± 1.5	55.1 ± 1.5	-
τ BDT	81.0 ± 1.8	83.1 ± 1.7	43.5 ± 2.0	48.3 ± 2.0	-
Particle identification	63.5 ± 2.1	57.9 ± 2.2	55.0 ± 2.7	56.7 ± 2.6	43.4 ± 1.4
Children mass cut	87.2 ± 1.9	80.7 ± 2.3	80.8 ± 2.8	87.2 ± 2.3	93.9 ± 0.6
Flight distance	98.5 ± 0.8	99.1 ± 0.6	98.8 ± 0.9	100	-
Vetoes	75.7 ± 2.7	64.0 ± 3.2	70.3 ± 3.6	67.4 ± 3.4	-
B mass window	-	-	-	-	99.8 ± 0.2
Total	0.00308 ± 0.00025	0.00210 ± 0.00020	0.00044 ± 0.00005	0.00051 ± 0.00005	0.0166 ± 0.0006

Table 4.6.3: Summary of efficiencies for the year 2018 for T5 ($\tau \to \pi\pi\pi\nu_\tau$) and T8 ($\tau \to \pi\pi\pi\pi^0\nu_\tau$) signal separated for charge categories and efficiencies of selection on normalization channel. All efficiencies are expressed as percentages (%). Only statistical uncertainties are provided. All efficiencies are corrected, as explained in the following Section.

4.6.1 Electron tracking efficiency

In LHCb, the electron tracking efficiency deserves special treatment, which is different from hadrons and muons. The corrections to the simulated signal sample (w_{trk}) applied to the tracking electron efficiency measurements are evaluated using the tag and probe method on a $B^+ \to (J/\psi \to e^+e^-)K^+$ sample, as documented in [213]. The method is used to measure efficiencies in an unbiased and model-independent way by determining how often a particle (the probe) is correctly reconstructed (or "tagged") by the detector in a particular decay channel. The channel is identified by the presence of a very reliably identified particle (the tag).
The corrections are evaluated per year of data taking as a function of the electron P_T, η, and ϕ. They encode the information about the efficiency of reconstructing the electron as a *long* track, provided that the track has been reconstructed as a *velo* track (see Section 2.3), therefore:

$$w_{trk} = \frac{\epsilon(\text{long}|\text{velo})_{\text{data}}}{\epsilon(\text{long}|\text{velo})_{\text{MC}}}. \tag{4.6.2}$$

Correction maps are shown in Appendix O (Figure O.0.1 for 2016, Figure O.0.2 for 2017 and Figure O.0.3 for 2018). Each bin content is the efficiency ratio of data over MC with the associated error for different ranges of η and is directly applied as weight on the candidates in the MC simulation. The binning scheme adopted for P_T as a function of η bins is represented in Table 4.6.4. For ϕ the following binning scheme is used: $[-\pi, -\frac{\pi}{2} - \frac{\pi}{8}, -\frac{\pi}{2} + \frac{\pi}{8}, \frac{\pi}{2} - \frac{\pi}{8}, \frac{\pi}{2} + \frac{\pi}{8}, \pi]$.

η **binning**	p_T **binning (MeV/c)**
$1.9 \leq \eta < 2.9$	[150, 520, 657, 780, 915, 1065, 1245, 1600, 1950, 2430, 3020, 4310, 5810, 50000]
$2.9 \leq \eta < 3.45$	[150, 760, 1475, 4000, 50000]
$3.45 \leq \eta < 4.0$	[150, 490, 760, 1300, 2000, 50000]
$4.0 \leq \eta < 4.5$	[150, 550, 785, 50000]

Table 4.6.4: Binning schemes of P_T for different η bins used to correct the electron tracking efficiency values in the simulation.

The electron tracking correction is on a per-candidate basis. Since the correction is not coupled with any associated selection, representing the tracking efficiency ratio between data and simulation, it can be applied at any stage. It has been incorporated by arbitrariness within the reconstruction at the first stage of the selection. Table 4.6.5 collects the correction applied to the efficiencies from the MC simulation divided per simulation year for both T5 ($\tau \to \pi\pi\pi\nu_\tau$) and T8 ($\tau \to \pi\pi\pi\pi^0\nu_\tau$) channels. The efficiencies are estimated from truth quantities in the simulation, and the corrections applied are evaluated in [214].

Sample	2016	2017	2018
T5	98.345 ± 0.009 %	99.041 ± 0.006 %	99.133 ± 0.007 %
T8	98.2675 ± 0.009 %	98.954 ± 0.007 %	99.146 ± 0.007 %

Table 4.6.5: Tracking efficiency correction for T5 and T8 MC simulated sample for different years.

4.6.2 L0 efficiency correction

The efficiencies of the three trigger categories mentioned in Section 4.4.3 are not correctly described in the simulation. Therefore, calibration samples are necessary to correct them. The weights are obtained from a calibration sample as an efficiency ratio between data and MC. The calibration sample used is $B \to J/\psi(\to e^+e^-)K$ for *eTOS* category and the normalization sample $B \to D^-D_s^+$ for *TIS* and *hTOS* categories. First, the efficiency of the control sample is computed using data and MC. Then, a correction factor is evaluated as the following ratio:

$$w_{L0} = \frac{\epsilon_{L0}^{data}}{\epsilon_{L0}^{MC}} \tag{4.6.3}$$

Where ϵ_{L0}^{data} and ϵ_{L0}^{MC} are the efficiency for a given L0 trigger decision evaluated on data and simulated sample, respectively, the correction weights are obtained using the TISTOS method, as discussed in 4.4.3, binning on different variables depending on the trigger decisions. They are then applied per event to the MC signal simulation. The effect of the weights on the MC simulation is shown for the three L0 categories in Table 4.6.6 for channel T5 ($\tau \to \pi\pi\pi\nu_\tau$) and in Table 4.6.7 for channel T8 ($\tau \to \pi\pi\pi\pi^0\nu_\tau$).

L0 category	2016 OC	2016 SC	2017 OC	2017 SC	2018 OC	2018 SC
eTOS	52.1 ± 0.7	55.5 ± 0.8	48.8 ± 0.7	56.0 ± 0.7	48.8 ± 0.9	51.7 ± 0.8
	45.7 ± 0.8	48.6 ± 0.8	39.6 ± 0.7	46.7 ± 0.7	41.8 ± 0.8	45.6 ± 0.8
TIS	31.2 ± 1.2	29.1 ± 1.1	34.4 ± 1.0	30.4 ± 1.0	33.9 ± 1.2	33.3 ± 1.2
	25.1 ± 1.1	23.4 ± 1.0	32.5 ± 1.0	28.9 ± 1.0	36.9 ± 1.2	37.6 ± 1.2
hTOS	6.3 ± 0.4	4.7 ± 0.3	8.5 ± 0.3	5.8 ± 0.3	7.1 ± 0.4	6.5 ± 0.4
	7.4 ± 0.4	5.5 ± 0.3	8.3 ± 0.3	5.7 ± 0.3	6.7 ± 0.4	6.1 ± 0.4

Table 4.6.6: L0 trigger efficiency before (top line) and after (bottom line) correction to the MC simulation T5 sample, for different charge combinations and years of data taking. The efficiencies are expressed as percentages.

eTOS trigger efficiency correction

The correction weight of *eTOS* category is:

$$w_{L0}^{eTOS} = \frac{\epsilon_{L0ETOS}^{data}}{\epsilon_{L0ETOS}^{MC}} \tag{4.6.4}$$

L0 category	2016 OC	2016 SC	2017 OC	2017 SC	2018 OC	2018 SC
eTOS	50.8 ± 0.6	51.2 ± 0.6	49.0 ± 0.6	51.3 ± 0.6	47.5 ± 0.9	47.2 ± 0.8
	44.1 ± 0.6	44.7 ± 0.6	39.8 ± 0.6	42.2 ± 0.6	41.4 ± 0.6	40.8 ± 0.6
TIS	33.3 ± 0.8	33.0 ± 0.8	35.1 ± 0.8	34.0 ± 0.8	36.1 ± 0.9	36.5 ± 0.9
	26.8 ± 0.8	26.5 ± 0.8	32.3 ± 0.8	32.3 ± 1.0	37.5 ± 0.9	37.9 ± 0.9
hTOS	6.1 ± 0.3	5.7 ± 0.3	7.3 ± 0.3	6.7 ± 0.3	7.6 ± 0.3	7.2 ± 0.3
	7.2 ± 0.3	6.7 ± 0.3	7.3 ± 0.3	6.7 ± 0.3	7.6 ± 0.3	7.3 ± 0.3

Table 4.6.7: L0 trigger efficiency before (top line) and after (bottom line) correction to the MC simulation T8 sample, for different charge combinations and years of data taking. The efficiencies are expressed as percentages.

with data and MC efficiency evaluated as:

$$\begin{aligned} \epsilon^{data}_{L0ETOS} &= \left(\frac{N_{TIS\&TOS}}{N_{TIS}}\right)^{data} = \left(\frac{N_{\text{L0E\_TOS}}}{N_{\text{TOTAL}}}\right)^{data}_{\text{L0M\_TIS|L0H\_TIS}} \\ \epsilon^{MC}_{L0ETOS} &= \left(\frac{N_{TIS\&TOS}}{N_{TIS}}\right)^{MC} = \left(\frac{N_{\text{L0E\_TOS}}}{N_{\text{TOTAL}}}\right)^{MC}_{\text{L0M\_TIS|L0H\_TIS}} \end{aligned} \tag{4.6.5}$$

where $N_{TIS\&TOS}$ denotes the fraction of candidates triggered simultaneously by `L0Muon_TIS` and `L0Electron_TOS` category, while N_{TIS} denotes the fraction of candidates triggered by `L0Muon_TIS` category or by `L0Hadron_TIS`. On the right side of the equation, a naming convention is adopted to label the events that are triggered by `L0Electron_TOS` ($N_{\text{L0E\_TOS}}$) over the total number of events (N_{TOTAL}) in a subsample tagged by `L0Muon_TIS` ($L0M\_TIS$) or by `L0Hadron_TIS` ($L0H\_TIS$).
Corrections, shown in Appendix P.1, are taken from the R_K and R_{K^*} analysis [50] and applied to the simulation to correct the `L0Electron_TOS` efficiencies in bins of electromagnetic calorimeter E_T and ECAL region. The correction is evaluated using $B \to J/\psi(\to e^+e^-)K$ sample. The `L0Electron` trigger line is fired whenever an electron deposits an amount of transverse energy in the electromagnetic calorimeter above a threshold energy in the ECAL. The ECAL has three different granularities, depending on how far the region is from the beam. Therefore, the resolution of the transverse energy deposited by the electron is expected to change depending on the region hit. The efficiency correction of the *eTOS* is computed as a function of the transverse energy E_T deposited in the ECAL and the three regions (inner, middle, outer).

TIS trigger efficiency correction

The *TIS* category contains events triggered by particles not belonging to the signal. It turns out that they are mostly triggered by other b-hadrons in the event. The efficiency on data and MC are computed on $B \to D^- D_s^+$ sample using the TISTOS

method. Hence, the weight to apply to the signal simulated sample is:

$$w_{L0}^{TIS} = \frac{\epsilon_{TIS}^{data}}{\epsilon_{TIS}^{MC}} \tag{4.6.6}$$

The above formula assumes that the TIS efficiency is independent of whether an electron fires the trigger for this calibration sample. The efficiencies on MC and data samples are parameterized as a function of the transverse momentum $p_T(B)$ of the signal B meson. It is expected that $p_T(B)$ is correlated with the transverse momentum of the hadronized system from the opposite b-quark and, therefore, related to TIS efficiency. Efficiencies are evaluated as follows:

$$\begin{aligned} \epsilon_{L0TIS}^{data} &= \left(\frac{N_{TIS\&TOS}}{N_{TOS}}\right)^{data} = \left(\frac{N_{\text{L0G\_TIS}}}{N_{\text{TOTAL}}}\right)^{data}_{\text{L0H\_TOS}} \\ \epsilon_{L0TIS}^{MC} &= \left(\frac{N_{TIS\&TOS}}{N_{TOS}}\right)^{MC} = \left(\frac{N_{\text{L0G\_TIS}}}{N_{\text{TOTAL}}}\right)^{MC}_{\text{L0H\_TOS}} \end{aligned} \tag{4.6.7}$$

where $N_{TIS\&TOS}$ denotes the fraction of candidates triggered simultaneously by `L0Global_TIS` and `L0Hadron_TOS` category, while N_{TOS} denotes the fraction of candidates triggered by `L0Hadron_TOS` category. On the right side of the equation, a naming convention is adopted to label the events that are triggered by `L0Global_TIS` (N_{L0G_TIS}) over the total number of events (N_{TOTAL}) in a sub-sample tagged by `L0Hadron_TOS` (L0H_TOS).
Signal is extracted from the calibration sample $B \to D^- D_s^+$ in the following way:

- Fiducial requirements (collected in Table 4.5.2) and mass window cuts on the intermediate charmed meson states ($\pm 50 \text{MeV}/c^2$ with respect to PDG values) are imposed on simulation and data;

- Residual background is further suppressed exploiting the *sPlot* technique [215]. It is possible to statistically subtract the background by fitting the invariant mass of the final states and re-weighting the dataset to show signal and background components. An example of application of the *sPlot* is shown in Appendix P.2 (Figure P.2.1).

Efficiencies are evaluated by dividing the selected calibration candidates into bins of p_T iso-populated. Corrections, shown in Figure P.3.1, are applied to the simulation.

hTOS trigger efficiency correction

For *hTOS* category, the `L0Hadron` trigger efficiency is measured on both data and simulated $B \to D^- D_s^+$ events. `L0Hadron` is fired when enough energy is deposited on the hadronic calorimeter (HCAL). The resolution of the deposited energy depends

on the detector granularity. Hence, also for *hTOS* category, the efficiencies are parameterized as a function of the transverse energy E_T and the two HCAL regions (inner, outer). The correction to the simulated sample in this case is:

$$w_{L0}^{hTOS} = \frac{\epsilon_{L0HTOS}^{data}}{\epsilon_{L0HTOS}^{MC}} \times \frac{1-\epsilon_{TIS}^{data}}{1-\epsilon_{TIS}^{MC}} \tag{4.6.8}$$

with data and MC efficiency evaluated as:

$$\begin{aligned} \epsilon_{L0H}^{data} &= \left(\frac{N_{TIS\&TOS}}{N_{TIS}}\right)^{data} = \left(\frac{N_{\text{L0H\_TOS}}}{N_{\text{TOTAL}}}\right)^{data}_{\text{L0M\_TIS|L0H\_TIS}} \\ \epsilon_{L0H}^{MC} &= \left(\frac{N_{TIS\&TOS}}{N_{TIS}}\right)^{MC} = \left(\frac{N_{\text{L0H\_TOS}}}{N_{\text{TOTAL}}}\right)^{MC}_{\text{L0M\_TIS|L0H\_TIS}} \end{aligned} \tag{4.6.9}$$

where $N_{TIS\&TOS}$ denotes the fraction of candidates triggered simultaneously by `L0Muon_TIS||L0Hadron_TIS` and `L0Hadron_TOS` category, while N_{TIS} denotes the fraction of candidates triggered by `L0Muon_TIS` or `L0Hadron_TIS` category. On the right side of the equation, a naming convention is adopted to label the events that are triggered by `L0Hadron_TOS` (N_{L0H_TOS}) over the total number of events (N_{TOTAL}) in a sub-sample tagged by `L0Muon_TIS` (L0M_TIS) or `L0Hadron_TIS` (L0H_TIS). The correction presented is exclusive for `L0Hadron` and keeps in consideration the effects of the interference with `TIS` trigger. Instead, there is no contribution from `L0Electron` trigger decision for the chosen calibration sample.
The signal is derived from the calibration sample following the same procedure described for *TIS* category. The sPlot is applied to four different datasets, and the invariant mass fits results are presented in Figure P.2.2.
Efficiencies are evaluated by dividing the events into HCAL regions (inner and outer) and considering iso-populated bins of the transverse energy deposit E_T of the triggering hadron for the calibration data selected events. Corrections are obtained according to Equation 4.6.8 and displayed in Figure P.4.1.

4.6.3 PID calibration

A well-known problem of the MC simulation is that the particle identification variables do not correctly reproduce the LHCb detector performances. Therefore, calibration using a control sample is required to correctly compute the PID cut efficiency. This can be done using the `PIDCalib2` software package [199].
These efficiencies depend on the kinematic properties of the particles and on the event occupancy. They are computed in three-dimensional bins, function of momentum p, pseudorapidity η and number of tracks n_{tracks}. The binning scheme is optimized to have bins narrow enough that PID cuts on the variable could be considered constant

but wide enough not to suffer large statistical fluctuations. Iso-populated bins for truth-matched signal samples are chosen for the different years, and contiguous bins are merged if they have efficiency values compatible at a level up to 5σ. The dependence on the number of tracks is integrated out from the analytical expression to derive an average two-dimensional distribution of the efficiency:

$$\langle \epsilon(p, \eta, n_{tracks}) \rangle = \int_{N_{tracks}} \epsilon(p, \eta, n_{tracks}) f(n_{tracks}) dn_{tracks} \tag{4.6.10}$$

In fact, the three-dimensional distribution of the efficiency, $\epsilon(p, \eta, n_{tracks})$, can be integrated over the track multiplicity n_{tracks}, assuming the unity-normalized distribution $f(n_{tracks})$ of track multiplicity is known. The problem is brought to the discrete case, not knowing the analytical distribution for efficiencies. Therefore, p, η, and n_{tracks} become discrete indices, and the integral becomes a sum:

$$\langle \epsilon(p, \eta, n_{tracks}) \rangle = \sum_{N_{tracks}} \epsilon_{p,\eta,n_{tracks}} f_{n_{tracks}} \tag{4.6.11}$$

Efficiency distributions for the kaon, pion and electron particle identification cuts in iso-populated bins of p, η and n_{tracks} are shown in Figure 4.6.1, Figure 4.6.2 and Figure 4.6.3, respectively, for different years of data taking. The optimal binning scheme is evaluated separately for each year. Two-dimensional distributions of efficiencies as a function of the momentum and pseudorapidity for kaon, pion and electron particle identification cuts for each year of data taking are shown for same-sign data in Figure Q.0.1 and for the normalization sample in Figure Q.0.2 in Appendix Q. The plots are obtained by integrating the dependence on the track multiplicity for opposite-sign data. This cannot be done directly on the MC sample since it does not correctly reproduce the distributions of the number of tracks in the event. For this analysis, we use the signal distribution of the number of tracks taken from the same-sign sample in the blinded region. In contrast, for the normalization channel, we use the distribution of the number of tracks for the selected candidates. Track multiplicity distributions are shown in Figure 4.6.4 for kaon, pion, and electron particle identification cuts superimposing the opposite-sign data (both opposite charge and same charge), same-sign data and the normalization sample. No big difference between the three distributions has been observed.

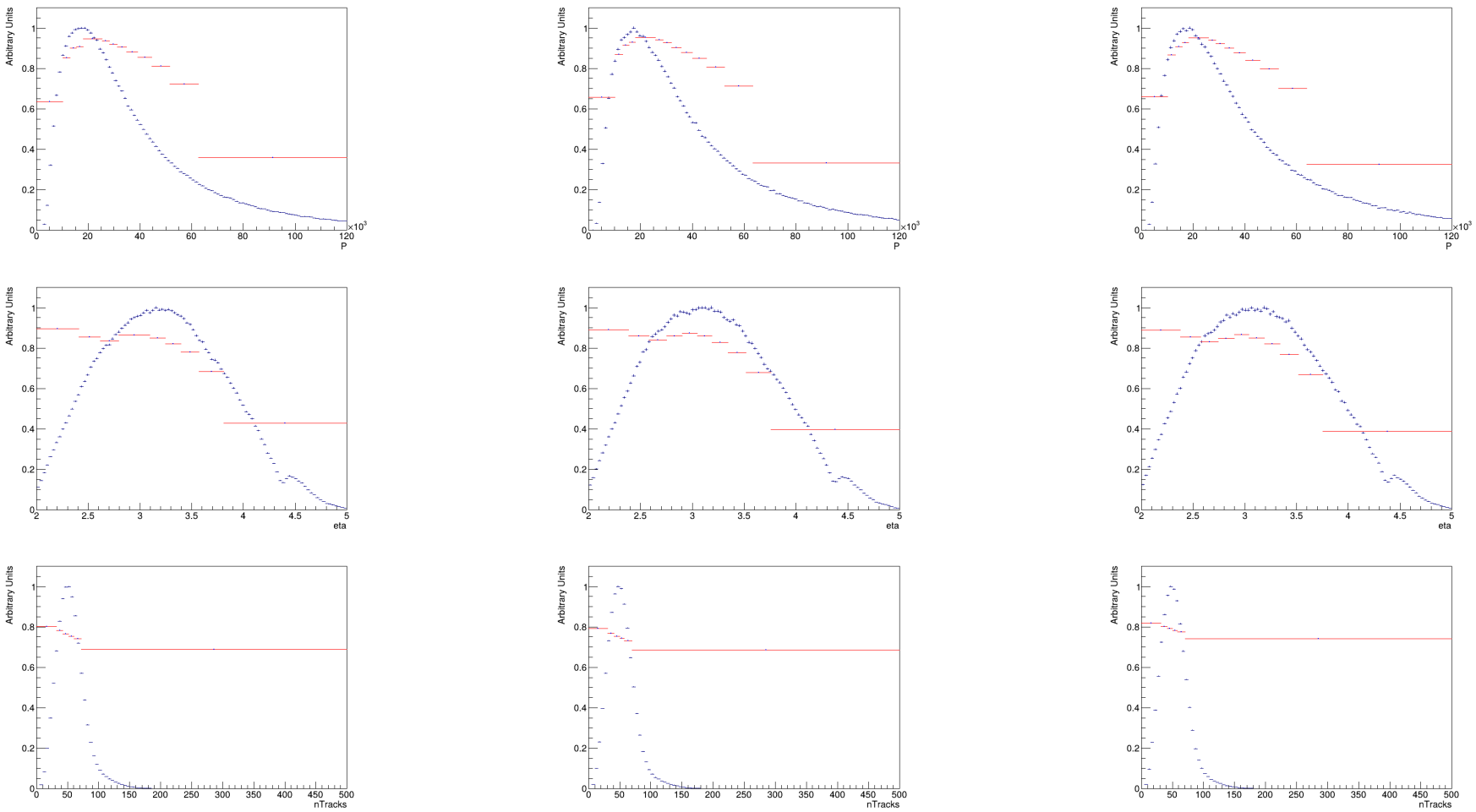

Figure 4.6.1: Efficiency distribution (red) for kaon particle identification cut $ProbNNk > 0.82$ as a function of momentum p (first row), pseudorapidity η (second row) and the track multiplicity n_{tracks} (third row), superimposed to the variable distribution itself (blue), for different year of data taking: 2016 (left), 2017 (centre) and 2018 (right).

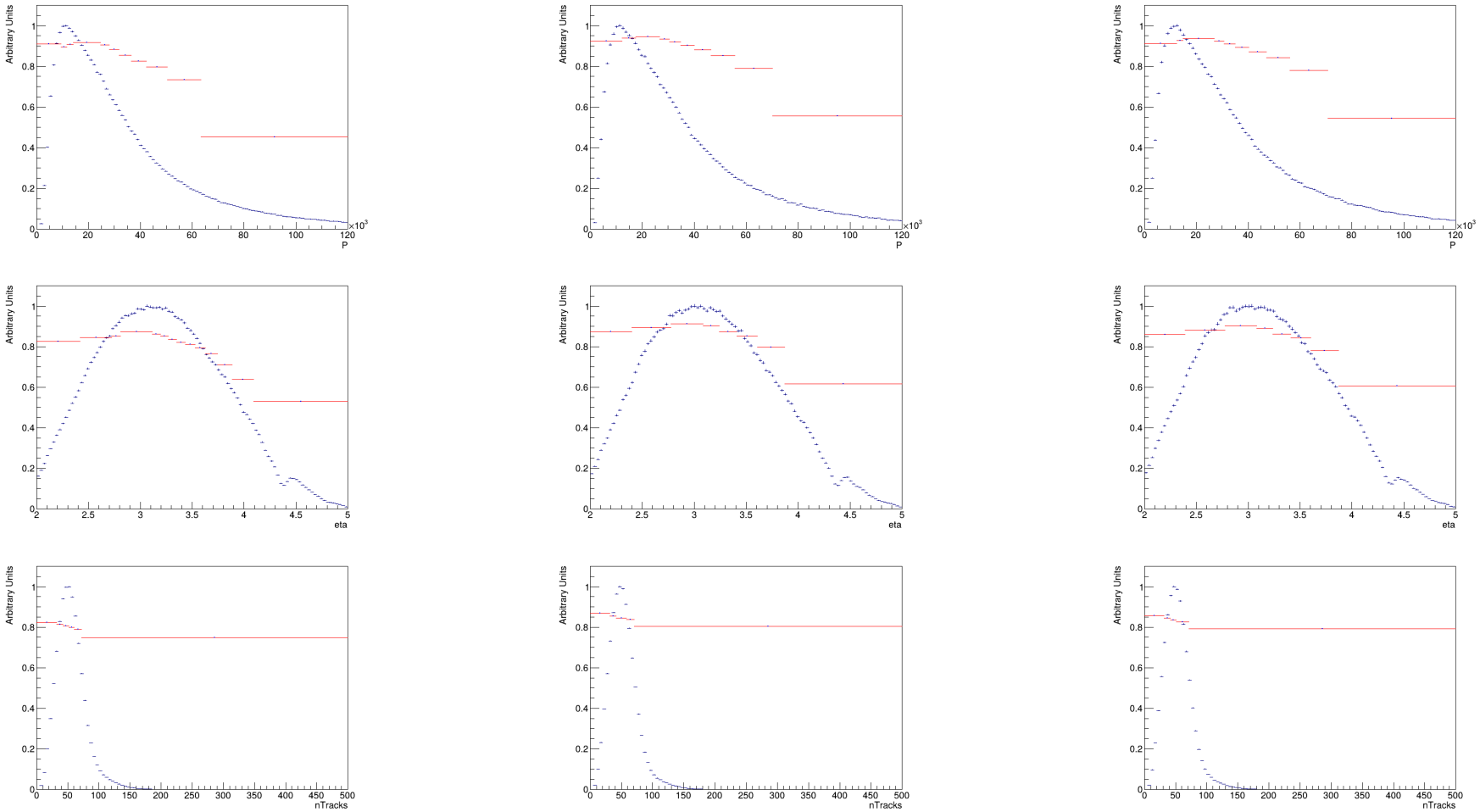

Figure 4.6.2: Efficiency distribution (red) for pion particle identification cut $ProbNN\pi > 0.725$ as a function of momentum p (first row), pseudorapidity η (second row) and the track multiplicity n_{tracks} (third row), superimposed to the variable distribution itself (blue), for different year of data taking: 2016 (left), 2017 (centre) and 2018 (right).

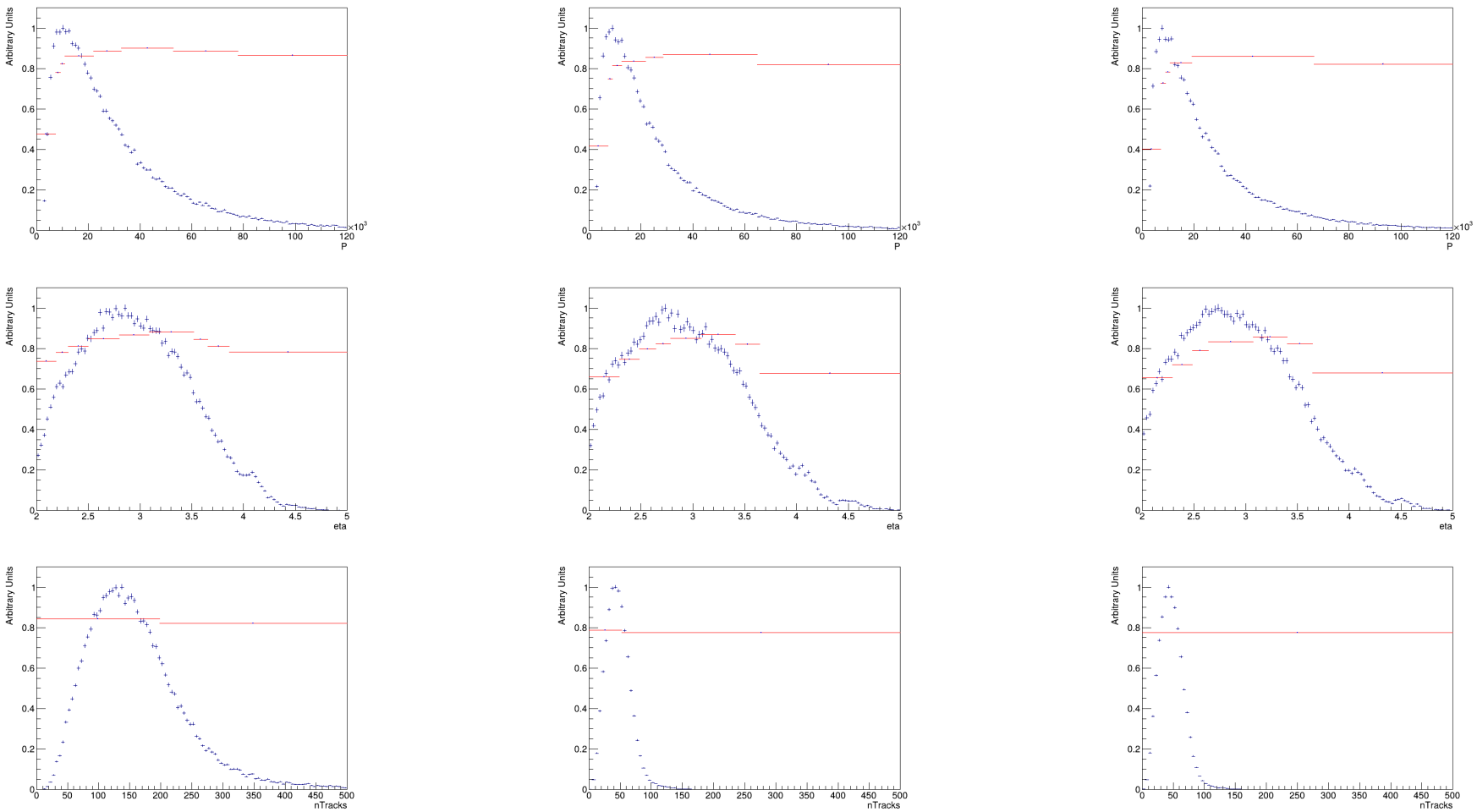

Figure 4.6.3: Efficiency distribution (red) for electron particle identification cut $ProbNNe > 0.125$ as a function of momentum p (first row), pseudorapidity η (second row) and the track multiplicity n_{tracks} (third row), superimposed with the variable distribution itself (blue), for different year of data taking: 2016 (left), 2017 (centre) and 2018 (right).

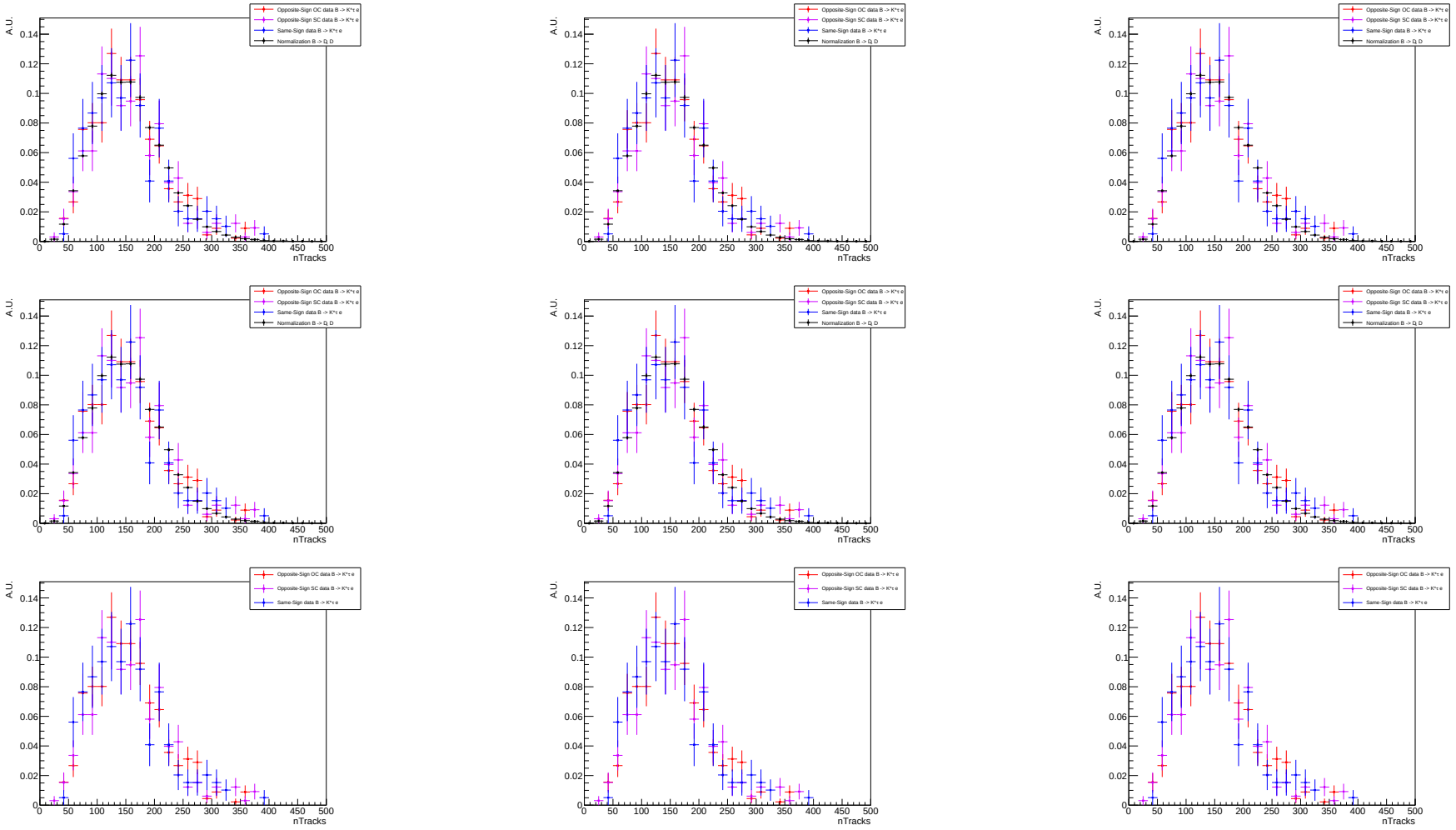

Figure 4.6.4: Track multiplicity distribution for cuts on $ProbNNk > 0.82$ (first row), $ProbNNpi > 0.725$ (second row) and $ProbNNk > 0.125$ (third row). Distributions are superimposed for opposite-sign data, both opposite-charge (red) and same-charge (pink), same-sign data (blue) and the normalization sample (black). Track multiplicity for the normalization sample is shown only for kaons and pions particle identification requirements. Events are divided per year of data taking: 2016 (left), 2017 (centre) and 2018 (right).

4.7 Fit to the mass of $B \to K^{*}\tau e$ candidates

The fit to the refitted mass distribution of the B^0 candidates for the events surviving the selection is performed separately for the OC $B^0 \to K^{*0}\tau^+e^-$ and the SC $B^0 \to K^{*0}\tau^-e^+$ cases. The signal parameterization also differs depending on the tau decay, T5 ($\tau \to \pi\pi\pi\nu_\tau$) or T8 ($\tau \to \pi\pi\pi\pi^0\nu_\tau$) and on to the bremsstrahlung category. In particular, events are classified as *brem* if at least one bremsstrahlung photon has been reconstructed and associated with the electron, otherwise as *nobrem*.
In the following sections, we describe how to derive the parameterization for signal and background components.

4.7.1 Signal model

The signal sample is parameterized using a Double-Sided Crystal Ball (DSCB) function $DSCB(x; m, \sigma, \alpha_L, \alpha_R, \eta_L, \eta_R)$ with symmetric $\sigma = \sigma_R = \sigma_L$, where L and R denote the left and right sides, respectively. The parameters are determined from the fit on the simulated sample, separately for SC and OC, T5 or T8, and for *brem* or *nobrem* events. The fraction of brem events is fixed from the simulation, where it is correctly represented. Table 4.7.1 shows this fraction for the various signal samples. All the shape parameters are then fixed in the fit to the data. The parameterization is independent of the year of data taking because no major differences are observed. The plots in Figure 4.7.1 and Figure 4.7.2 show the fit on the DTF mass in the region [4000,6400] MeV/c^2 for the two signal channels T5 and T8, respectively.

$B^0 \to K^{*0}\tau^+e^-$ (T5 oc)	$B^0 \to K^{*0}\tau^-e^+$ (T5 sc)	$B^0 \to K^{*0}\tau^+e^-$ (T8 oc)	$B^0 \to K^{*0}\tau^-e^+$ (T8 sc)
$(44.6 \pm 3.1)\%$	$(47.4 \pm 3.5)\%$	$(41.7 \pm 3.7)\%$	$(45.3 \pm 3.9)\%$

Table 4.7.1: Fraction of events belonging to the *brem* category.

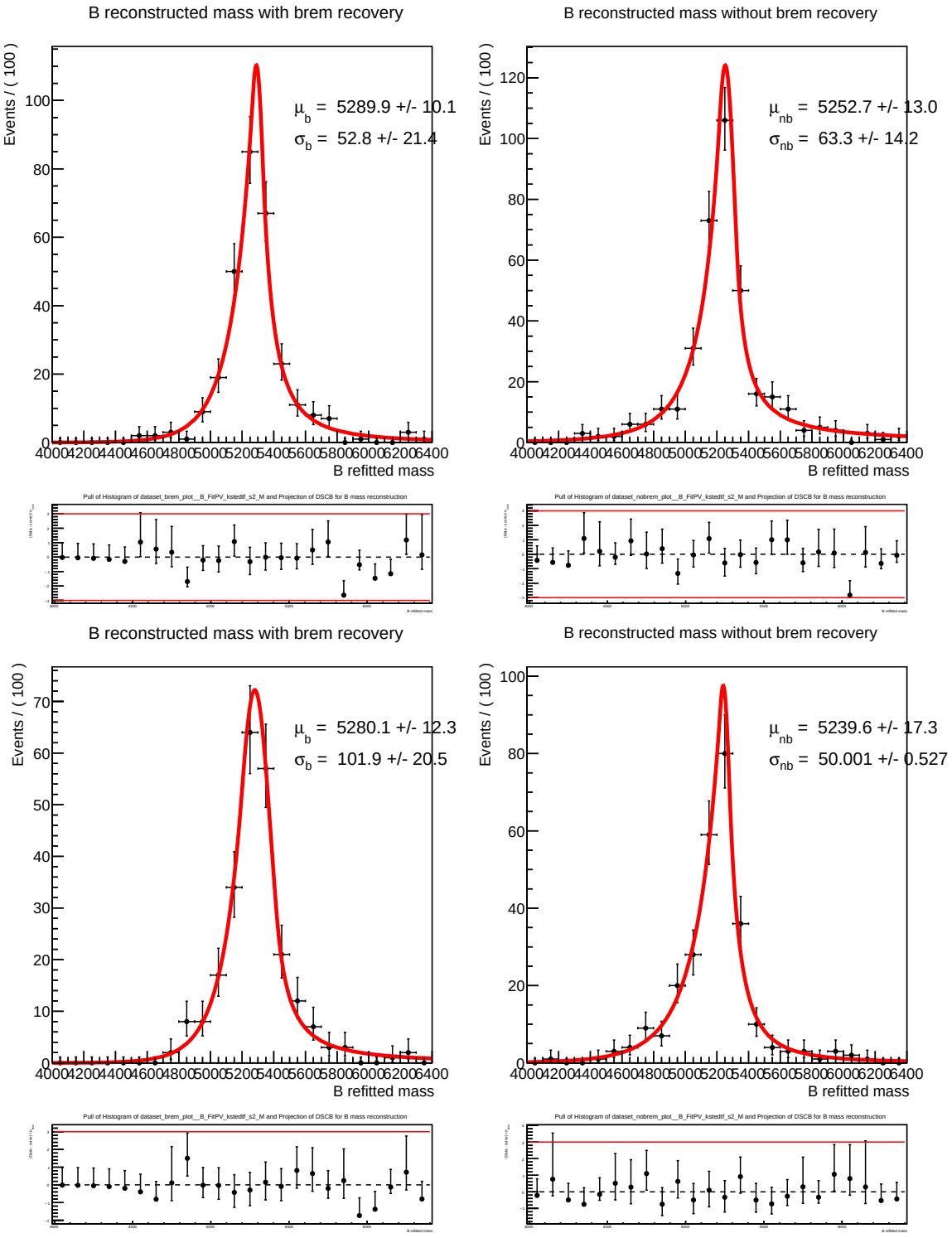

Figure 4.7.1: Fit to the B refitted mass distribution for T5 ($\tau \to \pi\pi\pi\nu_\tau$) MC simulation events in the opposite-charge case (top) and same-charge case (bottom). Events are divided into *brem* (left) and *nobrem* (right) categories. Parameters of the fit are displayed and fixed for the fit model on data. Pulls to the distributions are shown below the fit.

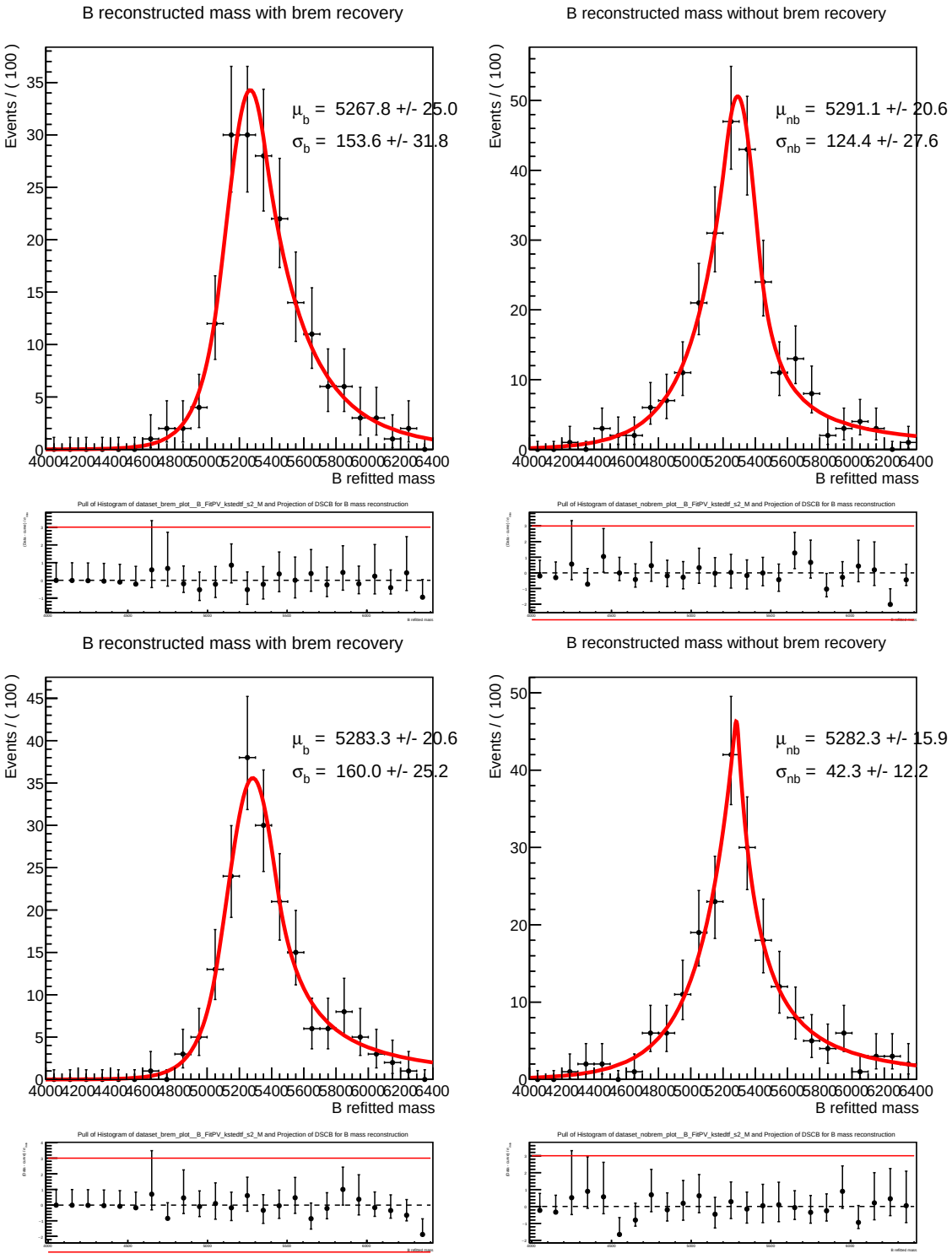

Figure 4.7.2: Fit to the B refitted mass distribution T8 ($\tau \to \pi\pi\pi\pi^0\nu_\tau$) MC simulation in the opposite-charge case (top) and same-charge case (bottom). Events are divided into *brem* (left) and *nobrem* (right) categories. Parameters of the fit are displayed and fixed for the fit model on data. Pulls to the distributions are shown below the fit.

4.7.2 Background shape parameterization

The parameterization of the background shape is taken from a control region. The control regions are obtained by inverting some selection cuts that have been performed. In particular, events belonging to four different regions of the anti-combinatorial output are used for the control sample definition. In addition, other sub-samples are extracted, inverting the IsoMVA cut and the requirement on the K^* mass. The collection of control samples used for the parameterization is reported in Table 4.7.2. These subsets are defined to balance the need for having enough statistics in each control sample and to be as close as possible to the signal region. For the region closest to the signal region, the bounds are set looser with respect to the signal selection to avoid possible signal leakage into the control region. For this reason, the upper limit of the ACMVA C4 cut (0.95) is set lower than the lower boundary of the signal region (0.9775), and the same is done for IsoMVA (upper limit: 0.4, selection limit: 0.48) and mass of the K^* meson (bounds: lower 827 MeV/c^2, upper 980 MeV/c^2; selection bounds: lower 842 MeV/c^2, upper 970 MeV/c^2).

Control sample	Cut
ACMVA C1	ACMVA$\in [-0.8, -0.2]$
ACMVA C2	ACMVA$\in [-0.2, 0.4]$
ACMVA C3	ACMVA$\in [0.4, 0.75]$
ACMVA C4	**ACMVA**$\in [\mathbf{0.75}, \mathbf{0.95}]$
IsoMVA	IsoMVA$\in [-0.4, 0.4]$
M_{K^*}	$M_{K^*} < 827$ MeV/c^2, $M_{K^*} > 980$ MeV/c^2

Table 4.7.2: Identification of control regions for the background parameterization. Four subsets are extracted, reverting the anti-combinatorial cut, one reverting the isolation cut, and the last one reverting the requirement on the mass of the K^*. The bold one (ACMVA C4) is the default one used for the background parameterization.

Distributions of the refitted mass for the control samples in Table 4.7.2 are shown in Figure 4.7.3 for opposite charge $B^0 \to K^{*0}\tau^+e^-$ events and in Figure 4.7.4 for same charge $B^0 \to K^{*0}\tau^-e^+$ events. DSCB functions with symmetric $\sigma = \sigma_L = \sigma_R$ are chosen as default parameterization for the background distribution. Each distribution is fit separately, and results are collected in Appendix S for OC and SC fits. The sample ACMVA C4, closest to the signal region, is chosen as the default control sample for the background parameterization. The other regions will be used to study the systematic uncertainty coming from this choice. The DSCB parameters determined fitting the ACMVA C4 region (see Figure S.0.4) are Gaussian constrained as described in Section 4.8.7. Background yields are, instead, left-floated.

As discussed in Section 4.4.9, the cut $m(Ke) < 1885$ MeV/c^2 allows to distinguish a sample that comprises possible physics backgrounds such as $B^0 \to D^{*-}\tau^+\nu$, with

$D^* \to \bar{D}^0\pi$, $\bar{D}^0 \to K^+e^-\bar{\nu}_e$ and $\tau^+ \to \pi^+\pi^-\pi^+\nu$. This background would not show a peaking structure due to the semileptonic decay of the D charmed meson. It would only be present in the OC sample. The comparison between the distributions of the control samples with and without the cut on $m(Ke)$ applied shows no strong discrepancies (see R.0.1 in Appendix R). If present, we conclude that this background component would be included and parameterized by the control sample.

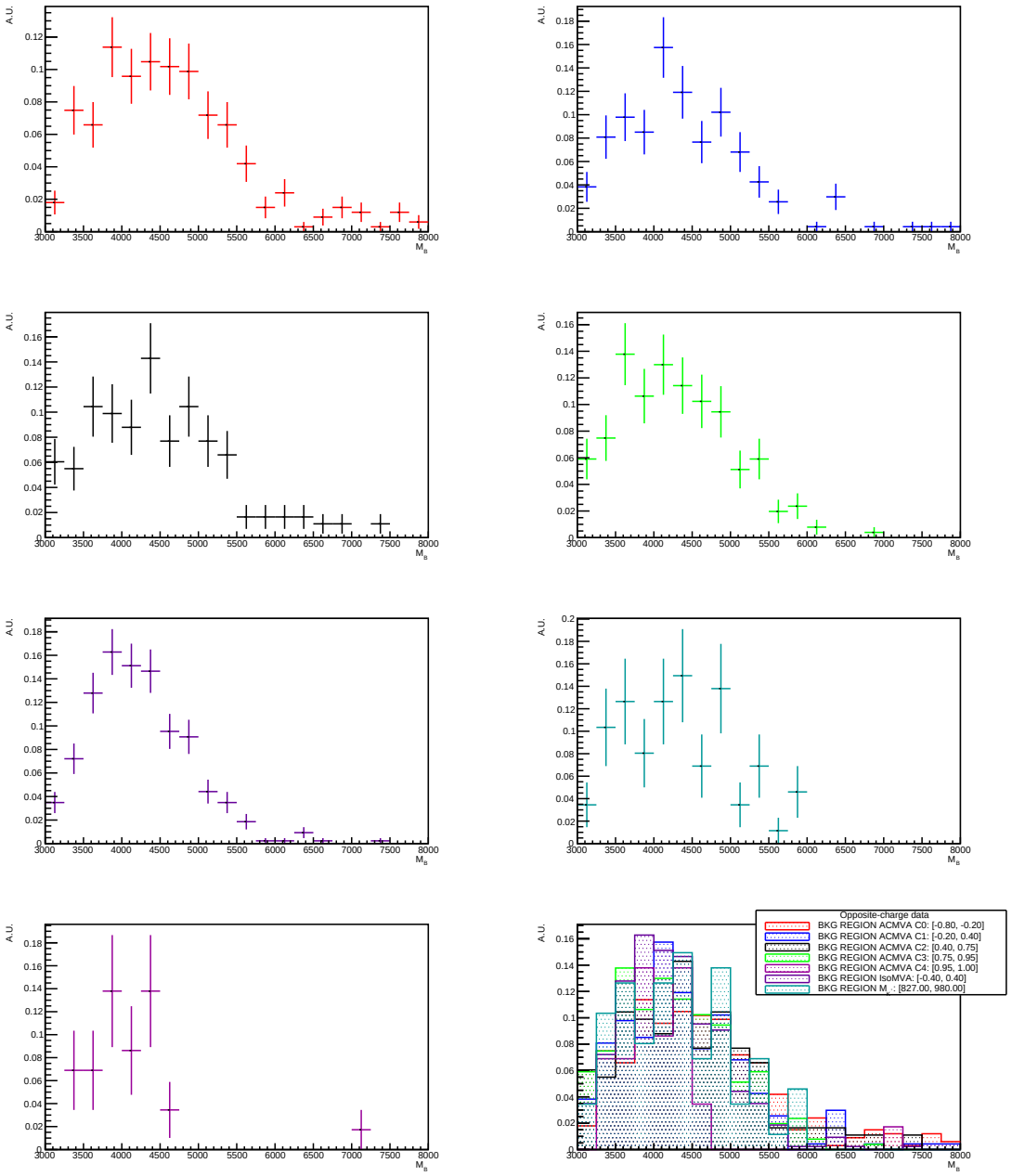

Figure 4.7.3: Distributions of the DTF mass of the candidates for the control sample ACMVA C1 (first row-left), ACMVA C2 (first row-right), ACMVA C3 (second row-left), ACMVA C4 (second row-right), IsoMVA (third row-left), M_{K^*} (third row-right), data sidebands (fourth row-left) and all distributions superimposed (fourth row-right) for OC events.

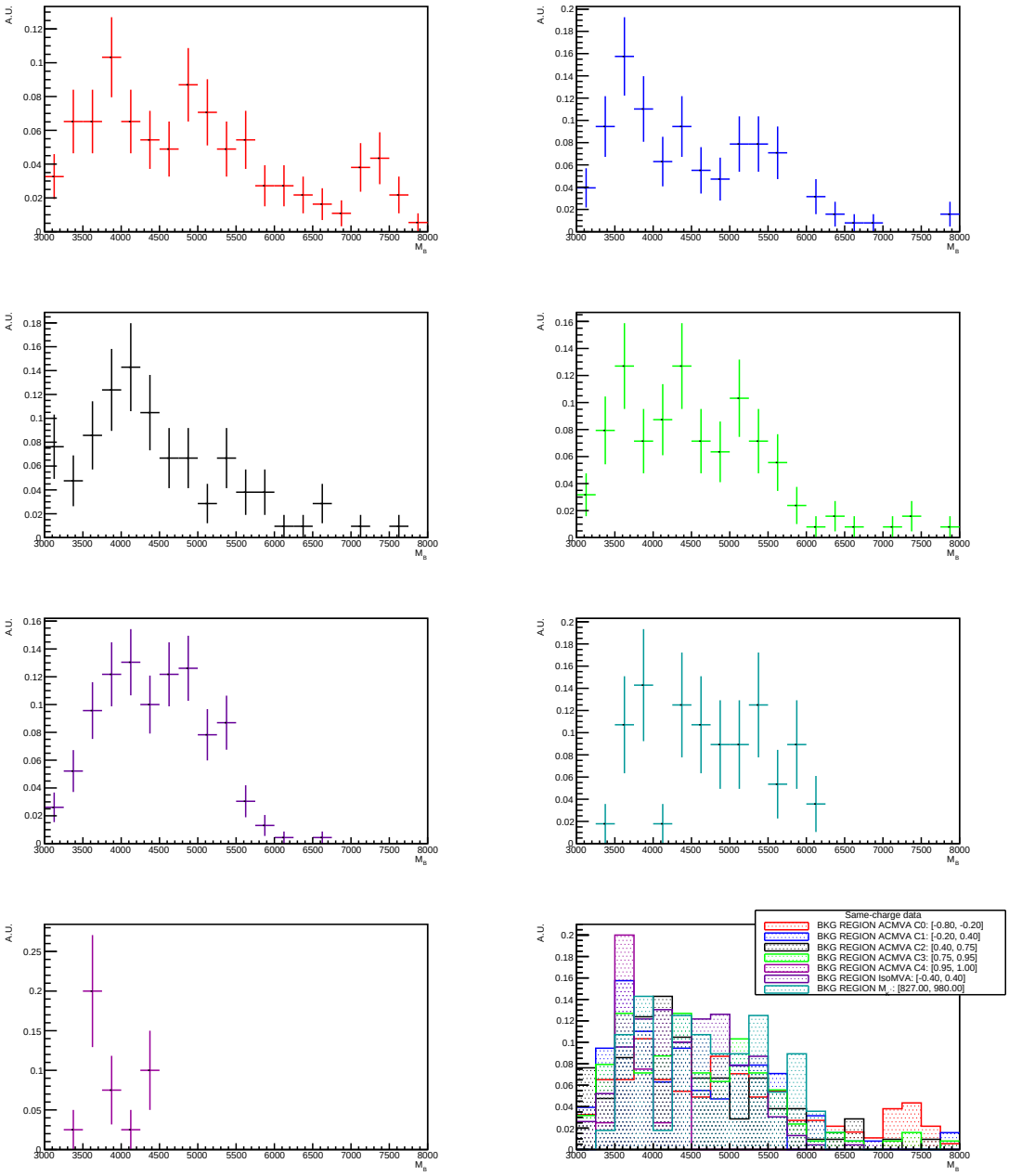

Figure 4.7.4: Distributions of the DTF mass of the candidates for the control sample ACMVA C1 (first row-left), ACMVA C2 (first row-right), ACMVA C3 (second row-left), ACMVA C4 (second row-right), IsoMVA (third row-left), M_{K^*} (third row-right), data sidebands (fourth row-left) and all distributions superimposed (fourth row-right) for SC events.

4.8 Systematic uncertainties

The normalization procedure allows the cancellation of the systematic uncertainties that are present analogously in the signal and in the normalization channel. Other uncertainties have to be correctly assessed. The main ones are associated with the refitted mass reconstruction, the efficiencies evaluation, the normalization channel fit (see Section 4.8.6), the background (see Section 4.8.7) parameterization, and the model used to generate signal events (see Section 4.8.8). Table 4.8.1 summarizes the different systematic components considered in the analysis.

Name	Systematic
Mass reconstruction	Discussed in Section 4.8.1
Tracking efficiency	1.4% for hadron and 0.6% for electron
PID efficiency	[0.3-1.8]% for signal sample and [2.3-3.9]% for normalization sample
Trigger efficiency	[0.4-0.5]% for *eTOS*, [2.8-4.5]% for *TIS*, [1.5-6]% for *hTOS*
Classifier cut efficiency	[0.5-2.2]% for ACMVA, [0.5-3.0]% for IsoMVA, [0.1-2.1]% for TauMVA
Normalization fit	∼0.2%
Background model	Discussed in Section 4.8.7
Signal model	Discussed in Section 4.8.8

Table 4.8.1: List of systematics included in the analysis.

4.8.1 Refitted mass reconstruction

A systematic uncertainty is associated to the mass reconstruction of the signal using the technique of refitting to include the transverse energy carried by the missing neutrino. The $B \to D^- D_s^+$control sample is used to assess this uncertainty. The sample candidates are reconstructed with five tracks in the final state, emulating the missing energy carried by the neutrino from τ decay. Truth-matched MC and data samples undergo fiducial requirements, trigger decisions, particle identification requirements, and cuts on the intermediate charmed meson mass. A fit to the refitted mass in the region [5150,5420] MeV/c^2 is then applied to both simulated and data events surviving the selection. The signal model used for the fit is a DSCB function with symmetric $\sigma = \sigma_R = \sigma_L$. The background component for the fit to data events is instead obtained using an exponential function. Results of the fit are collected in Figure 4.8.1. From data-MC discrepancies on the control sample, the following systematic uncertainties to the simulation are accessed:

- A systematic error is associated to the shift mean $\Delta\mu = |\mu_{MC} - \mu_{data}|$ of the refitted mass;
- A relative error is derived for the resolution as $\frac{\Delta\sigma}{\sigma} = \frac{|\sigma_{MC} - \sigma_{data}|}{\sigma_{MC}}$.

Signal parameters are Gaussian-constrained in the limit evaluation with the sum in quadrature of their fit uncertainties and the previously described errors.

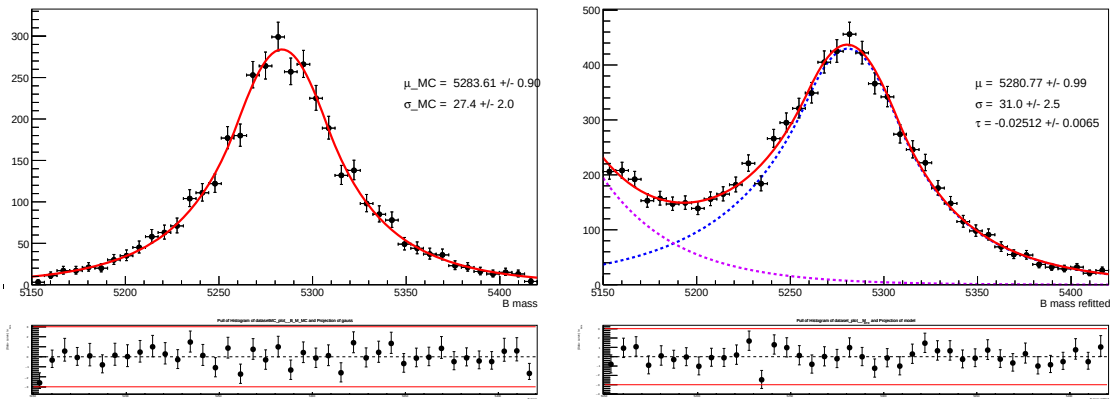

Figure 4.8.1: MC (left) and data (right) events of the control sample with one missing particle in the final state. Underlying fits, with main parameters and pulls, are also shown.

4.8.2 Tracking efficiency

As mentioned in Section 4.6.1, the tracking efficiencies can be separated from the total one by defining $\epsilon = \epsilon^{'}\epsilon_{trk}$. The ratio $k = \frac{\epsilon_{trk}^{signal}}{\epsilon_{trk}^{norm}}$ between the signal tracking efficiency and normalization efficiency enters inside the limit setting. The signal channel's final state comprises five hadrons and one electron, whilst the normalization channel consists of six hadrons. The ratio can be determined from the simulation without corrections for five hadrons in the final state since discrepancies would cancel out in the numerator and denominator. For the sixth hadron of the normalization channel and the electron of the signal, one should consider a correction, as explained in Section 4.6.1. The values of the ratio k are reported in Table 4.9.2 for 2016, Table 4.9.3 for 2017 and Table 4.9.4 for 2018. Systematic uncertainties of 1.4% for the remaining hadron from the normalization channel, evaluated from `TrackCalib` package [216], and 0.6% for the remaining electron (from [214]) from the signal channel are assigned to the ratio.

4.8.3 PID efficiency

While evaluating data-driven efficiencies for particle identification selection, we need to take into account four main sources of systematic uncertainties:

- The statistical uncertainty from the finite size of the simulated sample;
- The statistical uncertainty from the finite size of the calibration sample;
- The choice of the binning scheme used. The efficiencies are re-evaluated starting from different numbers of isopopulated bins. Efficiencies obtained with 8, 9, 11 and 12 bins are tested and compared to the default binning (10). The maximum difference of the efficiencies in these alternative binning schemes with respect to the nominal binning scheme is taken as systematic uncertainty;

- The systematic uncertainty from the sPlot technique used to separate signal from the background in the calibration sample. An uncertainty of 1‰ is assigned (from [217]).

The systematics described above are collected in Table 4.8.2 for signal and normalization simulated samples. The statistical uncertainty is dominant compared to the other uncertainties.

Simulated sample	2016	2017	2018
$B^0 \to K^{*0}\tau^+e^-$ T5 (OC)	$52.8 \pm 1.8 \pm 0.108 \pm 0.80 \pm 0.053$	$61.7 \pm 1.9 \pm 0.072 \pm 0.99 \pm 0.062$	$63.5 \pm 2.1 \pm 0.064 \pm 0.20 \pm 0.064$
$B^0 \to K^{*0}\tau^-e^+$ T5 (SC)	$54.9 \pm 1.7 \pm 0.108 \pm 1.03 \pm 0.055$	$58.1 \pm 1.9 \pm 0.073 \pm 0.75 \pm 0.058$	$57.9 \pm 2.2 \pm 0.065 \pm 0.25 \pm 0.058$
$B^0 \to K^{*0}\tau^+e^-$ T8 (OC)	$55.6 \pm 2.5 \pm 0.107 \pm 1.17 \pm 0.056$	$57.3 \pm 2.4 \pm 0.073 \pm 0.94 \pm 0.057$	$55.0 \pm 2.7 \pm 0.066 \pm 0.27 \pm 0.055$
$B^0 \to K^{*0}\tau^-e^+$ T8 (SC)	$57.8 \pm 2.4 \pm 0.107 \pm 0.99 \pm 0.058$	$57.3 \pm 2.3 \pm 0.073 \pm 0.92 \pm 0.057$	$56.7 \pm 2.6 \pm 0.067 \pm 0.26 \pm 0.057$
$B \to D^-D_s^+$	$34.9 \pm 1.4 \pm 0.004 \pm 1.35 \pm 0.034$	$41.2 \pm 1.5 \pm 0.005 \pm 1.12 \pm 0.041$	$44.2 \pm 1.4 \pm 0.004 \pm 1.01 \pm 0.044$

Table 4.8.2: Efficiency in percentage on the particle identification selection for the different MC simulations (signal T5, signal T8 and normalization samples) for different years. The first uncertainty is statistical; the second is related to the finite size of the calibration sample; the third comes from the choice of the binning scheme, and the last is from the use of the sPlot technique.

4.8.4 Systematic uncertainty on trigger efficiency

The systematic uncertainties related to the data-driven corrected efficiencies for the three categories of the trigger are treated differently for *eTOS* category and for *TIS*/*hTOS* categories. In the first case, systematic uncertainty contributions as evaluated in [50] for the R_K and R_{K^*} analysis are studied. The main sources of systematic uncertainties are related to the finite size of the simulated and data sample, the binning scheme, the choice of the TIS sample for the TISTOS efficiencies evaluation and the factorization of the TOS efficiencies. Regarding the other two trigger categories, we can identify four different origins of uncertainties:

- The finite sizes of data and simulated samples;
- The binning scheme that is chosen to parameterize the efficiencies. The corrected efficiencies are recomputed starting from other numbers of isopopulated bins. The maximum discrepancy with respect to the nominal number of bins is taken as systematic. For the *TIS* category, efficiencies are recomputed with 6, 7, 9 and 10 bins and compared with the nominal 8 bins for every year of data taking (2016/2017/2018), charge (OC/SC) and sample (T5/T8) combination. For the *hTOS* category, the nominal efficiencies calculated in 5 bins are compared with the ones obtained using 4, 6 and 7 bins.
- The correlation between the trigger lines of interest and those used as TAG. This correlation depends on the choice of the TAG sample used for the evaluation of the efficiency via the *TISTOS* method. The difference between the efficiency evaluated using another TAG sample and the nominal efficiency is evaluated using simulation and data to estimate this uncertainty. The alternative TAG sample is chosen as general as possible, excluding the nominal TAG events. The relative differences between efficiencies are evaluated for each bin of the correction. The correction, including these biases, is evaluated, and the difference with the nominal correction is taken as systematic.
- The MC correction to the kinematic of the B for the *TIS* category. The TIS correction depends on the transverse momentum of the reconstructed B. The P_T of the simulation is reweighted using data-driven corrections from $B \to D^- D_s^+$ sample. The efficiencies are re-evaluated after the corrections, and differences from the baseline are taken as systematics.

The systematic uncertainties described above are collected in Table 4.8.3 and Table 4.8.4, respectively, for T5 and T8 simulated samples. The contributions to the systematic uncertainties are assumed to be uncorrelated. Relative contributions from each source are presented as percentages of the total systematic uncertainties in Table

4.8.5 for the T5 channel and in Table 4.8.6 for the T8 channel.

L0 category	2016 OC	2016 SC	2017 OC	2017 SC	2018 OC	2018 SC
eTOS	$45.7 \pm 0.8 \pm 0.2$	$48.6 \pm 0.8 \pm 0.2$	$39.6 \pm 0.7 \pm 0.2$	$46.7 \pm 0.7 \pm 0.2$	$41.8 \pm 0.8 \pm 0.2$	$45.6 \pm 0.8 \pm 0.2$
TIS	$25.1 \pm 1.1 \pm 0.7$	$23.4 \pm 1.0 \pm 0.6$	$32.5 \pm 1.0 \pm 0.8$	$28.9 \pm 1.0 \pm 0.8$	$36.9 \pm 1.2 \pm 0.9$	$37.6 \pm 1.2 \pm 1.1$
hTOS	$7.4 \pm 0.4 \pm 0.4$	$5.5 \pm 0.3 \pm 0.3$	$8.3 \pm 0.3 \pm 0.4$	$5.7 \pm 0.3 \pm 0.2$	$6.7 \pm 0.4 \pm 0.2$	$6.1 \pm 0.4 \pm 0.1$

Table 4.8.3: L0 trigger efficiency uncertainties for the MC simulation T5 sample, for different charge combinations and years of data taking. The measurements of the efficiencies, expressed as percentages, are corrected as described in Section 4.6.2. The first (second) uncertainty refers to the statistical (systematic) uncertainty.

L0 category	2016 OC	2016 SC	2017 OC	2017 SC	2018 OC	2018 SC
eTOS	$44.1 \pm 0.6 \pm 0.2$	$44.7 \pm 0.6 \pm 0.2$	$39.8 \pm 0.6 \pm 0.2$	$42.2 \pm 0.6 \pm 0.2$	$41.4 \pm 0.6 \pm 0.2$	$40.8 \pm 0.6 \pm 0.2$
TIS	$26.8 \pm 0.8 \pm 0.8$	$26.5 \pm 0.8 \pm 0.7$	$32.3 \pm 0.8 \pm 0.9$	$32.3 \pm 1.0 \pm 0.9$	$37.5 \pm 0.9 \pm 1.0$	$37.9 \pm 0.9 \pm 1.2$
hTOS	$7.2 \pm 0.3 \pm 0.4$	$6.7 \pm 0.3 \pm 0.4$	$7.3 \pm 0.3 \pm 0.4$	$6.7 \pm 0.3 \pm 0.2$	$7.6 \pm 0.3 \pm 0.2$	$7.3 \pm 0.3 \pm 0.1$

Table 4.8.4: L0 trigger efficiency uncertainties for the MC simulation T5 sample, for different charge combinations and years of data taking. The measurements of the efficiencies, expressed as percentages, are corrected as described in Section 4.6.2. The first (second) uncertainty refers to the statistical (systematic) uncertainty.

TIS	2016 OC	2016 SC	2017 OC	2017 SC	2018 OC	2018 SC
Binning	84.3%	77.7%	52.0%	70.9%	57.9%	56.2%
Bias	1.1%	0.1%	0.1%	<0.1%	0.9%	0.8%
B kinematics correction	14.6%	22.2%	47.9%	29.1%	41.2%	43.0%
hTOS	2016 OC	2016 SC	2017 OC	2017 SC	2018 OC	2018 SC
Binning	99.9%	99.9%	98.4%	97.8%	$\sim$ 100%	$\sim$ 100%
Bias	0.1%	0.1%	1.6%	2.2%	<0.1%	<0.1%

Table 4.8.5: Relative contributions to *TIS* and *hTOS* trigger efficiency systematics from each source for MC simulation T5 sample.

TIS	2016 OC	2016 SC	2017 OC	2017 SC	2018 OC	2018 SC
Binning	79.2%	81.2%	99.9%	62.2%	95.1%	93.5%
Bias	0.1%	<0.1%	0.1%	0.1%	1.6%	1.2%
B kinematics correction	20.7%	18.8%	<0.1%	37.7%	3.3%	5.3%
hTOS	2016 OC	2016 SC	2017 OC	2017 SC	2018 OC	2018 SC
Binning	99.6%	99.9%	98.4%	96.4%	$\sim$ 100%	$\sim$ 100%
Bias	0.4%	0.1%	1.6%	3.6%	<0.1%	<0.1%

Table 4.8.6: Relative contributions to *TIS* and *hTOS* trigger efficiency systematics from each source for MC simulation T8 sample.

As an additional cross-check, the alignment of the HLT1 selection (`Hlt1TwoTrackMVA`) between data and MC is verified. Truth-matched simulation and data events are extracted from the $B \to D^- D_s^+$ control samples by applying all the selections described in Section 4.5 except for the trigger one. The L0 trigger selection (`L0Hadron_TOS||L0Hadron_TIS`) is then applied to both data and MC. A cut on the reconstructed mass of the B ($\pm 50 \text{MeV/c}^2$ with respect to its PDG value) is applied to extract signal samples, and Table 4.8.7 summarizes the corresponding efficiencies on data, and MC. No significant discrepancy is observed: the differences are within statistical errors. Therefore, no systematic uncertainty is added for the HLT1 selection.

$\epsilon_{HLT1TwoTrackMVA}$	2016	2017	2018
MC	99.17 ± 0.17	99.25 ± 0.15	99.24 ± 0.15
Data	99.25 ± 0.11	99.01 ± 0.13	99.04 ± 0.12

Table 4.8.7: Efficiencies comparison for `Hlt1TwoTrackMVA` for data and truth-matched simulation of $B \to D^- D_s^+$ control sample. No strong discrepancy is observed and no systematic is addressed in this case.

Finally, no systematic uncertainty is associated to the trigger efficiencies for the normalization sample. In that case, efficiencies are evaluated in a data-driven way.

4.8.5 Systematic uncertainty on classifier cuts efficiencies

Systematic errors on the classifier cuts' efficiencies are introduced to consider residual discrepancies between data and simulation. A comparison is performed between

$B \to D^- D_s^+$ data and MC samples for each classifier cut and separately for each year of data taking in the following way:

- Samples are obtained by applying fiducial requirements, trigger decisions, particle identification requirements, and cuts on the mass of the intermediate charmed mesons (± 20 MeV/c^2 around their PDG values) on both truth-matched MC events and data.
- The classifier is applied to the data and MC samples, the value of the cut providing efficiency on the $B \to D^- D_s^+$ MC sample equivalent to the one obtained by the default cut on $B \to K^* \tau e$ simulated sample is identified and applied to the samples.
- Efficiencies from MC are determined as the fraction of events passing the classifier cut in a mass region of [5200,5400] MeV/c^2, where the signal is expected.
- A fit is performed on data in the mass region of [5200,5400] MeV/c^2 before and after the application of the cut. The fit model adopted is a Gaussian for the signal and an exponential for the background. The signal yield is extracted from the fit through the background subtraction procedure. Efficiencies from data are then evaluated as the fraction of signal yields passing the classifier cut.
- The systematic uncertainty is the absolute value of the difference in efficiency between data and MC.

Results on the systematic uncertainties are collected in Table 4.8.8 for different years of data taking.

Selection	Year	$B^0 \to K^{*0}\tau^+e^-$ (T5 oc)	$B^0 \to K^{*0}\tau^-e^+$ (T5 sc)	$B^0 \to K^{*0}\tau^+e^-$ (T8 oc)	$B^0 \to K^{*0}\tau^-e^+$ (T8 sc)
ACBDT	2016	2.2%	1.3%	1.6%	1.5%
	2017	1.9%	1.7%	1.5%	1.5%
	2018	1.0%	0.6%	0.6%	0.5%
IsoFisher	2016	3.0%	3.1%	1.4%	2.0%
	2017	0.7%	0.5%	1.3%	1.0%
	2018	1.4%	1.4%	2.2%	1.8%
TauBDT	2016	2.1%	2.6%	0.6%	0.3%
	2017	0.4%	0.4%	1.6%	1.4%
	2018	0.9%	1.2%	0.2%	0.1%

Table 4.8.8: Classifier cut systematics for $B \to K^*\tau e$ divided divided per year. They are evaluated as discrepancies between data and simulation from $B \to D^-D_s^+$ sample.

4.8.6 Systematic uncertainty on the fit normalization channel fit

One potential source of systematic uncertainty is the fit model employed for obtaining the normalization channel yields. To evaluate this systematic uncertainty, a kernel estimation on the distribution of truth-matched simulated $B \to D^- D_s^+$ events after the selection is performed using a RooKeysPdf [218]. Results are shown in Figure 4.8.2. The distribution is used, in conjunction with the exponential function describing the background, to generate 1000 toys. The number of signal and background events in the toys are left fluctuating following a Poisson distribution.
The simulated datasets are then fitted using the normalization channel fit model (Gaussian for signal and exponential for background). Figure 4.8.3 shows the distribution of the difference between the mean of the Poisson distribution used in the signal generation and the yield resulting from the fit of each toy. A Gaussian fit is applied to these distributions. The ratio between the mean of the Gaussian and the mean of the Poisson distribution used for the toy generation represents the systematic uncertainty on the fit model for the normalization channel. The value of the systematic uncertainty is very small ($\sim 0.2\%$). Table 4.8.9 shows the number of normalization events passing the selection per year of data taking, with statistical and systematic errors associated.

Year	Yield
2016	$2054 \pm 45 \pm 4$
2017	$2086 \pm 45 \pm 4$
2018	$2730 \pm 52 \pm 5$

Table 4.8.9: Normalization yield for each year of data taking. Values are presented with statistical (first) and systematic (second) errors.

4.8.7 Systematic uncertainty on the background model

Three main systematic uncertainties are associated with the background parameterization. The first is related to determining the DSCB parameters from the fits to the control region. In the final fit, these parameters are Gaussian-constrained using values and errors determined in the fit to the control region.
The second one is related to the choice of the control sample. Alternative control regions are used to determine the DSCB parameters used in the fit to the blinded sample, as listed in Table 4.7.2. The fit results are shown in Appendix S. The expected background yields evaluated in the blinded region are shown in Figure 4.8.4 when using parameterizations from the alternative control regions. Given the variety of control samples used for the background parameterization, the following principle is adopted to determine the systematic uncertainties of the parameters. The mean and the sigma of the DSCB model are then Gaussian-constrained using as uncertainty

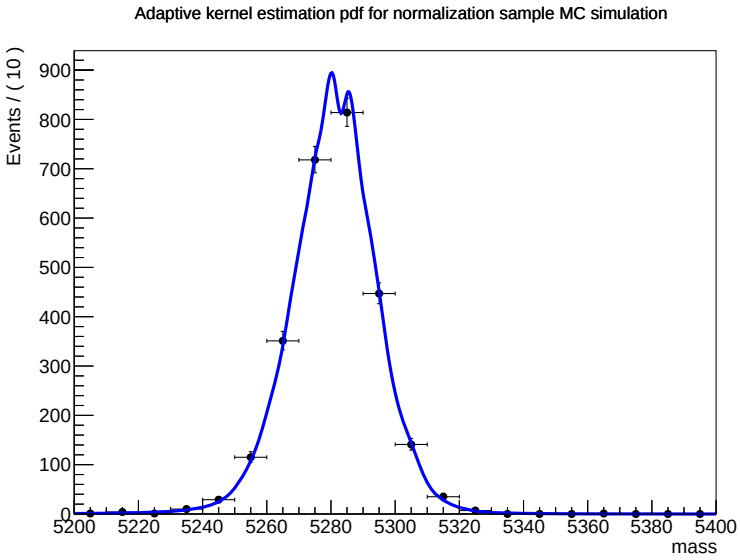

Figure 4.8.2: Kernel estimation for the true signal $B \to D^- D_s^+$ pdf.

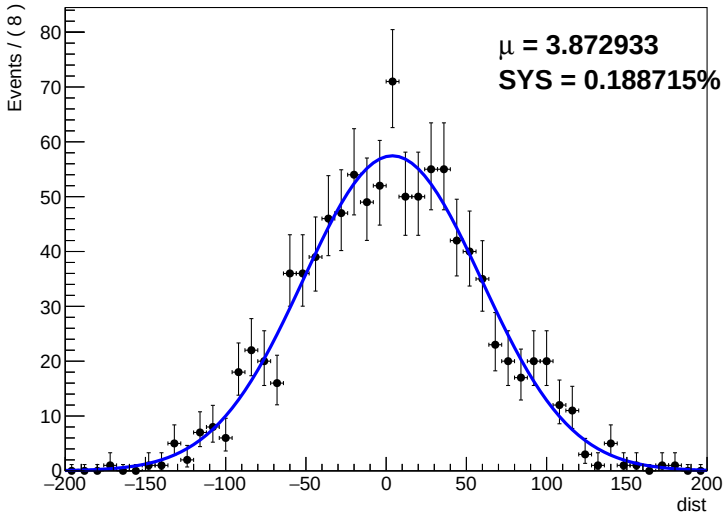

Figure 4.8.3: Distribution of the distance between the mean of the Poisson distribution used in the signal generation and the yield resulting from the fit of each generated toy. The mean of the Gaussian and systematic, evaluated as the ratio of this mean and the mean of the Poisson distribution, are also displayed.

half of the maximum spread of the central values from the fits performed using the alternative control regions. If this value is lower than the uncertainty on the parameter, the latter is used, as shown in Figure 4.8.5. Furthermore, two outliers distributions out of the six control samples are excluded from the evaluation of this uncertainty for each charge combination (ACMVA C1 and IsoMVA for OC, ACMVA C3 and M_{K^*} for SC).

Finally, the systematic uncertainty for the choice of the DSCB as analytic parameter-

ization is estimated using a kernel estimation of the background control samples and fitting them with the default DSCB. A bias term is added to the BR, and its value is constrained to a Gaussian with mean 0 and sigma set to the mean value of the bias distribution from a toy experiment. Results of the toy experiments are shown in Figure 4.8.6 in both cases of generation from DSCB and RooKeysPdf. Pulls to the BRs are shown in Figure 4.8.7. The systematic uncertainty associated with the bias is -1.98×10^{-7} for OC $B^0 \to K^{*0}\tau^+e^-$ events and 4.25×10^{-7} for SC $B^0 \to K^{*0}\tau^-e^+$ events.

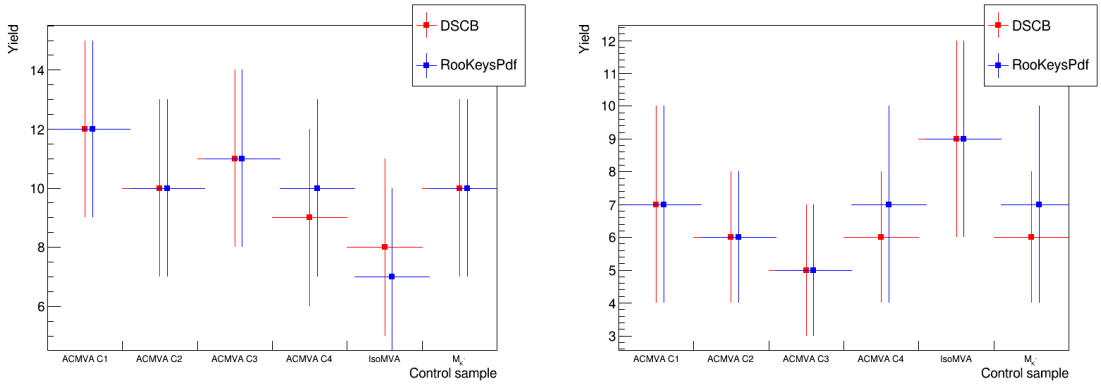

Figure 4.8.4: Background yields expected in the signal region from fit to the data for different control regions and parameterization (DSCB in red and RooKeysPdf in blue). On the right (left), yields are evaluated for opposite-charge (same-charge) data sample. Expected yields are compatible when obtained using DSCB and RooKeysPdf. Moreover, the background yield for various control samples is compatible within 1σ with the reference one (ACMVA C4).

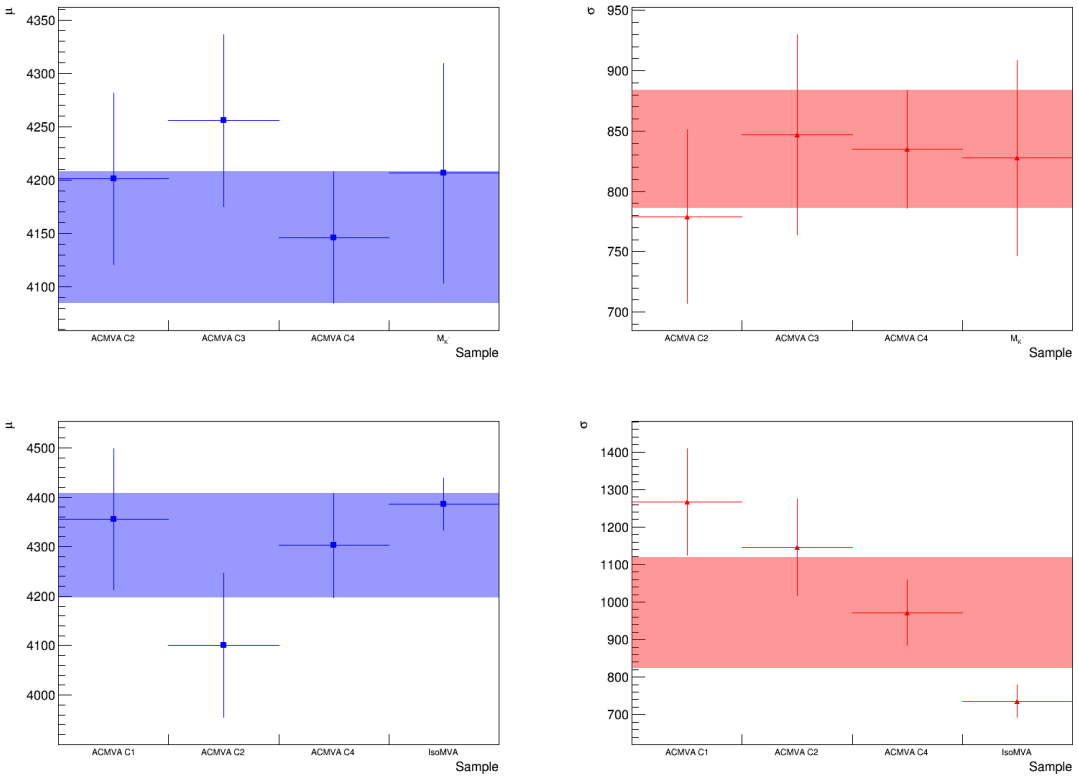

Figure 4.8.5: DSCB parameters for the background modelling fit for the different control samples. The mean (blue) and sigma (red) reference values are taken from the region closer to the signal region obtained by inverting the anti-combinatorial cut (ACMVA C4). The transparent band shows the error used for the Gaussian-constraining parameter values in the limit setting. The width of the bands is evaluated as explained in the text. The first (second) row refers to opposite(same)-charge events.

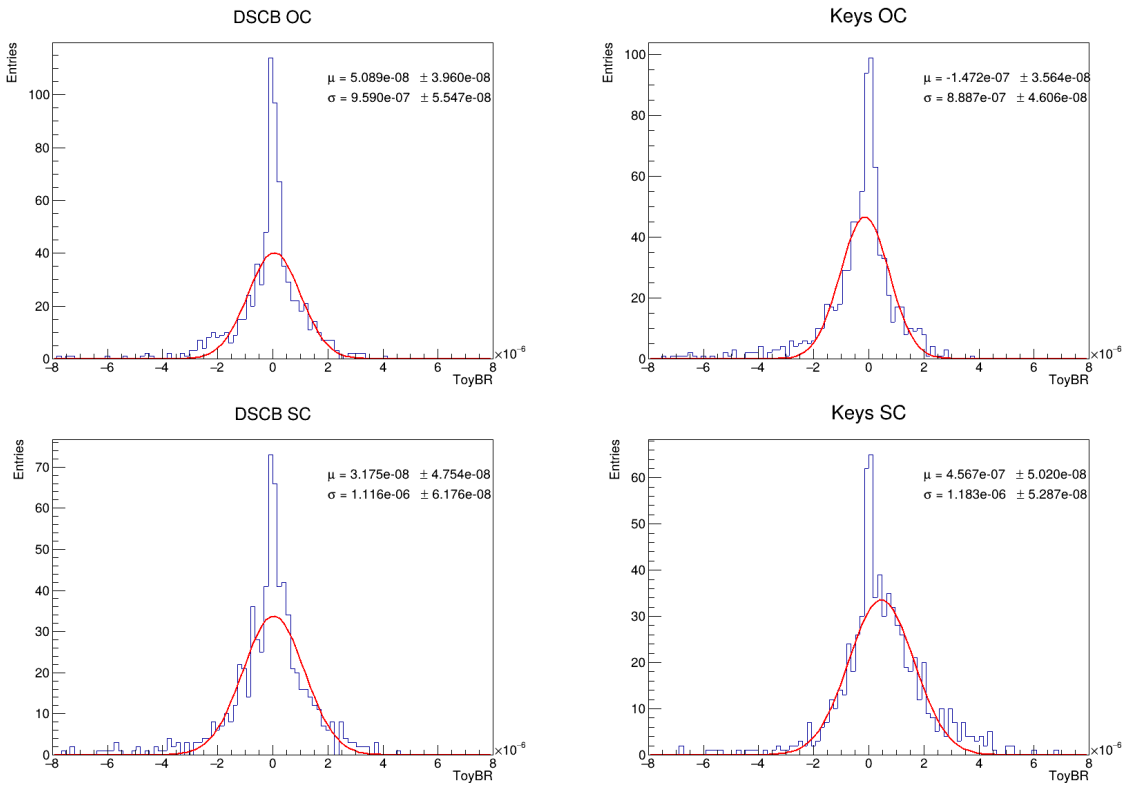

Figure 4.8.6: Distributions of the BR for toys generated from the background only assumption using the DSCB on the left and RooKeysPdf on the right. Generated toys are then fit using the DSCB model. An underlying Gaussian fit shows a mean compatible with 0 within 1σ (2σ) for SC (OC) in the DSCB case, proving no bias in toy generation. The difference between the means of the distributions is taken as systematics. Top (bottom) plots refer to OC (SC) events.

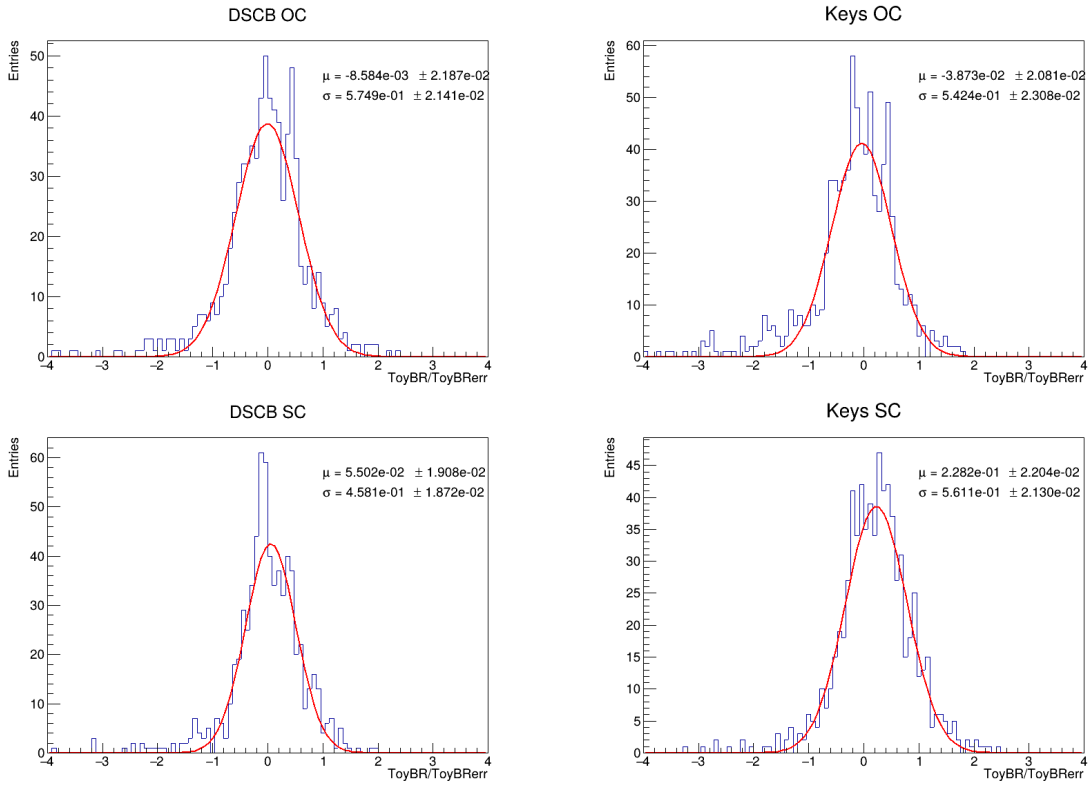

Figure 4.8.7: Distributions of the BR pulls for toys generated from the background only assumption using the DSCB (left) and RooKeysPdf (right) and then with the DSCB model. Pulls are then fit with a Gaussian. Top (bottom) plots refer to OC (SC) events.

4.8.8 Systematic uncertainty on the signal simulation

The topology of the decay is unknown. Therefore, the signal events are simulated under the assumption of a uniform phase space distribution of the K^*, τ, and electron. Instead of associating a systematic error to this premise, we provide the information needed for interpreting the experimental limits in different models. In particular, we provide the efficiency distribution as a function of the relevant kinematic properties, which are the squared invariant mass of $K^{*0}\tau$ and $e\tau$. Efficiencies for different samples T5 and T8 are summed up, weighting for their branching fraction. Efficiencies have been combined over the years, rescaling for the integrated luminosity.
The efficiency on each bin is evaluated by separating generation efficiency and selection efficiency ($\epsilon_{tot} = \epsilon_{gen} \times \epsilon_{sel}$), as described in Equation 4.8.1.

$$(\epsilon_{tot}^{corr})_{bin} = \sum_{years} \sum_{samples} (\epsilon_{gen})_{year,sample} \times \left(\frac{(\epsilon_{sel}^{MC})_{bin}}{\epsilon_{sel}^{MC}} \right)_{year,sample} \times (\epsilon_{sel}^{corr})_{year,sample} \times (w_{bin})_{year,sample} \times (w_{lumi})_{year} \times (w_{BR})_{sample} \tag{4.8.1}$$

where ϵ^{MC} is evaluated directly on the truth-matched simulated sample, while ϵ^{corr} is the efficiency, including data-driven corrections applied in the analysis. Data-driven corrections and generation efficiencies are assumed to be flat all over the phase space. The efficiencies are integrated over *samples* (T5/T8) and *years* (2016, 2017, 2018). The weights are defined as follows:

$$\begin{aligned} w_{bin} &= \frac{(Y_{gen}^{MC})_{bin}}{\sum_{bins} Y_{gen}^{MC}} \\ w_{lumi} &= \frac{\mathcal{L}_{year}}{\sum_{years} \mathcal{L}_{year}} \\ w_{BR} &= \frac{BR_{sample}}{\sum_{samples} BR_{sample}} \end{aligned} \tag{4.8.2}$$

Y_{gen}^{MC} represents the signal yield at generation level, $\mathcal{L}_{year}$ is the integrated luminosity for a given *year* and BR_{sample} is the branching ratio for $\tau \to \pi\pi\pi\nu_\tau$ or $\tau \to \pi\pi\pi\pi^0\nu_\tau$. In this way, the binned efficiencies result normalized to the total one:

$$\sum_{bins} (\epsilon_{tot}^{corr})_{bin} = \epsilon_{tot}^{corr} \tag{4.8.3}$$

The pseudo-Dalitz plots representing the efficiency maps are shown in Figure 4.8.9. The uncertainties referred to the efficiencies for each bin are shown in Figure **??**.

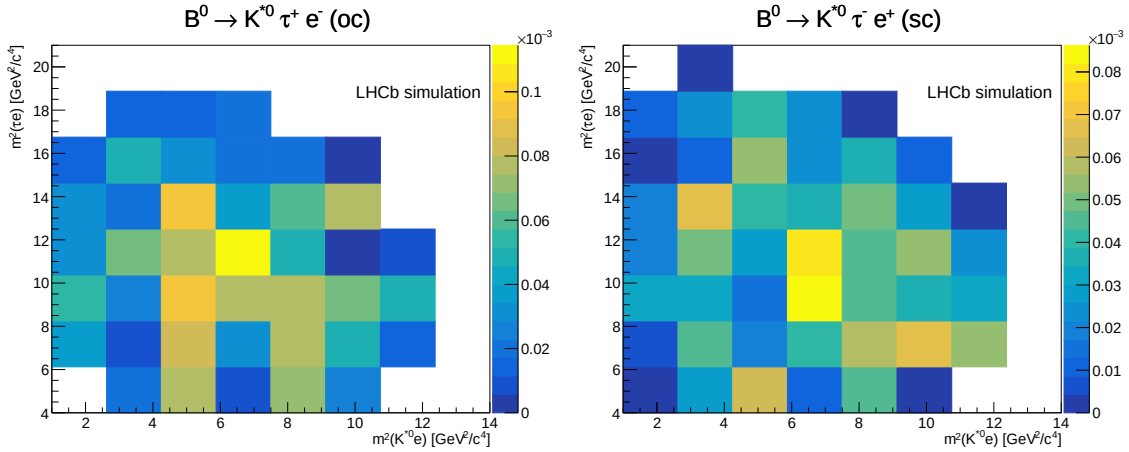

Figure 4.8.8: Efficiency maps as a function of the squared invariant mass of $K^{*0}\tau$ and $e\tau$. Plots are obtained integrating over the years (2016, 2017 or 2018), rescaled by luminosity, and sample (T5 or T8 channels), rescaled by the branching ratios. The left (right) frame refers to the OC (SC).

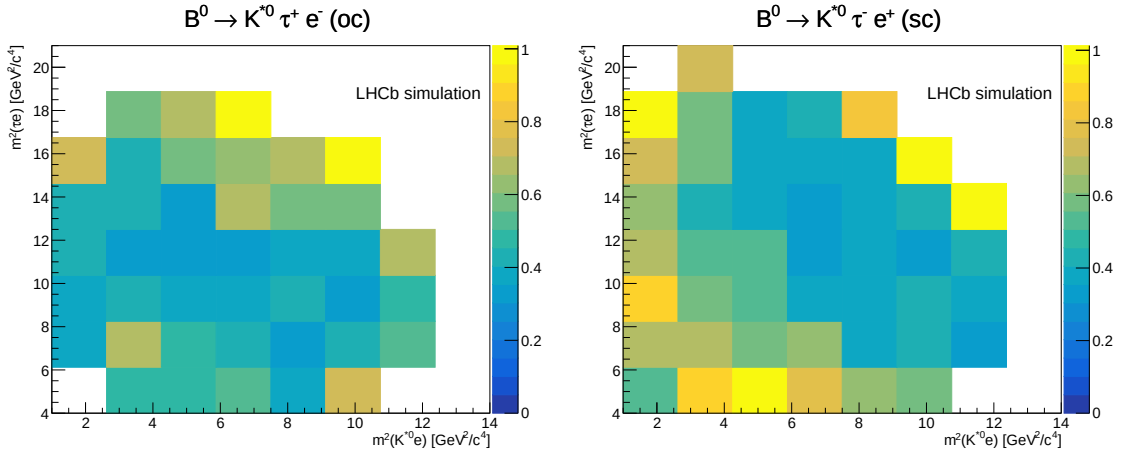

Figure 4.8.9: Relative uncertainties expressed as a fraction of the binned efficiencies shown in Figure 4.8.9. The left (right) frame refers to the OC (SC).

4.9 Results

The results before unblinding are collected in the following Section.

4.9.1 Fit to data

Fit to data is conducted separately for the OC $B^0 \to K^{*0}\tau^+e^-$ and SC $B^0 \to K^{*0}\tau^-e^+$ cases to determine the parameter of interest $BR(B^0 \to K^{*0}\tau e)$, using the signal and background parameterization described in Section 4.7. From the Equation 4.9.1, it is possible to express the signal yields as a function of the *single event sensitivity* α as:

$$\begin{aligned} Y_{5,\gamma} &= BR(B^0 \to K^{*0}\tau e) \times f_5(\gamma) \times \frac{1}{\alpha_5} \\ Y_{5,no\gamma} &= BR(B^0 \to K^{*0}\tau e) \times (1 - f_5(\gamma)) \times \frac{1}{\alpha_5} \\ Y_{8,\gamma} &= BR(B^0 \to K^{*0}\tau e) \times f_8(\gamma) \times \frac{1}{\alpha_8} \\ Y_{8,no\gamma} &= BR(B^0 \to K^{*0}\tau e) \times (1 - f_8(\gamma)) \times \frac{1}{\alpha_8} \end{aligned} \tag{4.9.1}$$

where $f(\gamma)$ is the fraction of signal event of *brem* category (γ index), $1 - f(\gamma)$ is the fraction of signal event of *nobrem* category ($no\gamma$ index) and

$$\begin{aligned} \alpha_5 &= \frac{1}{Y_{norm}} \times \frac{\epsilon^{'}_{norm} BR_{norm}}{k_5 \epsilon^{'}_5 BR_5} \\ \alpha_8 &= \frac{1}{Y_{norm}} \times \frac{\epsilon^{'}_{norm} BR_{norm}}{k_8 \epsilon^{'}_8 BR_8} \end{aligned} \tag{4.9.2}$$

The efficiencies $\epsilon^{'}_{norm}$, $\epsilon^{'}_5$ and $\epsilon^{'}_8$ are obtained by dividing the efficiencies in Section 4.6 by $\epsilon_{reco+str}$. Hence, the coefficient k_5 (k_8) represents the ratio between the signal T5 (T8) and normalization reconstruction and Stripping efficiencies. The branching ratios are defined as:

$$\begin{aligned} BR_5 &= BR(K^{*0} \to K^+\pi^-) \times BR(\tau^\pm \to 3\pi^\pm\nu_\tau) \\ BR_8 &= BR(K^{*0} \to K^+\pi^-) \times BR(\tau^\pm \to 3\pi^\pm\pi^0\nu_\tau) \\ BR_{norm} &= BR(B^0 \to D^-D_s^+) \times BR(D^- \to K^+\pi^-\pi^-) \\ &\quad \times BR(D_s^+ \to K^+K^-\pi^+) \end{aligned} \tag{4.9.3}$$

The values of the efficiencies and single event sensitivities α are presented in Tables 4.6.1 and 4.9.2 for 2016, Tables 4.6.2 and 4.9.3 for 2017 and Tables 4.6.3 and 4.9.4 for 2018, while the branching ratios are collected in Table 4.9.1.

The signal yields are expressed as a function of the parameter of interest $BR(B^0 \to$

Decay	Branching ratio
$B^0 \to D^- D_s^+$	$(7.2 \pm 0.8) \times 10^{-3}$
$D_s^+ \to K^+ K^- \pi^+$	$(9.38 \pm 0.16) \times 10^{-2}$
$D^- \to K^+ \pi^- \pi^-$	$(5.39 \pm 0.15) \times 10^{-2}$
$K^{*0} \to K^+ \pi^-$	$99.902 \pm 0.009\% \times \frac{2}{3}$
$\tau^\pm \to 3\pi^\pm \nu_\tau$	$9.31 \pm 0.05 \times 10^{-2}$
$\tau^\pm \to 3\pi^\pm \pi^0 \nu_\tau$	$4.62 \pm 0.05 \times 10^{-2}$

Table 4.9.1: Branching ratio and their errors for different channels contributing to signal and normalization [206]. The factor $\frac{2}{3}$ for $K^{*0} \to K^+ \pi^-$ comes from the total isospin conservation in strong processes. In this decay, the K^{*0} meson is isospin state $|\frac{1}{2}, -\frac{1}{2}>$, while π^- final state is $|1, -1>$ and K^+ is $|\frac{1}{2}, +\frac{1}{2}>$. The Clebsch-Gordan coefficient for the transition $< 1, -1, \frac{1}{2}, +\frac{1}{2} | \frac{1}{2}, -\frac{1}{2} >$ is $-\sqrt{\frac{2}{3}}$, therefore to calculate the probability amplitude it has to be squared the magnitude.

$K^{*0}\tau e$):

$$
\begin{aligned}
Y_{5,\gamma} &= (BR(B^0 \to K^{*0}\tau e) + biasBR + biasModel) \\
&\times \frac{BR_5}{BR_{norm}} \times \sum^{year} \left(Y_{norm} f_5(\gamma) \frac{\epsilon_5^{'} k_5}{\epsilon_{norm}^{'}} \right)_{year} \\
Y_{5,no\gamma} &= (BR(B^0 \to K^{*0}\tau e) + biasBR + biasModel) \\
&\times \frac{BR_5}{BR_{norm}} \times \sum^{year} \left(Y_{norm} (1 - f_5(\gamma)) \frac{\epsilon_5^{'} k_5}{\epsilon_{norm}^{'}} \right)_{year} \\
Y_{8,\gamma} &= (BR(B^0 \to K^{*0}\tau e) + biasBR + biasModel) \\
&\times \frac{BR_8}{BR_{norm}} \times \sum^{year} \left(Y_{norm} f_8(\gamma) \frac{\epsilon_8^{'} k_8}{\epsilon_{norm}^{'}} \right)_{year} \\
Y_{8,no\gamma} &= (BR(B^0 \to K^{*0}\tau e) + biasBR + biasModel) \\
&\times \frac{BR_8}{BR_{norm}} \times \sum^{year} \left(Y_{norm} (1 - f_8(\gamma)) \frac{\epsilon_8^{'} k_8}{\epsilon_{norm}^{'}} \right)_{year}
\end{aligned}
\tag{4.9.4}
$$

The background yields are floated, while all the other parameters are Gaussian-constrained, adding systematic and statistical errors in quadrature. The DSCB background shape parameters and the $biasModel$ are constrained as described in Section 4.8.7. The parameter $biasBR$ accounts for the bias observed in the fit procedure and is subtracted from the measurements. $biasBR$, is now evaluated as a bias term from MC toy generation and it will be evaluated after the unblinding for the OC and SC cases.

The fits to the blinded distribution of the invariant mass for the candidates remaining after the selection are shown in Figure 4.9.1 for the SC $B^0 \to K^{*0}\tau^- e^+$ and OC $B^0 \to K^{*0}\tau^+ e^-$ cases. Plots refer to the case when no systematic is included, and the background parameters are left floating. Figure 4.9.2 shows the distribution when considering all the systematic included and parameters Gaussian-constrained.

Decay channel	$B^0 \to K^{*0}\tau^+e^-$ (T5 oc)	$B^0 \to K^{*0}\tau^-e^+$ (T5 sc)	$B^0 \to K^{*0}\tau^+e^-$ (T8 oc)	$B^0 \to K^{*0}\tau^-e^+$ (T8 sc)
k	0.837 ± 0.017	0.891 ± 0.016	1.659 ± 0.021	1.648 ± 0.027
$\epsilon^{'}$	$0.00334 \pm 0.00047\%$	$0.00282 \pm 0.00030\%$	$0.000339 \pm 0.000044\%$	$0.000267 \pm 0.000038\%$
α	$(1.69 \pm 0.32) \times 10^{-6}$	$(2.31 \pm 0.42) \times 10^{-6}$	$(1.69 \pm 0.315) \times 10^{-5}$	$(2.17 \pm 0.41) \times 10^{-5}$

Table 4.9.2: Summary of sensitivities for the year 2016 for T5 ($\tau \to \pi\pi\pi\nu_\tau$) and T8 ($\tau \to \pi\pi\pi\pi^0\nu_\tau$) signal separated for charge categories. Statistical uncertainties are associated with the measures. k and $\epsilon^{'}$ parameters are also shown.

Decay channel	$B^0 \to K^{*0}\tau^+e^-$ (T5 oc)	$B^0 \to K^{*0}\tau^-e^+$ (T5 sc)	$B^0 \to K^{*0}\tau^+e^-$ (T8 oc)	$B^0 \to K^{*0}\tau^-e^+$ (T8 sc)
k	0.830 ± 0.013	0.903 ± 0.013	1.674 ± 0.022	1.673 ± 0.022
$\epsilon^{'}$	$0.00386 \pm 0.00044\%$	$0.00271 \pm 0.00032\%$	$0.000394 \pm 0.000048\%$	$0.000343 \pm 0.000044\%$
α	$(1.53 \pm 0.21) \times 10^{-6}$	$(2.06 \pm 0.35) \times 10^{-6}$	$(1.54 \pm 0.27) \times 10^{-5}$	$(1.76 \pm 0.32) \times 10^{-5}$

Table 4.9.3: Summary of sensitivities for the year 2017 for T5 ($\tau \to \pi\pi\pi\nu_\tau$) and T8 ($\tau \to \pi\pi\pi\pi^0\nu_\tau$) signal separated for charge categories. Statistical uncertainties are associated with the measures. k and $\epsilon^{'}$ parameters are also shown.

Decay channel	$B^0 \to K^{*0}\tau^+e^-$ (T5 oc)	$B^0 \to K^{*0}\tau^-e^+$ (T5 sc)	$B^0 \to K^{*0}\tau^+e^-$ (T8 oc)	$B^0 \to K^{*0}\tau^-e^+$ (T8 sc)
k	0.841 ± 0.013	0.911 ± 0.013	1.683 ± 0.022	1.667 ± 0.022
$\epsilon^{'}$	$0.00448 \pm 0.00043\%$	$0.00282 \pm 0.00030\%$	$0.000320 \pm 0.000037\%$	$0.000344 \pm 0.000044\%$
α	$(1.16 \pm 0.18) \times 10^{-6}$	$(1.70 \pm 0.27) \times 10^{-6}$	$(1.63 \pm 0.28) \times 10^{-5}$	$(1.40 \pm 0.23) \times 10^{-5}$

Table 4.9.4: Summary of sensitivities for the year 2018 for T5 ($\tau \to \pi\pi\pi\nu_\tau$) and T8 ($\tau \to \pi\pi\pi\pi^0\nu_\tau$) signal separated for charge categories. Statistical uncertainties are associated with the measures. k and $\epsilon^{'}$ parameters are also shown.

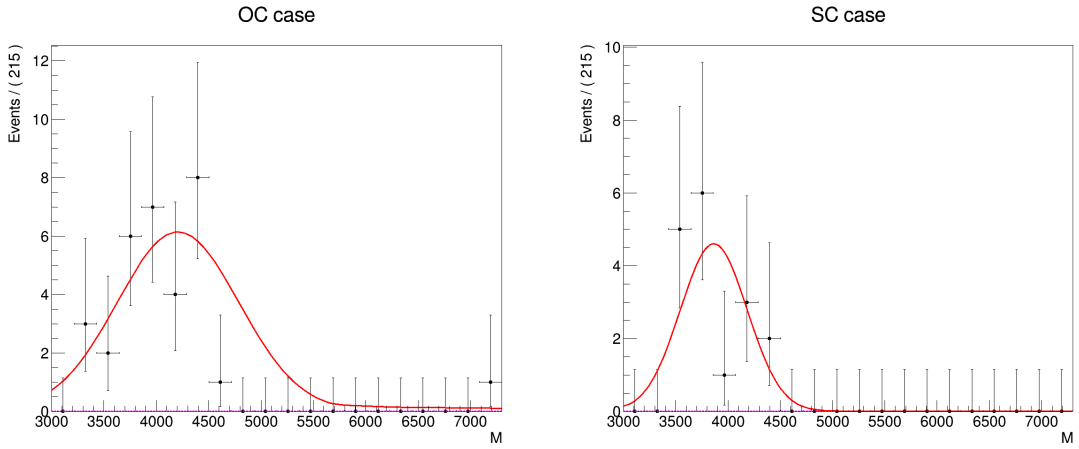

Figure 4.9.1: Fits to the invariant mass blinded for OC (left) and SC (right) events, leaving background parameters floating and without the inclusion of systematic uncertainties.

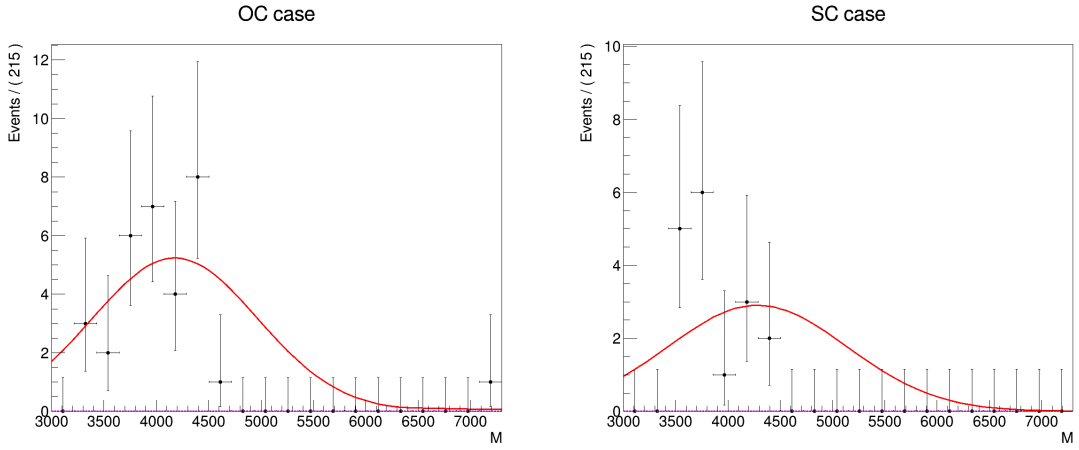

Figure 4.9.2: Fits to the invariant mass blinded for OC (left) and SC (right) events, including of systematics to the fit and Gaussian constraining the parameters.

4.9.2 Expected limits

The expected limits are estimated using the CLs method with asymptotic approximation. The events are divided in OC and SC and limit are evaluated on two toys MC, one for each charge combination. These toys are produced with background only hypothesis. Results of the fit to the distribution of the refitted mass of the toys are shown in Figure 4.9.3. Example of toys generated with a signal branching ratio of 3×10^{-6}, are reported in Figure 4.9.4 for the OC ($B^0 \to K^{*0}\tau^+e^-$) and SC ($B^0 \to K^{*0}\tau^-e^+$) decays. The expected limits are shown in Figure 4.9.5, where no systematic errors have been included. The 1σ (green) and 2σ (yellow) bands are shown. The effects on the expected limit produced by considering each systematic uncertainty sequentially, adding each systematic on top of the previous one, is collected in Table

4.9.5. The systematics considered are the following:

- *branching ratio*, on the BR in Eq. 4.9.3 and extracted from the PDG [206];
- *normalization yield*, as evaluated in Section 4.8.6;
- *efficiencies*, including both statistical and systematic effects (calculated in Sections 4.8.2, 4.8.4 and 4.8.5);
- *background parameterization*, which includes the fit parameters error and the choice of the control sample, as described in Section 4.8.7;
- *signal parameterization*, including the signal fit parameters uncertainties and the effect on mean and resolution of the mass reconstructed using the DTF method as described in Section 4.8.1;
- *bias model*, related to the choice of DSCB model for the background parameterization (see Section 4.8.7);
- *biasBR*, evaluated on toy MC generation. It will be re-evaluated once data will be unblinded.

The expected limit with the inclusion of systematic effects is produced and shown in Figure 4.9.6.

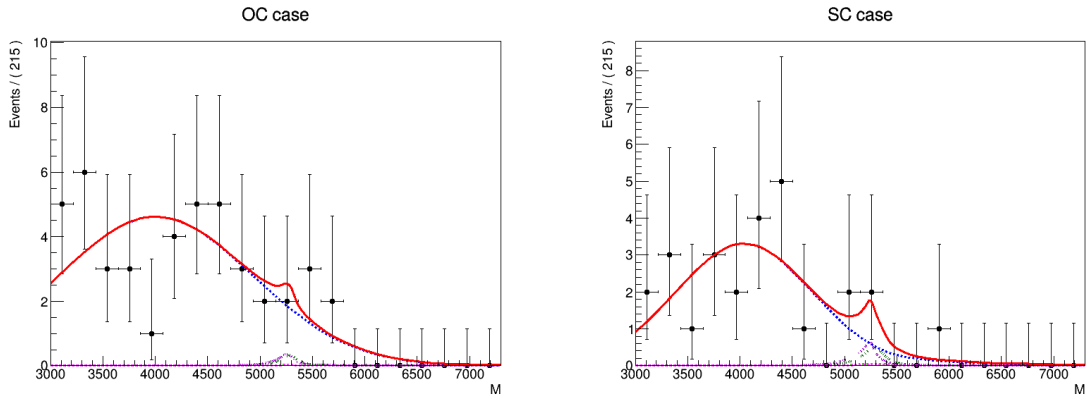

Figure 4.9.3: Fit to distributions of the refitted mass from toys MC used to estimate the limit for opposite charge (left) and same charge (right) cases. They are produced without signal hypothesis and and no systematic is included. In both cases, projections of background components are shown with dashed blue lines, while the four signal components are shown in dashed green lines for T5 *brem* category, dotted green lines for T8 *brem* category, dashed violet lines for T5 *nobrem* category and dotted green lines for T8 *nobrem* category.

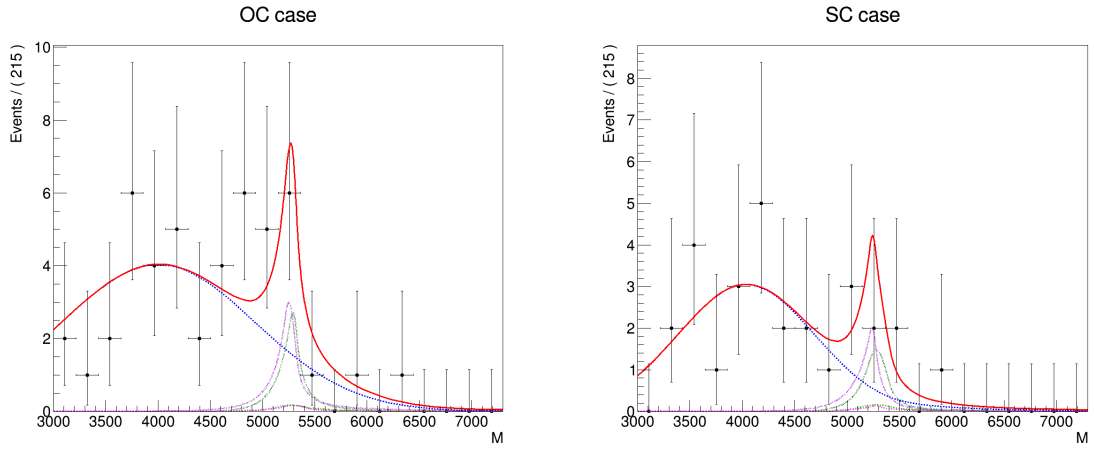

Figure 4.9.4: Fit to example to refitted mass from toys MC generated with a signal hypothesis of $BR(B^0 \to K^{*0}\tau e) = 3 \times 10^{-6}$ for opposite charge (left) and same charge (right) cases. In both cases, projections of background components are shown with dashed blue lines, while the four signal components are shown in dashed green lines for T5 *brem* category, dotted green lines for T8 *brem* category, dashed violet lines for T5 *nobrem* category and dotted green lines for T8 *nobrem* category.

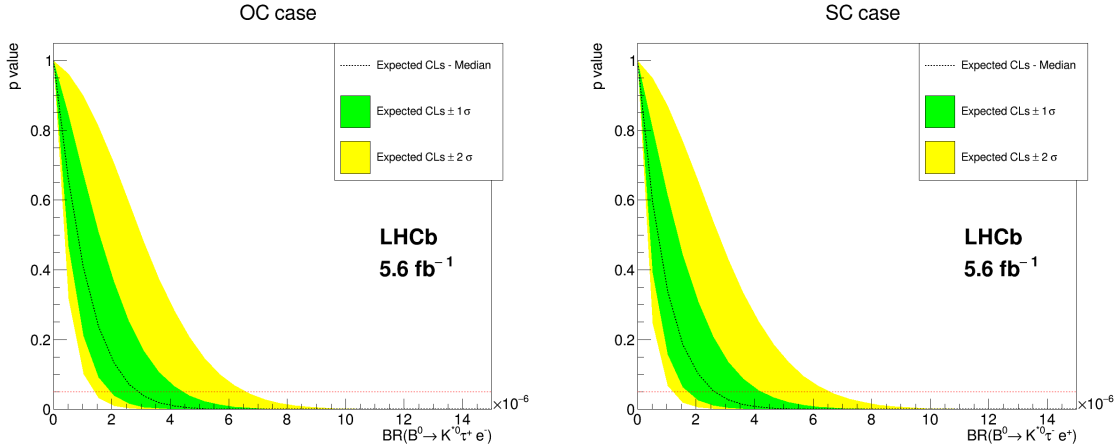

Figure 4.9.5: Expected limits obtained for opposite charge (left) and same charge (right) cases. Limits are obtained without including any systematic. Green (yellow) bands represent 1σ (2σ) uncertainty

Systematic	$B^0 \to K^{*0}\tau^+e^-$	$B^0 \to K^{*0}\tau^-e^+$
No systematic	$2.3(2.9) \times 10^{-6}$	$2.1(2.7) \times 10^{-6}$
BR errors	$2.4(3.0) \times 10^{-6}$ (+1.7%)	$2.1(2.7) \times 10^{-6}$ (+1.9%)
Normalization yield	$2.4(3.0) \times 10^{-6}$ (<0.1%)	$2.1(2.7) \times 10^{-6}$ (<0.1%)
Efficiency	$2.4(3.0) \times 10^{-6}$ (+1.9%)	$2.2(2.8) \times 10^{-6}$ (+3.3%)
Background parameterization	$2.8(3.5) \times 10^{-6}$ (+14.4%)	$2.6(3.3) \times 10^{-6}$ (+19.5%)
Signal parameterization	$2.8(3.5) \times 10^{-6}$ (+1.5%)	$2.6(3.4) \times 10^{-6}$ (+0.3%)
Bias model	$2.7(3.4) \times 10^{-6}$ (-2.8%)	$2.7(3.5) \times 10^{-6}$ (+3.2%)
BiasBR	$2.8(3.5) \times 10^{-6}$ (+1.8%)	$2.8(3.5) \times 10^{-6}$ (+0.9%)

Table 4.9.5: Effects on the expected limit degradation, including each component of the statistical and systematic uncertainties. The limit is estimated at 90%(95%) CL. The changes, in red, are expressed as percentages with respect to the limit evaluated in the previous step at 95% CL.

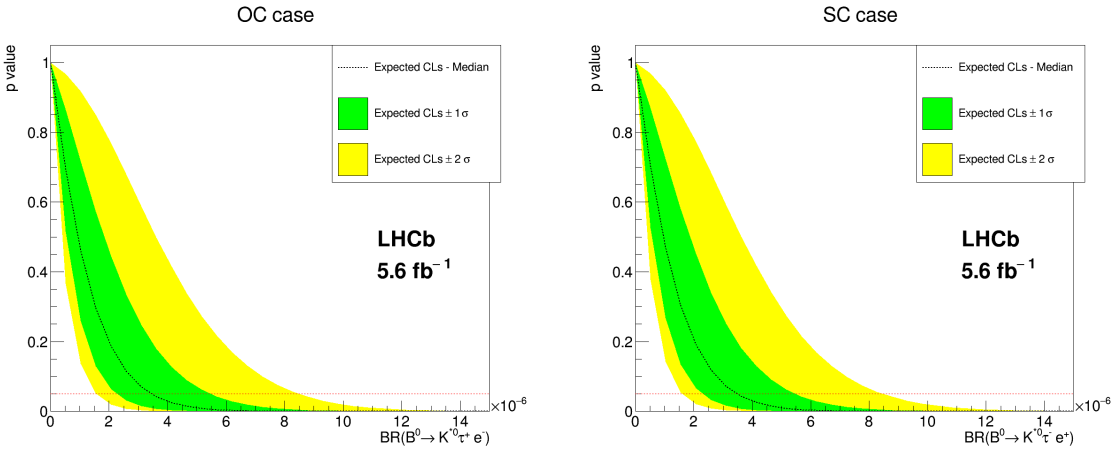

Figure 4.9.6: Expected limits obtained for opposite charge (left) and same charge (right) cases. Limits are obtained by considering all the systematics as Gaussian constraints. Green (yellow) bands represent 1σ (2σ) uncertainty

Conclusion

The work done during my PhD has been summarized and discussed in this thesis. It was split almost equally into software developments and implementation in the context of the online and offline processing of data for the LHCb Upgrade and analysis of data collected by the LHCb detector to search for the charged lepton flavour violating decays $B^0 \to K^{*0}\tau^{\pm}e^{\mp}$.

Concerning my contributions to the software for the LHCb Upgrade, one aspect is related to the development and documentation of ThOr functors and algorithms that use these structures. Within the LHCb Upgrade software, these functors play a crucial role in online and offline processing. In fact, analysts can use these tools to select and retrieve variables to analyse data for Run 3. I worked on the functors' logic simplification to allow users to define their own functor according to their needs. I also improved and extended the related documentation. In addition, I created a pipeline for the computation of the isolation quantities for the LHCb Upgrade, with direct application in many analyses, including the rarest like lepton flavour violating searches. Several analyses from different working groups currently employ this pipeline to save the information from the rest of the event online and to evaluate the isolation variables offline. Finally, my last activity in the LHCb Upgrade software concerned preparing trigger selections for numerous physics channels of the Rare Decays working group. The trigger selection has been optimized based on experience from past years, considering the bandwidth limitations expected in the LHCb Upgrade. Further improvements on these selections are expected from offline studies on data that are being collected.

The search for Lepton Flavour Violating decays $B^0 \to K^{*0}\tau^{\pm}e^{\mp}$ presented the challenge of reconstructing an electron and a tau lepton at the LHCb. It is the first search of such a decay in LHCb. The challenge has been faced through an efficient reconstruction method and well-optimized selections. The analysis has been conducted by dividing the dataset into charge combinations depending on the relative electric charge of the kaon and the electron. A very good sensitivity has been achieved, with an expected upper limit on the branching ratios of these decays of the order of $\mathcal{O}(10^{-6})$ for both charge combinations. This is comparable with analogous searches

with a muon instead of an electron in the final state, despite the additional challenges brought by the reconstruction of electrons in LHCb. Some systematic uncertainties are still under evaluation. Although some degradation of the upper limits is expected when including the systematics uncertainties, the sensitivity of the limit will probably remain of the same order of magnitude. The dataset will be unblinded after finalising the review process within the LHCb experiment.

Assuming the same detector performances and analysis strategy and efficiencies as in Run 2, the sensitivity of the search for $B^0 \to K^{*0}\tau^{\pm}e^{\mp}$ decay can be extrapolated for different values of the integrated luminosity $\mathcal{L}$, rescaling by a factor $\frac{1}{\sqrt{\mathcal{L}}}$. Table 4.9.6 reports these hypothetical sensitivities in different conditions, including the High Luminosity scenario. Further improvements are expected by the removal of the hardware trigger in Run 3, which will lead to a higher trigger efficiency and the removal of the related systematic uncertainties, and by the improved performances of the LHCb Upgrade detector.

Integrated luminosity	$B^0 \to K^{*0}\tau^{\pm}e^{\mp}$ bound
2016+2017+2018 (5.6fb^{-1})	$\sim 3 \times 10^{-6}$
Run 3 (14fb^{-1})	$\sim 2 \times 10^{-6}$
Run 4 (50fb^{-1})	$\sim 1 \times 10^{-6}$
Run 5+6 (450fb^{-1})	$\sim 3 \times 10^{-7}$

Table 4.9.6: Prospects of sensitivities to the bound at 90% CL on $B^0 \to K^{*0}\tau^{\pm}e^{\mp}$ decay, assuming similar performances of the detector for different data-taking periods. The current bounds are the ones expected from the analysis discussed in this thesis.

Appendices

Appendix A

The Standard Model formalism

As relativistic Quantum Field Theory (QFT), the SM acts in different kinds of fields:

- **Dirac spinor field** ψ, which corresponds to fermion field with spin-$\frac{1}{2}$. The Dirac spinor represents the components of elementary fermions. An important representation is the Dirac adjoint $\bar{\psi} = \psi^\dagger \gamma^0$, where $\psi^\dagger$ is the Hermitian adjoint of ψ and γ^0 is the time-like gamma matrix. The Lagrangian for the spinor field ψ is (in natural unit):
$$\mathcal{L} = i\bar{\psi}\gamma^\mu \partial_\mu \psi - m\bar{\psi}\psi \tag{A.0.1}$$
composed by a first kinetic term and a second mass term.

- **Scalar field** ϕ, which corresponds to boson field with spin-0. The Lagrangian describing the field is (in natural unit):
$$\mathcal{L} = \frac{1}{2}(\partial_\mu \phi)(\partial^\mu \phi) - \frac{1}{2}m^2\phi^2 \tag{A.0.2}$$

- **Vector field** A^μ, which correspond to boson field with spin-1. Similarly to the case of a scalar field, for a vector field A^μ it is possible to write a Lagrangian (in natural unit):
$$\mathcal{L} = -\frac{1}{16\pi}F^{\mu\nu}F_{\mu\nu} + \frac{1}{8\pi}m^2 A^\nu A_\nu \tag{A.0.3}$$
where $F^{\mu\nu} = \partial^\mu A^\nu - \partial^\nu A^\mu$ and the field equation becomes:
$$\partial_\mu F^{\mu\nu} + m^2 A^\nu = 0 \tag{A.0.4}$$

The free Dirac Lagrangian is invariant under global phase transformation but not under the local one. To guarantee the property of invariance under local phase transformation, a new term, which includes massless boson fields responsible for interactions, has to be added to the Lagrangian. Some of these massless fields acquire masses thanks to the Higgs mechanism (see Appendix C).

The entire SM Lagrangian encrypts the dynamics of fermions and bosons. It could be decomposed into three parts:

$$\mathcal{L} = \mathcal{L}_g + \mathcal{L}_f + \mathcal{L}_h \tag{A.0.5}$$

Where:

- $\mathcal{L}_g$ includes the kinetic and the self-interaction term of gauge bosons;
- $\mathcal{L}_f$ includes the kinetic of fermions and their interaction with gauge bosons;
- $\mathcal{L}_h$ is the Higgs boson sector, and it contains the masses of the particles.

Appendix B

Gauge invariance

A global symmetry is a symmetry that keeps properties invariant under transformation simultaneously applied at all points of space-time. In contrast, a local symmetry transformation is parameterized by space-time coordinates [219]. Gauge symmetry is a particular kind of symmetry under a gauge transformation[1]. The symmetries of a particular theory are encapsulated inside the gauge transformation that characterizes the gauge group and describes the invariant quantities of the physics.

For the abelian group $U(1)$, a global gauge transformation is a phase transformation of a field ψ such as:

$$\begin{aligned} \psi &\to \psi' = e^{i\alpha}\psi \\ \bar{\psi} &\to \bar{\psi}' = e^{-i\alpha}\bar{\psi} \end{aligned} \tag{B.0.1}$$

For α scalar number with the same value in each space-time point. If the value of α is a function of the phase-time point x, the gauge transformation is local and:

$$\begin{aligned} \psi &\to \psi' = e^{i\alpha(x)}\psi \\ \bar{\psi} &\to \bar{\psi}' = e^{-i\alpha(x)}\bar{\psi} \end{aligned} \tag{B.0.2}$$

For local gauge transformation, the derivative does not transform as the wavefunction; therefore, the Lagrangian is not invariant under local gauge transformation. Since the Lagrangian transforms as:

$$\mathcal{L} \to \mathcal{L}' = \mathcal{L} - (\bar{\psi}\gamma^{\mu}\psi)\partial_{\mu}\alpha(x) \tag{B.0.3}$$

Introducing a term in the complete Lagrangian that soaks up this extra term is

[1]The term gauge refers to the arbitrary choice of axis in the time-space

necessary. With the introduction a new field A_μ, which transforms as:

$$A_\mu \to A_{\mu'} = A_\mu - \frac{1}{q}\partial_\mu \alpha(x) \tag{B.0.4}$$

where q is the coupling constant that characterizes the field, it is possible to obtain a Lagrangian which is now locally invariant:

$$\mathcal{L} = [i\bar{\psi}\gamma^\mu \partial_\mu \psi - m\bar{\psi}\psi] - q\bar{\psi}\gamma^\mu \psi A_\mu \tag{B.0.5}$$

It is also possible to say that the original free Dirac Lagrangian is locally invariant under gauge transformation, only replacing the derivative with the newly defined "covariant" derivative:

$$\mathcal{D}_\mu = \partial_\mu + iqA_\mu \tag{B.0.6}$$

which introduce the vector field A_μ.

For example, the problem could be generalized for other symmetry groups in the non-abelian $SU(2)$ group case. In this case, it is possible to use the convention of representation of isospin doublet $\psi = \binom{\psi_1}{\psi_2}$ obtained by the combination of two Dirac spinor field ψ_1 and ψ_2 into a two-components column vector. The adjoint spinor will be $\bar{\psi} = (\bar{\psi}_1\, \bar{\psi}_2)$ and, under a local gauge transformation $\epsilon(x)$, they change as:

$$\begin{aligned} \psi &\to \psi' = e^{i\frac{\sigma_a}{2}\epsilon^a(x)}\psi \\ \bar{\psi} &\to \bar{\psi}' = e^{-i\frac{\sigma_a}{2}\epsilon^a(x)}\bar{\psi} \end{aligned} \tag{B.0.7}$$

where $a = 1, 2, 3$ and σ_a are the Pauli matrices. Proceeding in the same way as done before, it is possible to prove that the Lagrangian is invariant under local gauge transformation only if the following covariant derivative replaces the derivative:

$$\mathcal{D}_\mu = \partial_\mu + iqA^a_\mu \frac{\sigma_a}{2} \tag{B.0.8}$$

with the introduction of three new vector field A^a_μ $(a = 1, 2, 3)$ that transform as:

$$A_\mu \to A_{\mu'} = A_\mu - \frac{1}{q}\partial_\mu \epsilon^a(x) + \epsilon^a_{bc}\epsilon^b(x)A^c_\mu \tag{B.0.9}$$

where ϵ^a_{bc} is the *structure constant* of the group. Compared with Equation B.0.4, an extra term is associated with the non-commutative property of the Pauli matrices σ_a. This implies that an interaction exists between the vector fields. It is important to note that invariance is guaranteed only if the newly introduced field is massless.

Appendix C

Spontaneous symmetry breaking and the Higgs boson

The mechanism that allows the mediators of the weak interaction to become massive and the mediator of the electromagnetic interaction to remain massless is called SSB. The SSB is an excellent and elegant solution that allows keeping the Lagrangian invariant under gauge transformation $SU(2)_L \times U(1)_Y$ by the introduction of a new scalar Higgs field ϕ whose ground state breaks the $SU(2)_L$ symmetry.

When we consider the mass term in the Lagrangian written in Equation 1.1.4, we have:

$$m\bar{\psi}\psi = m(\bar{\psi}_R\psi_L + \bar{\psi}_L\psi_R) \tag{C.0.1}$$

Where ψ_L and ψ_R are the left-handed and right-handed components of the Dirac spinor ψ[1]. Such a term explicitly breaks symmetry for the $SU(2)_L$ gauge group because the left-handed components belong to a doublet representation of weak isospin, while right-handed components behave as singlets. To avoid explicitly breaking the gauge symmetries, the masses of the intermediate weak bosons and fermions are dynamically generated through their interaction with the newly introduced Higgs scalar field.

The introduction of the spin-0 Higgs field ϕ changes the SM Lagrangian with the new

[1]The chirality of the particle is a property which distinguishes fermion fields ψ in right-handed and left-handed components by respectively applying right-handed and left-handed projection operators:

$$\begin{aligned} \psi_R &= P_R\psi = \left(\frac{1+\gamma^5}{2}\right)\psi \\ \psi_L &= P_L\psi = \left(\frac{1-\gamma^5}{2}\right)\psi \end{aligned} \tag{C.0.2}$$

In the case of massless particles, it corresponds to the particle's helicity

term $\mathcal{L}_h$:

$$\begin{aligned}\mathcal{L}_h &= (\nabla_\mu \phi)^\dagger (\nabla^\mu \phi) - V(\phi) \\ &= (\nabla_\mu \phi)^\dagger (\nabla^\mu \phi) - \mu^2 \phi^\dagger \phi - \lambda (\phi^\dagger \phi)^2\end{aligned} \tag{C.0.3}$$

where μ and λ are complex constant. The potential assumes a parabolic shape for $\mu^2 > 0$ and the characteristic form of "Mexican hat" for $\mu^2 < 0$. In this case, the ground state with $\phi = 0$ corresponds only to a local minimum, and the set of global minima corresponds to all those values of ϕ such that $\phi^\dagger \phi = -\frac{\mu^2}{2\lambda}$. Even if one value is chosen for the minimum, the $SU(2)$ symmetry guarantees that any other minimum point can be reached using a gauge transformation in this group. The ground state is chosen to be:

$$\phi_0 = \sqrt{\frac{1}{2}} \begin{pmatrix} 0 \\ v \end{pmatrix} \text{ , with } v = \sqrt{\frac{-\mu^2}{\lambda}} \tag{C.0.4}$$

where v is the *vacuum expectation value* of the Higgs field. The choice of the vacuum doesn't share the symmetry of the Lagrangian in Equation C.0.3, leading to the spontaneous break of the $SU(2)$ symmetry. Symmetry-breaking is spontaneous because no external factor is responsible, and it happens just for the arbitrary selection of a particular ground state. The SSB just considered is a discrete symmetry[2]. The situation is more interesting in the case of continuous symmetries[3]. According to the Goldstone theorem [220], the spontaneous breaking of a continuous global symmetry will be accompanied by the appearance of one or more massless scalar (spin-0) particles. Instead of generating the mass for the weak interaction gauge fields, the SSB created another massless boson! The twist happens when the SSB is applied in the case of local gauge invariance. The Higgs field ϕ can be expanded with a perturbation $H(x)$ around the minimum of the potential, and it is possible to choose local gauge transformation (rotation), such that:

$$\phi' = \begin{pmatrix} 0 \\ v + H(x) \end{pmatrix} \tag{C.0.5}$$

that cancels off the massless boson term and allows the gauge field to acquire mass. The remaining real field $H(x)$ can be interpreted as a real particle, the Higgs boson. Another way to think about the Higgs mechanism is that the Goldstone boson is responsible for furnishing a third degree of freedom (longitudinal polarization) to the massless gauge field, which already carries two degrees of freedom (transverse polarization). The gauge mass field "eats" the Goldstone boson to acquire mass and a third polarization state. As a direct consequence, the vector bosons mediator of the weak interaction $W^\pm$ and Z^0 acquire masses and the Higgs boson as well, while the

[2] A symmetry that describes non-continuous changes in a system

[3] property of a system of remaining unchanged under smooth and continuous transformation

photon, associated with the electromagnetic field, is massless:

$$\begin{aligned} m_W^2 &= \frac{g^2 v^2}{4} \text{ for } \mathcal{W}_\mu^+ \text{ and } \mathcal{W}_\mu^- \\ m_Z^2 &= \frac{g^2 v^2}{4\cos^2\theta_W} \text{ for } \mathcal{Z}'_\mu \\ m_A^2 &= 0 \text{ for } \mathcal{A}_\mu \\ m_H^2 &= 2\lambda v^2 \text{ for } \mathcal{H} \end{aligned} \tag{C.0.6}$$

Furthermore, the Higgs field plays a crucial role in generating the masses of fermions indirectly through Yukawa interactions, i.e. interaction between fermion fields ψ and the Higgs field H. The Yukawa Lagrangian term can be written as:

$$\mathcal{L}_{Yukawa} = -y\bar{\psi}H\psi \tag{C.0.7}$$

Where y is the coupling constant associated with the fermion. When the Higgs field acquires a non-zero vacuum expectation value, leading to the SSB, this interaction term generates the mass terms for the fermion. The mass is proportional to the strength of the coupling constant:

$$m = g\frac{v}{\sqrt{2}} \tag{C.0.8}$$

Hence, the Higgs field would preferably couple with the heaviest quark available in the kinematic region.

Appendix D

CP-symmetry violation and time reversal

The CP-symmetry is a combination of charge conjugation symmetry and parity symmetry. According to this symmetry, the laws of physics are the same if particles and anti-particles are interchanged (charge conjugation symmetry) while their spatial coordinates are inverted (mirror symmetry). Until the discovery of CP-violation in the decays of neutral kaons in 1964 [221], the CP-symmetry was thought to be conserved in the weak interaction. Under CP transformation, a left-handed electron becomes a right-handed positron. In weak interaction, charge conjugation and parity are violated, meaning that the W mediator boson couples only with a left-handed electron or right-handed positron and not a right-handed electron or left-handed positron.

The K^0 meson was observed decaying via weak interaction into two different CP-eigenstates modes: $\pi^+\pi^-$ and $\pi^+\pi^-\pi^0$. The K^0 meson is described as an admixture of two separate CP (or mass) eigenstates: K_S^0, CP-even, with a shorter lifetime, and K_L^0, CP-odd with a longer lifetime. The mass eigenstates differ from the flavour eigenstates K^0 and $\bar{K}^0$, and their lifetime is related to the phase space in their decay. Since such violation can occur with different probability for particles and anti-particles, it is called *indirect*.

Direct CP-violation occurs instead when the decay rates of particles and anti-particles into the same final states differ in the amplitude of CP-conserving and CP-violating decay.

Closely linked to the CP-violation is the time reversal transformation T, which corresponds to the reversal of motion. Because of the CPT theorem, the conjunction of charge conjugation, parity, and time reversal constitutes an exact symmetry of

all the types of interactions. Hence, if CP-symmetry is violated, a violation of the T-symmetry must occur.

Appendix E

Unitary triangle

From the six orthogonality relations of the CKM matrix

$$V_{CKM} = \begin{pmatrix} V_{ud} & V_{us} & V_{ub} \\ V_{cd} & V_{cs} & V_{cb} \\ V_{td} & V_{ts} & V_{tb} \end{pmatrix} \tag{E.0.1}$$

it is possible to build six unitary triangles. Let's consider the relation:

$$V_{ud}V_{ub}^* + V_{cd}V_{cb}^* + V_{td}V_{tb}^* = 0 \tag{E.0.2}$$

which is particularly relevant for B-decays. By dividing the three sides by $|V_{cd}V_{cb}^*|$, it is possible to obtain the famous unitary triangle shown in Figure E.0.1.

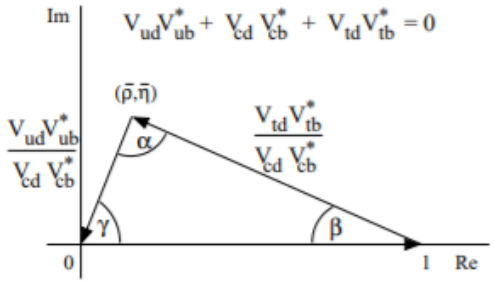

Figure E.0.1: Unitary triangle represented in the complex plane.

The apex of the triangle is given by

$$\bar{\rho} + i\bar{\eta} = \frac{V_{ud}V_{ub}^*}{V_{cd}V_{cb}^*} \tag{E.0.3}$$

with $\bar{\rho}$ and $\bar{\eta}$ that can be expressed through Wolfenstein parameters ρ and η

$$\begin{aligned} \bar{\rho} &= \rho\left(1 - \frac{1}{2}\lambda^2\right) + \mathcal{O}(\lambda^4) \\ \bar{\eta} &= \eta\left(1 - \frac{1}{2}\lambda^2\right) + \mathcal{O}(\lambda^4) \end{aligned} \tag{E.0.4}$$

and the angles of the unitary triangle are defined as:

$$\alpha = \arg\left[\frac{V_{td}V_{tb}^*}{V_{ud}V_{ub}^*}\right], \quad \beta = \arg\left[\frac{V_{cd}V_{cb}^*}{V_{td}V_{tb}^*}\right], \quad \gamma = \arg\left[\frac{V_{ud}V_{ub}^*}{V_{cd}V_{cb}^*}\right] \tag{E.0.5}$$

The studies on neutral kaons and B-meson systems can provide measurements of the triangle elements.

Appendix F

Neutrino oscillations

To better understand how neutrino oscillations work, it is more intuitive to start from a two-flavored neutrino mixing, as presented by Z.Maki, M.Nakagawa and S.Sakata in 1962 [66] and by Pontecorvo in 1967 [65]. Supposing a neutrino ν_α travels a path with length L and oscillates to a flavour ν_β when it reacts with the detector, it produces a charged lepton l_β (see Figure F.0.1). The probability of oscillation $\nu_\alpha \to \nu_\beta$ after a certain time t is:

$$P_{\nu_\alpha \to \nu_\beta}(t) = |\langle \nu_\beta | \nu_\alpha \rangle|^2 \tag{F.0.1}$$

The initial flavour state ν_α is a rotation of the mass eigenstate ν_i $(i = 1, 2)$ by a certain angle θ. It evolves in time as:

$$|\nu_\alpha(t)\rangle = \exp^{-iE_1 t} \cos\theta |\nu_1\rangle + \exp^{-iE_2 t} \cos\theta |\nu_2\rangle \tag{F.0.2}$$

In the relativistic limit of $t \sim L$, the oscillation probability is:

$$P_{\nu_\alpha \to \nu_\beta}(t) = \sin^2 2\theta \sin^2 \left(1.27 \frac{\Delta m^2([eV^2]) L([Km])}{4E([GeV])} \right) \tag{F.0.3}$$

where $\Delta m^2 = m_2^2 - m_1^2$ and $E_2 - E_1 = \Delta m^2 / 2E$. We must have $\theta \neq 0$ to have oscillation, which guarantees the mixing and at least one of the neutrinos to be massive. The ratio L/E makes it possible to deduce how sensitive an experiment can be to the neutrino mass squared difference. If neutrinos are naturally produced, as in the case of solar and atmospheric neutrinos, the fluxes and the distance between the source and the detector can be artificially controlled.

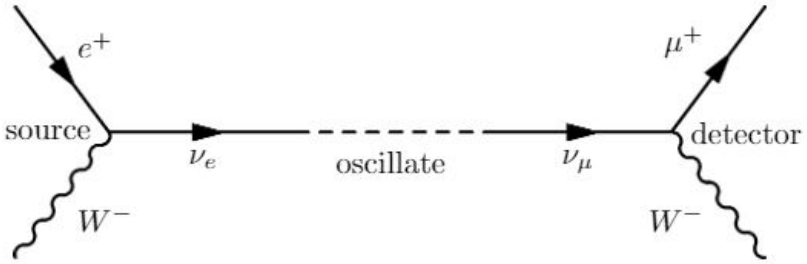

Figure F.0.1: Diagram of neutrino oscillation. Neutrinos are generated from the source with a given flavour, and after a certain time, they interact with detector material with a different flavour.

Appendix G

$Y_b \to X\tau l$ $(l = e, \mu, \tau)$ selections

The requirements applied to the lines in the `b_to_xtaul` module for the trigger selection are listed in the tables below.

Particle	Selection name	Cut	Description
K^{*0}	*Input particles filter*	$P > 2000$ [MeV], $P_T > 250$ [MeV], $IPCHI2 > 9$, $PID_K < 2$ (for π) $PID_K > 8$ (for K)	Filter on momentum, transverse momentum, impact parameter χ^2 and PID of children
	Combination cut	$700 < M < 1100$ [MeV], $DOCACHI2 < 20$	Requirements for the combinations on the mass and the significance of the distance of closest approach between particles
	Composite cut	$VTXCHI2 < 6$, $P_T > 1000$ [MeV]	Requirements on vertex fit quality and momentum of the composite
ρ^0	*Input particles filter*	$P > 1000$ [MeV], $P_T > 250$ [MeV], $IPCHI2 > 9$, $PID_K < 2$	Filter on momentum, transverse momentum, impact parameter χ^2 and PID of children
	Combination cut	$500 < M < 1200$ [MeV], $DOCACHI2 < 10$	Requirements for the combinations on the mass and the significance of the distance of closest approach between particles
	Composite cut	$VTXCHI2 < 6$, $P_T > 1000$ [MeV], $IPCHI2 < 9$	Requirements on vertex fit quality, momentum of the composite and significance of its impact parameter
ϕ	*Input particles filter*	$P > 2000$ [MeV], $P_T > 250$ [MeV], $IPCHI2 > 9$, $PID_K > 8$	Filter on momentum, transverse momentum, impact parameter χ^2 and PID of children
	Combination cut	$950 < M < 1100$ [MeV], $DOCACHI2 < 20$	Requirements for the combinations on the mass and the significance of the distance of closest approach between particles
	Composite cut	$VTXCHI2 < 9$, $P_T > 1000$ [MeV], $IPCHI2 > 9$	Requirements on vertex fit quality, momentum of the composite and significance of its impact parameter
η'	*Input particles filter*	π: $P > 1000$ [MeV], $P_T > 250$ [MeV], $IPCHI2 > 9$, $PID_K < 2$ γ: $E > 100$ [MeV], $E_T > 400$ [MeV] $ISNOTH > 0.3$, $E_{\frac{1}{9}NEUTRAL} > 0.2$, $ISPHOTON > 0.5$	Filter on momentum, transverse momentum, impact parameter χ^2 and PID of pions Filter on PID and deposited energy of photons
	Combination12 cut	$500 < M < 1200$ [MeV]	Requirement for the two-body (pions) combined mass
	Combination cut	$700 < M < 1300$ [MeV]	Requirement for the three-body combined mass
	Composite cut	$P_T > 1000$ [MeV]	Requirement on transverse momentum of the composite

Table G.0.1: Selection applied to some components in the hadronic sector for the trigger lines in the `b_to_xtaul` module. A brief description of the requirements imposed is provided.

Particle	Selection name	Cut	Description
K^+	*Particle filter*	$P > 4000$ [MeV], $P_T > 1000$ [MeV], $IPCHI2 > 9$, $PID_K > 8$	Filter on momentum, transverse momentum, impact parameter χ^2 and PID of the kaon
$K1^+$	*Input particles filter*	$P > 1000$ [MeV], $P_T > 250$ [MeV], $IPCHI2 > 9$, $PID_K < 2$ (for π) $PID_K > 8$ (for K)	Filter on momentum, transverse momentum, impact parameter χ^2 and PID of children
	Combination12 cut	$DOCACHI2 < 10$	Requirement on the significance of the distance of closest approach for the charged two-body combination ($K\pi$)
	Combination23 and Combination13 cut	$M < 1450$ [MeV], $DOCACHI2 < 10$	Requirement on the mass and on the significance of the distance of closest approach for the neutral two-body combination ($K\pi$ and $\pi\pi$)
	Combination cut	$700 < M < 1100$ [MeV], $DOCACHI2 < 20$	Requirements for the combinations on the mass and the significance of the distance of closest approach between particles
	Composite cut	$VTXCHI2 < 6$, $P_T > 1000$ [MeV], $IPCHI2 > 9$, $BPVFDCHI2 > 16$	Requirements of the composite on vertex fit quality, momentum, impact parameter χ^2 and flight distance chi^2 with respect to the primary vertex with minimum IP
pK	*Input particles filter*	$P > 2000$ [MeV], $P_T > 250$ [MeV], $IPCHI2 > 9$, $PID_P > 2$ (for p), $PID_P - PID_K > 0$ (for p), $PID_K > 8$ (for K)	Filter on momentum, transverse momentum, impact parameter χ^2 and PID of children
	Combination cut	$1300 < M < 5620$ [MeV], $DOCACHI2 < 20$	Requirements for the combinations on the mass and the significance of the distance of closest approach between particles
	Composite cut	$VTXCHI2 < 9$, $P_T > 1000$ [MeV], $BPVFDCHI2 > 16$	Requirements of the composite on vertex fit quality, momentum and lifetime and flight distance χ^2 with respect to the primary vertex with minimum IP

Table G.0.2: Selection applied to some components in the hadronic sector for the trigger lines in the `b_to_xtaul` module. A brief description of the requirements imposed is provided.

Particle	Selection name	Cut	Description
K_s^0 LL	*Input particles filter*	$P > 2000$ [MeV], $P_T > 0$ [MeV], $IPCHI2 > 9$, $PID_K <= 2$	Filter on momentum impact parameter χ^2 and PID of children
	Combination cut	$\|M - M_{PDG}\| < 50$ [MeV], $DOCACHI2 < 25$	Requirements for the combinations on the mass and the significance of the distance of closest approach between particles
	Composite cut	$VTXCHI2 < 20$, $\|M - M_{PDG}\| < 35$ [MeV], $BPVLTIME < 1$ [ps], $BPVFDCHI2 > 4$	Requirements of the composite on vertex fit quality, mass, lifetime and flight distance χ^2 with respect to the primary vertex with minimum IP
K_s^0 DD	*Input particles filter*	$P > 2000$ [MeV], $P_T > 0$ [MeV], $IPCHI2 > 9$	Filter on momentum impact parameter χ^2 of children
	Combination cut	$\|M - M_{PDG}\| < 80$ [MeV], $DOCACHI2 < 25$	Requirements for the combinations on the mass and the significance of the distance of closest approach between particles
	Composite cut	$VTXCHI2 < 20$, $\|M - M_{PDG}\| < 64$ [MeV], $BPVLTIME < 1$ [ps], $BPVFDCHI2 > 4$	Requirements of the composite on vertex fit quality, mass, lifetime and flight distance χ^2 with respect to the primary vertex with minimum IP
Λ^0 LL	*Input particles filter*	$P > 2000$ [MeV], $P_T > 0$ [MeV], $IPCHI2 > 9$, $PID_P > -2$ (for p), $PID_K <= 2$ (for π)	Filter on momentum impact parameter χ^2 and PID of children
	Combination cut	$\|M - M_{PDG}\| < 50$ [MeV], $DOCACHI2 < 25$	Requirements for the combinations on the mass and the significance of the distance of closest approach between particles
	Composite cut	$VTXCHI2 < 20$, $\|M - M_{PDG}\| < 35$ [MeV], $BPVLTIME < 1$ [ps], $BPVFDCHI2 > 4$	Requirements of the composite on vertex fit quality, mass, lifetime and flight distance χ^2 with respect to the primary vertex with minimum IP
Λ^0 DD	*Input particles filter*	$P > 2000$ [MeV], $P_T > 0$ [MeV], $IPCHI2 > 9$	Filter on momentum impact parameter χ^2 of children
	Combination cut	$\|M - M_{PDG}\| < 80$ [MeV], $DOCACHI2 < 25$	Requirements for the combinations on the mass and the significance of the distance of closest approach between particles
	Composite cut	$VTXCHI2 < 20$, $\|M - M_{PDG}\| < 64$ [MeV], $BPVLTIME < 1$ [ps], $BPVFDCHI2 > 4$	Requirements of the composite on vertex fit quality, mass, lifetime and flight distance χ^2 with respect to the primary vertex with minimum IP

Table G.0.3: Selection applied to $V0$ components in the hadronic sector for the trigger lines in the `b_to_xtaul` module. A brief description of the requirements imposed is provided.

Particle	Selection name	Cut	Description
τ	*Input particles filter*	$P > 2000$ [MeV], $P_T > 250$ [MeV], $IPCHI2 > 16$, $PID_K < 5$ $PID_E < 5$ $PID_P < 10$, $PID_MU < 10$	Filter on momentum, transverse momentum, impact parameter χ^2 and PID of children
	Combination12 and Combination13 cut	$400 < M < 1200$, $DOCACHI2 < 6$	Requirement on the significance of the distance of closest approach for the neutral two-body combination
	Combination23 cut	$DOCACHI2 < 6$	Requirement on the significance of the distance of closest approach for the charged two-body combination
	Combination cut	$640 < M < 1760$ [MeV], $SUM(P_T(\pi) > 800[MeV]) >= 1$, $SUM(IPCHI2(\pi) > 25) >= 1$	Requirements for the combinations on the mass and the significance of the distance of closest approach between particles Requirements on number of pions with minimum momentum and impact parameter chi^2
	Composite cut	$800 < M < 1600$, $VTXCHI2 < 6$, $P_T > 1000$ [MeV], $BPVFDCHI2 > 100$, $BPVDIRA > 0.99$	Requirements of the composite on vertex fit quality, momentum, mass flight distance chi^2 and cosine of the angle of the particle momentum with respect to the primary vertex with minimum IP
μ	*Particle filter*	$P > 3000$ [MeV], $P_T > 500$ [MeV], $IPCHI2 > 9$, $PID_MU > 2$, $ISMUON$	Filter on momentum, transverse momentum, impact parameter χ^2 and PID of the muon
e	*Particle filter*	$P > 3000$ [MeV], $P_T > 500$ [MeV], $IPCHI2 > 9$, $PID_E > 3$, $PID_E - PID_K > 0$	Filter on momentum, transverse momentum, impact parameter χ^2 and PID of the electron
$\tau - l$	*Combination cut*	$200 < M < 5000$ [MeV], $log(\sim \chi^2) > -1$ (if $\tau\tau$)	Requirement on the invariant mass of the dilepton system and on the vertex separation χ^2 between two taus.

Table G.0.4: Selection applied to the leptonic sector for the trigger lines in the `b_to_xtaul` module. A brief description of the requirements imposed is provided.

Particle	Selection name	Cut	Description
B^0, B^+ or Λ_b	*Combination cut*	$1800 < M < 11000$ [MeV]	Requirements on the mass for the combinations
	Composite cut	$2000 < M < 10000$, $VTXCHI2 < 80$, $P_T > 1000$ [MeV], $P > 3000$ [MeV], $BPVIPCHI2 < 40$ [MeV], $BPVFDCHI2 > 120$, $BPVDIRA > 0.995$	Requirements of the composite on vertex fit quality, momentum, mass impact parameter χ^2, flight distance χ^2 and cosine of the angle of the particle momentum with respect to the primary vertex with minimum IP

Table G.0.5: Selection applied to the signal parent of the decay for the trigger lines in the `b_to_xtaul` module. A brief description of the requirements imposed is provided.

Appendix H

Dataset details

Dataset details are provided as follows. Table H.0.1 shows the main features of the stripping lines used in the analysis for the preselection of signal and normalization channel. Table H.0.2 refers to MC simulation details.

StrippingLine	**Version**	**Yr.**	$\sqrt{s}$ **[TeV]**	**L** $[fb^{-1}]$	**Reco**
StrippingB2KstTauTau_TauE_Line	v28r2p2	2016	13	1.665	Reco16
StrippingB2KstTauTau_TauE_SameSign_Line	v28r2p2	2016	13	1.665	Reco16
StrippingB2KstTauTau_TauE_Line	v29r3p2	2017	13	1.715	Reco17
StrippingB2KstTauTau_TauE_SameSign_Line	v29r3p2	2017	13	1.715	Reco17
StrippingB2KstTauTau_TauE_Line	v34r2	2018	13	2.185	Reco18
StrippingB2KstTauTau_TauE_SameSign_Line	v34r2	2018	13	2.185	Reco18
StrippingB2XTau_DD_Line	v28r2p1	2016	13	1.665	Reco16
StrippingB2XTau_DD_Line	v29r2	2017	13	1.715	Reco17
StrippingB2XTau_DD_Line	v34	2018	13	2.185	Reco18

Table H.0.1: Main features of the datasets adopted in the analysis: stripping line, stripping version, year of simulated data, the center of mass energy, integrated luminosity, reconstruction version

MC	Event number	Events simulated	Yr.	Sim	Reco	Stripping	Trigger	TCK
$B \to K^* \tau e$ T5	11123000	3M	2016	Sim09l	Reco16	v28r2p1	v25r5p3	0x6139160F
$B \to K^* \tau e$ T8	11123400	3M	2016	Sim09l	Reco16	v28r2p1	v25r5p3	0x6139160F
$B \to K^* \tau e$ T5	11123000	3.5M	2017	Sim09k	Reco17	v29r2	v26r6p1	0x62661709
$B \to K^* \tau e$ T8	11123400	3.5M	2017	Sim10b	Reco17	v29r2	v26r6p1	0x62661709
$B \to K^* \tau e$ T5	11123000	3M	2018	Sim10b	Reco18	v34	v28r3p1	0x617d18a4
$B \to K^* \tau e$ T8	11123400	3M	2018	Sim10b	Reco18	v34	v28r3p1	0x617d18a4
$B \to D^- D_s^+$	11296012	1M	2016	Sim09f	Reco16	v28r1	v25r5p3	0x6139160F
$B \to D^- D_s^+$	11296012	1M	2017	Sim09h	Reco17	v29r2	v26r6p1	0x62661709
$B \to D^- D_s^+$	11296012	1M	2018	Sim09l	Reco18	v34	v28r3p1	0x617d18a4
$B^0 \to D^- \pi^+ \pi^- \pi^+$	11266009	400k	2016	Sim09c	Reco16	v28r2p1	v25r4	0x6138160F
$B^0 \to D^{*-} \pi^+ \pi^- \pi^+$	11266018	400k	2016	Sim09c	Reco16	v28r2p1	v25r4	0x6138160F
$B^0 \to D^0 X^+ e^- \nu_e$	11584040	400k	2016	Sim09d	Reco16	v28r2p1	v25r5p3	0x6139160F
$B^0 \to D^{*-} \tau^+ \nu_\tau$ T5	11160001	6M	2016	Sim09c-ReDecay01	v28r2p1	Reco16	v25r4	0x6138160F
$B^0 \to D^{*-} \tau^+ \nu_\tau$ T5	11160001	1M	2017	Sim09g-ReDecay01	v29r2	Reco17	v25r4	0x62661709
$B^0 \to D^{*-} \tau^+ \nu_\tau$ T8	11563020	6M	2016	Sim09c	v28r2p1	Reco16	v25r4	0x6138160F

Table H.0.2: Main features of the signal, normalization and other MC simulations adopted in the analysis: event number, number of events simulated, year of simulated data, simulation version, reconstruction version, stripping version, Moore version for the trigger and the Trigger Configuration Key (TCK)

Appendix I

Reconstruction and stripping selections

Reconstruction requirements using the DecayTreeFitter algorithm to consider the missing momentum of the neutrino are specified in Table I.0.1. The list of loose cuts, with description, is provided in Table I.0.3 for the signal channel and in Table I.0.4 for the normalization channel. Trigger filter (see Table I.0.2) is added to reduce the rates of the stripping lines for signal.

Particle	**Name**	**Cut**	**Description**
B^0	CombinationCut	$0 <$ AM < 12000 [MeV]	Combination and composite mass
	MotherCut	$2000 < M < 10000$ [MeV]	
$Y^{\pm}$	CombinationCut	AM > 100 [MeV]	Mass and vertex quality requirement
	MotherCut	VCHI2DOF < 150	

Table I.0.1: Additional requirements imposed during the reconstruction on the "fake" intermediate state particle introduced to allow using the DecayTreeFitter for the reconstruction of the decay with the inclusion of the missing momentum carried by the neutrino

Name	Trigger Decision	Description
HLT1FILTER	HLT_PASS_RE("Hlt1TrackMVADecision") or HLT_PASS_RE("Hlt1TwoTracksMVADecision")	Cut on track quality and impact parameter significance. MVA method with reconstruction quantities as input variables
HLT2FILTER	HLT_PASS_RE("Hlt2TopoE(2|3|4)BodyDecision") or HLT_PASS_RE("Hlt2Topo(2|3|4)BodyDecision")	MVA methods that exploits the topology properties of two, three and four body decays.

Table I.0.2: Trigger selection applied to the stripping line `StrippingB2KstTauTau_TauE_Line` and `StrippingB2KstTauTau_TauE_SameSign_Line`

Particle	Name	Cut	Description
Event	Filter	nSPD $<$ 600 HLT1FILTER HLT2FILTER	Filter on number of SPD hits and trigger selection to limit the number of candidates
B^0	CombinationCut	2000 $<$ AM $<$ 10000 [MeV]	Requirements on mass combinations, quality of the vertex, transverse momentum, impact parameter and its significance, flight distance significance, direction angle, distance from primary vertex
	Combination12Cut	m($K^*\tau$) $<$ 5000 [MeV]	
	MotherCut	VCHI2 $<$ 100 $P_T >$ 2000 [MeV] IPCHI2 $<$ 300 IP $<$ 0.6 FDCHI2 $>$ 80 DIRA $>$ 0.999 3 $<$ BPVVD $<$ 70 [mm]	
K^{*0}	StdLoosePions	$P_T >$ 250 [MeV] MIPCHI2DV(PRIMARY) $>$ 4	Requirements on decay products transverse momentum, impact parameter χ^2, track quality and particle identification. Requirements on invariant mass combination, transverse momentum, vertex quality, and distance from primary vertex of the composite
	StdNoPIDKaons	$P_T >$ 250 [MeV] MIPCHI2DV(PRIMARY) $>$ 4	
	DaughterCuts	π : TRCHI2DOF $<$ 4 ProbNNpi $>$ 0.5 K : TRCHI2DOF $<$ 4 ProbNNk $>$ 0.2	
	CombinationCut	700 $<$ AM $<$ 1100 [MeV]	
	MotherCut	$P_T >$ 1000 [MeV] VCHI2 $<$ 15 BPVVD $>$ 3 [mm]	
τ	StdLoosePions	$P_T >$ 250 [MeV] MIPCHI2DV(PRIMARY) $>$ 4	Requirements on decay products transverse momentum, momentum, impact parameter χ^2, track quality, ghost probability, and particle identification. Requirements on invariant mass combination, transverse momentum, max distance of closest approach of combinations, at least one pion with $P_T >$ 800MeV. Requirements on the composite mass, transverse momentum and vertex quality. Additionally, direction angle, distance quality, ρ and z distance from primary vertex of the composite
	DaughterCuts	TRCHI2DOF $<$ 4 PTRGHOSTPROB $<$ 0.4 ProbNNpi $>$ 0.55 $P_T >$ 250 [MeV] $P >$ 2000 [MeV] MIPCHI2DV(PRIMARY) $>$ 16	
	CombinationCut	400 $< AM <$ 2100 [MeV] $P_T >$ 800 [MeV] AMAXDOCA $<$ 0.2 [mm] ANUM($P_T >$ 800 [MeV]) $\geq$ 1	
	MotherCut	$P_T >$ 1000 [MeV] 500 $< M <$ 2000[MeV] BPVDIRA $>$ 0.99 VCHI2 $<$ 16 BPVVDCHI2 $>$ 16 0.1 $<$ BPVVDRHO $<$ 7 [mm] BPVVDZ $>$ 5 [mm]	
e	StdTightElectrons	RequiresDet = CALO RequiresDet = RICH DLL(e/π) $>$ 2 DLL(e/K) $>$ 0	Requirements on detector hits in calorimeter and RICH, particle identification, momentum and transverse momentum, impact parameter χ^2, and track quality
	Additional selection	$P_T >$ 500 [MeV] $P >$ 3000 [MeV] MIPCHI2DV(PRIMARY) $>$ 25 TRCHI2DOF $<$ 4	

Table I.0.3: List of cuts for the stripping selections applied during reconstruction using `StrippingB2KstTauTau_TauE_Line`. The `HLT1FILTER` and `HLT2FILTER` requirements are explicit in Table I.0.2

Particle	Name	Cut	Description
B^0	CombinationCut	$2000 <$ AM < 7000 [MeV] APT > 1900 [MeV] BPVDIRA > 0.99 BPVVD > 90 [mm] VCHI2DOF < 90 BPVVDCHI2 < 225	Requirements on invariant mass, transverse momentum, vertex quality. Cuts on direction angle, vertex distance and quality from primary vertex. Requirement on transverse momentum of composite, children, grandchildren, and sum of transverse momentum of final states.
	MotherCut	$P_T > 2000$ [MeV] P_T(CHILD) > 4000 [MeV] P_T(GCHILD) > 2000 [MeV] SUM(P_T)(final state) > 7000 [MeV]	
D^+ or D_s^+	StdLoosePions	$P_T > 250$ [MeV] MIPCHI2DV(PRIMARY) > 4	Requirements on decay products transverse momentum, momentum, impact parameter χ^2, particle identification ghost probability and track quality. Requirements on combinations mass, transverse momentum, max distance of closest approach and at least one child with $P_T > 800$MeV. Cut on charm meson mass, composite transverse momentum, mass and vertex quality. Additionally, direction angle, distance quality, ρ and z distance from primary vertex of the composite
	StdLooseKaons	$P_T > 250$ [MeV] MIPCHI2DV(PRIMARY) > 4 DLL(K/π) > -5	
	DaughterCuts	π : TRCHI2DOF < 4 PTRGHOSTPROB < 0.4 ProbNNpi > 0.55 $P_T > 250$ [MeV] $P > 2000$ [MeV] MIPCHI2DV(PRIMARY) > 16 K : TRCHI2DOF < 4 PTRGHOSTPROB < 0.4 $P_T > 250$ [MeV] $P > 2000$ [MeV] MIPCHI2DV(PRIMARY) > 16	
	Combination12Cut	$AM < 5000$ [MeV]	
	CombinationCut	$P_T > 800$ [MeV] AMAXDOCA < 0.2 [mm] ANUM($P_T > 800$ [MeV]) ≥ 1 D : $1750 < AM < 2080$ [MeV] D_s : $1938 < AM < 1998$ [MeV]	
	MotherCut	$P_T > 1000$ [MeV] $500 < M < 2000$[MeV] BPVDIRA > 0.99 VCHI2 < 16 BPVVDCHI2 > 16 $0.1 <$ BPVVDRHO < 7 [mm] BPVVDZ > 5 [mm]	

Table I.0.4: List of cuts for the stripping selections applied while reconstructing $B \to D^- D_s^+$using `StrippingB2XTau_DD_Line`

Appendix J

Trigger decisions studies

The optimization study performed at the trigger level is done using the significance as a figure of merit, as presented in Equation 4.4.1. Initially, the study is performed for L0 trigger lines, where several lines are compared, as shown in Figure J.0.1. Only the more efficient decisions with good figures of merit value are retained. Moreover, lines retained are ranked based on their significance. Similar approach is adopter for HLT1 (Figure J.0.2) and HLT2 (Figure J.0.3 and Figure J.0.4) selections.

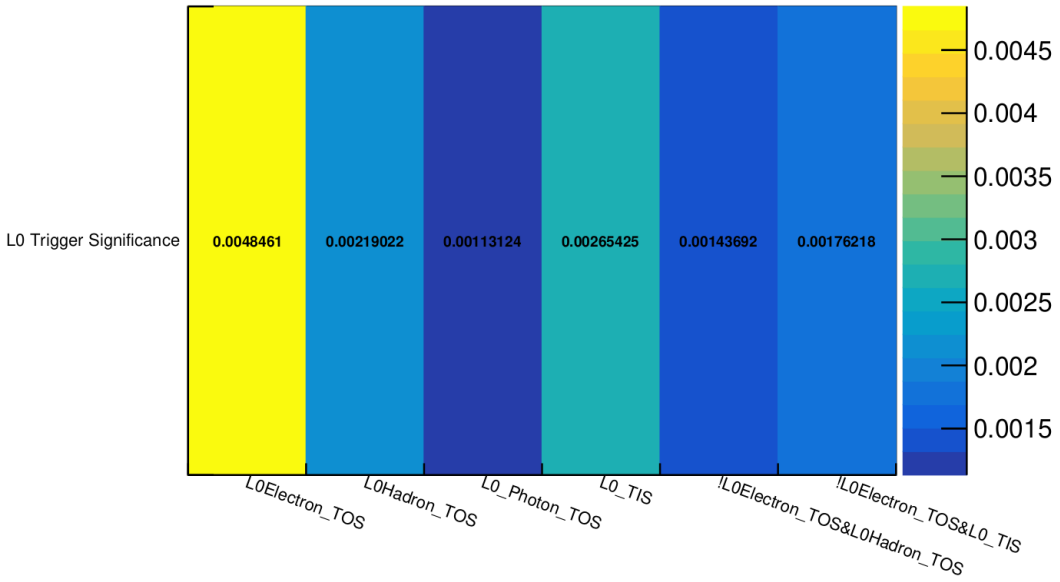

Figure J.0.1: L0 trigger decisions significance for different hardware trigger lines. `L0ElectronDecisionTOS` is the most discriminating decision, but it is not highly efficient ($< 35\%$). The second most discriminating decision is `L0GlobalTIS`, followed by `L0HadronDecisionTOS`. `L0PhotonDecisionTOS`, which considers possible events with bremsstrahlung emissions, brings a negligible contribution in terms of efficiency, and it is not considered.

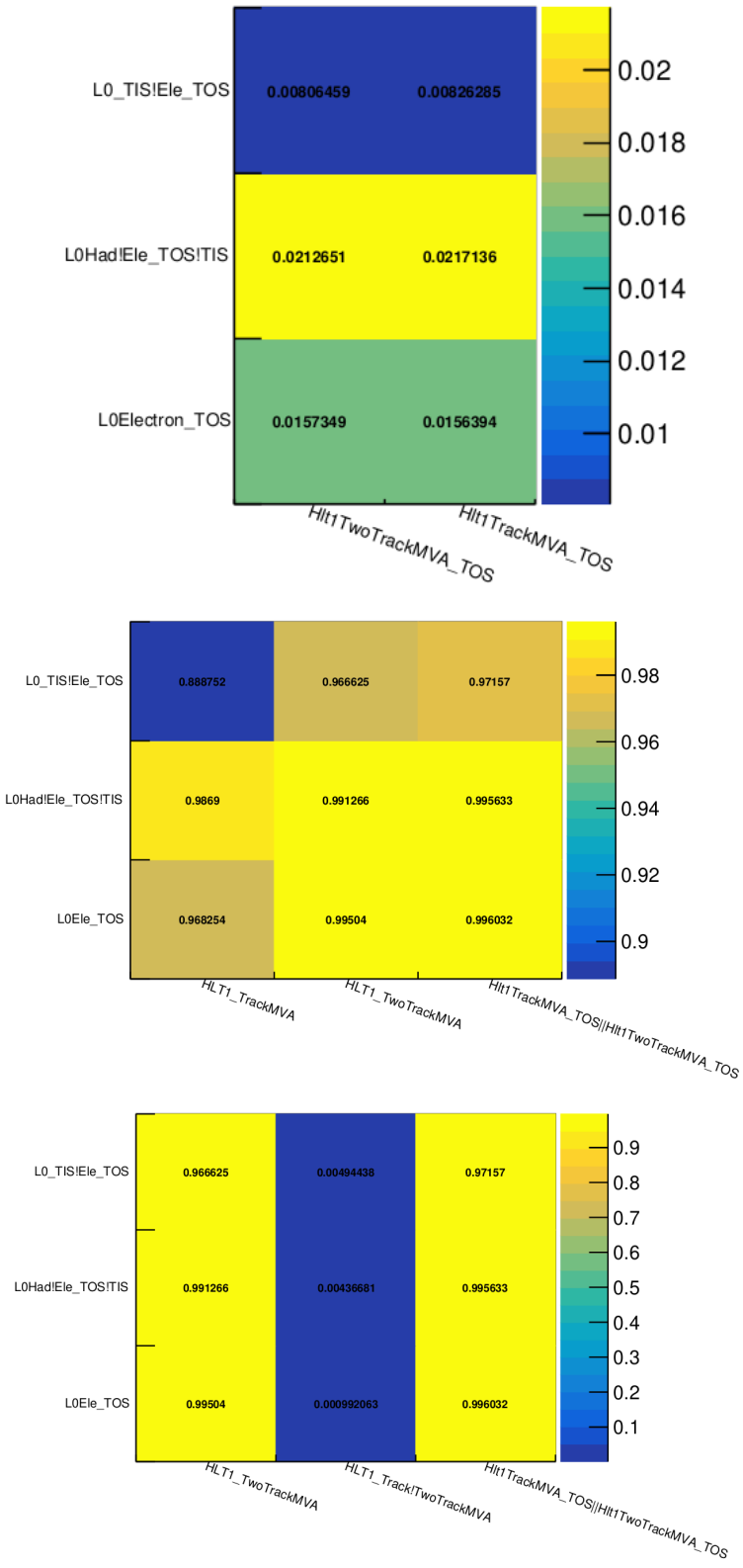

Figure J.0.2: Significance (top) and efficiencies (center and bottom) for `HLT1OneTrackMVA_TOS` and `HLT1TwoTrackMVA_TOS` divided into L0 categories. Significances are close to each other, and the choice of the trigger line is made by looking at the efficiencies of each line. `HLT1TwoTrackMVA_TOS` results being more efficient and when adding `HLT1OneTrackMVA_TOS` there is not much gain in efficiency.

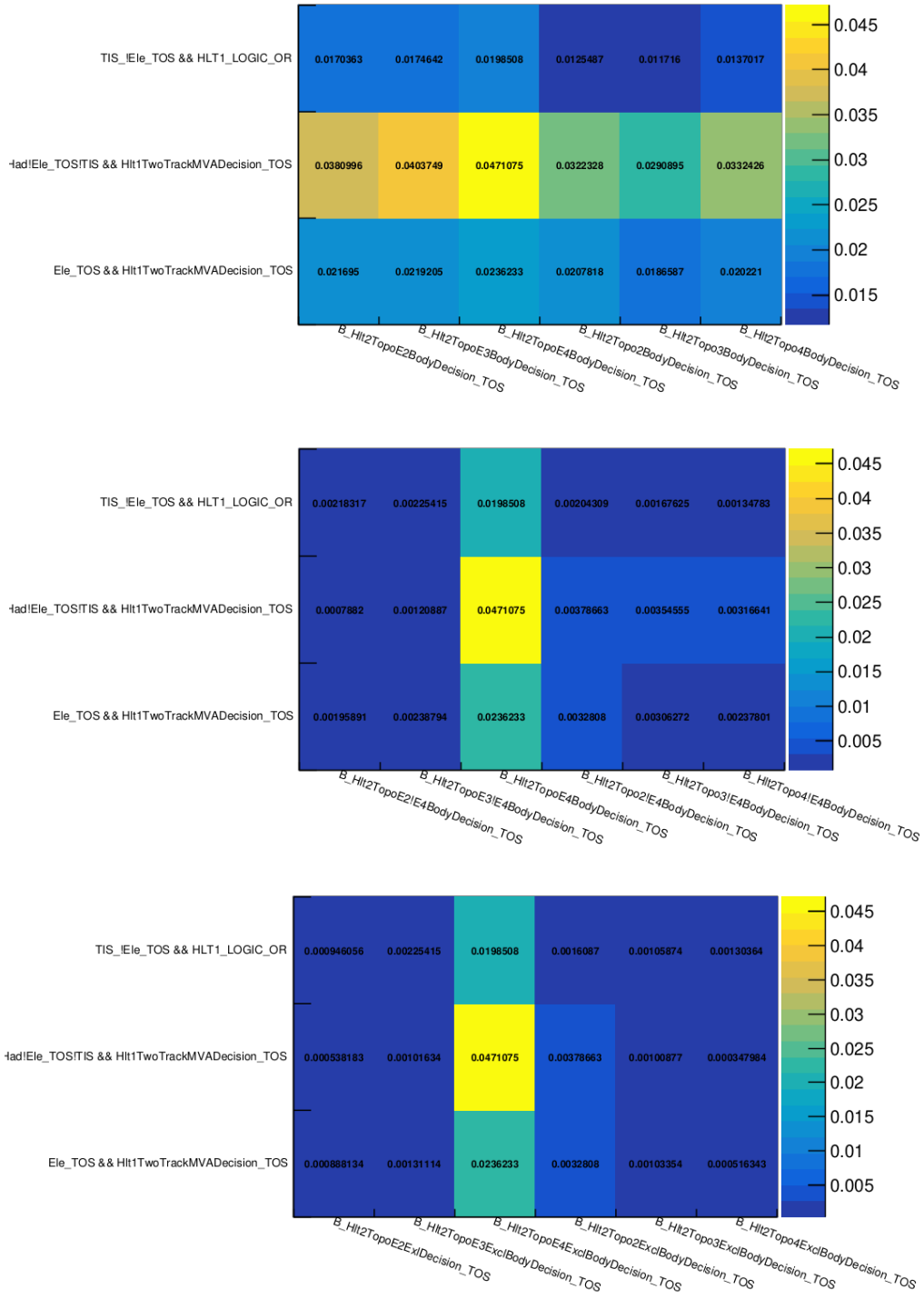

Figure J.0.3: Significance study for exclusive HLT2 decisions, part 1/2. Each study is divided into L0 categories: the first, second and third rows of each table represent the categories `TIS`, `hTOS` and `eTOS`, respectively. The procedure applied to make the selection is the following: at the k^{th} step, once excluded $k-1$ trigger lines with higher significance, the line giving the maximum of significance is chosen for each category, and it is excluded for the next step. No more lines were included if the efficiency of the decision was considered irrelevant to the selection.

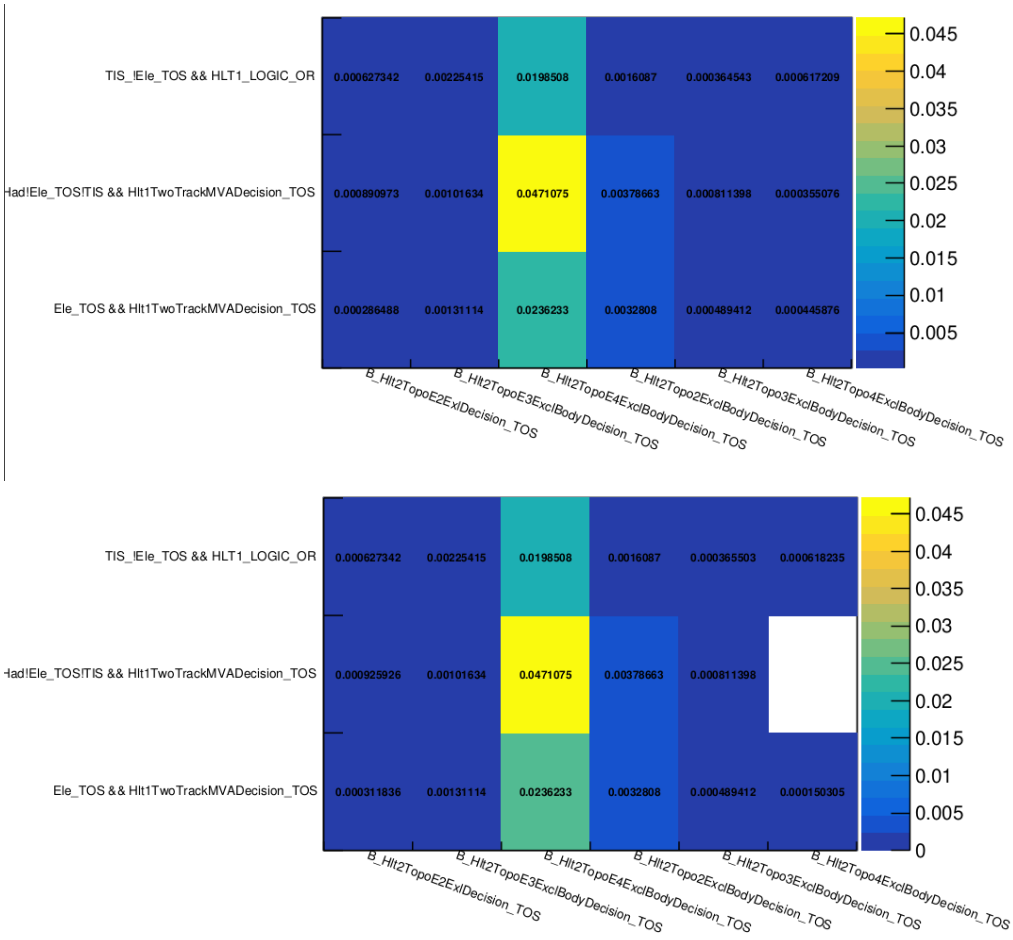

Figure J.0.4: Significance study for exclusive HLT2 decisions, part 2/2. Each study is divided into L0 categories: the first, second and third rows of each table represent the categories `TIS`, `hTOS` and `eTOS`, respectively. The procedure applied to make the selection is the following: at the k^{th} step, once excluded $k-1$ trigger lines with higher significance, the line giving the maximum of significance is chosen for each category, and it is excluded for the next step. No more lines were included if the efficiency of the decision was considered irrelevant to the selection. The empty bin (blank space) refers to a line with zero significance.

Appendix K

MVA methods

K.1 ACBDT

The set of hyperparameters used for the classifier configuration is collected in Table K.1.1. The ROC curves are used to compare different methods employed for the classifier training. The output of the best one (`BDTG_LLR`) is presented in Figure K.1.1. Figure K.1.2 shows the correlation between the output of the classifier and the refitted mass for truth-matched simulation, OS sidebands and SS data. No strong correlation has been observed.

NTrees	MinNodeSize	BoostType	Shrinkage	BaggedSampleFraction	nCuts	MaxDepth
1000	5%	Grad	0.05	0.6	30	3

Table K.1.1: Hyper-parameters used for training the ACMVA. NTrees and MinNodeSize define the number of trees in the forest and the minimum fraction of training events required in the leaf node, respectively. The BoostType represent the boosting algorithm type (gradient boosting), while Shrinkage is the learing rate. BaggedSampleFraction is the fraction of training dataset used to build each tree, the remaining part is used for the validation of the boosting process. nCuts parameter is used to set the number of grid points used for the split optimization and MaxDepth is the maximum depth of each individual tree.

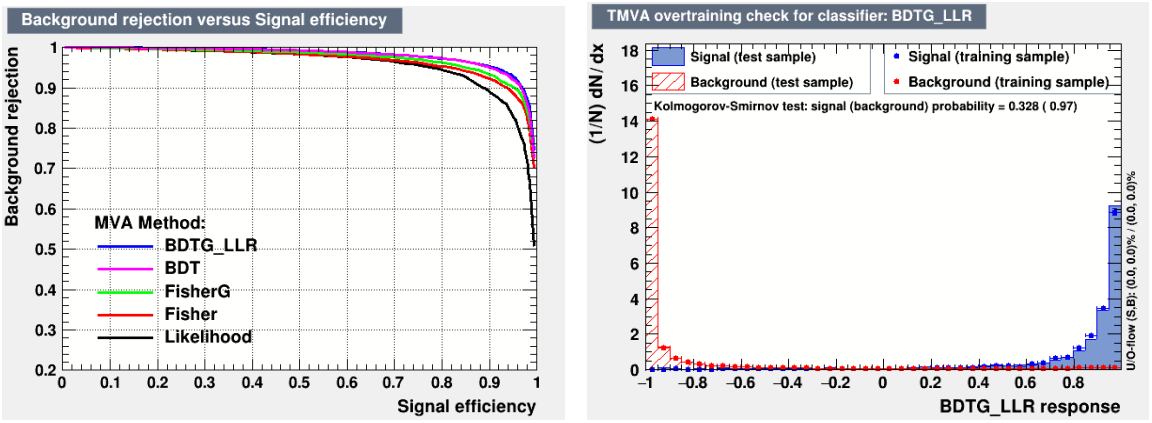

Figure K.1.1: On the left: ROC curves for different methods trained. The method giving the best performance is `BDTG_LLR` (AUC=0.981). On the right: `BDTG_LLR` output after the application to training (solid lines) and testing (dots) samples of data (red) and MC simulation (blue).

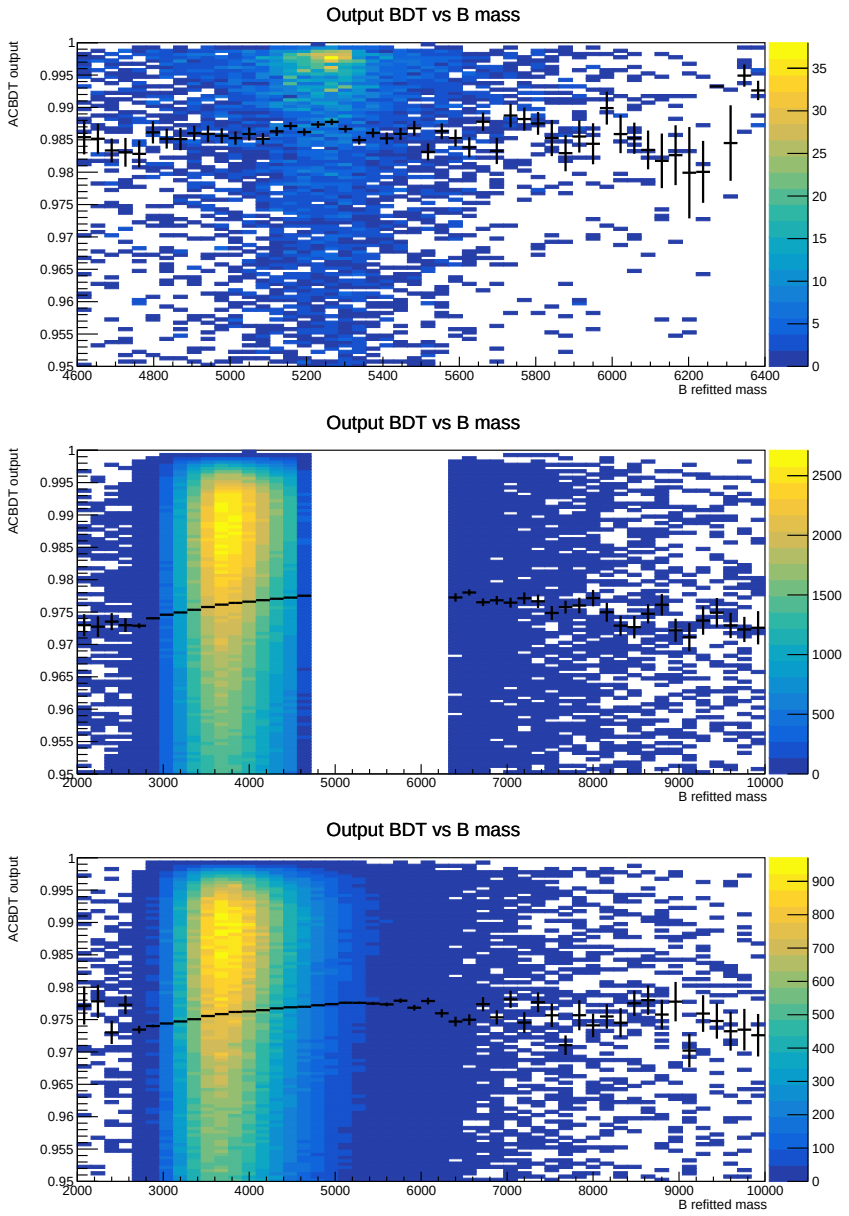

Figure K.1.2: Mass dependency for the anti-combinatorial classifier output for the simulation sample in the signal region (top) and for the OS (middle) and SS (bottom) data in [2000, 9000] MeV region (the signal region has been blinded for the OS data). The superposed dots are obtained by profiling the classifier output for each mass bin. No strong correlation between the output and the mass has been observed.

K.1.1 Input variable validation

The classifier input variables are validated by comparing data and truth-matched MC events of the control sample $B \to D^- D_s^+$. No strong discrepancies are found; therefore, the simulation is not re-weighted. Any possible difference is considered in the systematic calculation for the efficiencies.

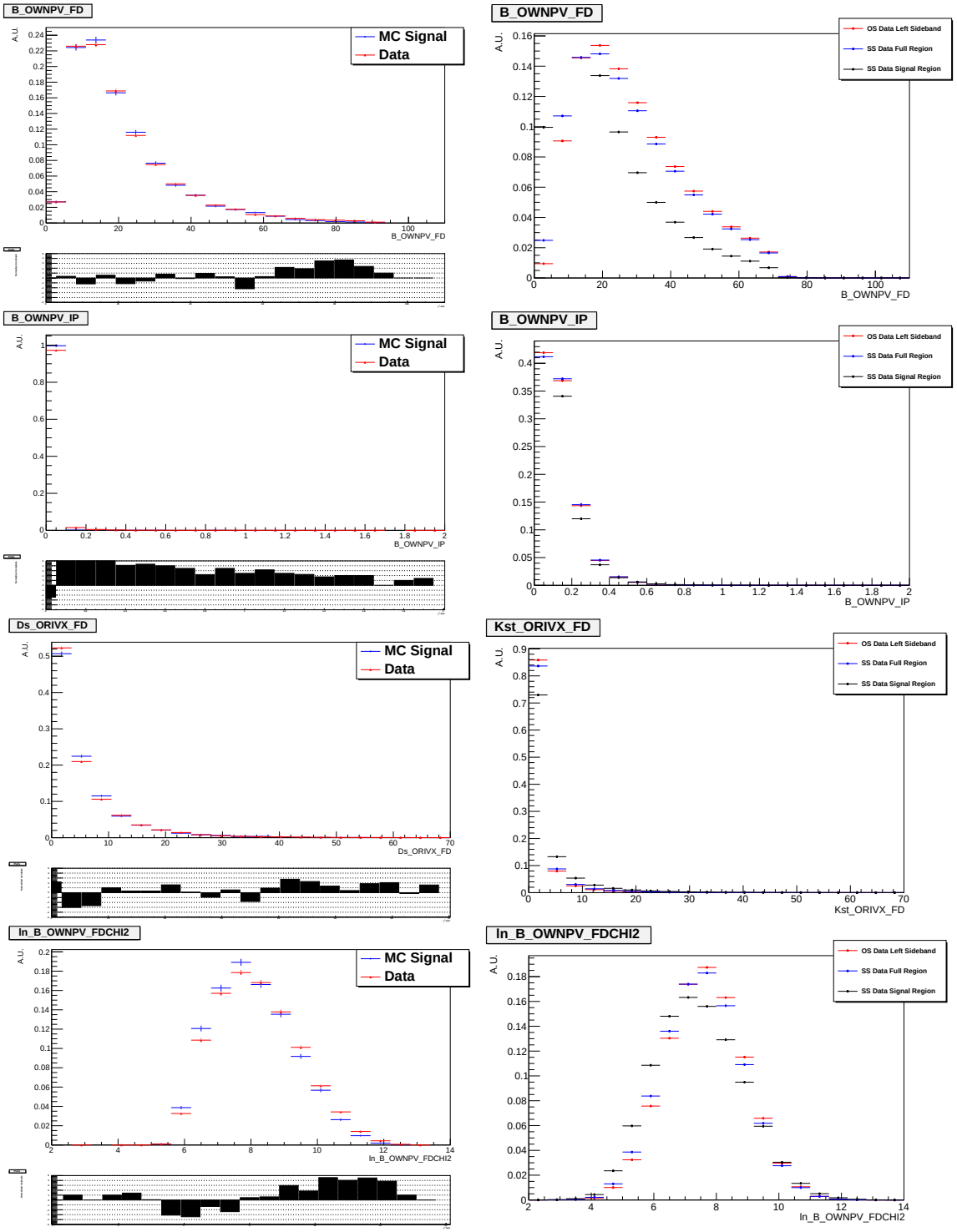

Figure K.1.3: Anti-combinatorial input variable validation, part 1/2. On the left: validation distributions for data (red) and MC simulation (blue) using $B \to D^- D_s^+$ control sample for the input variables of the anti-combinatorial classifier with pulls distribution on the bottom of the plots. MC candidates are truth-matched to correctly represent the sample, while for data, the selection described in Section 4.4.4 has been applied. On the right: Distributions of the same variables for $B \to K^* \tau e$ OS data (blue), SS data in the full region (black) and in the signal region (red).

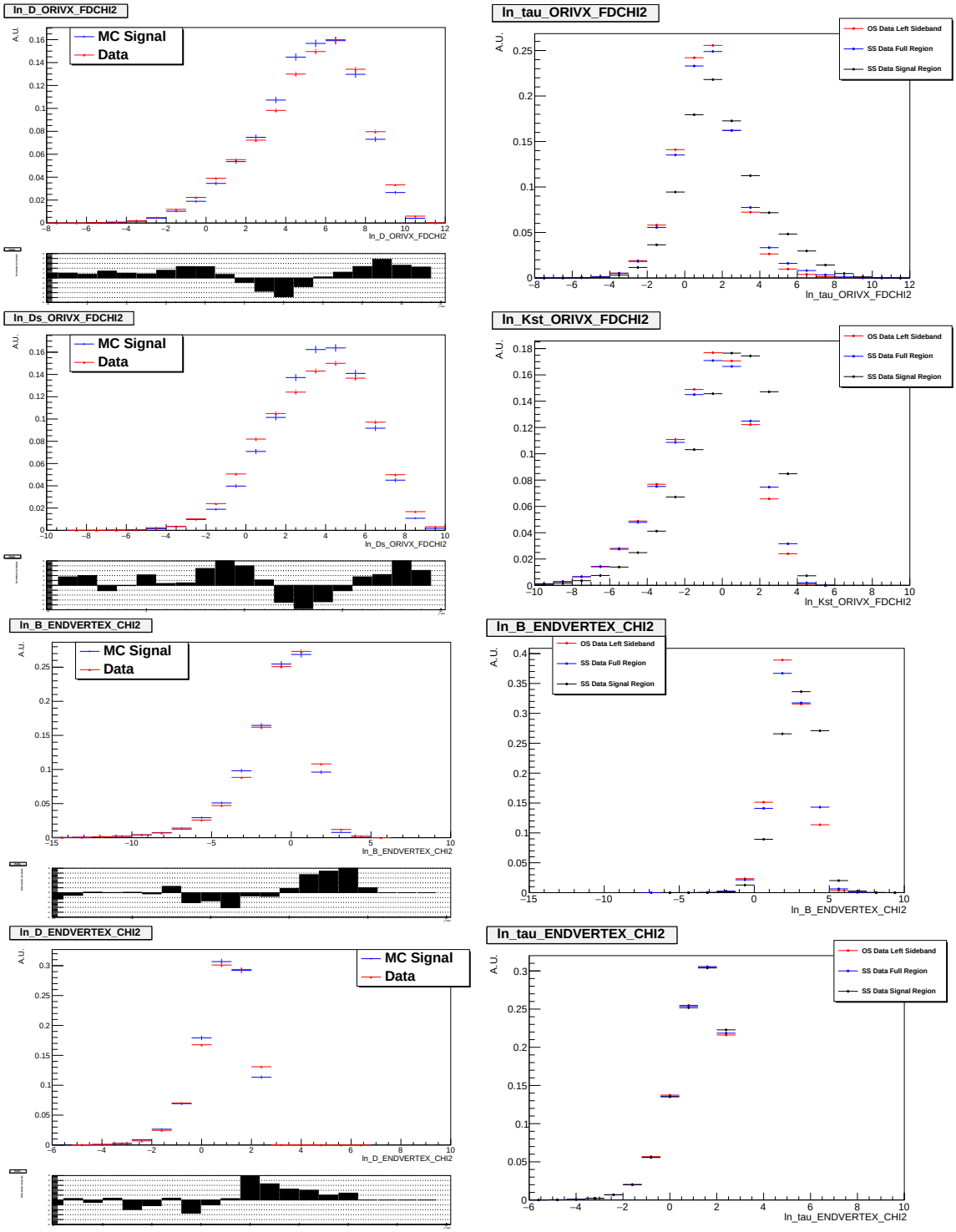

Figure K.1.4: Anti-combinatorial input variable validation, Part 2/2. On the left: validation distributions for data (red) and MC simulation (blue) using $B \to D^- D_s^+$ control sample for the input variables of the anti-combinatorial classifier with pulls distribution on the bottom of the plots. MC candidates are truth-matched to correctly represent the sample, while for data, the selection described in Section 4.4.4 has been applied. On the right: Distributions of the same variables for $B \to K^* \tau e$ OS data (blue), SS data in the full region (black) and in the signal region (red).

K.2 IsoFisher

The set of hyperparameters used for the classifier configuration is collected in Table K.2.1. The ROC curves are used to compare different methods employed for the classifier training. The methods which have better performances in this case, like `BDTG_LLR` or `BDT`, are more correlated with the mass and/or show large overtraining. `Fisher` method is the one adopted for the classifier of this analysis. Its output distribution is presented in Figure K.2.1. Figure K.2.2 shows the correlation between the output of the classifier and the refitted mass for truth-matched simulation, OS sidebands and SS data. No strong correlation has been observed.

PDFInterpolMVAPdf	NbinsMVAPdf	NsmoothMVAPdf
Spline2	50	10 (number of smoothing iterations)

Table K.2.1: Hyper-parameters used for training the IsoMVA. PDFInterpolMVAPdf parameter is used to define the probability function for the interpolation (in this case a quadratic polynomial). NbinsMVAPdf and NsmoothMVAPdf define the number of bins for the training and the smoothing iterations applied, respectively.

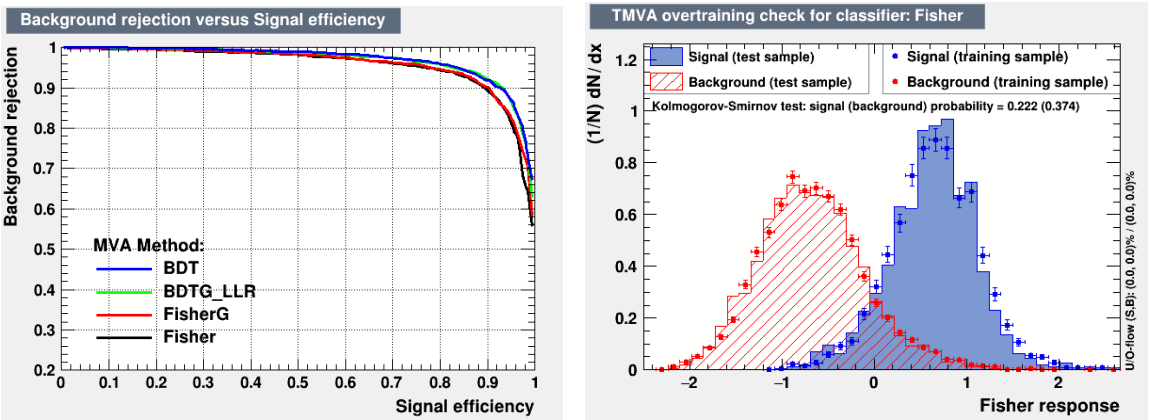

Figure K.2.1: On the left: ROC curves for different methods trained. The results of all the methods tested gave similar AUC performances ($\text{AUC}_{\texttt{BDT}} = 0.968 \pm 0.001$, $\text{AUC}_{\texttt{BDTG\_LLR}} = 0.967 \pm 0.002$, $\text{AUC}_{\texttt{FisherG}} = 0.958 \pm 0.001$, $\text{AUC}_{\texttt{Fisher}} = 0.955 \pm 0.003$). However, the `Fisher` method shows less over-training. On the right: `Fisher` output after the application to training (solid lines) and testing (dots) samples of data in full region (red) and in signal region (blue).

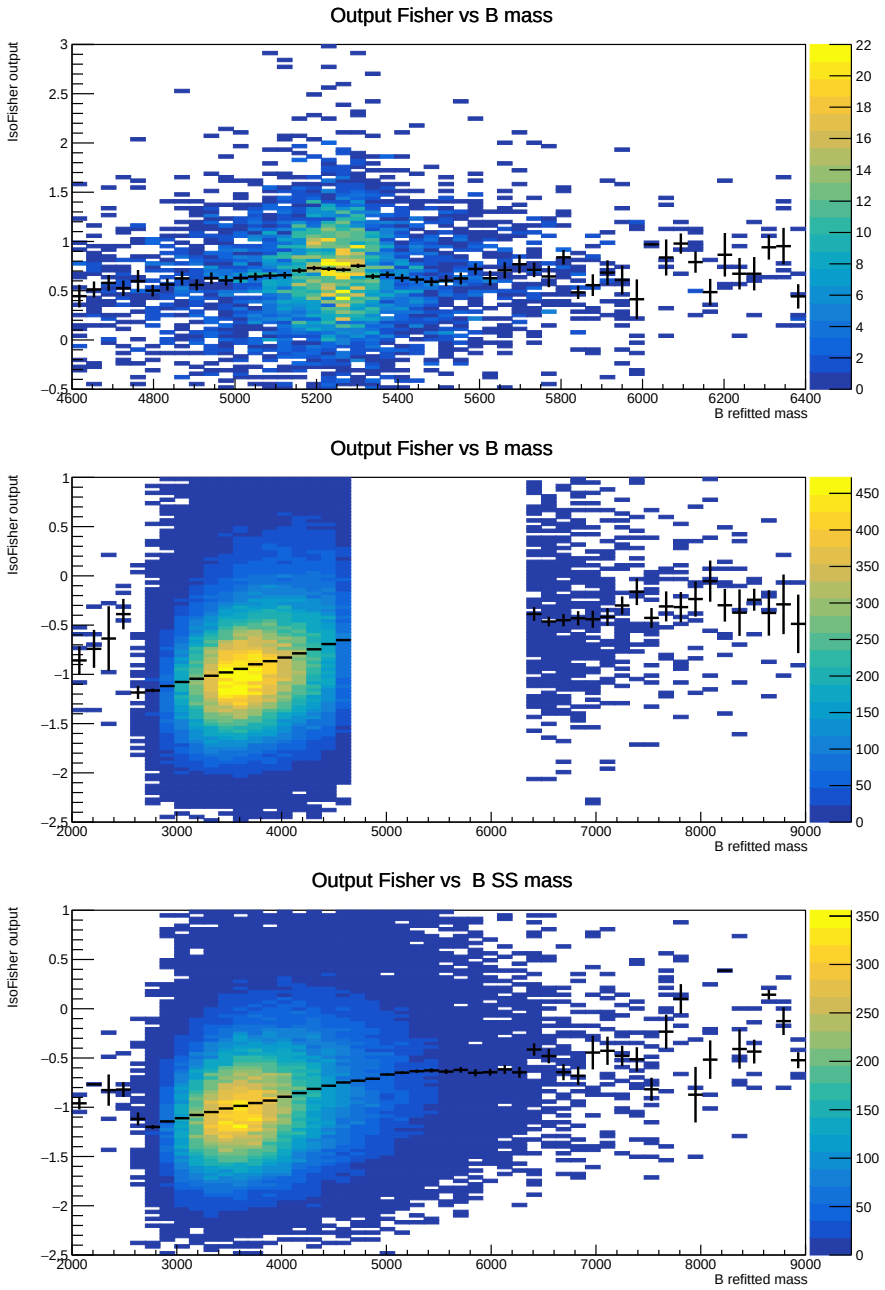

Figure K.2.2: Mass dependency for the isolation classifier output for the simulation sample in the signal region (top) and for the OS (middle) and SS (bottom) data in [2000, 9000] MeV region. The signal region has been blinded for the OS data. The superposed dots are obtained by profiling the classifier output for each mass bin. Correlation between the output and the mass has been observed for both SS and OS data samples.

K.2.1 Input variable validation

The classifier input variables are validated by comparing data and truth-matched MC events of the filtered control sample $B \to D^- D_s^+$. No strong discrepancies are found; therefore, the simulation is not re-weighted. Any possible difference is considered in the systematic calculation for the efficiencies.

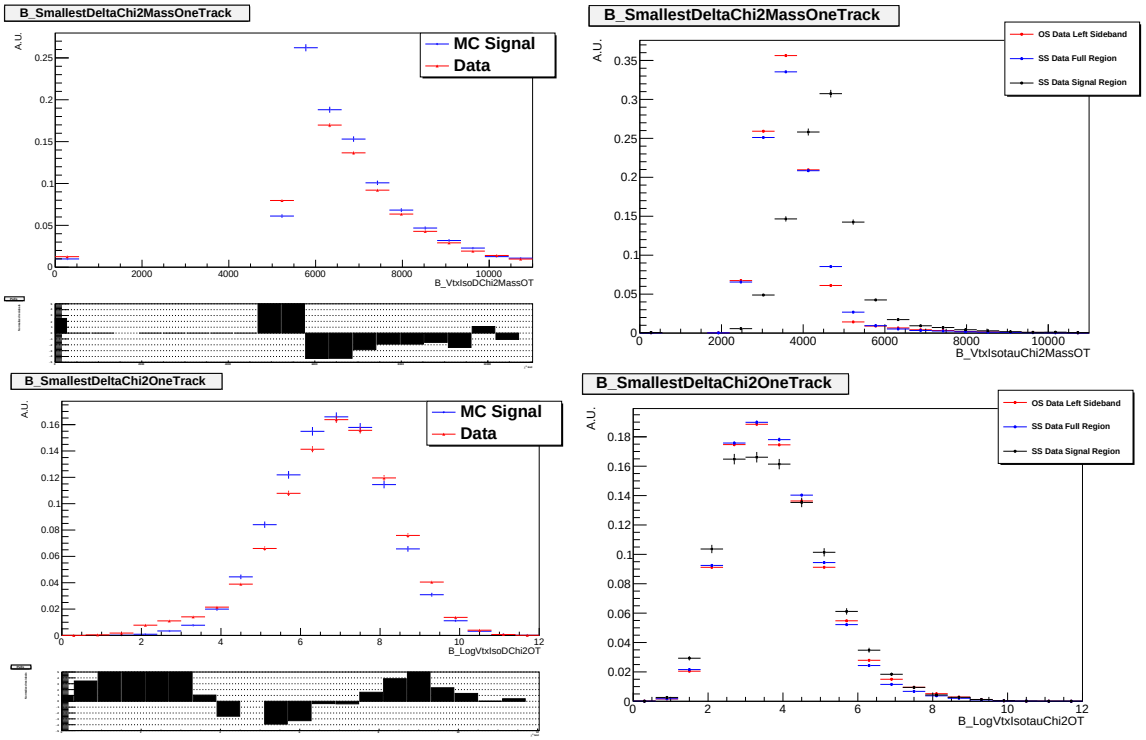

Figure K.2.3: Isolation input variable validation, part 1/3. On the left: validation distributions for data (red) and MC simulation (blue) using $B \to D^- D_s^+$ control sample for the input variables of the isolation classifier with pulls distribution on the bottom of the plots. MC candidates are truth-matched to correctly represent the sample, while for data, the selection described in Section 4.4.4 has been applied. On the right: Distributions of the same variables for $B \to K^* \tau e$ OS data (blue), SS data in the full region (black) and in the signal region (red).

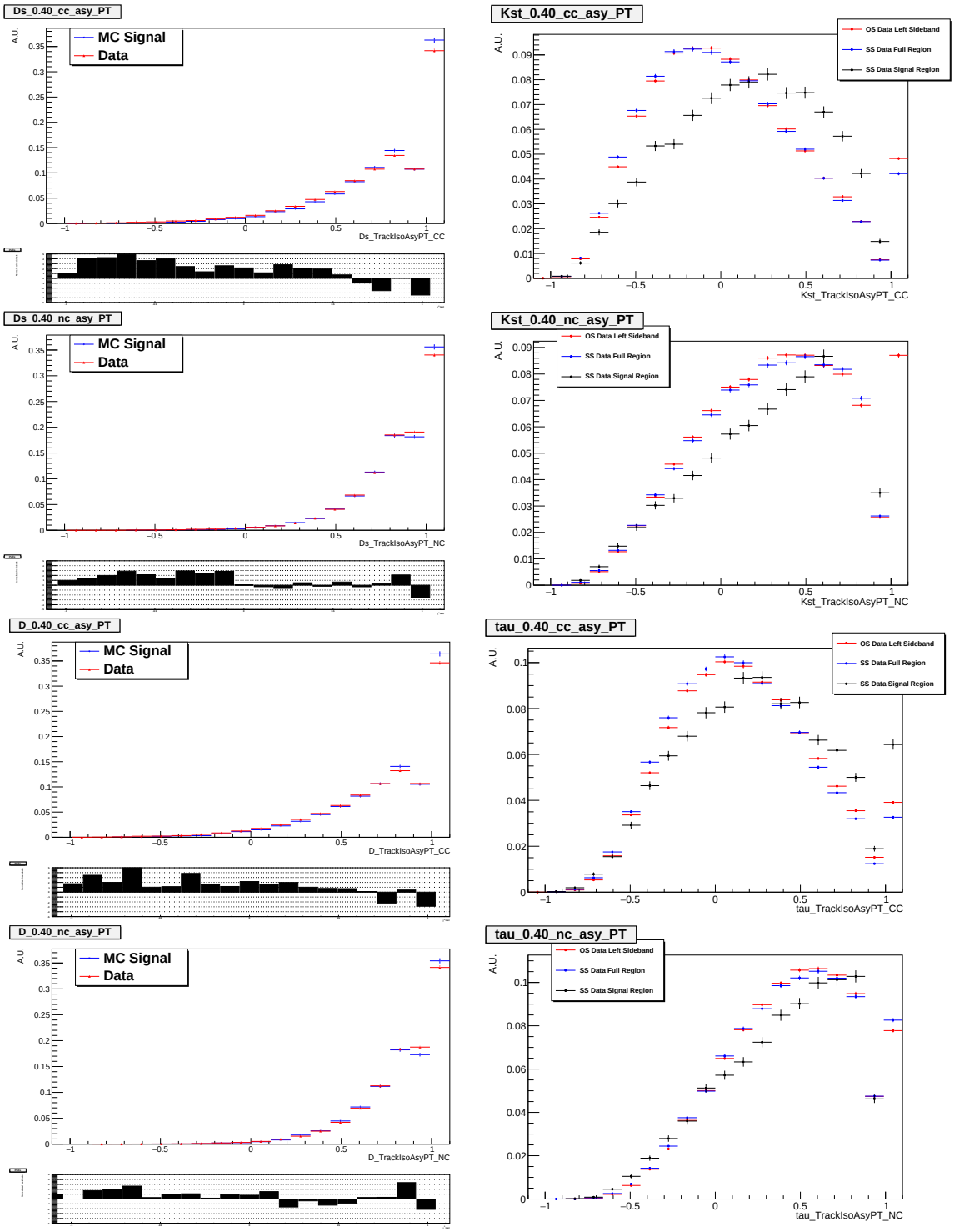

Figure K.2.4: Isolation input variable validation, part 2/3. On the left: validation distributions for data (red) and MC simulation (blue) using $B \to D^- D_s^+$ control sample for the input variables of the isolation classifier with pulls distribution on the bottom of the plots. MC candidates are truth-matched to correctly represent the sample, while for data, the selection described in Section 4.4.4 has been applied. On the right: Distributions of the same variables for $B \to K^* \tau e$ OS data (blue), SS data in the full region (black) and in the signal region (red).

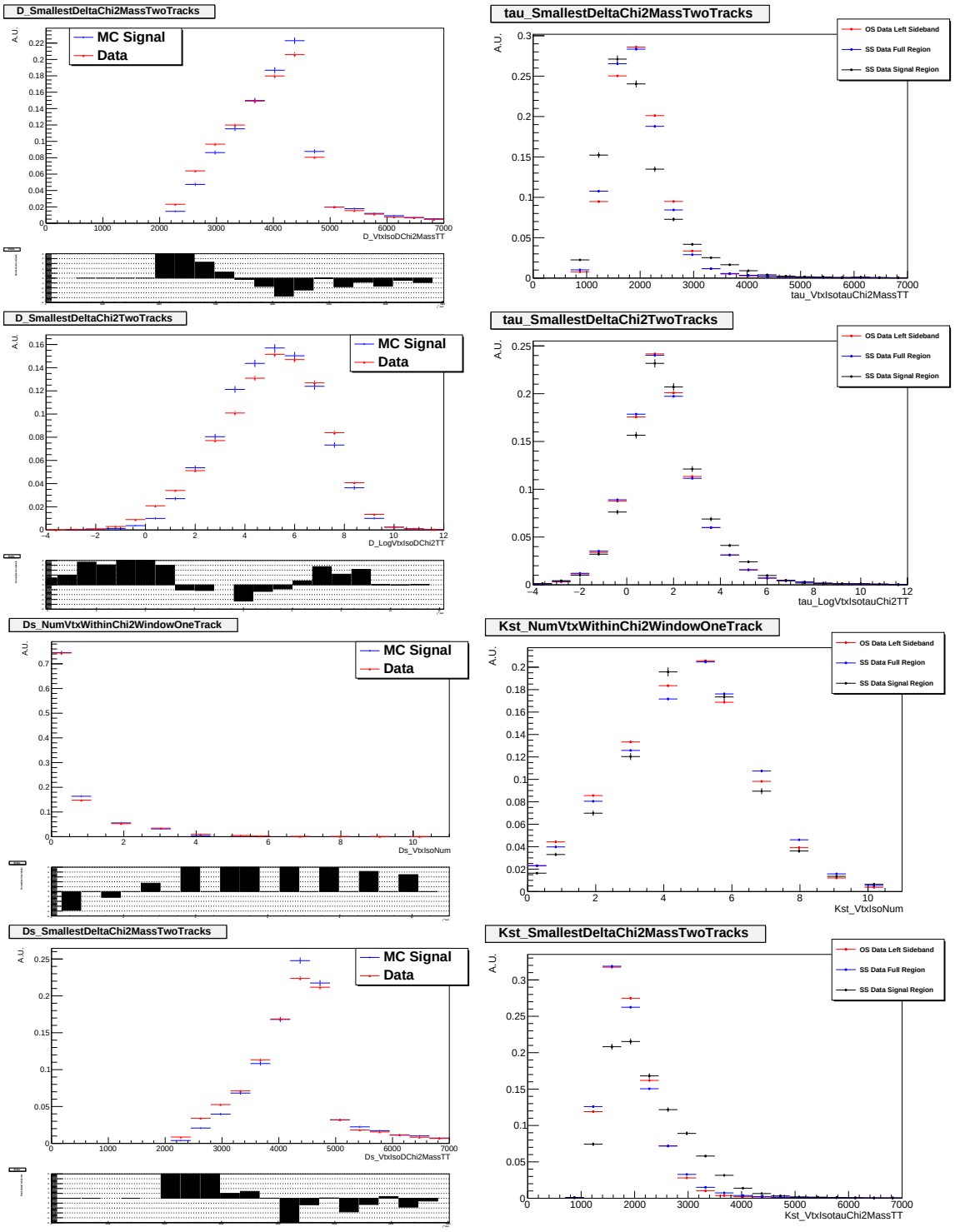

Figure K.2.5: Isolation input variable validation, part 3/3. On the left: validation distributions for data (red) and MC simulation (blue) using $B \to D^- D_s^+$control sample for the input variables of the isolation classifier with pulls distribution on the bottom of the plots. MC candidates are truth-matched to correctly represent the sample, while for data, the selection described in Section 4.4.4 has been applied. On the right: Distributions of the same variables for $B \to K^* \tau e$ OS data (blue), SS data in the full region (black) and in the signal region (red).

K.3 TauBDT

The mass dependency on the BDT output is represented in Figure K.3.1.

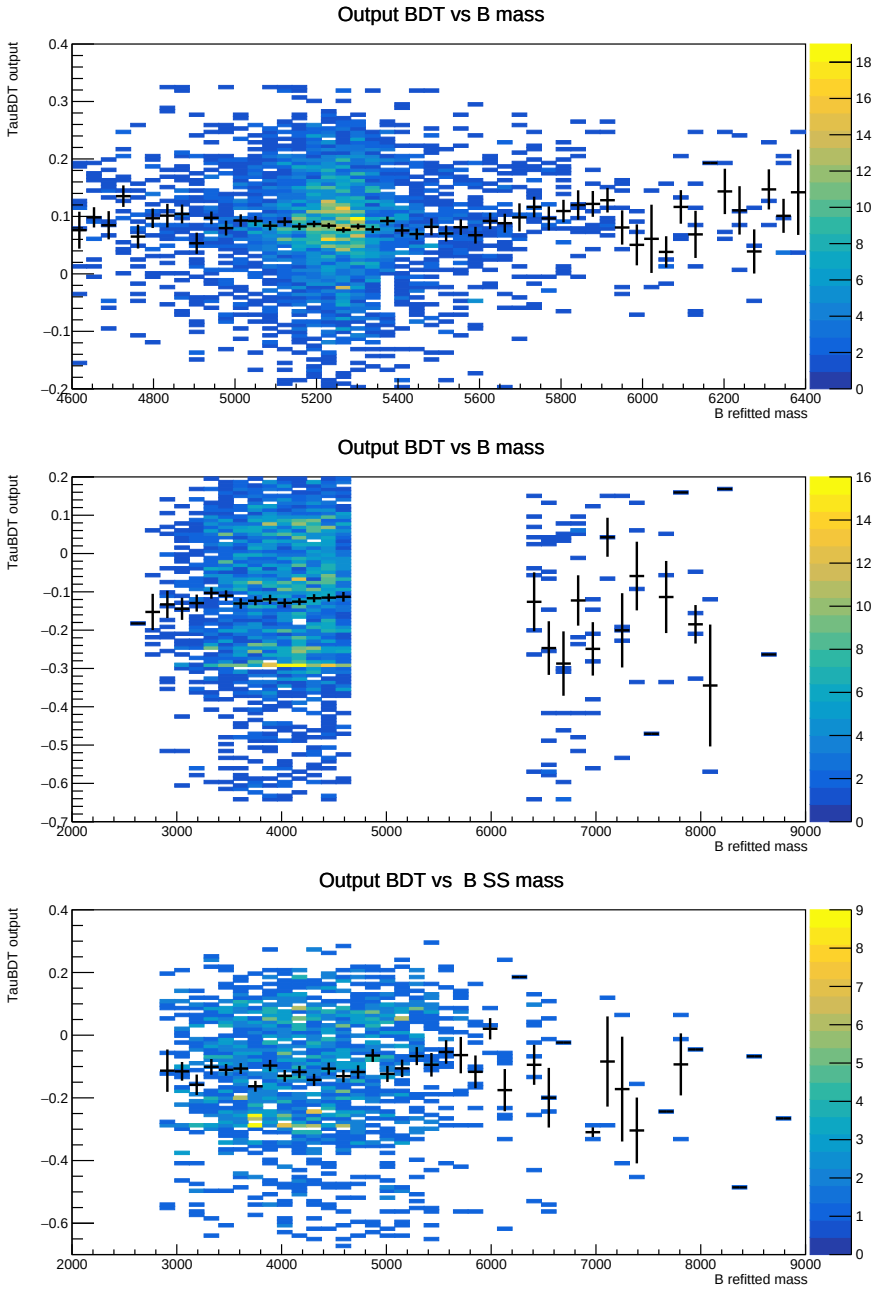

Figure K.3.1: Mass dependency for the τ classifier output for the simulation sample in the signal region (top) and for the OS (middle) and SS (bottom) data in [2000, 9000] MeV region (the signal region has been blinded for the OS data). The superposed dots are obtained by profiling the classifier output for each mass bin. No strong correlation between the output and the mass has been observed.

Appendix L

Flight distance

Flight distance, as well as its significance, are used as input of the anti-combinatorial classifier to discriminate background. Besides the `ACBDT` cut, flight distance and flight distance χ^2 cuts are applied to remove possible contaminating backgrounds. These cuts are very efficient and help to clean the control regions chosen for the background parameterization and obtain reverting the `ACBDT` requirement. Distributions for truth-matched simulated events, OS data and SS data are provided in Figures L.0.1, L.0.2 and L.0.3 respectively.

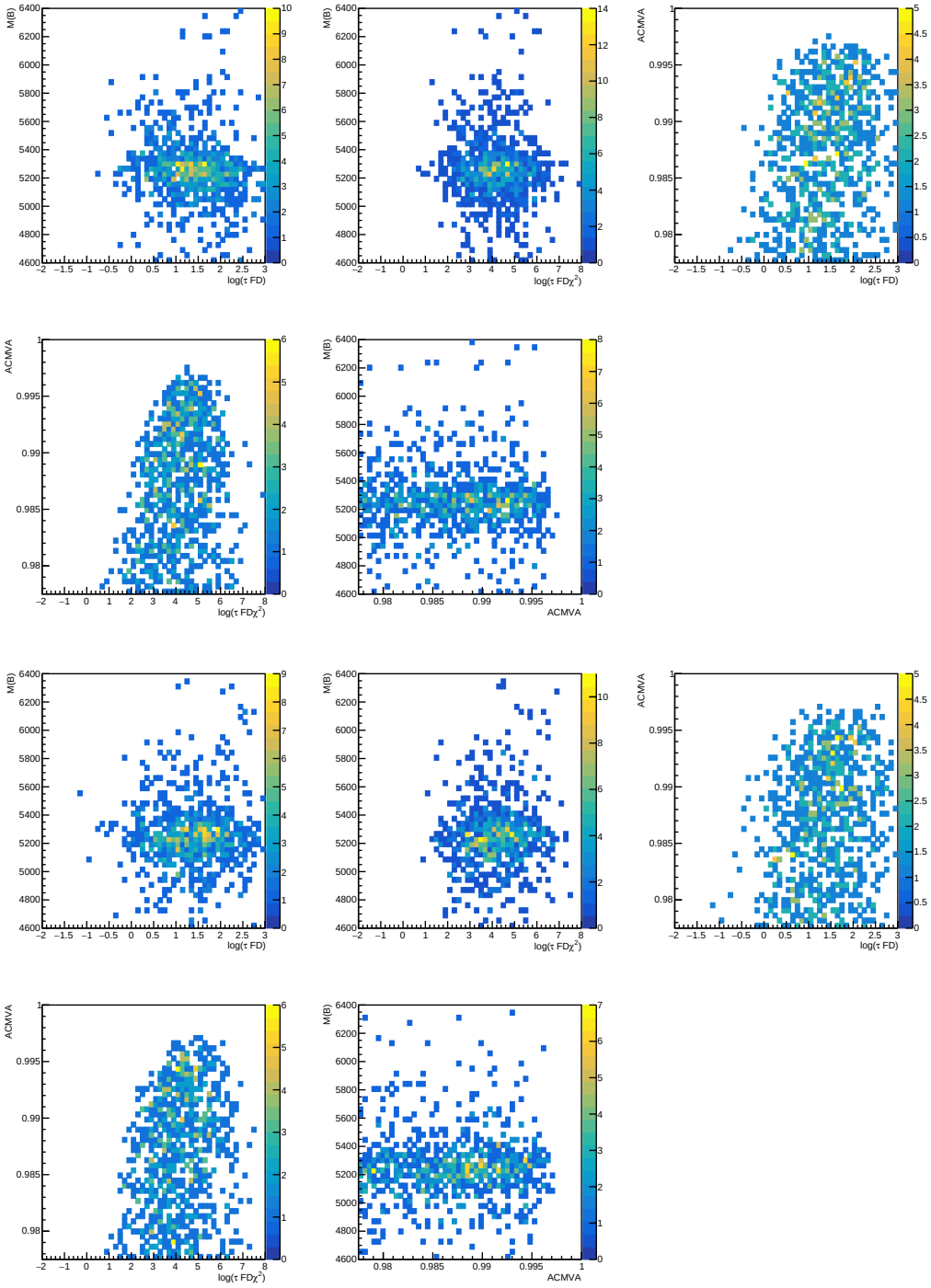

Figure L.0.1: Distributions refer to the truth-matched simulated events passing the selection for the OC category (top five frames) and SC category (bottom five frames). The dependencies between the τ flight distance and its significance with the refitted mass or the ACBDT cut are shown.

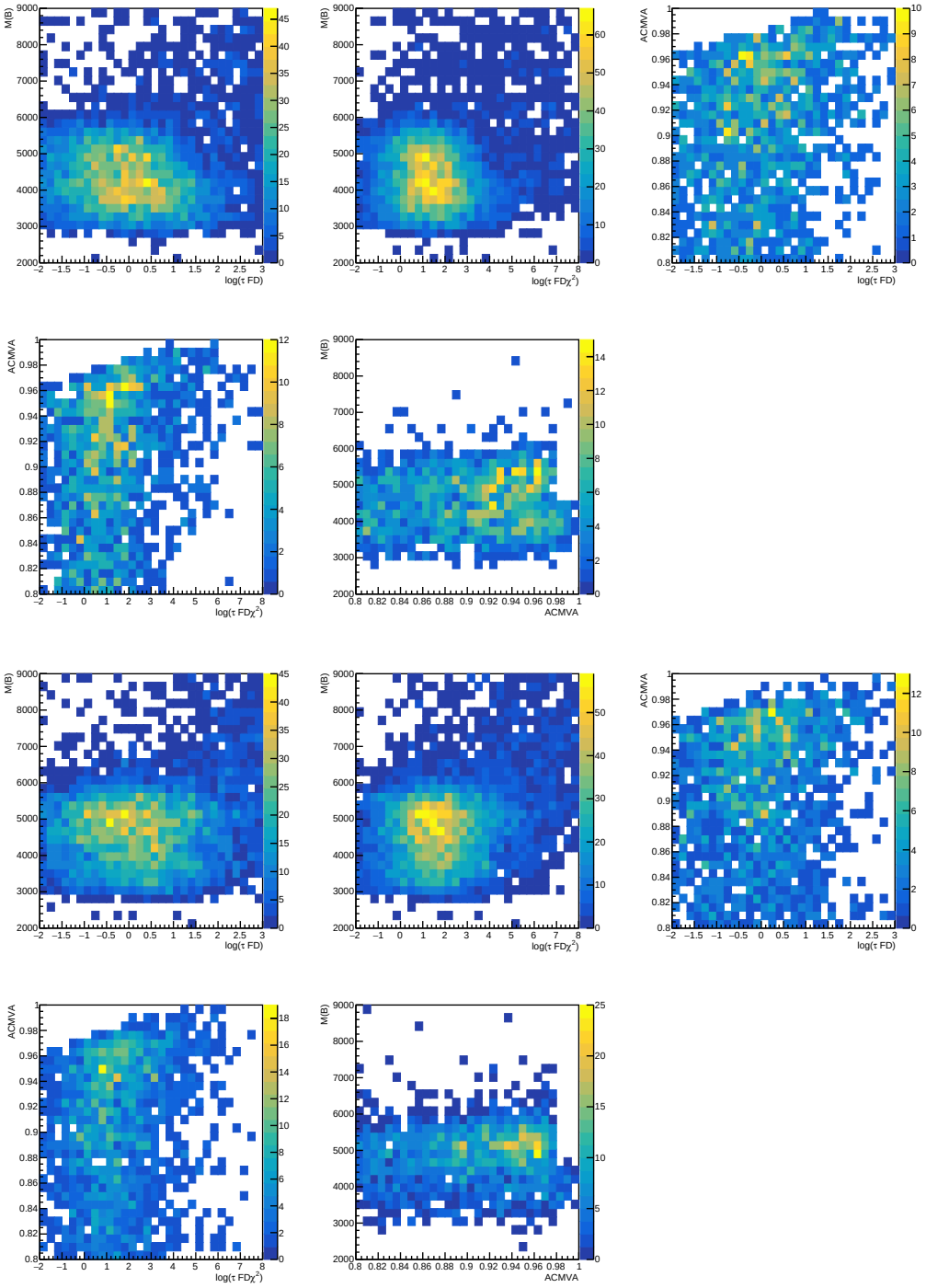

Figure L.0.2: Distributions refer to the OS events passing the selection with reverted ACBDT cut for the OC category (top five frames) and SC category (bottom five frames). The dependencies between the τ flight distance and its significance with the refitted mass or the ACBDT cut are shown.

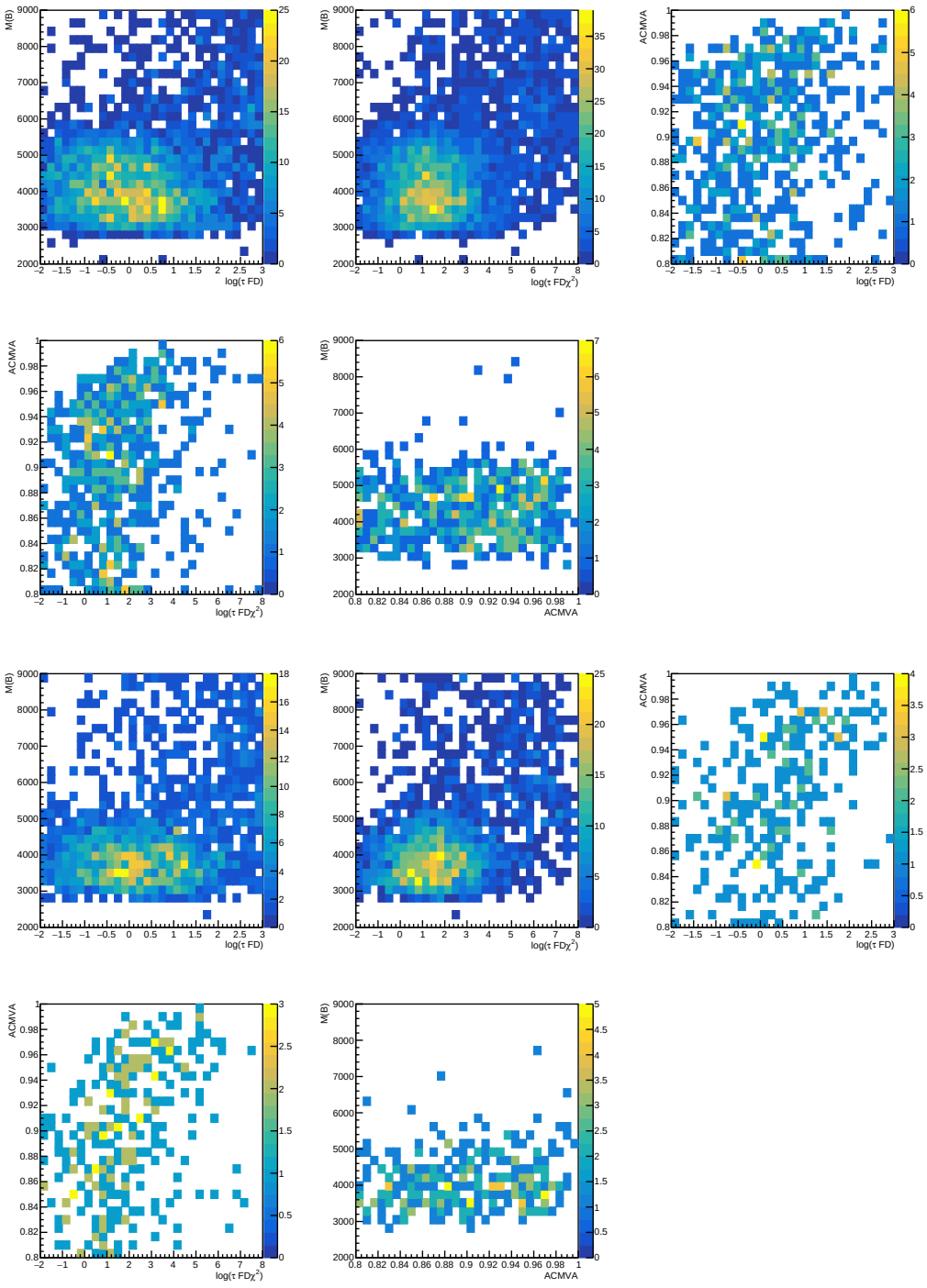

Figure L.0.3: Distributions refer to the SS events passing the selection without anti-combinatorial cut applied for the OC category (top five frames) and SC category (bottom five frames). The dependencies between the τ flight distance and its significance with the refitted mass or the ACBDT cut are shown.

L.0.1 Hadronic channels

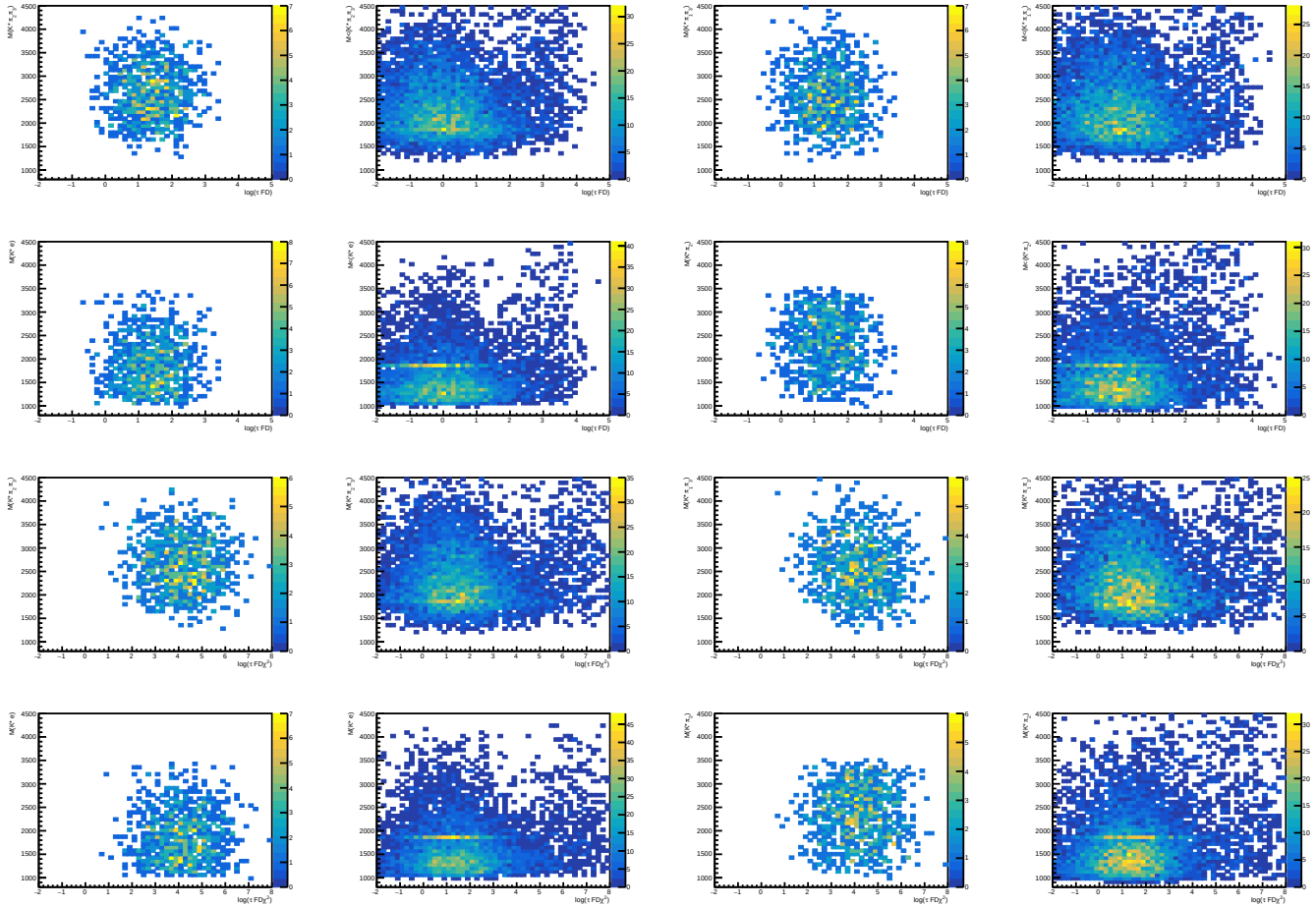

Figure L.0.4: Invariant mass of combinations of hadrons in the final state as a function of the logarithm of τ flight distance (top frames) and its significance (bottom frames) for signal MC (left) and background control region extracted from the OS data reverting the anti-combinatorial cut (right) for OC samples.

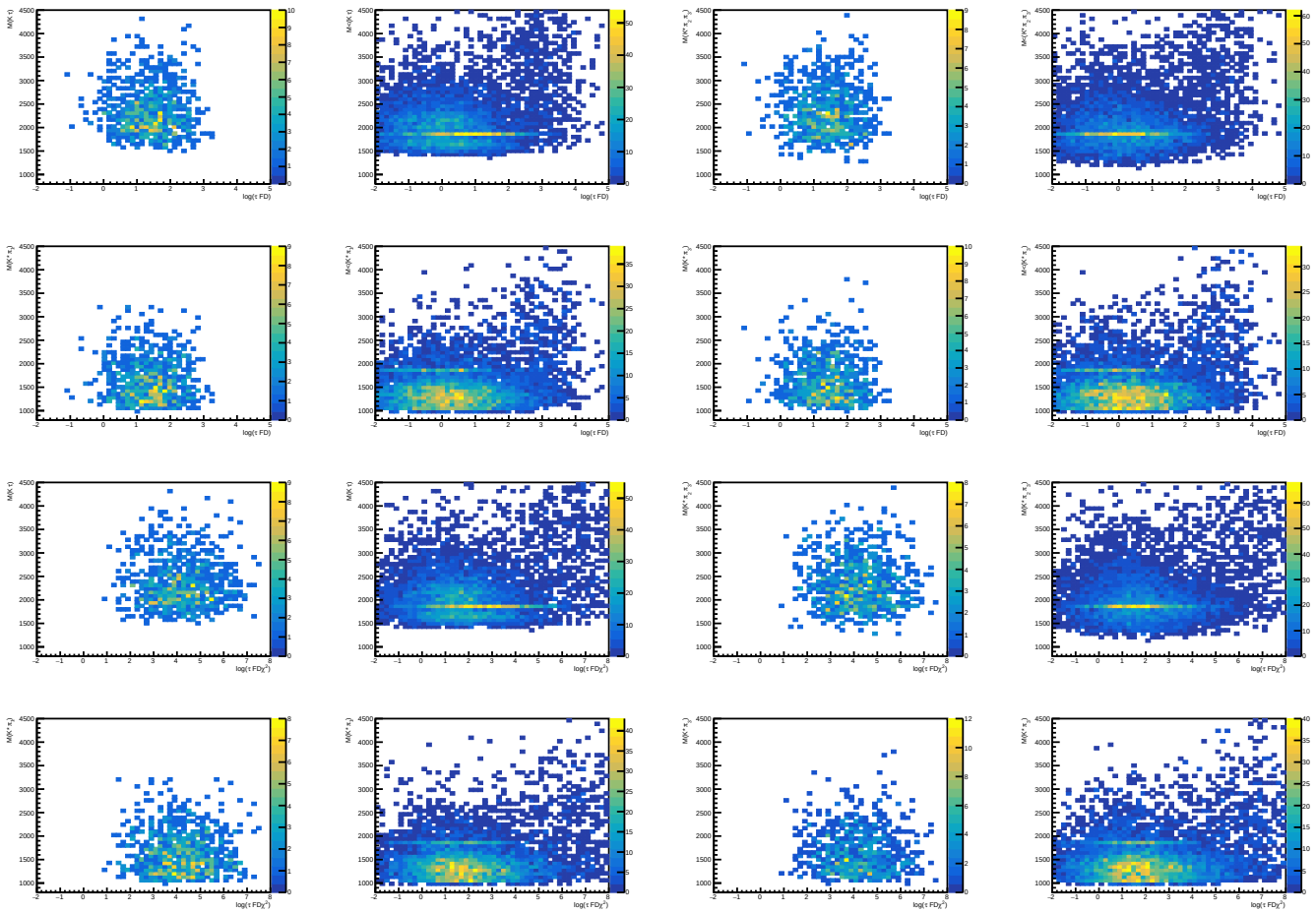

Figure L.0.5: Invariant mass of combinations of hadrons in the final state as a function of the logarithm of τ flight distance (top frames) and its significance (bottom frames) for signal MC (left) and background control region extracted from the OS data reverting the anti-combinatorial cut (right) for SC samples.

Appendix M

Invariant mass combinations

Distributions of invariant mass combinations are divided into charge combinations. As follows, only peaking distributions that correspond to potentially dangerous physics backgrounds are reported. Invariant masses are vetoed in correspondence with the peaks on the mass of D^0 for neutral combinations or D^+ for charged combinations. Vetoes applied have a width of ± 60 MeV/c^2 with PDG value as the central value. Also mis-identification cases are considered, changing the mass hypothesis accordingly.

M.1 Opposite-charge

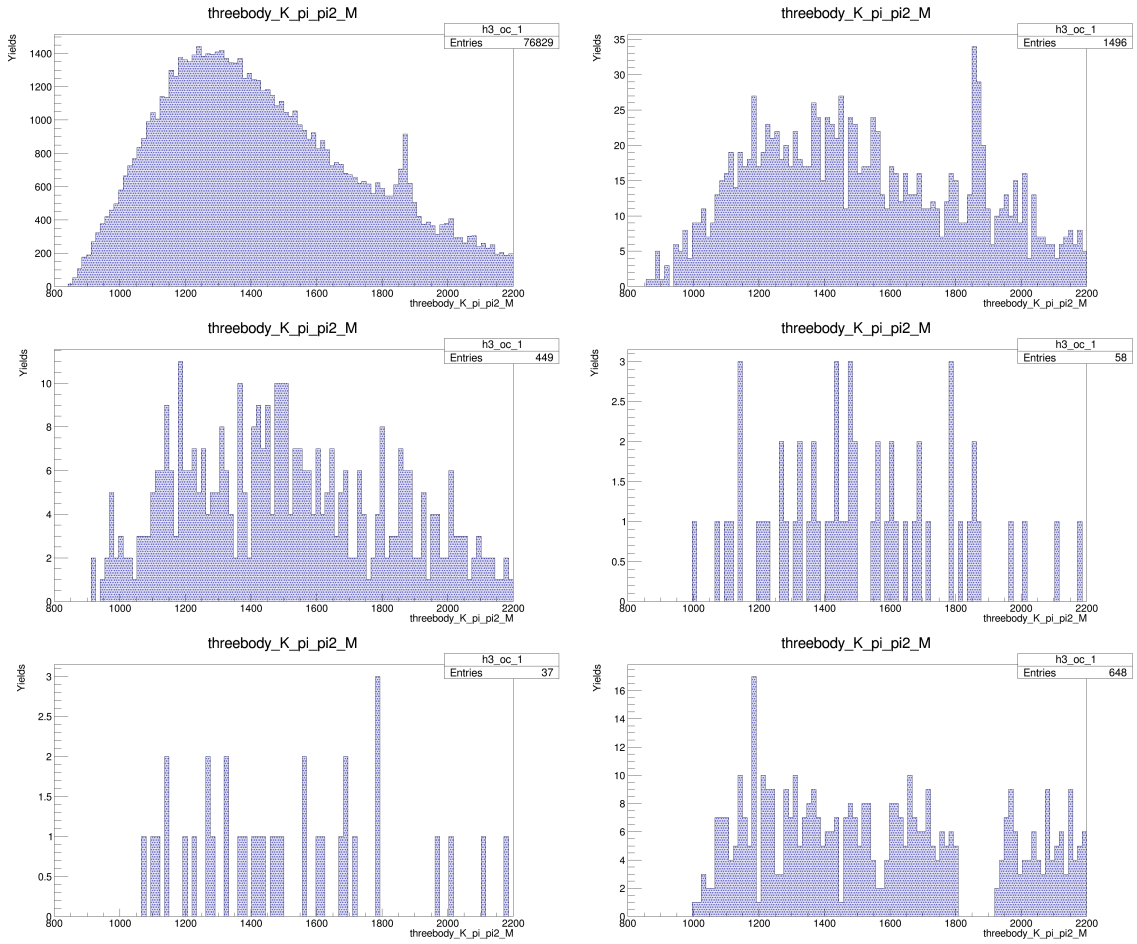

Figure M.1.1: Invariant mass distributions of kaon and pion from K^* decay and one pion from τ lepton decay for $B^0 \to K^{*0}\tau^+e^-$ (OC). Distributions in each frame represent events passing different stages of the selection: anti-combinatorial cut (top-left), isolation (top-right), τ BDT (center-left), all the selection excluding mass vetoes (center-right), including mass vetoes (bottom-left), and background control from opposite-sign data in the signal region with reversed anti-combinatorial cut (bottom-right).

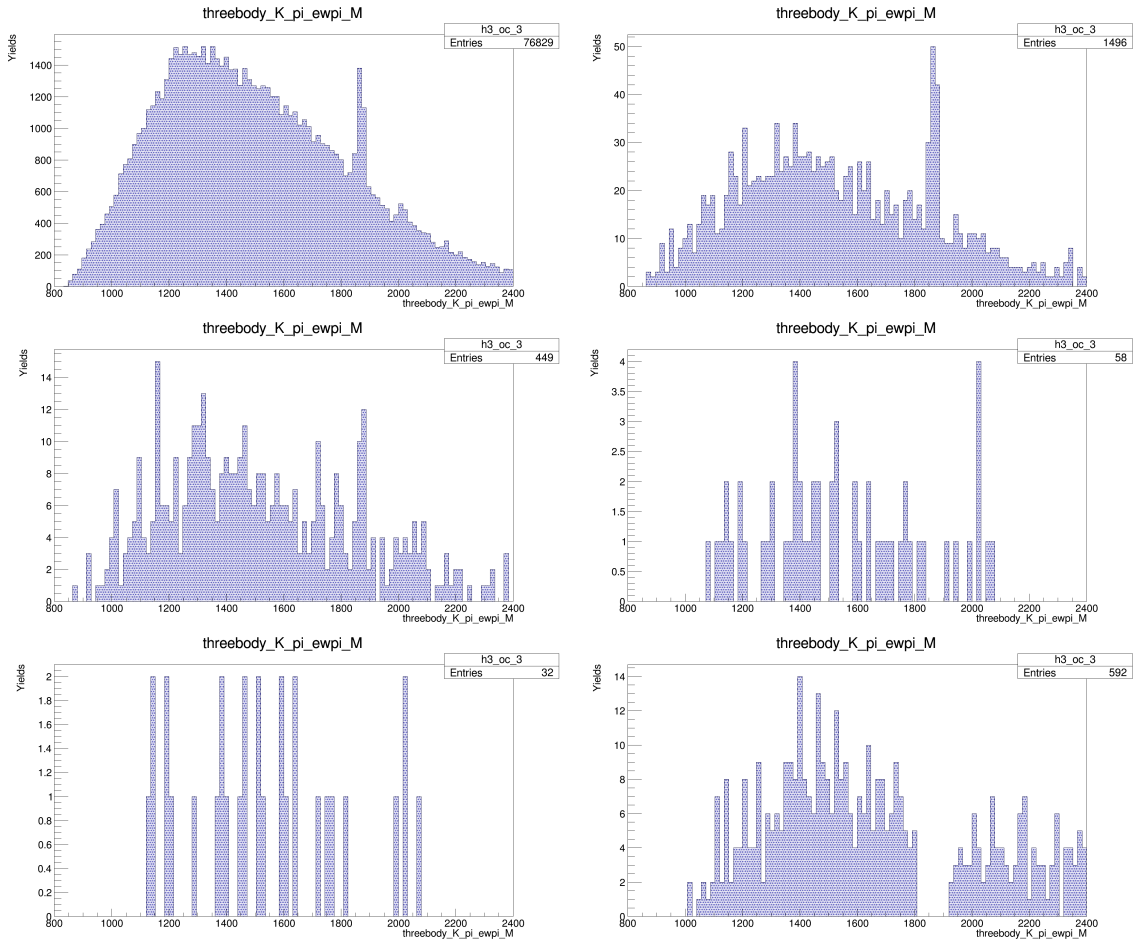

Figure M.1.2: Invariant mass distributions of a pion misidentified as an electron and kaon and pion from K^* decay for $B^0 \to K^{*0}\tau^+e^-$ (OC). Distributions in each frame represent events passing different stages of the selection: anti-combinatorial cut (top-left), isolation (top-right), τ BDT (center-left), all the selection excluding mass vetoes (center-right), including mass vetoes (bottom-left), and background control from opposite-sign data in the signal region with reversed anti-combinatorial cut (bottom-right).

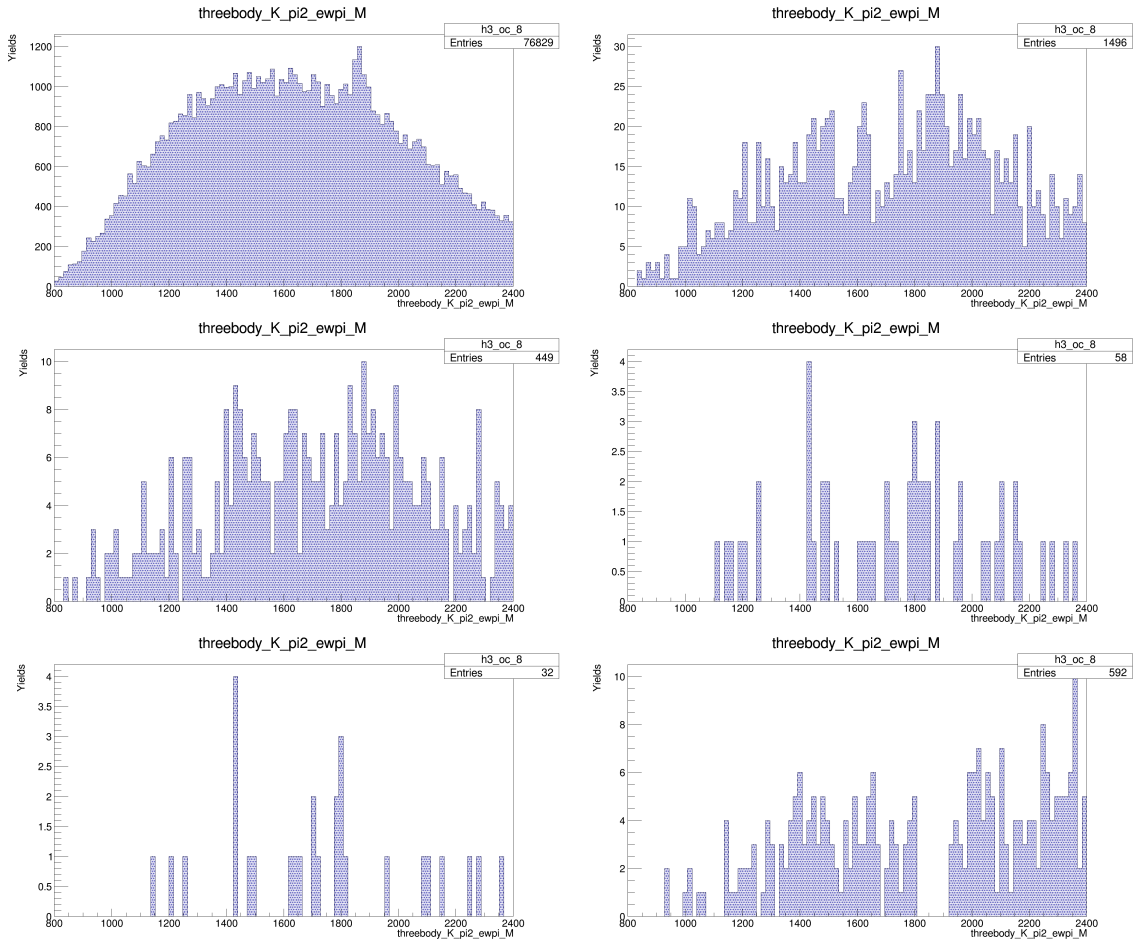

Figure M.1.3: Invariant mass distributions of kaon, pion misidentified as electron and one pion from τ lepton decay for $B^0 \to K^{*0}\tau^+e^-$ (OC). Distributions in each frame represent events passing different stages of the selection: anti-combinatorial cut (top-left), isolation (top-right), τ BDT (center-left), all the selection excluding mass vetoes (center-right), including mass vetoes (bottom-left), and background control from opposite-sign data in the signal region with reversed anti-combinatorial cut (bottom-right).

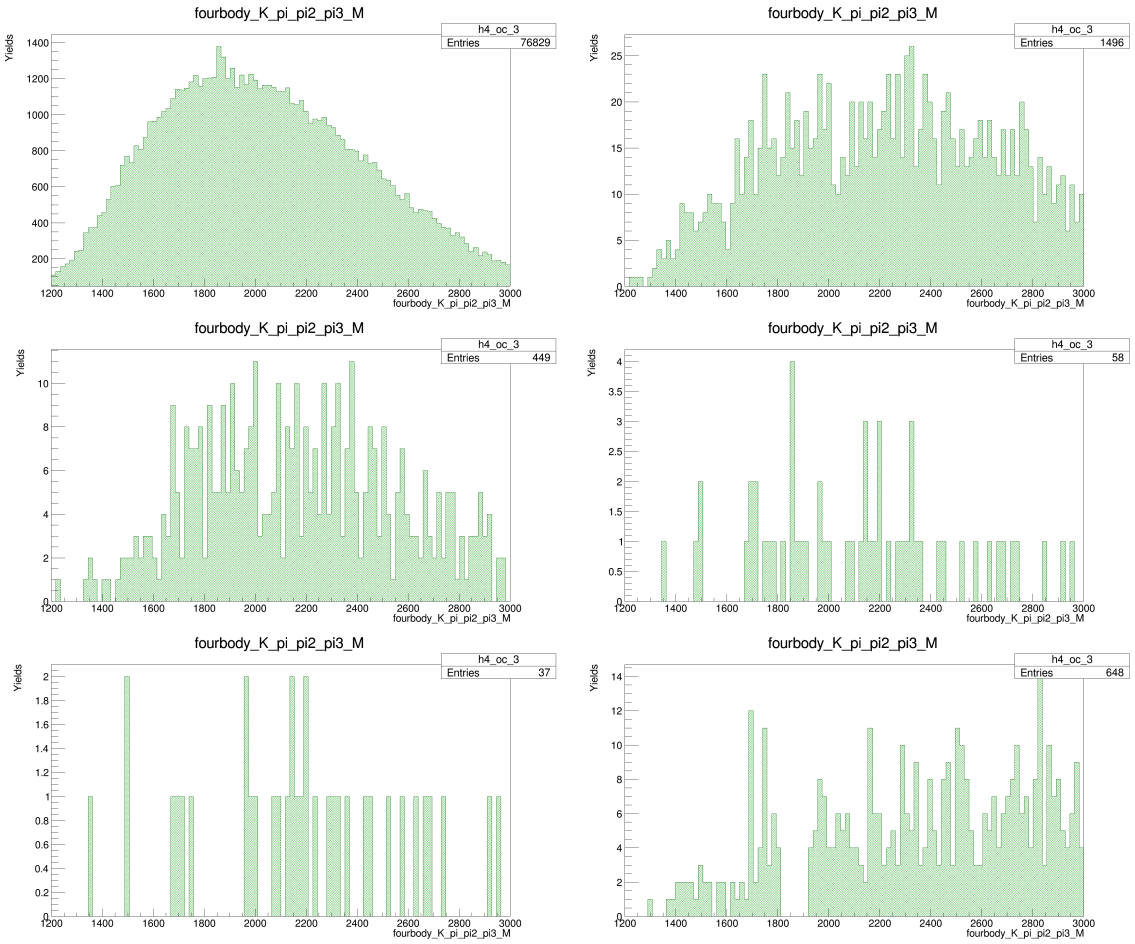

Figure M.1.4: Invariant mass distributions of kaon and pion from K^* decay and two pions from τ lepton decay for $B^0 \to K^{*0}\tau^+e^-$ (OC). Distributions in each frame represent events passing different stages of the selection: anti-combinatorial cut (top-left), isolation (top-right), τ BDT (center-left), all the selection excluding mass vetoes (center-right), including mass vetoes (bottom-left), and background control from opposite-sign data in the signal region with reversed anti-combinatorial cut (bottom-right).

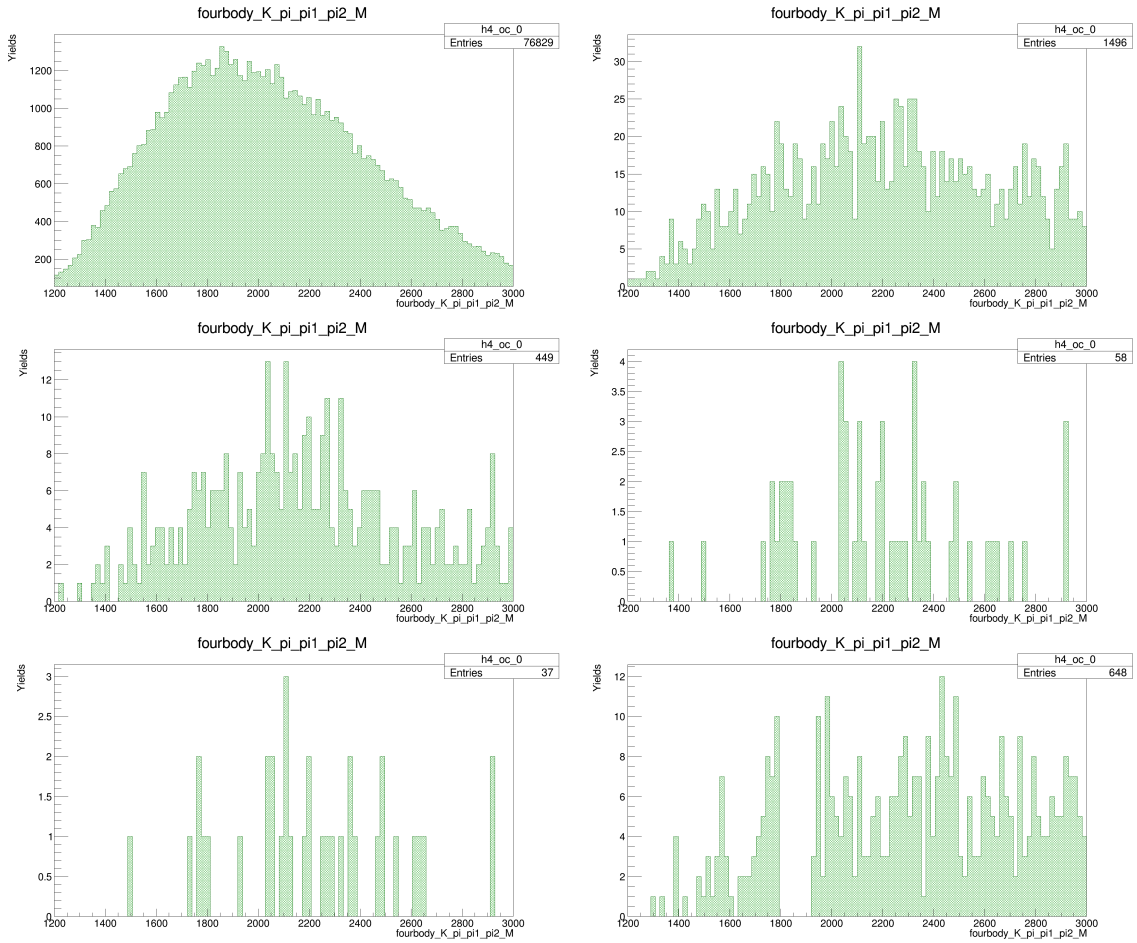

Figure M.1.5: Invariant mass distributions of kaon and pion from K^* decay and two pions from τ lepton decay for $B^0 \to K^{*0}\tau^+e^-$ (OC). Distributions in each frame represent events passing different stages of the selection: anti-combinatorial cut (top-left), isolation (top-right), τ BDT (center-left), all the selection excluding mass vetoes (center-right), including mass vetoes (bottom-left), and background control from opposite-sign data in the signal region with reversed anti-combinatorial cut (bottom-right).

M.2 Same-charge

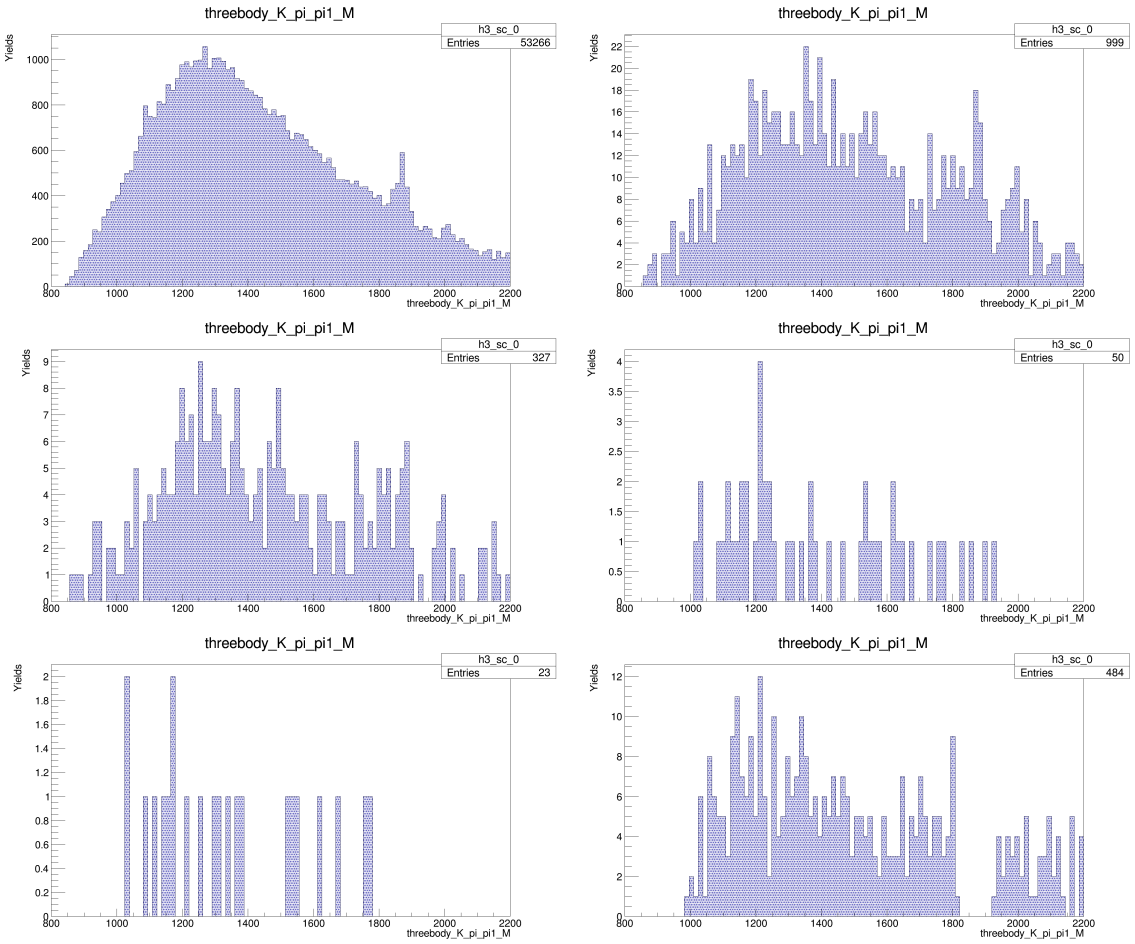

Figure M.2.1: Invariant mass distributions of kaon and pion from K^* decay and one pion from τ lepton decay for $B^0 \to K^{*0}\tau^- e^+$ (SC). Distributions in each frame represent events passing different stages of the selection: anti-combinatorial cut (top-left), isolation (top-right), τ BDT (center-left), all the selection excluding mass vetoes (center-right), including mass vetoes (bottom-left), and background control from opposite-sign data in the signal region with reversed anti-combinatorial cut (bottom-right).

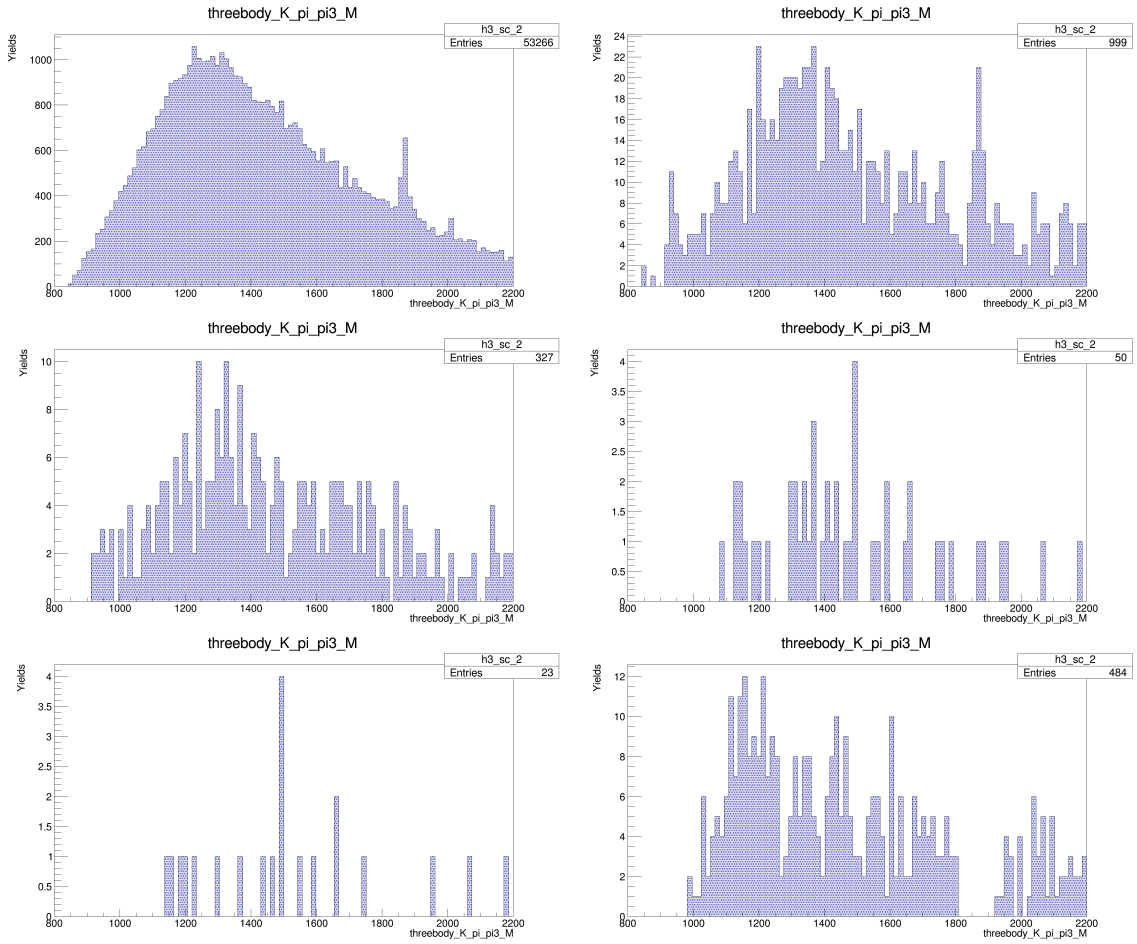

Figure M.2.2: Invariant mass distributions of kaon and pion from K^* decay and one pion from τ lepton decay for $B^0 \to K^{*0}\tau^- e^+$ (SC). Distributions in each frame represent events passing different stages of the selection: anti-combinatorial cut (top-left), isolation (top-right), τ BDT (center-left), all the selection excluding mass vetoes (center-right), including mass vetoes (bottom-left), and background control from opposite-sign data in the signal region with reversed anti-combinatorial cut (bottom-right).

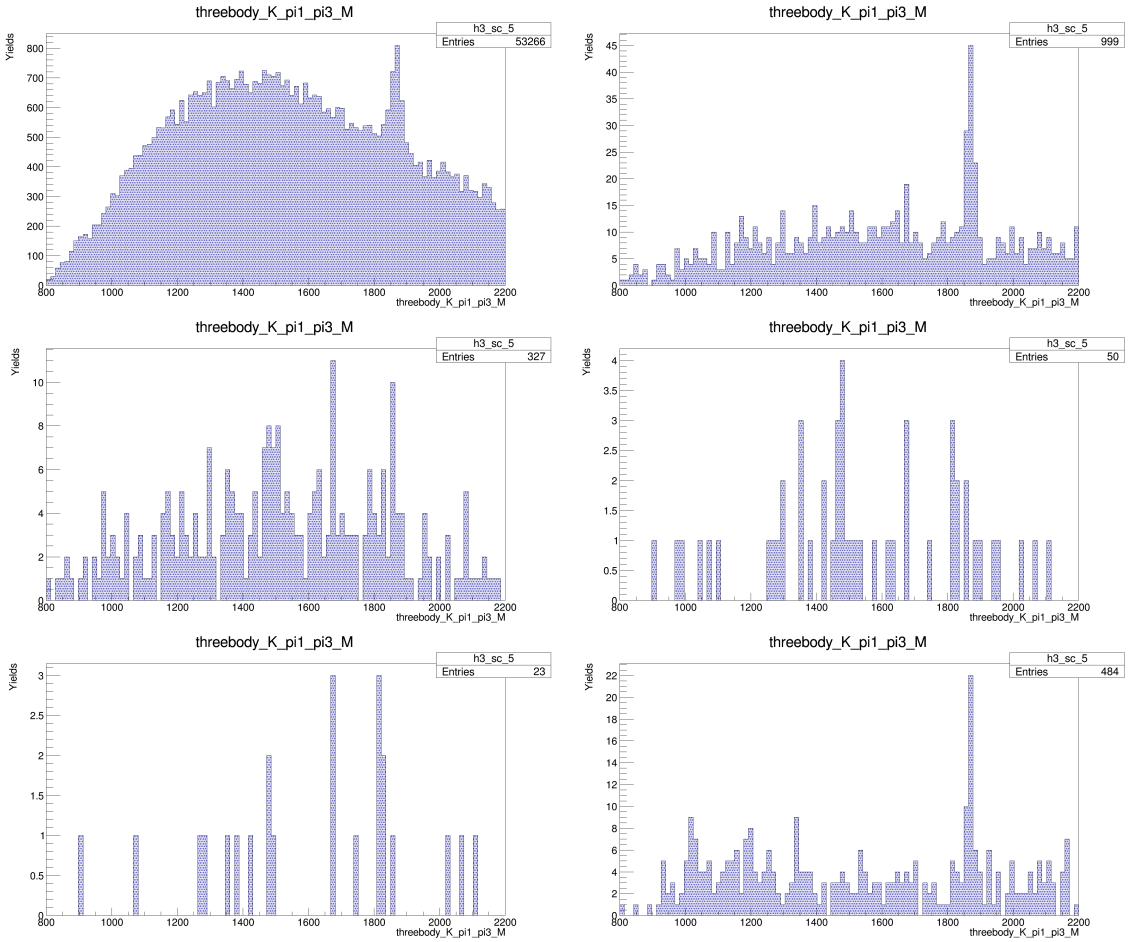

Figure M.2.3: Invariant mass distributions of kaon and two pions from τ lepton decay for $B^0 \to K^{*0}\tau^- e^+$ (SC). Distributions in each frame represent events passing different stages of the selection: anti-combinatorial cut (top-left), isolation (top-right), τ BDT (center-left), all the selection excluding mass vetoes (center-right), including mass vetoes (bottom-left), and background control from opposite-sign data in the signal region with reversed anti-combinatorial cut (bottom-right).

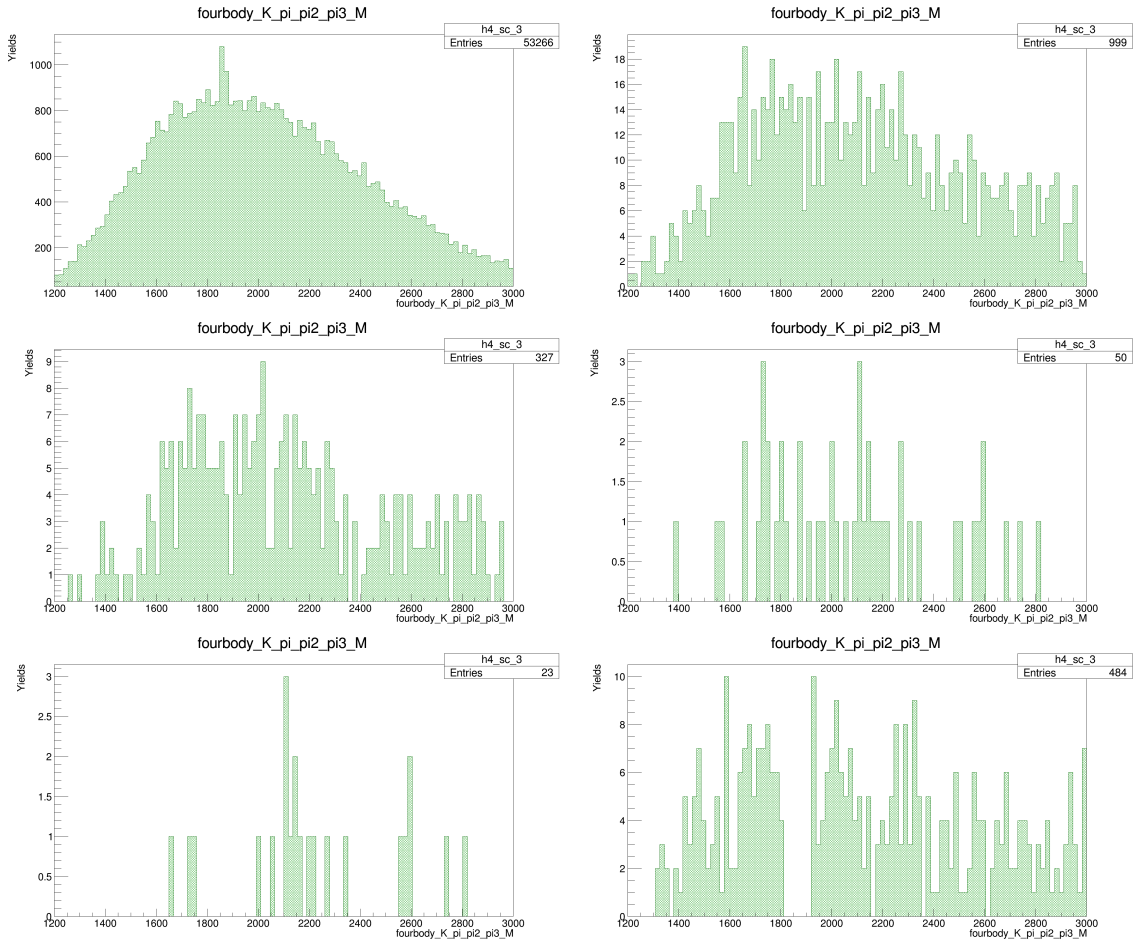

Figure M.2.4: Invariant mass distributions of kaon and pion from K^* decay and two pions from τ lepton decay for $B^0 \to K^{*0}\tau^- e^+$ (SC). Distributions in each frame represent events passing different stages of the selection: anti-combinatorial cut (top-left), isolation (top-right), τ BDT (center-left), all the selection excluding mass vetoes (center-right), including mass vetoes (bottom-left), and background control from opposite-sign data in the signal region with reversed anti-combinatorial cut (bottom-right).

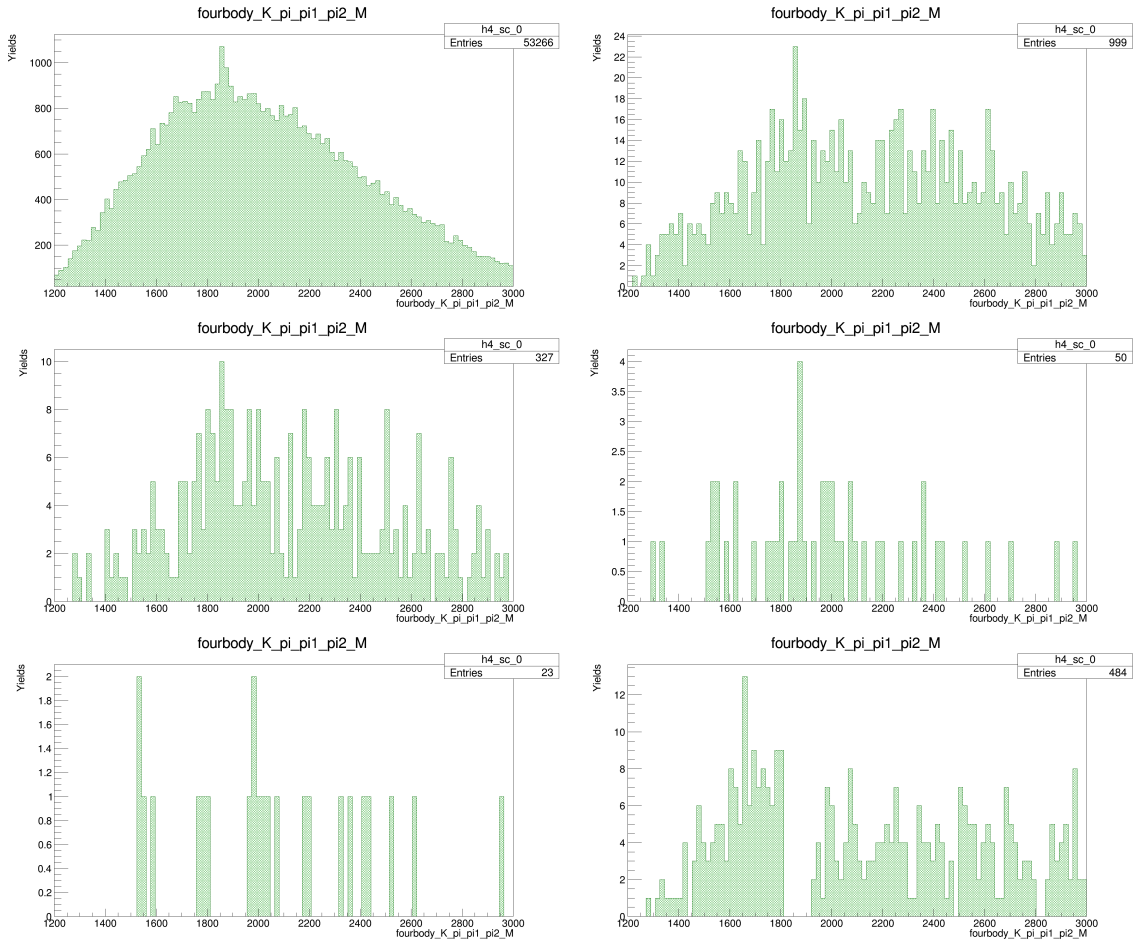

Figure M.2.5: Invariant mass distributions of kaon and pion from K^* decay and two pions from τ lepton decay for $B^0 \to K^{*0}\tau^- e^+$ (SC). Distributions in each frame represent events passing different stages of the selection: anti-combinatorial cut (top-left), isolation (top-right), τ BDT (center-left), all the selection excluding mass vetoes (center-right), including mass vetoes (bottom-left), and background control from opposite-sign data in the signal region with reversed anti-combinatorial cut (bottom-right).

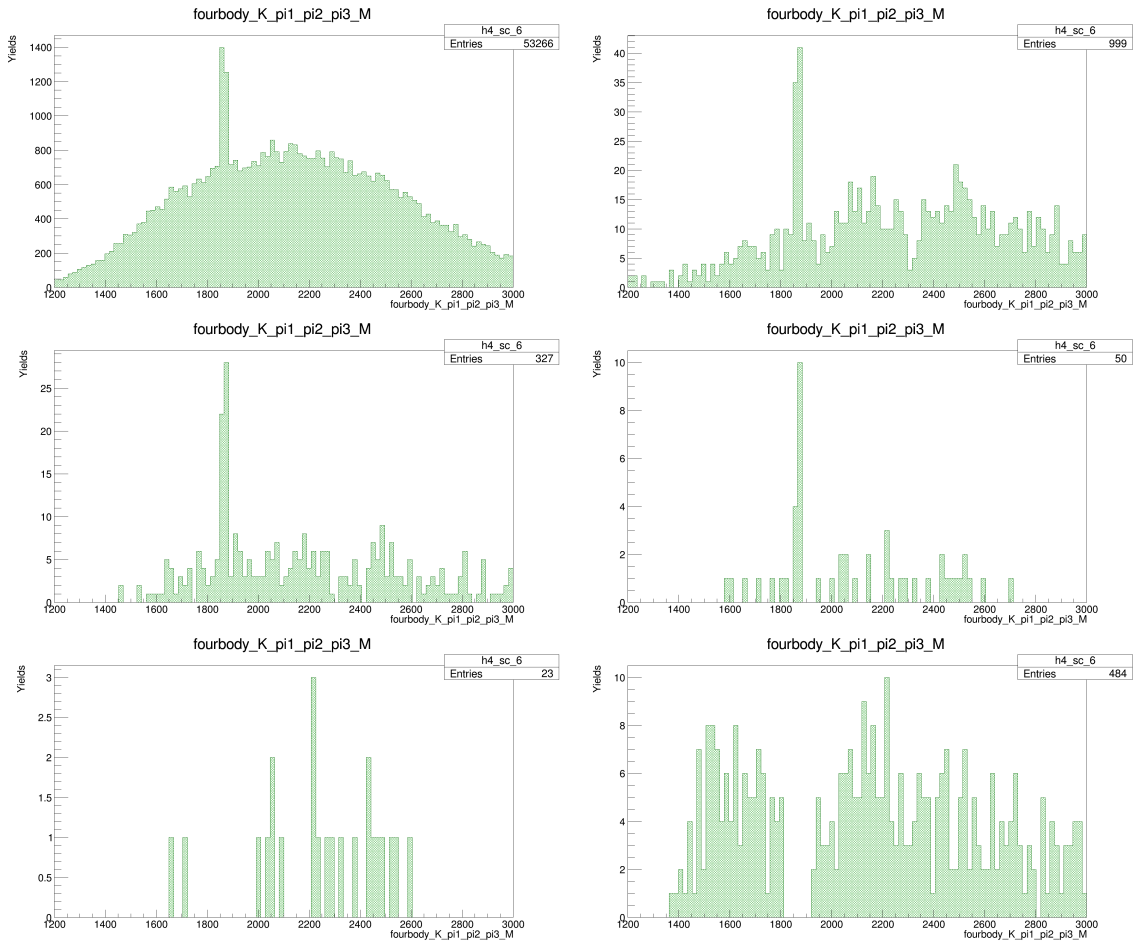

Figure M.2.6: Invariant mass distributions of kaon and three pions from τ lepton decay for $B^0 \to K^{*0}\tau^- e^+$ (SC). Distributions in each frame represent events passing different stages of the selection: anti-combinatorial cut (top-left), isolation (top-right), τ BDT (center-left), all the selection excluding mass vetoes (center-right), including mass vetoes (bottom-left), and background control from opposite-sign data in the signal region with reversed anti-combinatorial cut (bottom-right).

Appendix N

Cross-check on physics backgrounds

The impact of the selection chain is cross-checked, simulating samples of some potentially dangerous physics backgrounds with a topology or final state similar to the signal ones. It is worth noting that this is just a cross-check since it is hard to simulate all the potential backgrounds and, for the sample simulated, to collect a sample large enough to have a precise estimate of the events surviving this analysis's strong selection. As will be discussed in the following sections, the background estimation for the limit set will be based on a data-driven method.
The following MC simulations are checked.

- Semileptonic cascades of $B^0 \to D^{*-}\tau^+\nu_\tau$, with $D^{*-} \to (\bar{D}^0 \to \pi^- K^+)\pi^-$ and both hadronic decay modes of $\tau \to \pi\pi\pi\nu_\tau$
  and $\tau \to \pi\pi\pi\pi^0\nu_\tau$;

- Inclusive semileptonic cascades of $B^0 \to D^0 X^+ e^-\nu_e$;

- Fully-hadronic decays with mis-ID in the final stat $B^0 \to D^{*-}\pi^+\pi^-\pi^+$
  $(D^{*-} \to (\bar{D}^0 \to \pi^- K^+)\pi^-)$ and $B^0 \to D^-\pi^+\pi^-\pi^+(D^0 \to \pi^+ K^-)$;

- Double mis-ID $B \to D^- D_s^+$, with $D^- \to K^+\pi^-\pi^-$and $D_s^+ \to K^+K^-\pi^+$.

The expected yields of physics background surviving the selection chain and inside the signal region are estimated using the normalization channel:

$$N_{bkg} = N_{norm} \times \frac{\epsilon_{bkg}}{\epsilon_{norm}} \times \frac{\mathcal{B}_{bkg}}{\mathcal{B}_{norm}} \tag{N.0.1}$$

where ϵ_{bkg} and ϵ_{norm} are the selection efficiency on background simulated sample and normalization sample, N_{norm} are the normalization yields after the selection and $\frac{\mathcal{B}_{bkg}}{\mathcal{B}_{norm}}$ is the branching fraction ratio between the background channel and the normalization one. Events are simulated as reported in Table H.0.2 for 2016. The $B^0 \to D^{*-}\tau^+\nu_\tau$ T5 channel (with $\tau \to \pi\pi\pi\nu_\tau$) was also simulated for 2017. The

expected background yield is rescaled based on luminosity for years of data taking 2016, 2017, and 2018, according to the following relation:

$$N_{tot} = N_{sim} \times \frac{\mathcal{L}_{tot}}{\mathcal{L}_{sim}} \tag{N.0.2}$$

where N_{sim} and N_{tot} are, respectively, the yield expected for the years of the simulation and for the three years of data taking 2016, 2017, and 2018; while $\frac{\mathcal{L}_{tot}}{\mathcal{L}_{sim}}$ is the ratio between the total integrated luminosity of the three years and the years of the simulated sample. The results are collected in Table N.0.1.

Decay channel	Branching ratio	Generator cut efficiency	Selection efficiency	Events after selection	Events expected in 2016+2017+2018 data
$B^0 \to D^{*-}\tau^+\nu_\tau$, with $D^{*-} \to \bar{D}^0\pi^-$ $\bar{D}^0 \to \pi^-K^+$ $\tau \to \pi\pi\pi\nu_\tau$	$(3.93 \pm 0.23) \times 10^{-5}$	$15.92 \pm 0.22\%$	$< (4.4 \times 10^{-8})$	0	< 0.2
$B^0 \to D^{*-}\tau^+\nu_\tau$, with $D^{*-} \to \bar{D}^0\pi^-$ $\bar{D}^0 \to \pi^-K^+$ $\tau \to \pi\pi\pi\pi^0\nu_\tau$	$(1.95 \pm 0.15) \times 10^{-5}$	$15.59 \pm 0.21\%$	$< (0.9 \times 10^{-7})$	0	< 0.7
$B^0 \to D^0X^+e^-\nu_e$, with $D^0 \to \pi^+K^-$	$(4.0 \pm 1.6) \times 10^{-3}$	$33.34 \pm 0.07\%$	$< (2.7 \times 10^{-6})$	0	$< 2 \times 10^3$
$B \to D^-D_s^+$, with $D^- \to K^+\pi^-\pi^-$ $D_s^+ \to K^+K^-\pi^+$	$(3.63 \pm 0.41) \times 10^{-5}$	$12.54 \pm 0.05\%$	$< (4.9 \times 10^{-9})$	0	< 1.5
$B^0 \to D^-\pi^+\pi^-\pi^+$, with $D^0 \to \pi^+K^-$	$(5.63 \pm 0.57) \times 10^{-5}$	$15.39 \pm 0.03\%$	$< (2.6 \times 10^{-6})$	0	< 15
$B^0 \to D^{*-}\pi^+\pi^-\pi^+$, with $D^{*-} \to \bar{D}^0\pi^-$ $D^0 \to \pi^-K^+$	$(1.93 \pm 0.08) \times 10^{-4}$	$12.7 \pm 0.02\%$	$< (3.4 \times 10^{-4})$	0	< 11300

Table N.0.1: MC simulated events of physics background channel surviving the selection. It came out that no event is passing the selection. The expected background is estimated in data for the simulated year and re-scaled for the integrated luminosity for the years 2016, 2017 and 2018.

Appendix O

Electron tracking corrections

Electron tracking maps are evaluated using $B \to J/\psi(\to e^+e^-)K$ sample in [213]. The corrections are applied to the signal simulation in bins of η, ϕ and P_T.

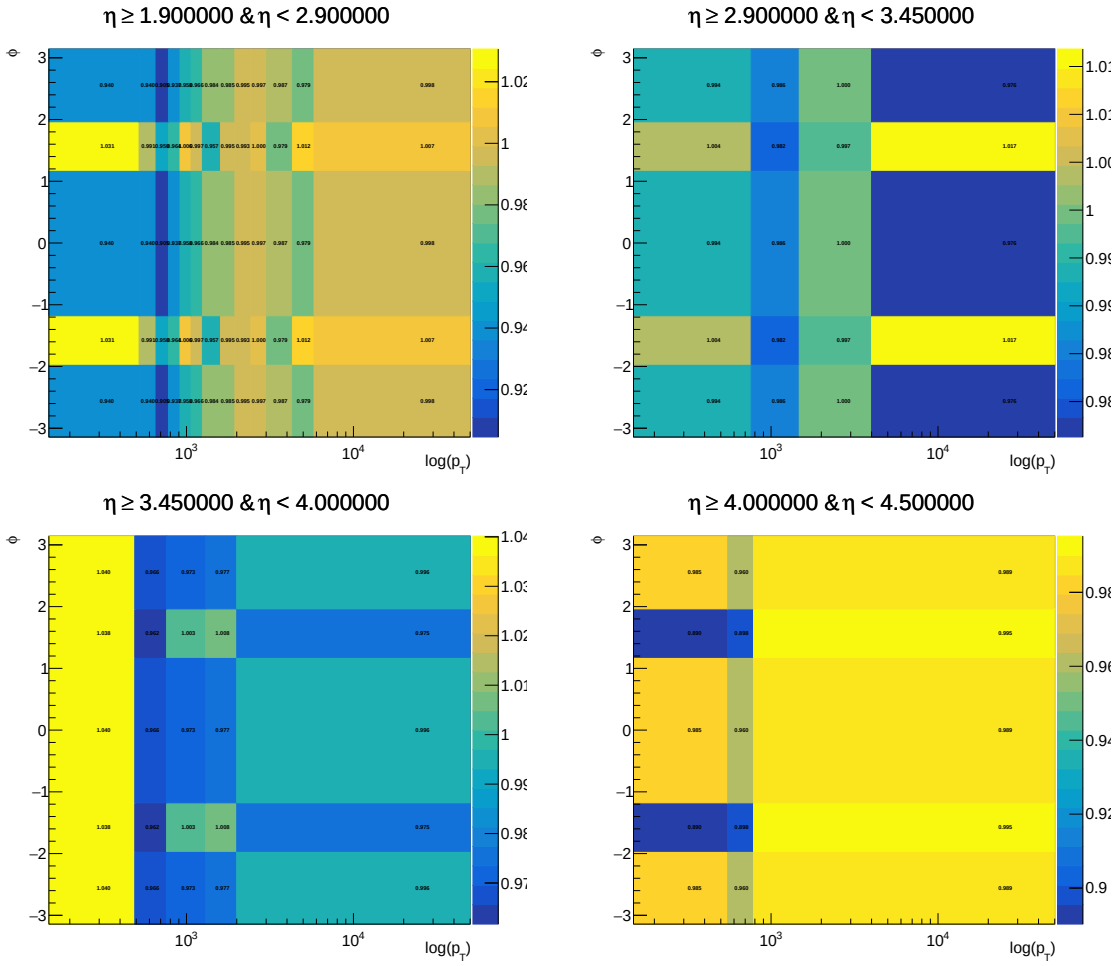

Figure O.0.1: Electron tracking efficiency correction maps for different bins of η for 2016 year of data taking.

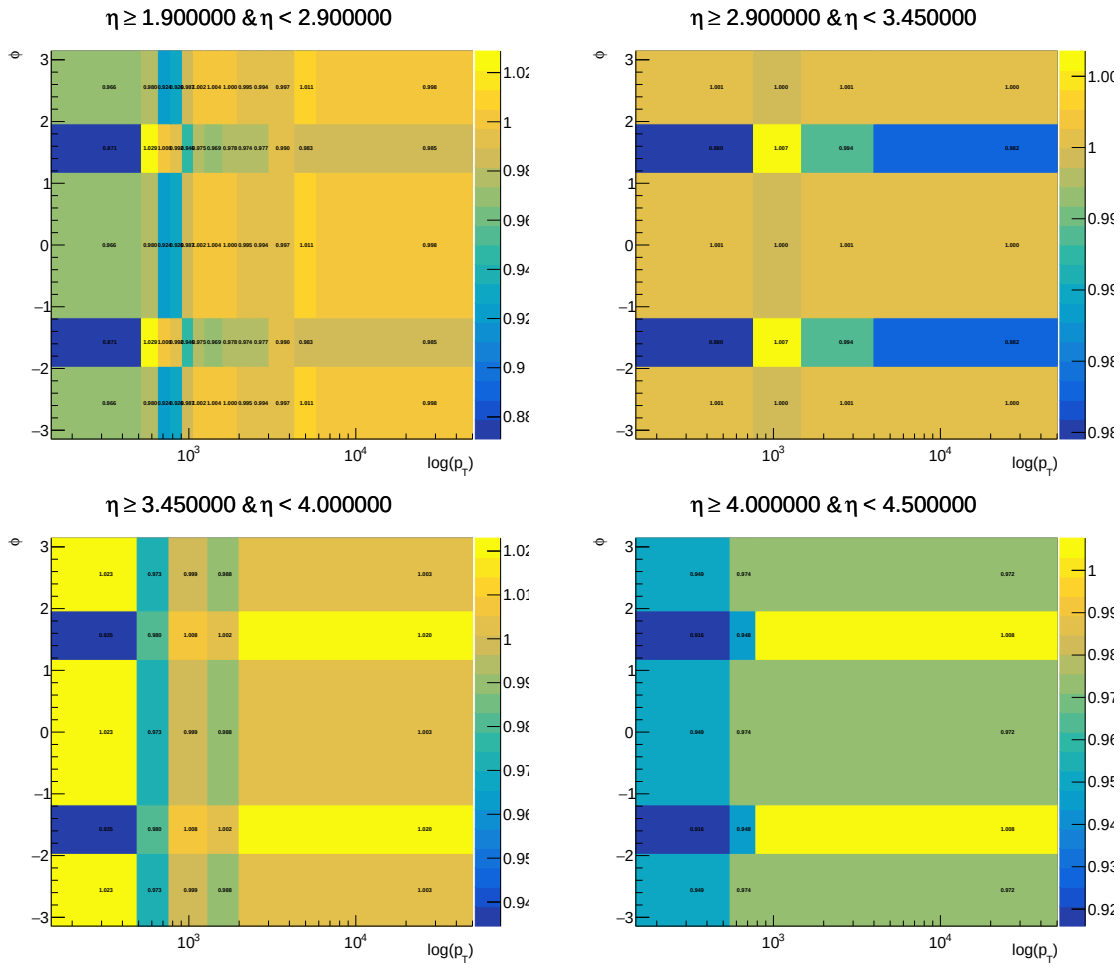

Figure O.0.2: Electron tracking efficiency correction maps for different bins of η for 2017 year of data taking.

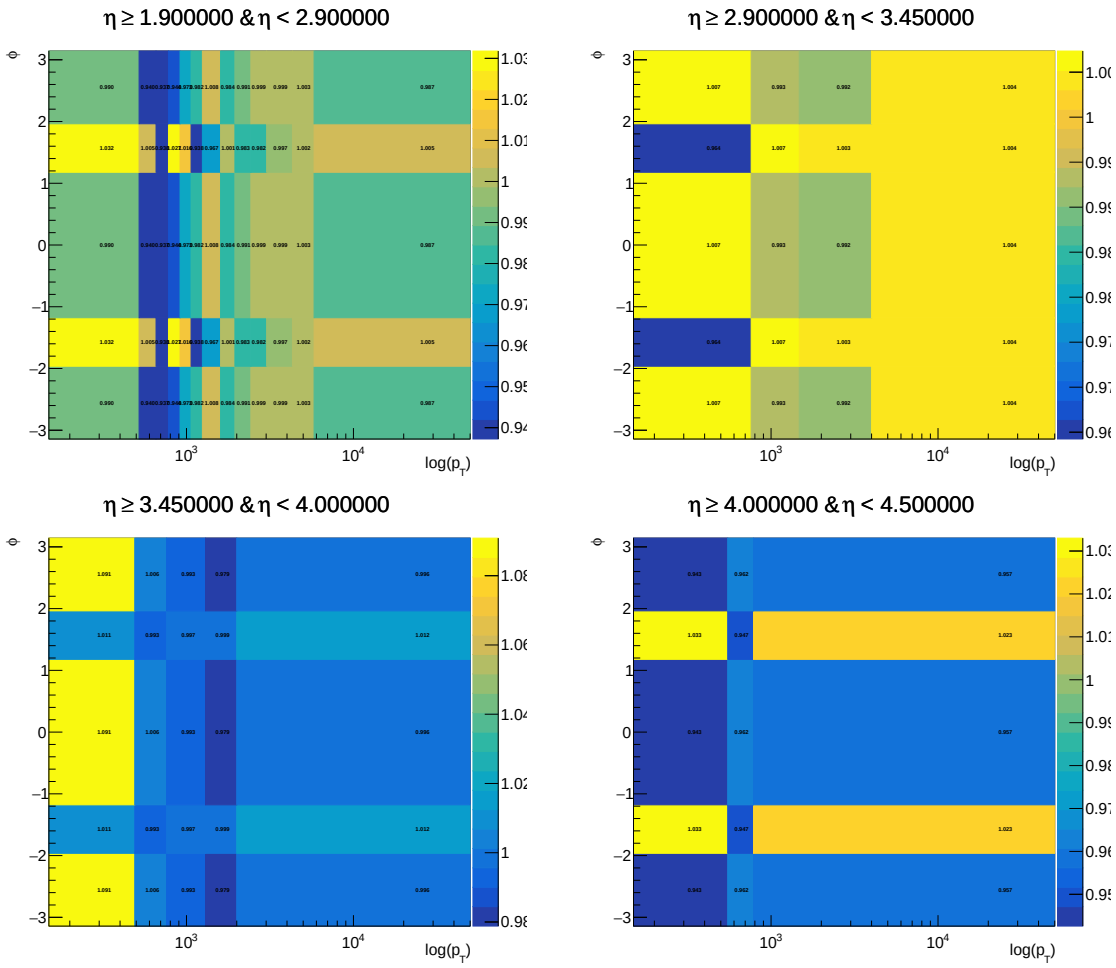

Figure O.0.3: Electron tracking efficiency correction maps for different bins of η for 2018 year of data taking.

Appendix P

Trigger correction

P.1 *eTOS* trigger corrections

Correction maps are shown in Figure P.1.1 for different years in bins of the transverse energy E_T deposited in the ECAL and the calorimeter regions. The weights, taken from [50], are then applied to the signal simulation to correct the efficiencies.

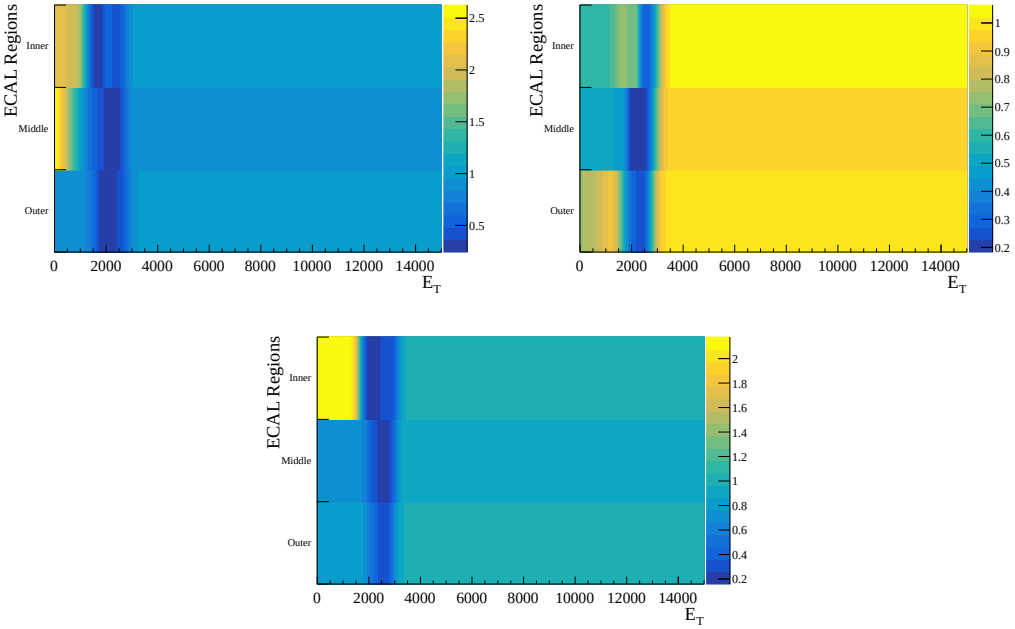

Figure P.1.1: `L0Electron_TOS` correction maps as a function of the ECAL regions and transverse energy for different years of simulation and data taking: 2016 (top-left), 2017 (top right) and 2018 (bottom)

P.2 sPlots method

sPlot technique [215] is adopted to derive the contribution of different components from a variable distribution. The sPlot reweights the dataset without adding cuts. This procedure is applied to derive the P_T distribution of signal and background components for the *TIS* category (Figure P.2.1). As an example, the 2016 year of data taking is shown. An example is also shown in the case of *hTOS* category (Figure P.2.2) for the 2016 year.

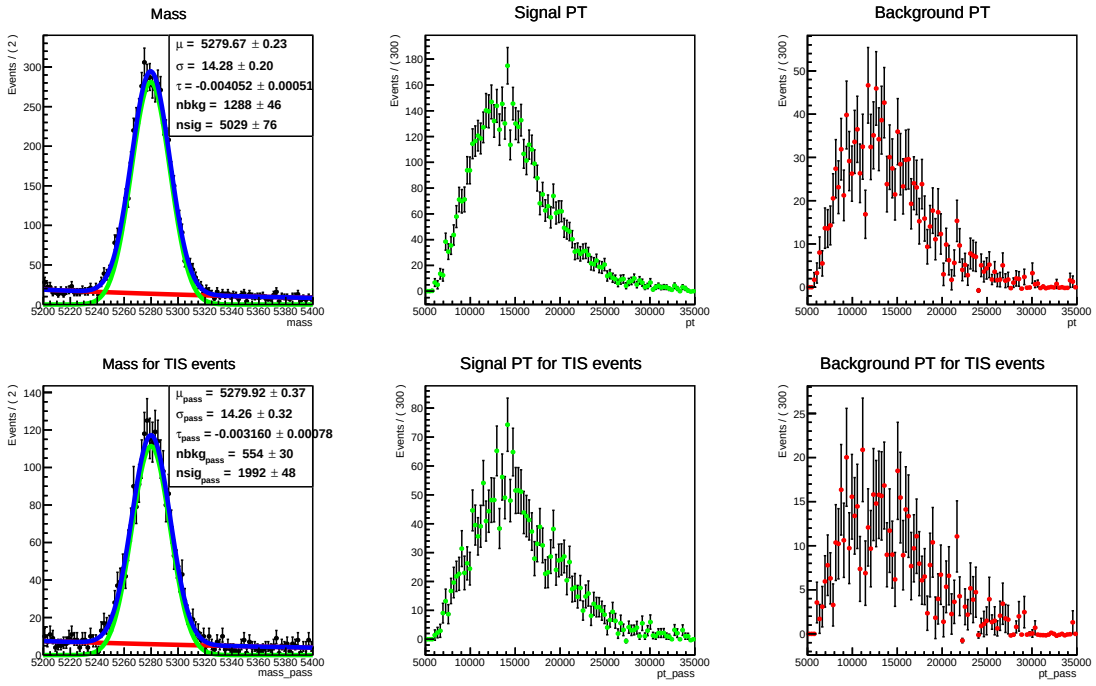

Figure P.2.1: *sPlot* technique to re-weight the datasets before (odd rows) and after (even rows) the application of `L0Global_TIS` trigger line decision. The invariant mass of final states is fitted using a Gaussian model for the signal (green) and an exponential for the background (red). Distributions for P_T of signal (green dots) and background (red dots) components for the re-weighted dataset are shown in both cases. Distributions refer to 2016 year of data-taking, respectively.

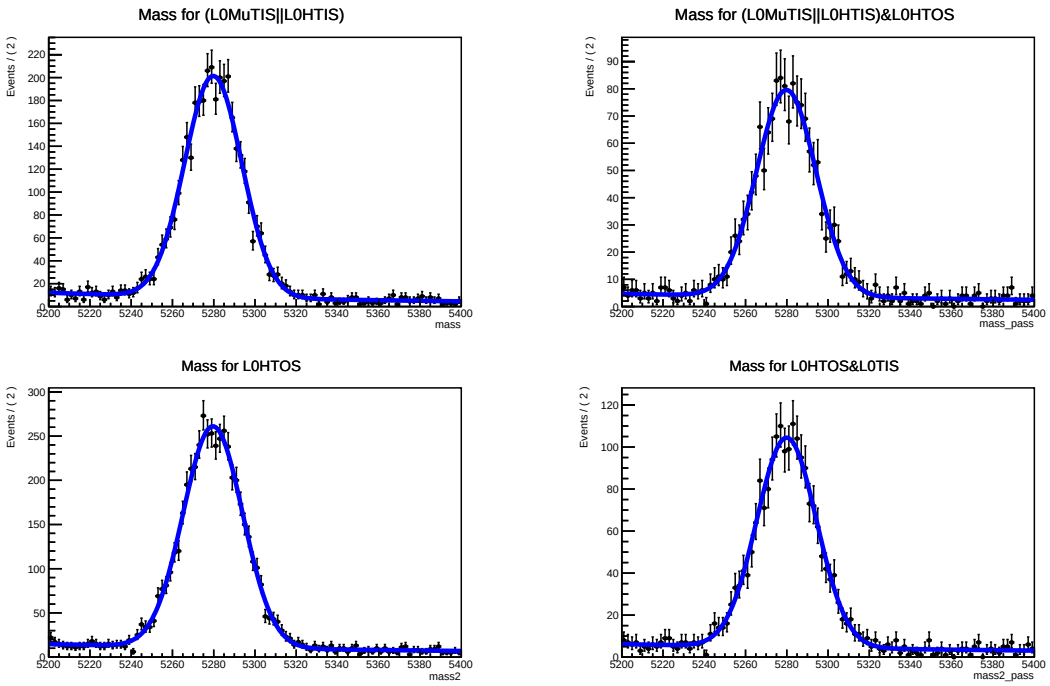

Figure P.2.2: Example of application of *sPlot* technique to re-weight four different datasets. In all cases, the invariant mass of final states is fitted using a Gaussian model for the signal and an exponential for the background. The fits are applied to events respectively fired by `L0Muon_TIS` or `L0Hadron_TIS`(top-left), `L0Hadron_TOS` and `L0Muon_TIS||L0Hadron_TIS` (top-right), `L0Hadron_TOS` (bottom-left), `L0Global_TIS` and `L0Hadron_TOS` (bottom-right). The example refers to 2018 year of data-taking.

P.3 *TIS* trigger corrections

Correction maps evaluated for *TIS* category are shown in Figure P.3.1 for different years of data taking.

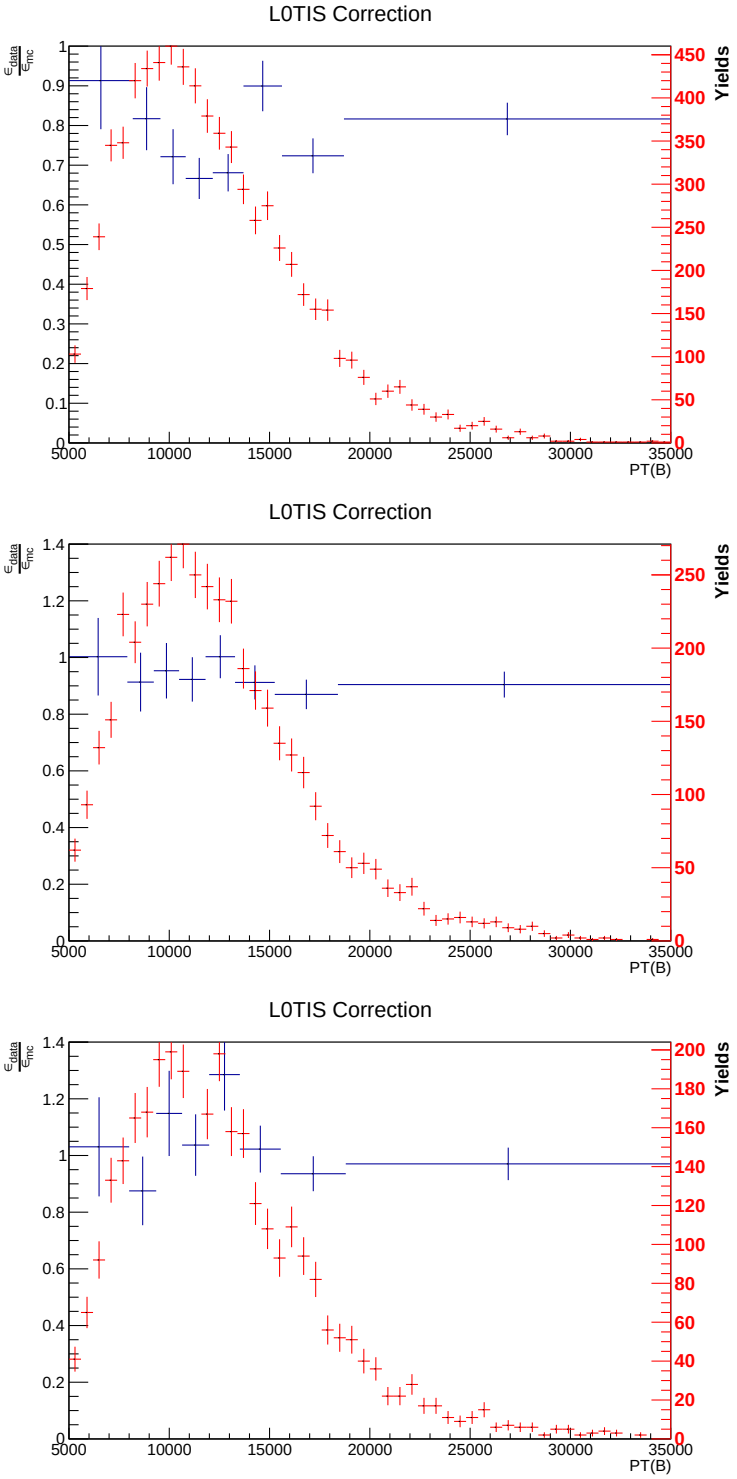

Figure P.3.1: Data-driven corrections (blue) using the calibration sample $B \to D^- D_s^+$ are superimposed to signal $B \to K^* \tau e$ simulation distribution of transverse momentum of the B^0 meson (red). Top, center, and bottom plots refer respectively to 2016, 2017 and 2018 year of data taking.

P.4 *hTOS* trigger corrections

Correction maps evaluated for *hTOS* category are shown in Figure P.4.1 for different years of data taking.

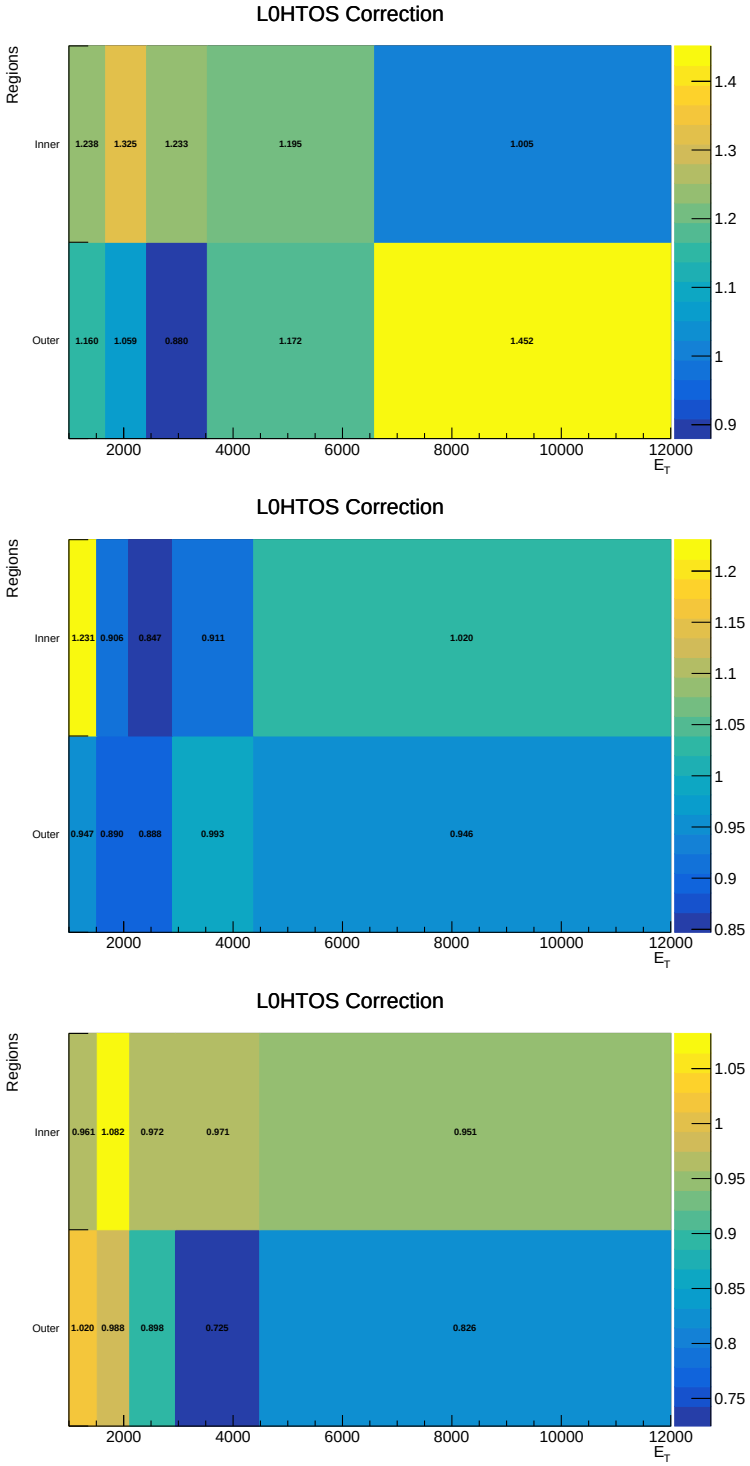

Figure P.4.1: 2D representation of data-driven corrections as a function of HCAL region and transverse energy deposited by the triggering hadron. Top, center, and bottom plots refer to 2016, 2017, and 2018 years of data taking.

Appendix Q

PID calibration

The particle identification efficiency is obtained directly from calibration samples. When the efficiencies are applied to the simulation, the dependency on the track multiplicity is integrated out using a control sample. For signal simulation, SS data are used as a control sample (see Figure Q.0.1), while for the normalization channel we use events extracted from $B \to D^- D_s^+$ data (see Figure Q.0.2).

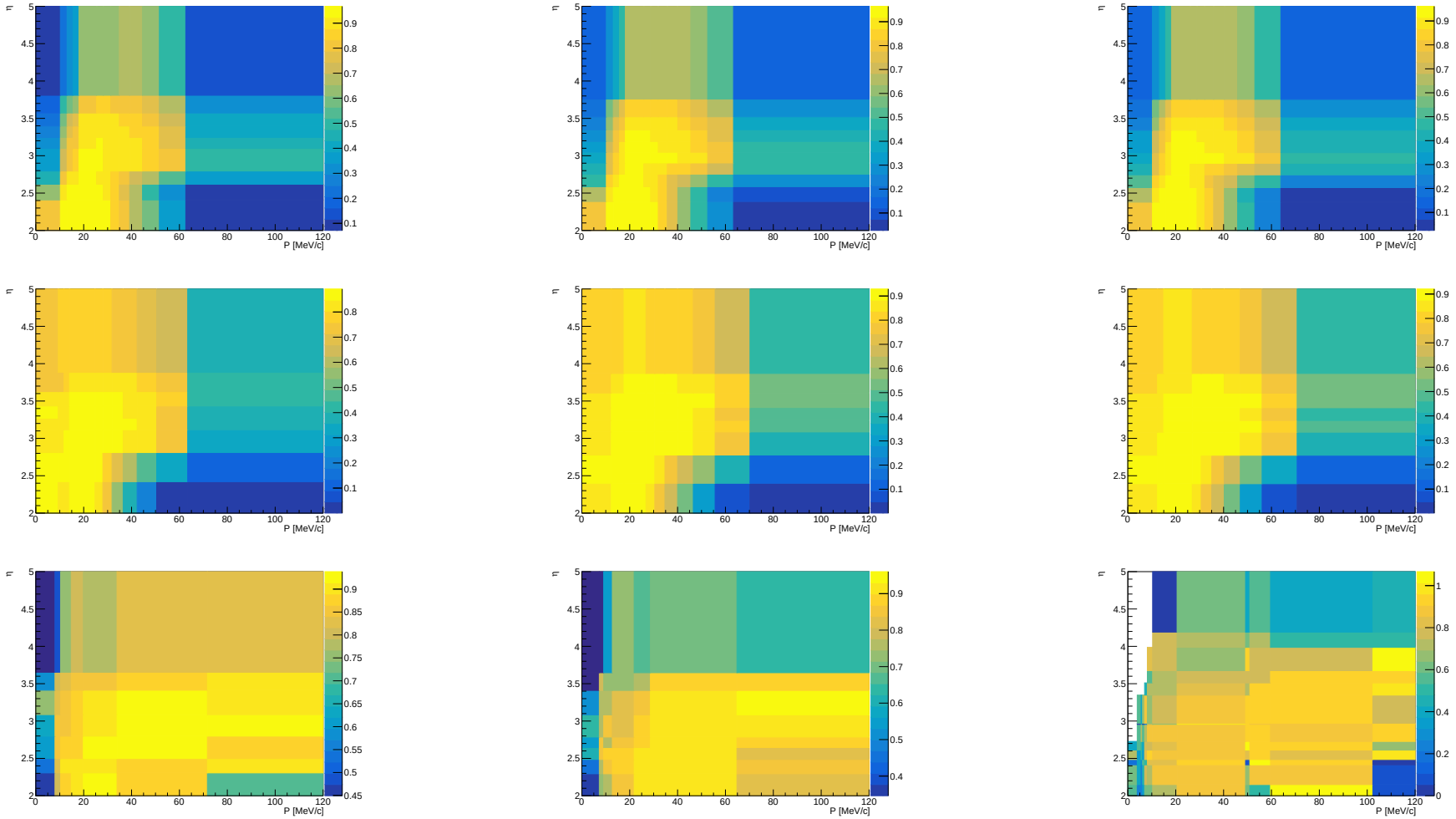

Figure Q.0.1: Efficiency projection of particle identification cut for kaons (first row), pions (second row) and electron (third row) as a function of momentum p and pseudorapidity η for different years of data taking: 2016 (left), 2017 (center), and 2018 (right). Distributions are obtained by integrating the number of tracks for SS data.

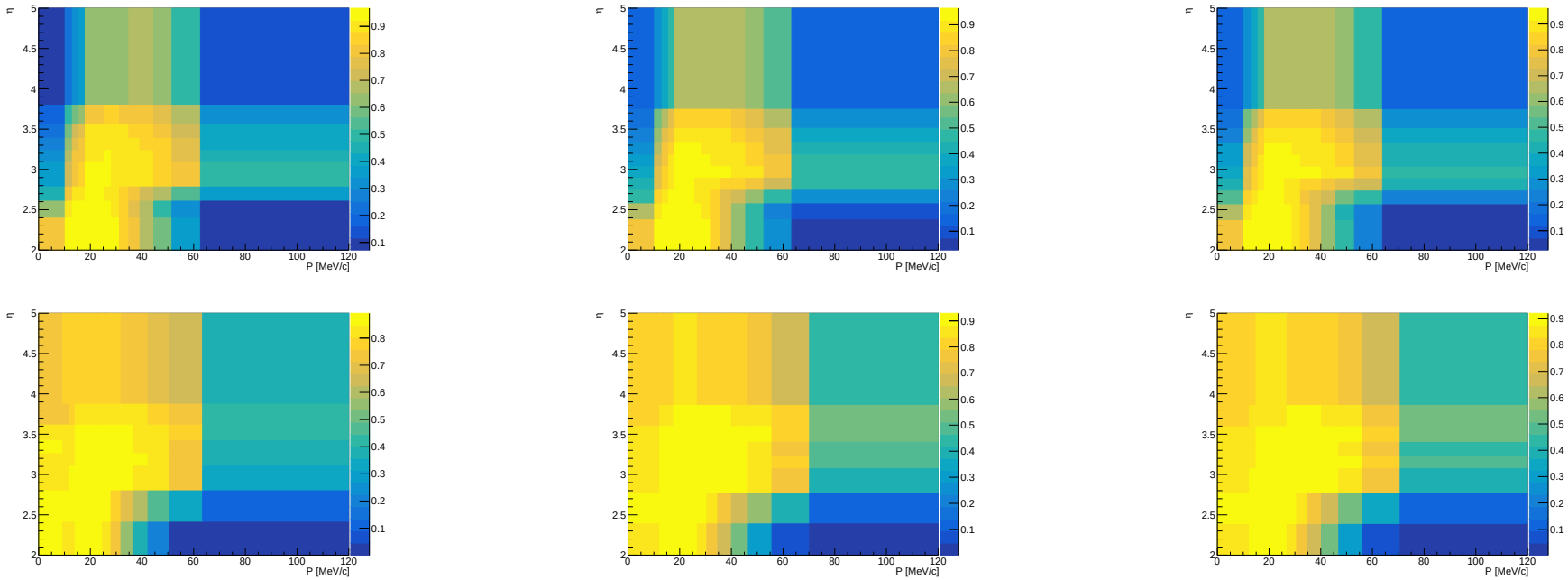

Figure Q.0.2: Efficiency projection of particle identification cut for kaons (first row) and pions (second row) as a function of momentum p and pseudorapidity η for different years of data taking: 2016 (left), 2017 (center), and 2018 (right). Distributions are obtained by integrating the number of tracks for normalization data.

Appendix R

Background modelling check

A test is performed on the background to decide whether the veto on semileptonic is needed. From the control samples used for the background parameterization, we extract a subsample containing the physical semileptonic background with $D \to Ke\nu$ described in Section 4.4.9 from the control samples used for the background parameterization. Test results are provided in Figure R.0.1.

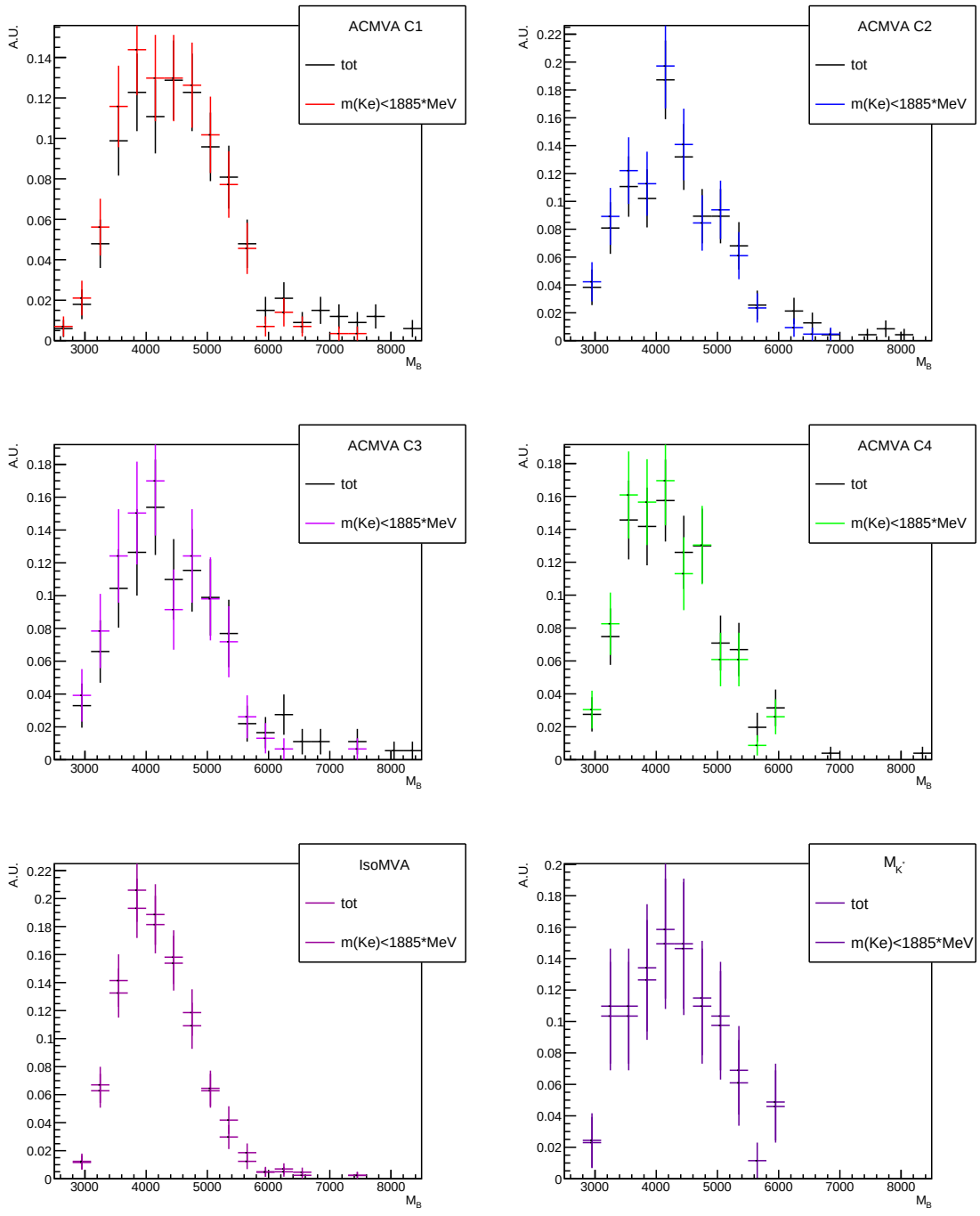

Figure R.0.1: Distribution of the mass for the control samples without applying cut on the invariant mass $m(Ke)$ (black) and applying $m(Ke) < 1885$. Since no big difference has been observed between the two distributions in any of the control sample, we parameterize the shape of the background, including semileptonic decays with an intermediate charm meson $D^0 \to K^- e^+ \nu_e$.

Appendix S

Tests on background fit

The control samples used for the background parameterization are fit using the DSCB model. Moreover, a kernel density estimation of the distributions is performed using RooKeysPdf. The procedures are repeated on OS data, with a number of yields that are left floating. Results, with fit parameters shown in Table S.0.1, are collected in Figure S.0.1, S.0.2, S.0.3, S.0.4, S.0.5 and S.0.6.

ACMVA C1	μ	σ	α_R	η_R	α_L	η_L
OC	4380.6 ± 52.3	811.5 ± 51.4	1.87 ± 0.16	0.611 ± 0.254	2.26 ± 0.69	3.5 ± 1.8
SC	4321.9 ± 128.0	1195.4 ± 133.8	1.38 ± 0.62	9.72 ± 0.65	1.30 ± 0.70	3.2 ± 2.0
ACMVA C2	μ	σ	α_R	η_R	α_L	η_L
OC	4156.4 ± 58.6	747.1 ± 55.8	1.70 ± 0.20	1.78 ± 0.91	2.69 ± 0.22	1.1 ± 0.6
SC	4148.6 ± 136.9	1139.5 ± 127.1	1.50 ± 0.44	5.36 ± 0.39	1.11 ± 0.69	3.3 ± 1.7
ACMVA C3	μ	σ	α_R	η_R	α_L	η_L
OC	4261.0 ± 69.3	786.0 ± 71.5	1.79 ± 0.19	0.53 ± 0.26	1.79 ± 0.52	1.48 ± 0.74
SC	4053.0 ± 120.0	414.0 ± 210.6	0.41 ± 0.22	9.58 ± 0.50	0.69 ± 0.28	0.49 ± 0.33
ACMVA C4	μ	σ	$\alpha_{\mathbf{R}}$	$\eta_{\mathbf{R}}$	$\alpha_{\mathbf{L}}$	$\eta_{\mathbf{L}}$
OC	$\mathbf{4165.4 \pm 54.2}$	$\mathbf{798.5 \pm 43.1}$	$\mathbf{2.74 \pm 0.33}$	$\mathbf{0.498 \pm 0.112}$	$\mathbf{1.60 \pm 0.69}$	$\mathbf{3.2 \pm 1.2}$
SC	$\mathbf{4298.0 \pm 86.8}$	$\mathbf{915.1 \pm 70.6}$	$\mathbf{2.92 \pm 1.71}$	$\mathbf{1.83 \pm 0.40}$	$\mathbf{1.64 \pm 0.70}$	$\mathbf{3.4 \pm 2.0}$
IsoMVA	μ	σ	α_R	η_R	α_L	η_L
OC	4152.4 ± 39.5	647.2 ± 42.1	2.07 ± 0.74	2.2 ± 1.4	2.49 ± 0.44	2.2 ± 1.4
SC	4386.3 ± 52.7	735.3 ± 43.2	2.56 ± 0.74	4.28 ± 2.44	2.8 ± 0.5	1.1 ± 0.7
$\mathbf{M_{K^*}}$	μ	σ	α_R	η_R	α_L	η_L
OC	4204.9 ± 92.3	808.0 ± 72.9	3.7 ± 2.2	3.5 ± 2.2	2.15 ± 0.43	1.91 ± 0.35
SC	4725.0 ± 8.8	730.3 ± 6.9	3.01 ± 0.43	9.4 ± 4.6	3.24 ± 2.34	5.84 ± 0.60

Table S.0.1: DSCB parameters from fit on each control sample. Errors are determined by the fit. In bold, ACMVA C4 is the baseline for the background parameterization. The other samples are used to determine the systematic uncertainties of the fit parameters.

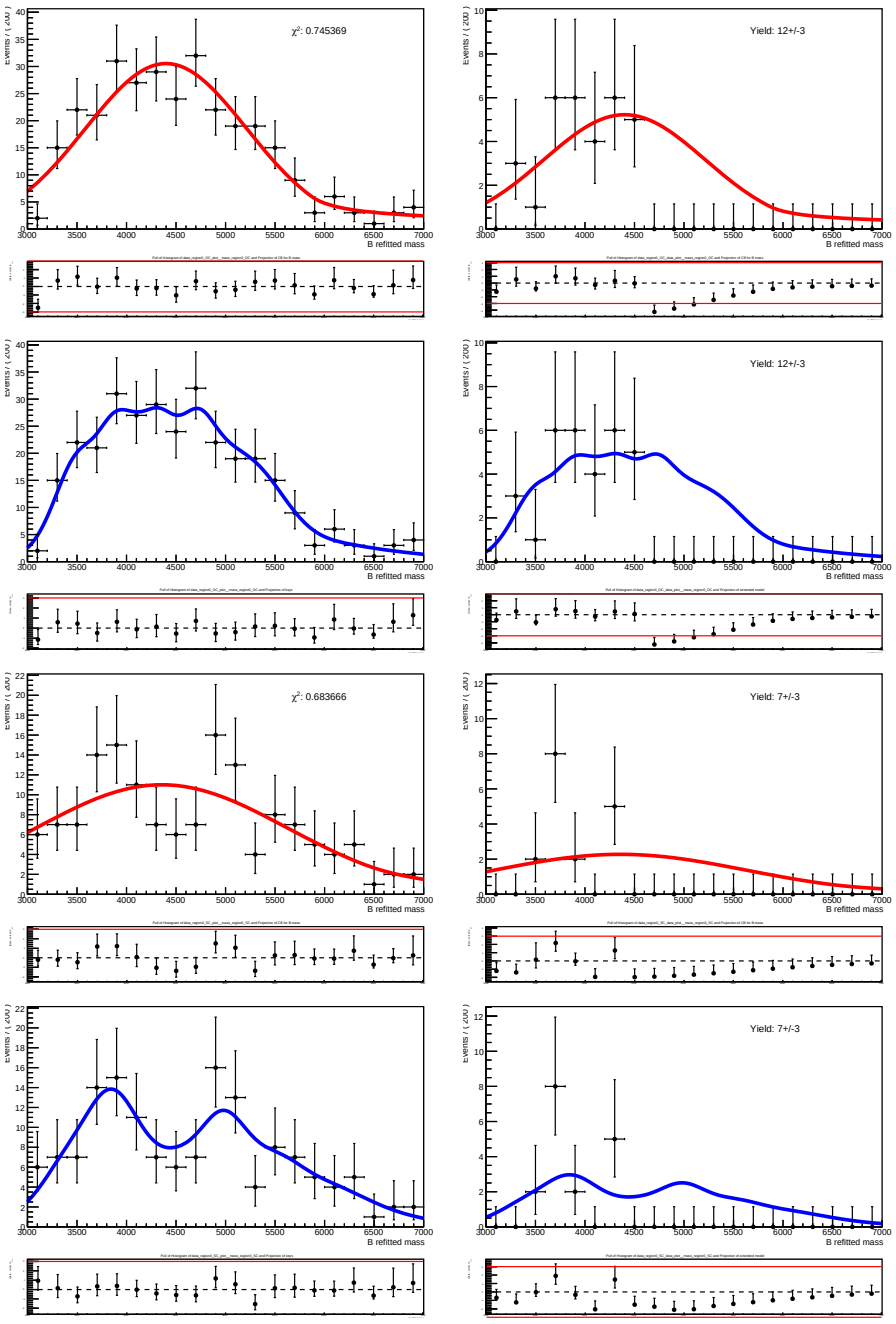

Figure S.0.1: Fits to control sample region ACMVA C1 (left) and blinded data (right), fixing the shape and leaving floating just the background yield. DSCB (red) and RooKeysPdf (blue) are used to model the background. The first (last) four frames refer to OC (SC) events.

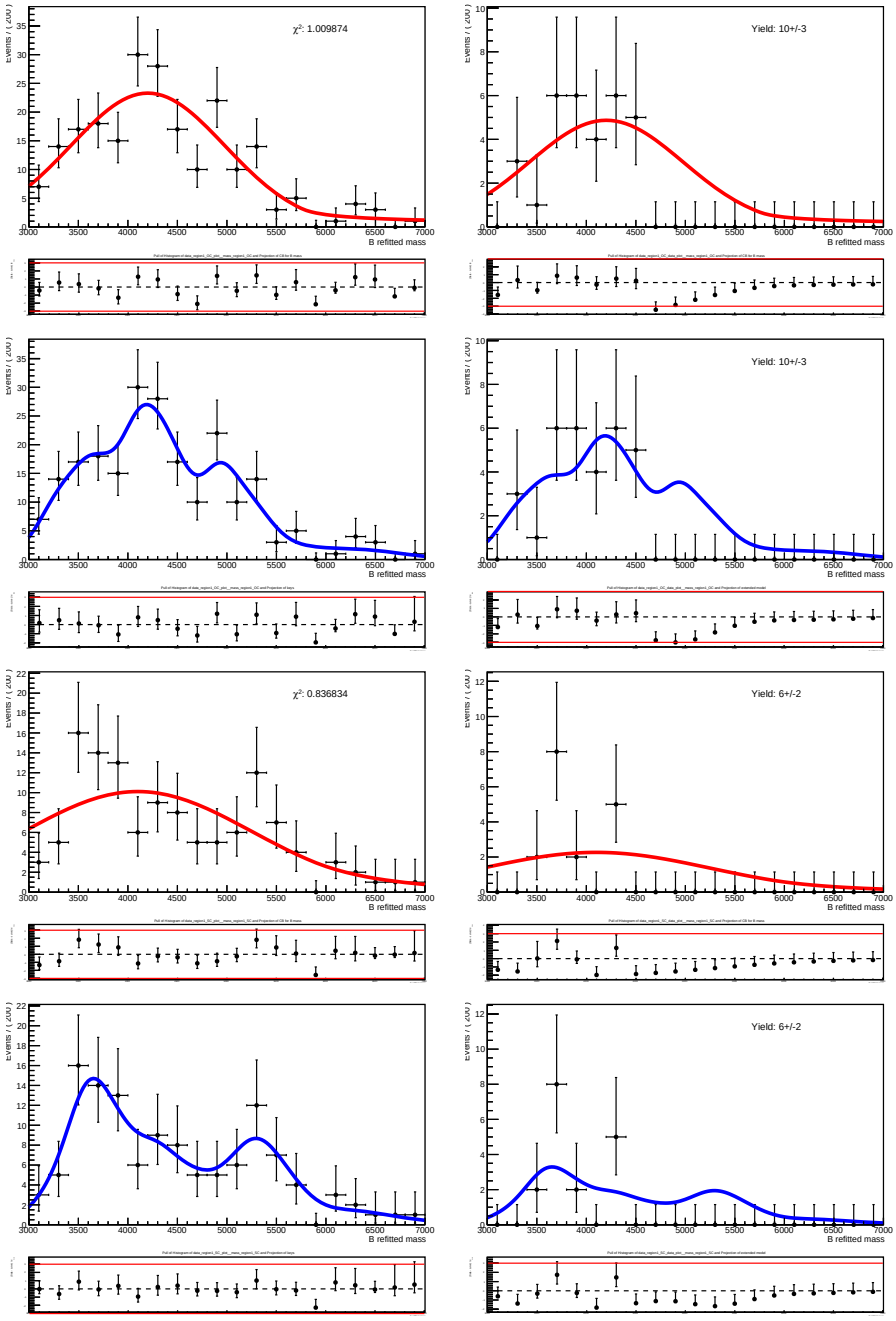

Figure S.0.2: Fits to control sample region ACMVA C2 (left) and blinded data (right) fixing the shape and leaving floating just the background yield. DSCB (red) and RooKeysPdf (blue) are used to model the background. The first (last) four frames refer to OC (SC) events.

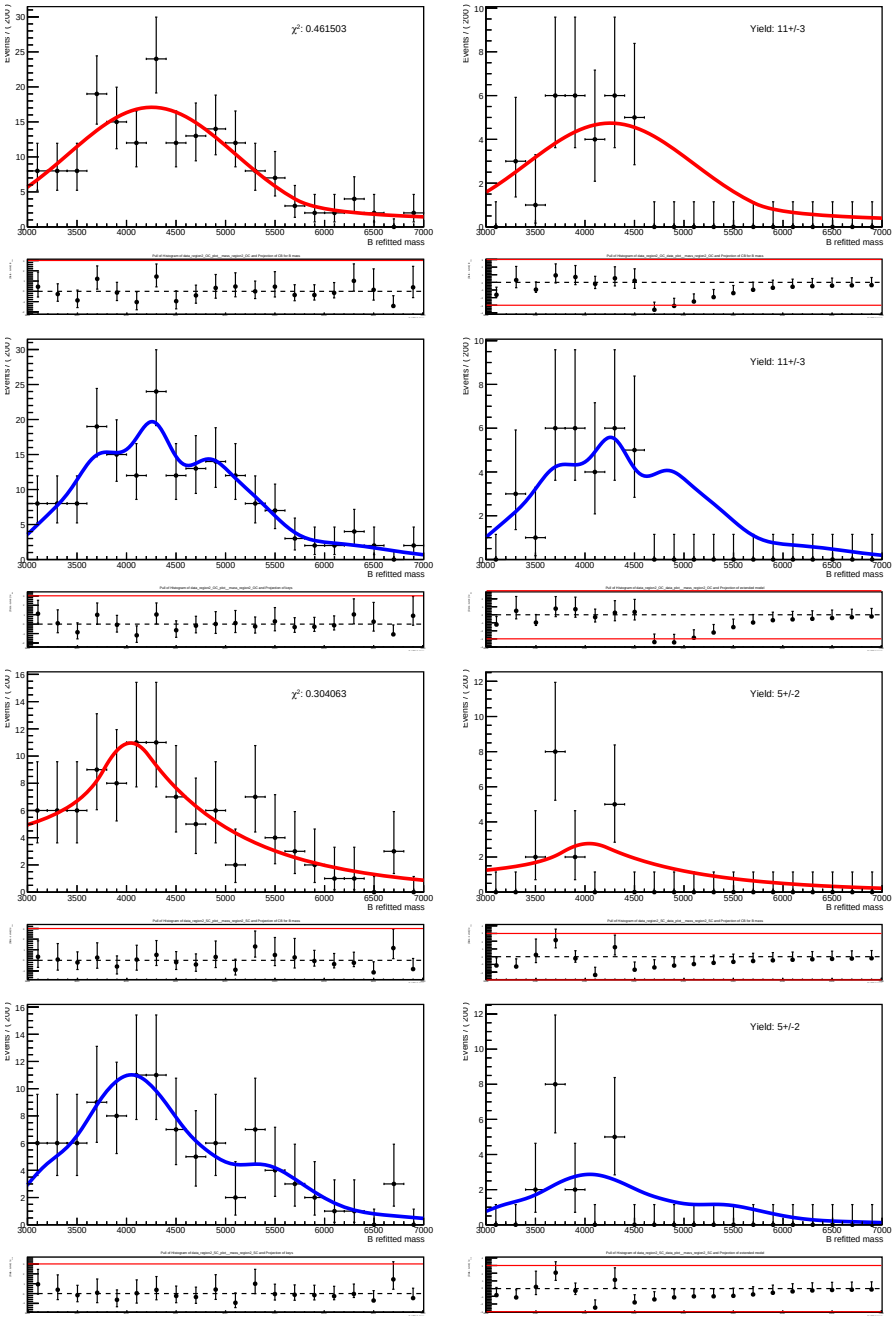

Figure S.0.3: Fits to control sample region ACMVA C3 (left) and blinded data (right) fixing the shape and leaving floating just the background yield. DSCB (red) and RooKeysPdf (blue) are used to model the background. The first (last) four frames refer to OC (SC) events.

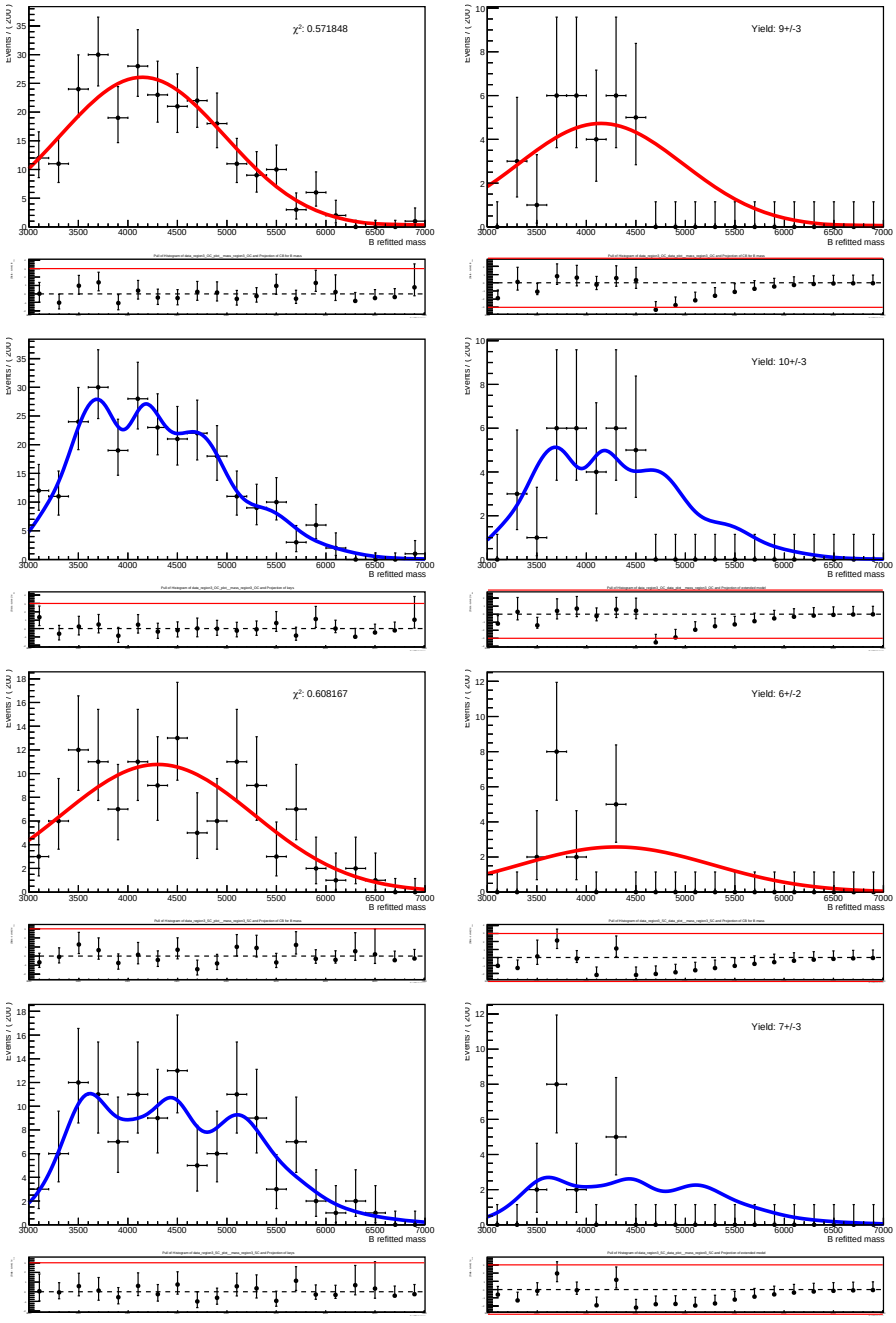

Figure S.0.4: Fits to control sample region ACMVA C4 (left) and blinded data (right), fixing the shape and leaving floating just the background yield. DSCB (red) and RooKeysPdf (blue) are used to model the background. The first (last) four frames refer to OC (SC) events.

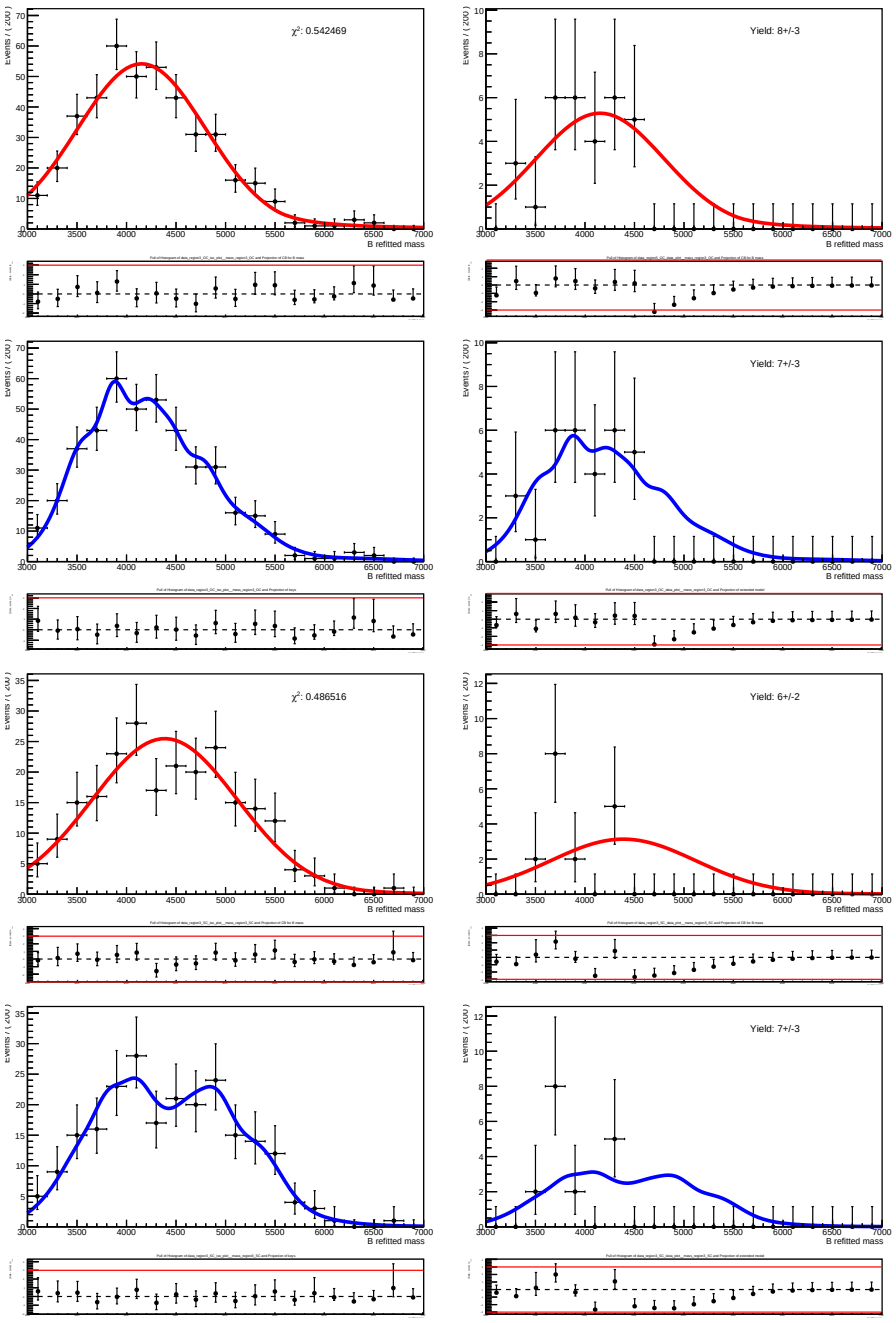

Figure S.0.5: Fits to control sample region IsoMVA (left) and blinded data (right) fixing the shape and leaving floating just the background yield. DSCB (red) and RooKeysPdf (blue) are used to model the background. The first (last) four frames refer to OC (SC) events. Background yield is extracted in the signal region from the fit on OS data.

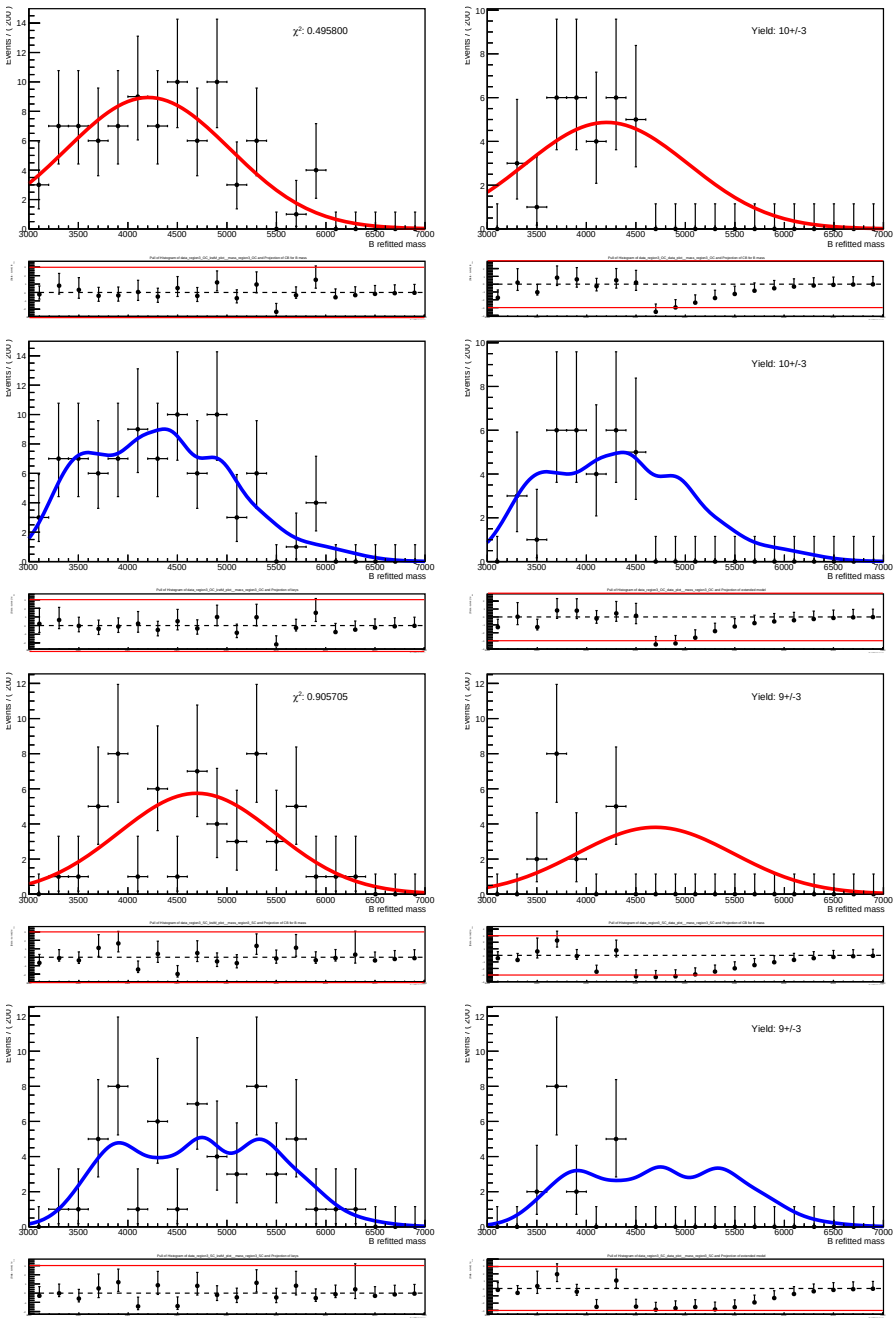

Figure S.0.6: Fits to control sample region M_{K^*} (left) and blinded data (right) fixing the shape and leaving floating just the background yield. DSCB (red) and RooKeysPdf (blue) are used to model the background. The first (last) four frames refer to OC (SC) events. Background yield is extracted in the signal region from the fit on OS data.

List of Figures

List of Tables

Listings

Bibliography

[1] C. P. Burgess and G. D. Moore, *The standard model: A primer*, Cambridge University Press, 2006.

[2] L. Calibbi and G. Signorelli, *Charged lepton flavour violation: An experimental and theoretical introduction*, Rivista del Nuovo Cimento **41** (2017) .

[3] P. A. M. Dirac, *The Principles of Quantum Mechanics*, Clarendon Press, Oxford, 1930.

[4] R. Mann, *An Introduction to Particle Physics and the Standard Model*, CRC Press, 2010.

[5] Wikipedia, *Fermion — Wikipedia, the free encyclopedia*, `http://en.wikipedia.org/w/index.php?title=Fermion&oldid=1184753197`, 2024.

[6] S. Braibant, G. Giacomelli, and M. Spurio, *Particles and Fundamental Interactions: An Introduction to Particle Physics*, Springer, 2011.

[7] A. Bettini, *Introduction to Elementary Particle Physics (2nd ed.)*, Cambridge University Press., 2014.

[8] W. N. Cottingham and D. A. Greenwood, *An Introduction to the Standard Model of Particle Physics*, Cambridge University Press, 2 ed., 2007.

[9] R. P. Feynman, *Space-time approach to quantum electrodynamics*, Phys. Rev. **76** (1949) 769.

[10] D. J. Griffiths, *Introduction to elementary particles; 2nd rev. version*, Physics textbook, Wiley, New York, NY, 2008.

[11] S. Weinberg, *A model of leptons*, Phys. Rev. Lett. **19** (1967) 1264.

[12] J. C. Taylor, *The theory of weak interactions*, Reports on Progress in Physics **27** (1964) 407.

[13] A. Salam and J. C. Ward, *Weak and electromagnetic interactions*, Il Nuovo Cimento **11** (1959) 568–577.

[14] H. Leutwyler, *On the history of the strong interaction*, Mod. Phys. Lett. A **29** (2014) 1430023, arXiv:1211.6777.

[15] CERN, *The Standard Model*, https://home.cern/science/physics/standard-model, 2023.

[16] L. Di Lella and C. Rubbia, *The Discovery of the W and Z Particles*, Adv. Ser. Direct. High Energy Phys. **23** (2015) 137.

[17] ATLAS Collaboration, *Observation of a new particle in the search for the Standard Model Higgs boson with the ATLAS detector at the LHC*, Physics Letters B **716** (2012) 1.

[18] CMS Collaboration, *Observation of a new boson at a mass of 125 GeV with the CMS experiment at the LHC*, Physics Letters B **716** (2012) 30.

[19] E. Fermi, J. Orear, A. H. Rosenfeld, and R. A. Schluter, *Nuclear physics, a course given by Enrico Fermi at the University of Chicago.*, University of Chicago Press, 1953.

[20] N. Cabibbo, *Unitary symmetry and leptonic decays*, Phys. Rev. Lett. **10** (1963) 531.

[21] M. Kobayashi and T. Maskawa, *CP-Violation in the Renormalizable Theory of Weak Interaction*, Progress of Theoretical Physics **49** (1973) 652.

[22] L. Wolfenstein, *Parametrization of the Kobayashi-Maskawa Matrix*, Phys. Rev. Lett. **51** (1983) 1945.

[23] A. e. a. Bevan, *The physics of the b factories*, The European Physical Journal C **74** (2014) .

[24] BaBar collaboration, D. Boutigny *et al.*, *BaBar technical design report*, , BaBar Technical Design Report EPAC Meeting, SLAC-R-0457.

[25] Belle collaboration, *The Belle detector*, Nuclear Instruments and Methods in Physics Research Section A: Accelerators, Spectrometers, Detectors and Associated Equipment **479** (2002) 117, Detectors for Asymmetric B-factories.

[26] Belle II collaboration, *Belle II Technical Design Report*, arXiv:1011.0352.

[27] LHCb collaboration, R. Aaaij *et al.*, *The LHCb Detector at the LHC*, Journal of Instrumentation **3** (2008) S08005.

[28] S. Willenbrock, *Symmetries of the Standard Model*, Springer, 2005.

[29] B. G. Sidharth, J. C. Murillo, M. Michelini, and M. Perea, *Fundamental Physics and Physics Education Research*, Springer, 2021.

[30] Super-Kamiokande Collaboration, Y. Fukuda *et al.*, *Evidence for oscillation of atmospheric neutrinos*, Phys. Rev. Lett. **81** (1998) 1562.

[31] T2K collaboration, *Evidence of electron neutrino appearance in a muon neutrino beam*, Phys. Rev. D **88** (2013) 032002.

[32] NOvA collavoration, *First measurement of muon-neutrino disappearance in NOvA*, Physical Review D **93** (2016) .

[33] Double Chooz collaboration, *Measurement of θ_{13} in Double Chooz using neutron captures on hydrogen with novel background rejection techniques*, Journal of High Energy Physics **2016** (2016) .

[34] OPERA Collaboration, *Observation of a first $\nu\tau$ candidate event in the OPERA experiment in the CNGS beam*, Physics Letters B **691** (2010) 138.

[35] I. Esteban *et al.*, *Global analysis of three-flavour neutrino oscillations: synergies and tensions in the determination of θ_{23}, δ_{CP}, and the mass ordering*, JHEP **01** (2019) 106, arXiv:1811.05487.

[36] D. Guadagnoli and P. Koppenburg, *Lepton-flavor violation and lepton-flavor-universality violation in b and c decays*, arXiv:2207.01851.

[37] LHCb collaboration, R. Aaij *et al.*, *Measurement of the ratios of branching fractions $\mathcal{R}(D^*)$ and $\mathcal{R}(D^0)$*, Phys. Rev. Lett. **131** (2023) 111802, arXiv:2302.02886.

[38] LHCb collaboration, R. Aaij *et al.*, *Test of lepton flavor universality using B0→D*-τ+ντ decays with hadronic τ channels*, Phys. Rev. D **108** (2023) 012018, arXiv:2305.01463.

[39] LHCb, R. Aaij *et al.*, *Measurement of the branching fraction ratios $R(D^+)$ and $R(D^{*+})$ using muonic τ decays*, arXiv:2406.03387.

[40] Belle-II collaboration, I. Adachi *et al.*, *A test of lepton flavor universality with a measurement of $R(D^*)$ using hadronic B tagging at the Belle II experiment*, arXiv:2401.02840.

[41] Belle collaboration, M. Huschle *et al.*, *Measurement of the branching ratio of $\bar{B} \to D^{(*)}\tau^-\bar{\nu}_\tau$ relative to $\bar{B} \to D^{(*)}\ell^-\bar{\nu}_\ell$ decays with hadronic tagging at Belle*, Phys. Rev. D **92** (2015) 072014, arXiv:1507.03233.

[42] Belle collaboration, S. Hirose *et al.*, *Measurement of the τ lepton polarization and $R(D^*)$ in the decay $\bar{B} \to D^* \tau^- \bar{\nu}_\tau$*, Phys. Rev. Lett. **118** (2017) 211801, arXiv:1612.00529.

[43] Belle, G. Caria *et al.*, *Measurement of $\mathcal{R}(D)$ and $\mathcal{R}(D^*)$ with a semileptonic tagging method*, Phys. Rev. Lett. **124** (2020) 161803, arXiv:1910.05864.

[44] BaBar collaboration, J. P. Lees *et al.*, *Evidence for an excess of $\bar{B} \to D^{(*)} \tau^- \bar{\nu}_\tau$ decays*, Phys. Rev. Lett. **109** (2012) 101802, arXiv:1205.5442.

[45] BaBar collaboration, J. P. Lees *et al.*, *Measurement of an Excess of $\bar{B} \to D^{(*)} \tau^- \bar{\nu}_\tau$ Decays and Implications for Charged Higgs Bosons*, Phys. Rev. D **88** (2013) 072012, arXiv:1303.0571.

[46] S. L. Glashow, D. Guadagnoli, and K. Lane, *Lepton Flavor Violation in B Decays?*, Phys. Rev. Lett. **114** (2015) 091801, arXiv:1411.0565.

[47] Heavy Flavor Averaging Group, *The Heavy Flavor Averaging Group*, https://hflav.web.cern.ch/, 2024. Accessed: 2024-06-11.

[48] LHCb, R. Aaij *et al.*, *Test of lepton universality in beauty-quark decays*, Nature Phys. **18** (2022) 277, arXiv:2103.11769, [Addendum: Nature Phys. 19, (2023)].

[49] LHCb, R. Aaij *et al.*, *Test of lepton universality in $b \to s\ell^+\ell^-$ decays*, Phys. Rev. Lett. **131** (2023) 051803, arXiv:2212.09152.

[50] LHCb, R. Aaij *et al.*, *Measurement of lepton universality parameters in $B^+ \to K^+\ell^+\ell^-$ and $B^0 \to K^{*0}\ell^+\ell^-$ decays*, Phys. Rev. D **108** (2023) 032002, arXiv:2212.09153.

[51] Planck Collaboration, *Planck 2018 results. VI. Cosmological parameters*, Astronomy & Astrophysics **641** (2020) A6, arXiv:1807.06209.

[52] S. Alam *et al.*, *The clustering of galaxies in the completed SDSS-III Baryon Oscillation Spectroscopic Survey: cosmological analysis of the DR12 galaxy sample*, Monthly Notices of the Royal Astronomical Society **470** (2017) 2617, arXiv:1607.03155.

[53] KATRIN Collaboration, M. Aker *et al.*, *Improved Upper Limit on the Neutrino Mass from a Direct Kinematic Method by KATRIN*, Phys. Rev. Lett. **123** (2019) 221802.

[54] GERDA Collaboration, M. Agostini *et al.*, *Improved Limit on Neutrinoless Double-β Decay of ^{76}Ge from GERDA Phase II*, Phys. Rev. Lett. **120** (2018) 132503.

[55] KamLAND-Zen collaboration, A. Gando *et al.*, *Search for Majorana Neutrinos near the Inverted Mass Hierarchy Region with KamLAND-Zen*, Phys. Rev. Lett. **117** (2016) 082503.

[56] A. V. Borisov and A. P. Isaev, *Neutrino Mass in Effective Field Theory*, `arXiv:2312.17714`.

[57] H. Georgi, H. R. Quinn, and S. Weinberg, *Hierarchy of interactions in unified gauge theories*, Phys. Rev. Lett. **33** (1974) 451.

[58] H. Fritzsch and P. Minkowski, *Unified interactions of leptons and hadrons*, Annals of Physics **93** (1975) 193.

[59] R. Davis, D. S. Harmer, and K. C. Hoffman, *Search for Neutrinos from the Sun*, Phys. Rev. Lett. **20** (1968) 1205.

[60] B. T. Cleveland *et al.*, *Measurement of the solar electron neutrino flux with the Homestake chlorine detector*, Astrophys. J. **496** (1998) 505.

[61] SAGE collaboration, *Solar neutrino flux measurements by the Soviet-American Gallium Experiment (SAGE) for half the 22 year solar cycle*, J. Exp. Theor. Phys. **95** (2002) 181.

[62] GALLEX collaboration, *GALLEX solar neutrino observations: Results for GALLEX IV*, Physics Letters B **447** (1999) 127.

[63] GNO collaboration, *Complete results for five years of GNO solar neutrino observations*, Phys. Lett. B **616** (2005) 174.

[64] SAGE collaboration, *Measurement of the solar neutrino capture rate with gallium metal. III: Results for the 2002–2007 data-taking period*, Phys. Rev. C **80** (2009) 015807.

[65] B. Pontecorvo, *Neutrino Experiments and the Problem of Conservation of Leptonic Charge*, Zh. Eksp. Teor. Fiz. **53** (1967) 1717, Soviet Journal of Experimental and Theoretical Physics.

[66] Z. Maki, M. Nakagawa, and S. Sakata, *Remarks on the Unified Model of Elementary Particles*, Progress of Theoretical Physics **28** (1962) 870.

[67] N. Cabibbo, *Time reversal violation in neutrino oscillation*, Physics Letters B **72** (1978) 333.

[68] S. M. Bilenky, J. Hošek, and S. T. Petcov, *On the oscillations of neutrinos with Dirac and Majorana masses*, Physics Letters B **94** (1980) 495.

[69] V. Barger, K. Whisnant, and R. J. N. Phillips, CP *Nonconservation in Three-Neutrino Oscillations*, Phys. Rev. Lett. **45** (1980) 2084.

[70] M. Ardu, *Effective Field Theory for Lepton Flavour Violation*, theses, Université de Montpellier, 2023, tel-04534872.

[71] D. Bečirević, F. Jaffredo, A. Peñuelas, and O. Sumensari, *New Physics effects in leptonic and semileptonic decays*, JHEP **05** (2021) 175, arXiv:2012.09872.

[72] A. Angelescu *et al.*, *Single leptoquark solutions to the B-physics anomalies*, Phys. Rev. D **104** (2021) 055017, arXiv:2103.12504.

[73] I. Plakias and O. Sumensari, *Lepton Flavor Violation in Semileptonic Observables*, arXiv:2312.14070.

[74] S. Descotes-Genon, D. A. Faroughy, I. Plakias, and O. Sumensari, *Probing lepton flavor violation in meson decays with LHC data*, Eur. Phys. J. C **83** (2023) 753, arXiv:2303.07521.

[75] M. I. Ali, U. Chattopadhyay, N. Rajeev, and J. Roy, *SMEFT analysis of charged lepton flavor violating B-meson decays*, Phys. Rev. D **109** (2024) 075028, arXiv:2312.05071.

[76] R. Alonso, B. Grinstein, and J. Martin Camalich, $SU(2)\times U(1)$ *gauge invariance and the shape of new physics in rare B decays*, Phys. Rev. Lett. **113** (2014) 241802, arXiv:1407.7044.

[77] D. M. Straub, *flavio: a Python package for flavour and precision phenomenology in the Standard Model and beyond*, arXiv:1810.08132.

[78] C. Borschensky, B. Fuks, A. Jueid, and A. Kulesza, *Scalar leptoquarks at the LHC and flavour anomalies: a comparison of pair-production modes at NLO-QCD*, JHEP **11** (2022) 006, arXiv:2207.02879.

[79] J. Fuentes-Martín, G. Isidori, M. König, and N. Selimović, *Vector Leptoquarks Beyond Tree Level III: Vector-like Fermions and Flavor-Changing Transitions*, Phys. Rev. D **102** (2020) 115015, arXiv:2009.11296.

[80] J. Aebischer *et al.*, *Confronting the vector leptoquark hypothesis with new low- and high-energy data*, Eur. Phys. J. C **83** (2023) 153, arXiv:2210.13422.

[81] Particle Data Group, R. L. Workman and Others, *Review of Particle Physics*, PTEP **2022** (2022) 083C01.

[82] D. Bečirević, N. Košnik, O. Sumensari, and R. Zukanovich Funchal, *Palatable Leptoquark Scenarios for Lepton Flavor Violation in Exclusive* $b \to s\ell_1\ell_2$ *modes*, JHEP **11** (2016) 035, arXiv:1608.07583.

[83] S. Davidson *et al.*, *Charged Lepton Flavor Violation*, arXiv:2209.00142.

[84] LHCb collaboration, R. Aaij *et al.*, *Search for the lepton-flavour violating decays* $B^0_{(s)} \to e^\pm\mu^\mp$, JHEP **03** (2018) 078, arXiv:1710.04111.

[85] BaBar collaboration, B. Aubert *et al.*, *Search for the rare decay* $B \to \pi l^+ l^-$, Phys. Rev. Lett. **99** (2007) 051801, arXiv:hep-ex/0703018.

[86] Belle collaboration, S. Choudhury *et al.*, *Test of lepton flavor universality and search for lepton flavor violation in* $B \to K\ell\ell$ *decays*, JHEP **03** (2021) 105, arXiv:1908.01848.

[87] LHCb collaboration, R. Aaij *et al.*, *Search for the lepton-flavour violating decays* $B^0 \to K^{*0}\mu^\pm e^\mp$ *and* $B^0_s \to \phi\mu^\pm e^\mp$, JHEP **06** (2023) 073, arXiv:2207.04005.

[88] LHCb collaboration, R. Aaij *et al.*, *Search for Lepton-Flavor Violating Decays* $B^+ \to K^+\mu^\pm e^\mp$, Phys. Rev. Lett. **123** (2019) 241802, arXiv:1909.01010.

[89] BaBar collaboration, B. Aubert *et al.*, *Measurements of branching fractions, rate asymmetries, and angular distributions in the rare decays* $B \to K\ell^+\ell^-$ *and* $B \to K^*\ell^+\ell^-$, Phys. Rev. D **73** (2006) 092001, arXiv:hep-ex/0604007.

[90] Belle collaboration, O. Seon *et al.*, *Search for Lepton-number-violating* $B^+ \to D^- l^+ l'^+$ *Decays*, Phys. Rev. D **84** (2011) 071106, arXiv:1107.0642.

[91] LHCb collaboration, R. Aaij *et al.*, *Search for the lepton-flavour-violating decays* $B^0_s \to \tau^\pm\mu^\mp$ *and* $B^0 \to \tau^\pm\mu^\mp$, Phys. Rev. Lett. **123** (2019) 211801, arXiv:1905.06614.

[92] LHCb collaboration, R. Aaij *et al.*, *Search for the lepton-flavour violating decays* $B^0 \to K^{*0}\tau^\pm\mu^\mp$, JHEP **06** (2023) 143, arXiv:2209.09846.

[93] Belle collaboration, S. Watanuki *et al.*, *Search for the Lepton Flavor Violating Decays* $B^+ \to K^+\tau^\pm l^\mp (l = e, \mu)$ *at Belle*, Phys. Rev. Lett. **130** (2023) 261802, arXiv:2212.04128.

[94] LHCb collaboration, R. Aaij *et al.*, *Search for the lepton-flavor violating decay* $B^0_s \to \phi\mu^\pm\tau^\mp$, arXiv:2405.13103.

[95] Belle Collaboration, *Search for* $B^0 \to \tau^\pm\ell^\mp$ $(\ell = e, \mu)$ *with a hadronic tagging method at Belle*, Phys. Rev. D **104** (2021) , arXiv:2108.11649.

[96] Belle, L. Nayak *et al.*, *Search for* $B^0_s \to \ell^\mp\tau^\pm$ *with the Semi-leptonic Tagging Method at Belle*, JHEP **08** (2023) 178, arXiv:2301.10989.

[97] Belle Collaboration, *Search for the Lepton Flavor Violating Decays* $B^+ \to K^+\tau^\pm\ell^\mp$ $(\ell = e,\ \mu)$ *at Belle*, Phys. Rev. Lett. **130** (2023) 261802.

[98] BaBar collaboration, *Search for the decay modes $B^{\pm} \to h^{\pm}\tau\ell$*, Phys. Rev. D **86** (2012) 012004.

[99] KTeV collaboration, E. Abouzaid *et al.*, *Search for lepton flavor violating decays of the neutral kaon*, Phys. Rev. Lett. **100** (2008) 131803, arXiv:0711.3472.

[100] A. Sher *et al.*, *An Improved upper limit on the decay $K^+ \to \pi^+\mu^+e^-$*, Phys. Rev. D **72** (2005) 012005, arXiv:hep-ex/0502020.

[101] NA62 collaboration, E. Cortina Gil *et al.*, *Search for Lepton Number and Flavor Violation in K^+ and π^0 Decays*, Phys. Rev. Lett. **127** (2021) 131802, arXiv:2105.06759.

[102] BNL collaboration, D. Ambrose *et al.*, *New limit on muon and electron lepton number violation from K0(L) —> mu+- e-+ decay*, Phys. Rev. Lett. **81** (1998) 5734, arXiv:hep-ex/9811038.

[103] BESIII collaboration, M. Ablikim *et al.*, *Search for the Lepton Flavor Violation Process $J/\psi \to e\mu$ at BESIII*, Phys. Rev. D **87** (2013) 112007, arXiv:1304.3205.

[104] LHCb collaboration, R. Aaij *et al.*, *Searches for 25 rare and forbidden decays of D^+ and D_s^+ mesons*, JHEP **06** (2021) 044, arXiv:2011.00217.

[105] LHCb collaboration, R. Aaij *et al.*, *Search for the lepton-flavour violating decay $D^0 \to e^{\pm}\mu^{\mp}$*, Phys. Lett. B **754** (2016) 167, arXiv:1512.00322.

[106] BaBar collaboration, J. P. Lees *et al.*, *Search for lepton-flavor-violating decays $D^0 \to X^0 e^{\pm}\mu^{\mp}$*, Phys. Rev. D **101** (2020) 112003, arXiv:2004.09457.

[107] Belle collaboration, S. Patra *et al.*, *Search for charged lepton flavor violating decays of Υ (1S)*, JHEP **05** (2022) 095, arXiv:2201.09620.

[108] BaBar collaboration, J. P. Lees *et al.*, *Search for Lepton Flavor Violation in $\Upsilon(3S) \to e^{\pm}\mu^{\mp}$*, Phys. Rev. Lett. **128** (2022) 091804, arXiv:2109.03364.

[109] ATLAS collaboration, G. Aad *et al.*, *Search for the charged-lepton-flavor-violating decay $Z \to e\mu$ in pp collisions at $\sqrt{s} = 13$ TeV with the ATLAS detector*, Phys. Rev. D **108** (2023) 032015, arXiv:2204.10783.

[110] CMS collaboration, A. Hayrapetyan *et al.*, *Search for the lepton-flavor violating decay of the Higgs boson and additional Higgs bosons in the $e\mu$ final state in proton-proton collisions at $\sqrt{s} = 13$ TeV*, Phys. Rev. D **108** (2023) 072004, arXiv:2305.18106.

[111] CMS, A. Tumasyan *et al.*, *Search for charged-lepton flavor violation in top quark production and decay in pp collisions at* $\sqrt{s}$ *= 13 TeV*, JHEP **06** (2022) 082, arXiv:2201.07859.

[112] Belle, R. Dhamija *et al.*, *Search for charged-lepton flavor violation in* $\Upsilon(2S) \to \ell^{\mp}\tau^{\pm}$ *($\ell = e, \mu$) decays at Belle*, JHEP **02** (2024) 187, arXiv:2309.02739.

[113] BaBar collaboration, J. P. Lees *et al.*, *Search for Charged Lepton Flavor Violation in Narrow Upsilon Decays*, Phys. Rev. Lett. **104** (2010) 151802, arXiv:1001.1883.

[114] ATLAS collaboration, G. Aad *et al.*, *Search for lepton-flavor-violation in Z-boson decays with τ-leptons with the ATLAS detector*, Phys. Rev. Lett. **127** (2022) 271801, arXiv:2105.12491.

[115] CMS collaboration, *Search for lepton-flavor violating decays of the Higgs boson in the $\mu\tau$ and $e\tau$ final states in proton-proton collisions at $\sqrt{s}$ = 13 TeV pp collisions*, Physical Review D **104** (2021) .

[116] ATLAS, G. Aad *et al.*, *Search for charged-lepton-flavor violating $\mu\tau qt$ interactions in top-quark production and decay in pp collisions at s=13 TeV with the ATLAS detector at the LHC*, Phys. Rev. D **110** (2024) 012014, arXiv:2403.06742.

[117] ATLAS collaboration, G. A. et al. *Searches for lepton-flavour-violating decays of the higgs boson into $e\tau$ and $\mu\tau$ in $\sqrt{s}$ = 13 tev pp collisions with the atlas detector*, Journal of High Energy Physics **2023** (2023) .

[118] C. A. Gottardo, *Search for charged lepton-flavour violation in top-quark decays at the LHC with the ATLAS detector*, PhD thesis, Bonn U., 2018, arXiv:1809.09048.

[119] MEG collaboration, A. M. Baldini *et al.*, *Search for the lepton flavour violating decay $\mu^+ \to e^+\gamma$ with the full dataset of the MEG experiment*, Eur. Phys. J. C **76** (2016) 434, arXiv:1605.05081.

[120] SINDRUM collaboration, U. Bellgardt *et al.*, *Search for the Decay $\mu^+ \to e^+e^+e^-$*, Nucl. Phys. B **299** (1988) 1.

[121] C. Dohmen *et al.*, *Test of lepton-flavour conservation in $\mu \to e$ conversion on titanium*, Physics Letters B **317** (1993) 631.

[122] SINDRUM II collaboration, W. H. Bertl *et al.*, *A Search for muon to electron conversion in muonic gold*, Eur. Phys. J. C **47** (2006) 337.

[123] J. Kaulard *et al.*, *Improved limit on the branching ratio of $\mu^- \to e^+$ conversion on titanium*, Physics Letters B **422** (1998) 334.

[124] BaBar collaboration, B. Aubert *et al.*, *Searches for Lepton Flavor Violation in the Decays tau$^{\pm} \to e^{\pm}\gamma$ and tau$^{\pm} \to \mu^{\pm}\gamma$*, Phys. Rev. Lett. **104** (2010) 021802, arXiv:0908.2381.

[125] K. Hayasaka *et al.*, *Search for Lepton Flavor Violating Tau Decays into Three Leptons with 719 Million Produced Tau+Tau- Pairs*, Phys. Lett. B **687** (2010) 139, arXiv:1001.3221.

[126] Belle collaboration, Y. Miyazaki *et al.*, *Search for Lepton-Flavor-Violating and Lepton-Number-Violating $\tau \to \ell hh'$ Decay Modes*, Phys. Lett. B **719** (2013) 346, arXiv:1206.5595.

[127] Belle collaboration, Y. Miyazaki *et al.*, *Search for Lepton Flavor Violating tau- Decays into \ell-K0s and \ell-K0sK0s*, Phys. Lett. B **692** (2010) 4, arXiv:1003.1183.

[128] Belle collaboration, Y. Miyazaki *et al.*, *Search for lepton flavor violating tau-decays into l- eta, l- eta-prime and l- pi0*, Phys. Lett. B **648** (2007) 341, arXiv:hep-ex/0703009.

[129] BaBar collaboration, B. Aubert *et al.*, *Search for Lepton Flavor Violating Decays $\tau^{\pm} \to \ell^{\pm}\pi^0$, $\ell^{\pm}\eta$, $\ell^{\pm}\eta'$*, Phys. Rev. Lett. **98** (2007) 061803, arXiv:hep-ex/0610067.

[130] Belle collaboration, N. Tsuzuki *et al.*, *Search for lepton-flavor-violating τ decays into a lepton and a vector meson using the full Belle data sample*, JHEP **06** (2023) 118, arXiv:2301.03768.

[131] L. Evans and P. Bryant, *LHC Machine*, Journal of Instrumentation **3** (2008) S08001.

[132] ATLAS collaboration, *The ATLAS Experiment at the CERN Large Hadron Collider*, Journal of Instrumentation **3** (2008) S08003.

[133] CMS collaboration, *The CMS experiment at the CERN LHC*, Journal of Instrumentation **3** (2008) S08004.

[134] ALICE collaboration, *The ALICE experiment at the CERN LHC*, Journal of Instrumentation **3** (2008) S08002.

[135] LHCf collaboration, *The LHCf detector at the CERN Large Hadron Collider*, Journal of Instrumentation **3** (2008) S08006.

[136] MoEDAL collaboration, J. Pinfold *et al.*, *Technical Design Report of the MoEDAL Experiment*, https://cds.cern.ch/record/1181486, 2009.

[137] CERN, *CERN releases analysis of LHC Incident*, https://home.cern/news/press-release/cern/cern-releases-analysis-lhc-incident, 2008.

[138] S. Fenkart, *Electrical perturbation uproots Run 3 operations*, https://cerncourier.com/a/electrical-perturbation-uproots-run-3-operations/. 24 August 2023.

[139] R. Calaga, *Crab cavities for High Luminosity LHC*, https://cds.cern.ch/record/2673544/files/thxa03.pdf, 2019.

[140] I. Raynova, *Crab cavities: colliding protons head-on*, https://home.cern/news/news/accelerators/crab-cavities-colliding-protons-head, 2017.

[141] B. Schmidt, *The High-Luminosity upgrade of the LHC: Physics and Technology Challenges for the Accelerator and the Experiments*, Journal of Physics: Conference Series **706** (2016) 022002.

[142] LHCb collaboration, R. Aaij *et al.*, *Measurement of the inelastic pp cross-section at a centre-of-mass energy of 13 TeV*, JHEP **06** (2018) 100, arXiv:1803.10974.

[143] LHCb collaboration, R. Aaij *et al.*, *Measurement of the b-quark production cross-section in 7 and 13 TeV*, Physical Review Letters **118** (2017) .

[144] LHCb collaboration, C. Elsasser, *$\bar{b}b$ production angle plots*, https://lhcb.web.cern.ch/lhcb/speakersbureau/html/bb_ProductionAngles.html.

[145] LHCb collaboration, *LHCb Integrated luminosity*, https://lbgroups.cern.ch/online/OperationsPlots/index.htm, 2024.

[146] J. Albrecht *et al.*, *Luminosity scenarios for LHCb Upgrade II*, https://cds.cern.ch/record/2653011, 2019.

[147] LHCb collaboration, *LHCb operations*, https://twiki.cern.ch/twiki/bin/view/LHCb/LHCbOperations, 2024.

[148] LHCb collaboration, R. Aaij *et al.*, *LHCb VELO (VErtex LOcator): Technical Design Report*, CERN-LHCC-2001-011, 2001.

[149] LHCb collaboration, R. Aaij *et al.*, *LHCb magnet: Technical Design Report*, CERN-LHCC-2000-007, 2000.

[150] LHCb collaboration, R. Aaij *et al.*, *LHCb inner tracker: Technical Design Report*, CERN-LHCC-2002-029, 2002.

[151] LHCb collaboration, R. Aaij *et al.*, *LHCb outer tracker: Technical Design Report*, CERN-LHCC-2001-024, 2001.

[152] LHCb collaboration, R. Aaij *et al.*, *LHCb RICH: Technical Design Report*, CERN-LHCC-2000-037, 2000.

[153] LHCb collaboration, R. Aaij *et al.*, *LHCb calorimeters: Technical Design Report*, CERN-LHCC-2000-036, 2000.

[154] LHCb collaboration, R. Aaij *et al.*, *LHCb muon system: Technical Design Report*, CERN-LHCC-2001-010, 2001.

[155] LHCb collaboration, R. Aaij *et al.*, *LHCb trigger system: Technical Design Report*, CERN-LHCC-2003-031, 2003.

[156] M. Williams *et al.*, *The HLT2 Topological Lines*, https://cds.cern.ch/record/1323557, 2011.

[157] LHCb, R. Aaij *et al.*, *The LHCb Upgrade I*, JINST **19** (2024) P05065, arXiv:2305.10515.

[158] LHCb collaboration, *The LHCb upgrade I*, arXiv:2305.10515.

[159] LHCb collaboration, R. Aaij *et al.*, *Computing Model of the Upgrade LHCb experiment*, CERN-LHCC-2018-014, 2018.

[160] A. Piucci, *The LHCb Upgrade*, Journal of Physics: Conference Series **878** (2017) 012012.

[161] L. collaboration, *Implications of LHCb measurements and future prospects*, The European Physical Journal C **73** (2013) .

[162] L. E. LHCb Collaboration, *Future physics potential of LHCb*, tech. rep., CERN, Geneva, 2022.

[163] LHCb collaboration, *Letter of Intent for the LHCb Upgrade*, https://cds.cern.ch/record/1333091, 2011.

[164] LHCb, *Simultaneous determination of the CKM angle γ and parameters related to mixing and CP violation in the charm sector*, .

[165] LHCb, R. Aaij *et al.*, *Measurement of CP Violation in $B0\to\psi(\to\ell+\ell-)KS0(\to\pi+\pi-)$ Decays*, Phys. Rev. Lett. **132** (2024) 021801, arXiv:2309.09728.

[166] LHCb, R. Aaij *et al.*, *Observation of CP Violation in Charm Decays*, Phys. Rev. Lett. **122** (2019) 211803, arXiv:1903.08726.

[167] R. Quagliani, *Study of double charm B decays with the LHCb experiment at CERN and track reconstruction for the LHCb upgrade*, theses, Université Paris Saclay (COmUE) ; University of Bristol, 2017, tel-03563283.

[168] LHCb collaboration, R. Aaij *et al.*, *LHCb VELO Upgrade Technical Design Report*, CERN-LHCC-2013-021, 2013.

[169] T. Poikela *et al.*, *VeloPix: the pixel ASIC for the LHCb upgrade*, Journal of Instrumentation **10** (2015) C01057.

[170] LHCb collaboration, R. Aaij *et al.*, *LHCb Tracker Upgrade Technical Design Report*, CERN-LHCC-2014-001, 2014.

[171] T. O. White, *Scintillating fibres*, Nuclear Instruments and Methods in Physics Research Section A: Accelerators, Spectrometers, Detectors and Associated Equipment **273** (1988) 820.

[172] C. Joram, G. Haefeli, and B. Leverington, *Scintillating fibre tracking at high luminosity colliders*, Journal of Instrumentation **10** (2015) C08005.

[173] P. Hopchev, *SciFi: A large Scintillating Fibre Tracker for LHCb*, arXiv:1710.08325.

[174] LHCb collaboration, R. Aaij *et al.*, *LHCb PID Upgrade Technical Design Report*, CERN-LHCC-2013-022, 2013.

[175] LHCb collaboration, E. Picatoste, *LHCb Calorimeter Upgrade Electronics*, in *International Conference on Calorimetry for the High Energy Frontier*, 363–368, 2013. CHEP2013.

[176] LHCb collaboration, *Framework TDR for the LHCb Upgrade: Technical Design Report*, CERN-LHCC-2012-007, 2012.

[177] LHCb collaboration, *LHCb's unique approach to real-time data processing.*, https://lhcb-outreach.web.cern.ch/2023/03/01/lhcbs-unique-approach-to-real-time-data-processing/.

[178] LHCb collaboration, *Architecture of the LHCb Upgrade trigger*, https://lhcbdoc.web.cern.ch/lhcbdoc/moore/master/design/architecture.html.

[179] LHCb collaboration, *Welcome to allen's documentation!*, https://allen-doc.docs.cern.ch/index.html.

[180] LHCb collaboration, *Welcome to the data processing & analysis (dpa) project*, https://lhcb-dpa.web.cern.ch/lhcb-dpa/index.html.

[181] LHCb collaboration, *RTA and DPA dataflow diagrams for Run 1, Run 2, and the upgraded LHCb detector*, https://cds.cern.ch/record/2730181, 2020.

[182] LHCb collaboration, *Thor functors*, https://lhcbdoc.web.cern.ch/lhcbdoc/moore/master/selection/thor_functors.html.

[183] GeeksforGeeks, *Functors in C++*, https://www.geeksforgeeks.org/functors-in-cpp/. 2023.

[184] LHCb collaboration, *Control flow - Moore documentation*, https://lhcbdoc.web.cern.ch/lhcbdoc/moore/master/pyconf/control_flow.html.

[185] LHCb collaboration, *Gaudi documentation*, https://gaudi-framework.readthedocs.io/en/latest/.

[186] S. M. Mniszewski *et al.*, *Enabling particle applications for exascale computing platforms*, The International Journal of High Performance Computing Applications **35** (2021) 572–597.

[187] LHCb collaboration, *Thor functors reference*, https://lhcbdoc.web.cern.ch/lhcbdoc/moore/master/selection/thor_functors_reference.html.

[188] A. Mathad *et al.*, *Funtuple: A new n-tuple component for offline data processing at the lhcb experiment*, Computing and Software for Big Science **8** (2024) .

[189] M. Clemencic *et al.*, *LHCb conditions database operation assistance systems*, J. Phys. Conf. Ser. **396** (2012) 052022.

[190] LHCb collaboration, *Gitconddb*, https://lhcb-core-doc.web.cern.ch/lhcb-core-doc/GitCondDB.html.

[191] LHCb collaboration, *Store event information*, https://lhcb-davinci.docs.cern.ch/examples/tupling/option_davinci_tupling_eventinfo.html.

[192] R. Aaij *et al.*, *A comprehensive real-time analysis model at the LHCb experiment*, JINST **14** (2019) P04006, arXiv:1903.01360.

[193] J. Cerasoli, *Search for the rare $B^0 \to K^{*0}\tau^+\tau^-$ decay with the LHCb experiment*, PhD thesis, CPPM, Marseille, 2021, Thèse de doctorat dirigée par Mancinelli, Giampiero et Cogan, Julien Physique des particules et astroparticules Aix-Marseille 2021.

[194] A. Venkateswaran, *Probing lepton flavour universality with $B^0 \to K^{*0}\tau^+\tau^-$* , PhD thesis, Syracuse University, 2022, Dissertation 09 Mar 2022.

[195] LHCb collaboration, *Relation tables and isolation variables*, https://lhcb-davinci.docs.cern.ch/examples/tupling/option_davinci_tupling_relation_isovariables.html.

[196] S. Jadach, J. H. Kuhn, and Z. Was, *TAUOLA - a library of Monte Carlo programs to simulate decays of polarized tau leptons*, Computer Physics Communications **64** (1991) 275.

[197] Z. Was, *Tau lepton production and decays: perspective of multi-dimensional distributions and Monte Carlo methods*, Nuclear and Particle Physics Proceedings **287-288** (2017) 15, The 14th International Workshop on Tau Lepton Physics.

[198] R. Alonso, B. Grinstein, and J. Martin Camalich, *Lepton universality violation and lepton flavor conservation in B-meson decays*, JHEP **10** (2015) 184, arXiv:1505.05164.

[199] L. Anderlini *et al.*, *The PIDCalib package*, LHCb-PUB-2016-021, 2016.

[200] T. Sjöstrand, S. Mrenna, and P. Skands, *A brief introduction to PYTHIA 8.1*, Comput. Phys. Commun. **178** (2008) 852, arXiv:0710.3820.

[201] D. J. Lange, *The EvtGen particle decay simulation package*, Nucl. Instrum. Meth. **A462** (2001) 152.

[202] Geant4 collaboration, S. Agostinelli *et al.*, *Geant4: A simulation toolkit*, Nucl. Instrum. Meth. **A506** (2003) 250.

[203] Geant4 collaboration, J. Allison *et al.*, *Geant4 developments and applications*, IEEE Trans. Nucl. Sci. **53** (2006) 270.

[204] LHCb collaboration, R. Aaij *et al.*, *Search for the rare decay* $B^+ \to \mu^+\mu^-\mu^+\nu_\mu$, Eur. Phys. J. **C79** (2019) 675, arXiv:1812.06004.

[205] J. Maratas, S. Monteil, and G. Wormser, *A technique for partial reconstruction of decays involving a resonance in the decay chain*, https://cds.cern.ch/record/1646080, 2014.

[206] Particle Data Group, P. A. Zyla *et al.*, *Review of particle physics*, to be published in Prog. Theor. Exp. Phys. **6** (2020) 083C01.

[207] W. D. Hulsbergen, *Decay chain fitting with a kalman filter*, Nuclear Instruments and Methods in Physics Research Section A: Accelerators, Spectrometers, Detectors and Associated Equipment **552** (2005) 566–575.

[208] S. Tolk, J. Albrecht, F. Dettori, and A. Pellegrino, *Data driven trigger efficiency determination at LHCb*, LHCb-PUB-2014-039, 2014.

[209] S. Tolk, J. Albrecht, F. Dettori, and A. Pellegrino, *Data driven trigger efficiency determination at LHCb*, https://cds.cern.ch/record/1701134, 2014.

[210] A. Hoecker *et al.*, *TMVA 4 — Toolkit for Multivariate Data Analysis with ROOT. Users Guide.*, arXiv:physics/0703039.

[211] CERN, *TMVACrossValidation.C File Reference*, https://root.cern/doc/master/TMVACrossValidation_8C.html.

[212] G. Punzi, *Sensitivity of searches for new signals and its optimization*, eConf **C030908** (2003) MODT002, arXiv:physics/0308063.

[213] LHCb collaboration, *Measurement of the electron reconstruction efficiency at LHCb*, Journal of Instrumentation **14** (2019) P11023.

[214] LHCb collaboration, *Electron tracking efficiency*, https://twiki.cern.ch/twiki/bin/viewauth/LHCbInternal/Velo2longElectronTrackingEfficiency.

[215] M. Pivk and F. R. Le Diberder, *SPlot: A Statistical tool to unfold data distributions*, Nucl. Instrum. Meth. A **555** (2005) 356, arXiv:physics/0402083.

[216] LHCb collaboration, *TrackCalib*, https://twiki.cern.ch/twiki/bin/view/LHCb/TrackCalib.

[217] *PIDCalib Packages*, https://twiki.cern.ch/twiki/bin/view/LHCb/PIDCalibPackage.

[218] K. Cranmer, *Kernel estimation in high-energy physics*, Computer Physics Communications **136** (2001) 198–207.

[219] L. M. Lederman and C. T. Hill, *Symmetry and the Beautiful Universe*, G - Reference, Information and Interdisciplinary Subjects Series, Prometheus Books, 2004.

[220] J. Goldstone, A. Salam, and S. Weinberg, *Broken symmetries*, Phys. Rev. **127** (1962) 965.

[221] J. H. Christenson, J. W. Cronin, V. L. Fitch, and R. Turlay, *Evidence for the* 2π *Decay of the* K_2^0 *Meson*, Phys. Rev. Lett. **13** (1964) 138.